A multi-domain biophysical computational model of cardiac action potential propagation in cell monolayers

Charles Peter James Houston

A thesis presented for the degree of

Doctor of Philosophy

ElectroCardioMaths Programme

Centre for Cardiac Engineering

National Heart & Lung Institute

Imperial College London

January 2021

Declaration

I declare that this thesis, and the research therein, is the product of my own work and does not contain material previously written or published by another person or submitted for another award, except where acknowledgement has been given in the text.

The copyright of this thesis rests with the author. Unless otherwise indicated, its contents are licensed under a Creative Commons Attribution 4.0 International Licence (CC BY).

Under this licence, you may copy and redistribute the material in any medium or format for both commercial and non-commercial purposes. You may also create and distribute modified versions of the work. This on the condition that you credit the author.

When reusing or sharing this work, ensure you make the licence terms clear to others by naming the licence and linking to the licence text. Where a work has been adapted, you should indicate that the work has been changed and describe those changes.

Please seek permission from the copyright holder for uses of this work that are not included in this licence or permitted under UK Copyright Law.

Abstract

The goal of this thesis is to develop a biophysically and geometrically accurate discrete-cell computational model of cardiac action potential propagation in HL1-6 cell monolayers. HL1-6 cells are a murine atrial cell line which have slow conduction velocity in a monolayer enabling propagation to be captured experimentally at the cellular level, which is crucial in validating simulations as they shift towards advising clinical treatments.

The biological model is first characterised by means of recording propagation using fluorescence microscopy. HL1-6 cell monolayers exhibit self-sustaining activity similar to re-entry/rotors observed *in vivo*. This activity is found to require a minimum area in which to initiate, and remains anchored around distinct lines of conduction block/slowing.

A Bayesian calibration approach is investigated to capture biological variability and experimental uncertainty in action potential models. In retrospective analyses of two human atrial cell models, simpler model structures generally resulted in higher confidence in parameter estimates. The method is applied to construct an action potential model of an HL1-6 myocyte, which compares well to experimental measurements of individual ion currents, action potentials and calcium transients, and exhibits automaticity akin to the *in vitro* model.

A multi-domain computational model of action potential propagation is developed using the spectral/hp element method and validated against theoretical and experimental results. When combined with the HL1-6 action potential model in realistic monolayer geometries, meandering self-sustaining activity could be initiated, requiring sufficient area to avoid terminating on a boundary. Increasing gap junction resistance along a thin line anchored the activity in a fashion qualitatively similar to that observed *in vitro*.

Acknowledgements

This thesis, and the work therein, would not have been possible without the tireless support, insightful conversations and inspiring teaching of many individuals and teams. If I have managed to achieve anything, it is only as a result of being raised on their shoulders.

I would like to start by thanking my primary supervisors: Dr Chris Cantwell, Dr Rasheda Chowdhury and Dr Emmanuel Dupont. Chris, I will be eternally grateful for the time you dedicated to our project and the many fruitful discussions and scribblings, particularly during the final stages of what ended up being an unfortunately testing year. Rasheda, your breadth of expertise in cardiac research and cell biology combined with your natural ability to teach for understanding were instrumental to my own work, as well as to so many others. Emman, thank you for the many conversations and debates with a truly passionate scientist, helping to inspire and drive this research forward.

Thank you to all in the continually evolving ElectroCardioMaths group, now part of the Imperial Centre for Cardiac Engineering, led by Professor Nicholas Peters. Nick, you have created something extremely special with this team of diverse individuals, not least of all fertile ground for novel research. Thank you for your advice and support during my time in the group, and your welcome challenges to always keep us focused on the ultimate goal of improving lives of patients. Thank you also to all in NHLI who advised and provided training throughout various stages of this project. In particular, to Mr Stephen Rothery for his expertise in microscopy and for entertaining my more 'ambitious' experiments.

This work would not have been possible without the generous support of the British

Heart Foundation, who also support so many important scientific projects throughout the UK. The BHF Centre of Research Excellence nurtures the kind of cross-disciplinary collaboration essential in the drive towards improving lives through cardiac research, and I am honoured to have been a part of it.

To all my friends through running, sub-wardening and beyond, thank you for adding colour to life outside of academia. Chats over coffees and lunches were welcome breaks, and often indirectly useful for research. Sometimes all you need after a long day of work is a conversational run around Hyde Park or along the Thames, or a less-conversational interval session with Thames Valley Harriers, all of which I look back on fondly. To my trail running friends, thanks for the adventures to places with slightly steeper gradients than London. Running a hall full of undergraduates alongside research was certainly 'character-building' at times, but the company was consistently stellar.

Eve, thank you for always selflessly being there to help me enjoy the brighter side of life, especially during the locked-down final stages of writing.

Lastly, I am fortunate to have the continuous support, guidance and encouragement of a loving and inspiring family. Without you, I would not be who I am today.

Far better it is to dare mighty things...even though checkered by failure, than to rank with those timid spirits who neither enjoy nor suffer much because they live in the gray twilight that knows not victory or defeat.

– Theodore Roosevelt

What I cannot create, I do not understand.

– Richard Feynman

Table of contents

Declaration . . . 2
Abstract . . . 3
Acknowledgements . . . 4
Table of contents . . . 11
List of figures . . . 14
List of tables . . . 16
List of abbreviations . . . 17

1 Introduction **18**
1.1 Physiological background . . . 18
1.1.1 Cardiac contraction . . . 18
1.1.2 Genesis of an action potential . . . 19
1.1.3 Gap junctions . . . 21
1.1.4 Action potential propagation . . . 23
1.1.5 Self-sustaining activity . . . 23
1.1.6 *In vitro* models of arrhythmia . . . 25
1.2 Computational background . . . 26
1.2.1 Modelling an action potential . . . 27
1.2.2 Continuum models of cardiac propagation . . . 27
1.2.3 Discrete models of cardiac propagation . . . 28
1.2.4 Uncertainty and variability in cardiac modelling . . . 30
1.3 Thesis outline . . . 31

2 Self-sustaining activity in HL1-6 cell monolayers **34**
2.1 Introduction . . . 34
2.2 Methods . . . 35
2.2.1 Cell culture . . . 35
2.2.2 Cryo-preservation . . . 36
2.2.3 Seeding round colonies of controlled area . . . 36
2.2.4 Anisotropic monolayers . . . 37
2.2.5 Optical mapping . . . 37
2.2.6 Imaging cell morphology . . . 39
2.2.7 Quantifying occurrence of triggers and self-sustaining activity . . . 39
2.2.8 Stability of triggers and self-sustaining activity . . . 40
2.2.9 Data processing and analysis . . . 40
2.2.10 Statistical analysis . . . 42
2.3 Results . . . 43
2.3.1 Prevalence of self-sustaining activity in microscopic colonies . . . 43
2.3.2 Spatial stability of triggers and self-sustaining activity . . . 44

2.3.3 Characteristics of self-sustaining activity . . . 46
2.3.4 Closer look at the core of self-sustaining activity . . . 49
2.3.5 Comparing recordings of self-sustaining activity with voltage and Ca^{2+} dyes . . . 53
2.3.6 Self-sustaining activity in anisotropic monolayers . . . 56
2.4 Discussion . . . 59
2.4.1 Self-sustaining activity can be initiated from few triggers but requires a minimum area . . . 60
2.4.2 Natural triggers remain spatially stable while self-sustaining activity can form in multiple locations . . . 61
2.4.3 The 'cores' of the stable self-sustaining activity have distinct shapes 62
2.4.4 Cells within the core of the self-sustaining circuit may exhibit activation activity . . . 64
2.4.5 The core of self-sustaining activity aligns with the direction of anisotropy in the monolayer . . . 66
2.4.6 Limitations . . . 67

3 Likelihood-free inference of action potential model parameters 69
3.1 Introduction . . . 69
3.2 Methods . . . 72
3.2.1 Action potential models . . . 72
3.2.2 Data sets and calibration . . . 74
3.2.3 Approximate Bayesian computation . . . 76
3.2.4 Extending approximate Bayesian computation to quantify model discrepancy . . . 80
3.2.5 Calibration algorithm settings . . . 80
3.2.6 Implementation . . . 81
3.2.7 Action potential simulations . . . 82
3.3 Results . . . 83
3.3.1 Existing gating parameter uncertainties . . . 83
3.3.2 Recalibrating to a unified data set . . . 85
3.3.3 Comparing to a standardised model . . . 87
3.3.4 Effect on action potential . . . 99
3.3.5 Including model discrepancy . . . 102
3.4 Discussion . . . 104
3.4.1 Incomplete data sets reduce the ability to identify parameter values 105
3.4.2 Complete data sets do not necessarily reduce the uncertainty around all parameters in more complex models . . . 106
3.4.3 Reducing structural complexity is a trade-off between parameter identifiability and tailoring for specific currents . . . 107
3.4.4 Channel models should be calibrated with both patch clamp data and observing changes in action potentials . . . 110
3.4.5 Model discrepancy can be included as additional parameters in approximate Bayesian computation . . . 110
3.4.6 Limitations . . . 111

4 An HL1-6 action potential model accounting for biological variability and uncertainty 113
4.1 Introduction . . . 113
4.2 Methods . . . 115
4.2.1 Model structure . . . 115
4.2.2 Likelihood-free inference settings . . . 118
4.2.3 Ion channel calibration data sets . . . 119
4.2.4 Whole cell calibration . . . 120
4.2.5 Sensitivity analysis . . . 125
4.2.6 Automaticity . . . 125
4.2.7 Validation through ion channel blocking . . . 126
4.3 Results . . . 127
4.3.1 Fast Na^+ current (I_{Na}) . . . 127
4.3.2 L-type Ca^{2+} current (I_{CaL}) . . . 129
4.3.3 T-type Ca^{2+} current (I_{CaT}) . . . 133
4.3.4 Rapidly-activating delayed rectifier K^+ current (I_{Kr}) . . . 135
4.3.5 4-AP-sensitive K^+ currents (I_{to}, I_{ss}) . . . 135
4.3.6 Hyperpolarisation-activated 'funny' current (I_f) . . . 137
4.3.7 Inward rectifier K^+ current (I_{K1}) . . . 138
4.3.8 Background currents (I_{Nab}, I_{Cab}) . . . 140
4.3.9 Sarcolemmal pump and exchanger currents (I_{NCX}, I_{NaK}, I_{pCa}) . . . 141
4.3.10 Sarcoplasmic reticulum fluxes (J_{RyR}, J_{SERCA}, J_{leak}, J_{tr}) . . . 142
4.3.11 Channel gating functions . . . 143
4.3.12 Complete cell calibration . . . 143
4.3.13 Parameter sensitivity . . . 149
4.3.14 Spontaneous automaticity . . . 154
4.3.15 Effect of blocking ion channel currents . . . 155
4.3.16 Restitution properties . . . 160
4.4 Discussion . . . 161
4.4.1 Standardised ion channel gating models calibrated well to experimental data . . . 161
4.4.2 The complete cell model closely matches experimental data and accounts for variability . . . 163
4.4.3 Incorporating the 'funny' current results in spontaneous automaticity in a subset of model variants . . . 164
4.4.4 Blocking ion channels has a similar qualitative effect to experimental measurements in the original cell line . . . 166
4.4.5 Limitations . . . 167

5 A multi-domain discrete-cell model of action potential propagation 169
5.1 Introduction . . . 169
5.1.1 The cable equation . . . 171
5.2 Methods . . . 176
5.2.1 Spectral/hp element method . . . 176
5.2.2 Numerical implementation in one dimension . . . 182
5.2.3 Numerical implementation in three dimensions . . . 184
5.2.4 Parallelisation . . . 190
5.2.5 Simulation setup . . . 192

5.3 Results . . . 196
5.3.1 Validating the numerical implementation in one dimension . . . 196
5.3.2 Model validation in three dimensions . . . 198
5.3.3 Propagation along a cable of cells . . . 200
5.3.4 Parallel scaling performance . . . 201
5.4 Discussion . . . 205

6 Investigating the genesis of self-sustaining rotational activity 209
6.1 Introduction . . . 209
6.2 Methods . . . 211
6.2.1 Creating a representative monolayer geometry . . . 211
6.2.2 Monolayer geometries . . . 213
6.2.3 Incorporating the HL1-6 cell model . . . 214
6.2.4 Simulation set-up . . . 216
6.2.5 Stimulation protocols . . . 217
6.3 Results . . . 218
6.3.1 Creating HL1-6 cell monolayer geometries . . . 218
6.3.2 Calibrating gap junction resistance . . . 221
6.3.3 Validation through pharmacological block of ion currents . . . 224
6.3.4 Conduction velocity restitution . . . 225
6.3.5 Monolayer size requirement for self-sustaining activity . . . 227
6.3.6 Increasing variability of gap junction resistance . . . 228
6.3.7 Concentrated increase in gap junction resistance . . . 230
6.4 Discussion . . . 232
6.4.1 Conduction velocity calibration and validation . . . 233
6.4.2 Restitution . . . 234
6.4.3 Lack of automaticity in the monolayer . . . 234
6.4.4 Simulated self-sustaining activity . . . 235
6.4.5 Limitations . . . 238

7 Conclusions and future work 239

Bibliography 264

A Appendices 265
A.1 Human atrial model equations and numerical results from calibration . . . 265
A.1.1 Fast Na^+ channel, I_{Na} . . . 265
A.1.2 L-type Ca^{2+} channel, I_{CaL} . . . 270
A.1.3 Transient outward K^+ channel, I_{to} . . . 275
A.1.4 Ultra-rapidly activating delayed rectifier K^+ channel, I_{Kur} . . . 279
A.2 Voltage-clamp protocols and summary statistic functions for human atrial experiments . . . 284
A.2.1 Fast Na^+ channel, I_{Na} . . . 284
A.2.2 L-type Ca^{2+} channel, I_{CaL} . . . 286
A.2.3 Transient outward K^+ channel, I_{to} . . . 288
A.2.4 Ultra-rapidly activating delayed rectifier K^+ channel, I_{Kur} . . . 292
A.3 HL1-6 cell model calibration results . . . 294
A.4 Derivation of the cable equation . . . 298

A.5 Derivation of constant transmembrane potential held at one end of 1D discretely-coupled cells 300
A.6 Derivation of analytical solution to injected current into a cable of 1D discretely-coupled cells 302

List of Figures

1.1 Conduction system of the heart . . . 19

2.1 Seeding drop monolayers . . . 37
2.2 Conduction delay visualisation algorithm . . . 43
2.3 Occurrence of self-sustaining activity in HL1-6 monolayers . . . 44
2.4 Quantifying natural triggers in HL1-6 monolayers . . . 45
2.5 Spatial stability of triggers and self-sustaining activity . . . 46
2.6 Electrical uncoupling activation maps . . . 47
2.7 Conduction delay maps of self-sustaining activity . . . 48
2.8 Convex hull perimeter estimation . . . 48
2.9 Perimeter compared to dominant frequency, and conduction velocities at circuit core . . . 49
2.10 Comparing morphology to conduction block region . . . 50
2.11 Activity in the vicinity of the core of the self-sustaining circuit . . . 52
2.12 Dual optical mapping of voltage and Ca^{2+} transients . . . 54
2.13 Comparing voltage and Ca^{2+} recordings . . . 57
2.14 Results from anisotropy experiments . . . 58

3.1 Demonstrating existing parameter uncertainty . . . 84
3.2 Relative standard deviation of parameter posterior distributions for original and unified data set calibration . . . 86
3.3 Posterior gating functions for Nygren model after calibration to original and unified data sets . . . 88
3.4 Posterior gating functions for Courtemanche model after calibration to original and unified data sets . . . 89
3.5 Comparing a standardised model calibration with fewer parameters to original models . . . 90
3.6 Calibration of fast Na^+ channel model . . . 92
3.7 Calibration of L-type Ca^{2+} channel model . . . 94
3.8 Calibration of transient outward K^+ channel model . . . 96
3.9 Calibration of ultra-rapidly activating delayed rectifier K^+ channel model . . . 98
3.10 Effect of variability on action potential measurements . . . 100
3.11 Effect of variability on action potential traces . . . 101
3.12 Including discrepancy as a calibration parameter . . . 103

4.1 HL1-6 fast Na^+ channel model . . . 130
4.2 HL1-6 L-type Ca^{2+} current model . . . 132
4.3 HL1-6 T-type Ca^{2+} current model . . . 134
4.4 HL1-6 delayed rectifier potassium current model . . . 136

4.5 HL1-6 4-AP sensitive K^+ current models . . . 137
4.6 HL1-6 'funny' and inward rectifying current models . . . 139
4.7 Steady-state probabilities and time constants for all channels . . . 144
4.8 Relative standard deviation of calibrated parameter posterior distributions for channels in HL1-6 cell model . . . 145
4.9 Whole cell calibration (1) . . . 146
4.10 Whole cell calibration (2) . . . 147
4.11 Correlation between whole cell calibration measurements . . . 148
4.12 Current and voltage traces during an action potential . . . 150
4.13 Calcium handling during an action potential . . . 151
4.14 Sensitivity of HL1-6 cell model conductances (action potential) . . . 152
4.15 Sensitivity of HL1-6 cell model conductances (calcium transient) . . . 153
4.16 HL1-6 cell model automaticity . . . 156
4.17 Dose response curves for ion channel blocking . . . 157
4.18 Ion current blocking response . . . 159
4.19 Restitution of HL1-6 cell model . . . 160

5.1 The continuous cable equation and equivalent circuit . . . 172
5.2 The discontinuous cable equation and equivalent circuit . . . 173
5.3 Analytical solution for a discretely-coupled cable of cells with constant sub-threshold potential at either end . . . 175
5.4 Analytical solution for a discretely-coupled cable of cells with injected current 177
5.5 Parallel implementation for split-rank interfaces . . . 191
5.6 One-dimensional cable simulation results compared to analytical solution for fixed potentials . . . 197
5.7 One-dimensional cable simulation results compared to analytical solution for injected current . . . 198
5.8 Three-dimensional simulations results compared to analytical solution for fixed potential at cable ends . . . 199
5.9 Three-dimensional simulation results compared to analytical solution for current injected into cable . . . 200
5.10 Simulated action potential propagation along an idealised cable . . . 202
5.11 Strong scaling properties of multi-domain model . . . 203
5.12 Weak scaling properties of multi-domain model . . . 204

6.1 Generated 1 mm^2 virtual monolayer . . . 214
6.2 Lower surface of mesh at corner of 4 mm^2 virtual monolayer . . . 215
6.3 Segmentation of confocal microscopy image slices . . . 220
6.4 Measured cross-sectional areas of cells in monolayer . . . 221
6.5 Process to estimate monolayer height . . . 222
6.6 Activation maps and virtual electrograms for gap junction resistance calibration . . . 223
6.7 Gap junction resistance calibration . . . 224
6.8 Effect of blocking fast sodium current and L-type calcium current on conduction velocity through monolayer . . . 225
6.9 Restitution properties of monolayer . . . 226
6.10 Rotational activity terminates at boundary in 1 mm^2 monolayer . . . 227
6.11 Rotational activity self-sustaining in 4 mm^2 monolayer . . . 228

6.12 Effect of increasing variability in gap junction resistance on self-sustaining activity . . . 229
6.13 Effect of increasing gap junction resistance along a line . . . 231
6.14 Comparing conduction block heat maps generated from simulation and experiment . . . 232

A.1 Fast Na^+ current protocols . . . 286
A.2 L-type Ca^{2+} current protocols . . . 289
A.3 Transient outward K^+ current protocols . . . 291
A.4 Ultra-rapidly activating delayed rectifier K^+ current protocols . . . 293

List of Tables

3.1 Patch clamp data sets . . . 75

4.1 HL1-6 model pre-defined parameters with values and sources . . . 117
4.2 Temperature adjustment values . . . 120
4.3 Experimental conditions of data sources . . . 121
4.4 Whole cell calibration parameters . . . 122
4.5 Whole cell calibration experimental conditions . . . 124
4.6 Experimental data set for whole cell calibration . . . 124
4.7 Action of ion channel blocking agents . . . 158

5.1 Parameters to generate analytical cable solutions. . . . 176
5.2 One-dimensional cable simulation parameters and values . . . 192

6.1 Default simulation parameters . . . 216

A.1 Nygren I_{Na} model equations . . . 265
A.2 Numerical results for calibration of Nygren I_{Na} model . . . 266
A.3 Courtemanche I_{Na} model equations . . . 267
A.4 Numerical results for calibration of Courtemanche I_{Na} model . . . 268
A.5 Numerical results for calibration of standardised I_{Na} model . . . 269
A.6 Nygren I_{CaL} model equations . . . 270
A.7 Numerical results for calibration of Nygren I_{CaL} model . . . 271
A.8 Courtemanche I_{CaL} model equations . . . 272
A.9 Numerical results for calibration of Courtemanche I_{CaL} model . . . 273
A.10 Numerical results for calibration of standardised I_{CaL} model . . . 274
A.11 Nygren I_{to} model equations . . . 275
A.12 Numerical results for calibration of Nygren I_{to} model . . . 276
A.13 Courtemanche I_{to} model equations . . . 277
A.14 Numerical results for calibration of Courtemanche I_{to} model . . . 277
A.15 Numerical results for calibration of standardised I_{to} model . . . 278
A.16 Nygren I_{sus} (I_{Kur}) model equations . . . 279
A.17 Numerical results for calibration of Nygren I_{Kur} model . . . 280
A.18 Courtemanche I_{Kur} model equations . . . 281
A.19 Numerical results for calibration of Courtemanche I_{Kur} model . . . 282
A.20 Numerical results for calibration of standardised I_{Kur} model . . . 283
A.21 Numerical results for calibration of HL1-6 I_{Na} model . . . 294
A.22 Numerical results for calibration of HL1-6 I_{CaL} model . . . 294
A.23 Numerical results for calibration of HL1-6 I_{CaT} model . . . 295
A.24 Numerical results for calibration of HL1-6 I_{Kr} model . . . 295

A.25 Numerical results for calibration of HL1-6 I_{to} model 295
A.26 Numerical results for calibration of HL1-6 I_{ss} model 296
A.27 Numerical results for calibration of HL1-6 I_{f} model 296
A.28 Numerical results for calibration of HL1-6 I_{K1} model 296
A.29 Numerical results for calibration of HL1-6 whole cell model 297

List of abbreviations

ABC	Approximate Bayesian computation
APD	Action potential duration
AV	Atrio-ventricular
C	Courtemanche
CaT	Ca^{2+} transient
DMSO	Dimethyl sulfoxide
HBSS	Hank's Balanced Salt Solution
HPDI	Highest posterior density interval
I-V	Current-voltage
MPI	Message Passing Interface
N	Nygren
RSD	Relative standard deviation
S	Standardised
SA	Sino-atrial
TTX	Tetrodotoxin

Chapter 1

Introduction

1.1 Physiological background

1.1.1 Cardiac contraction

The heart is a muscle that regularly contracts to pump blood through the body's vascular system. In humans, the organ has four chambers which fill with blood: two smaller atria (left and right) and two larger ventricles (left and right). During a normal heartbeat, the atria initially contract to push blood into the ventricles which subsequently provide a stronger contraction to pump blood into the wider cardiovascular system. A single contraction of the heart is the result of coordinated contractions of billions of individual cardiac myocytes. These contractions are initiated by regular (or irregular) electrical waves which propagate through the cardiac tissue [1, 2].

In a normal functioning heart, the electrical waves leading to this contraction are initiated from a small group of cells in the right atrium called the sino-atrial (SA) node. These cells spontaneously beat at a regular frequency and modulate the heart rate. From the SA node, electrical waves spread across the rest of the atrial tissue via fast conduction channels and (slower) cell to cell conduction, leading to the atria contracting and pumping blood into the ventricles. The atria and ventricles (in a healthy heart) are electrically separated by non-conductive tissue except for a small region known as the atrio-ventricular (AV) node. The electrical conductive channels in the atria lead to this node, where the

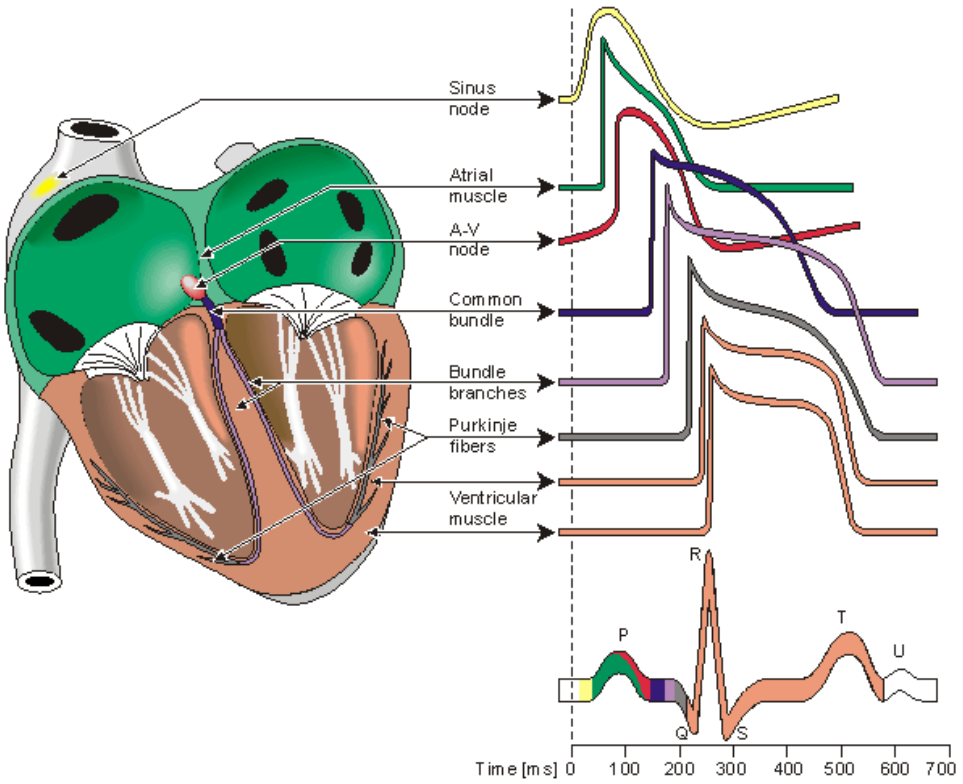


Figure 1.1: Conduction system of the human heart generating an electrocardiogram, adapted from Web open access version of [1]. The traces on the right show representative action potentials from cells in different heart regions. The resulting electrocardiogram is shown in the bottom right graph. Colour is used to indicate the location of specific cells in the organ, and the order of activation in the electrocardiogram.

specialised cells provide a delay until propagation continues into the ventricles. The electrical impulse then travels along further specialised conduction channels to the apices of the ventricles, before spreading across the entire ventricular tissue [1]. Figure 1.1 shows how these activation waves travel through the organ and relate to an electrocardiogram measuring the electrical activity from the body surface.

1.1.2 Genesis of an action potential

The electrical activity driving the function of the heart is composed of the action potential signals from many individual cardiomyocytes [3]. The space within each cell is separated from its surrounding environment by a lipid bilayer membrane. The membrane has selective permeability to different ions (predominantly Na^+, Ca^{2+}, K^+ and Cl^-) and this permeability is mediated by ion-selective protein pores embedded in the membrane which form ion channels, exchangers and pumps. As a result of the selective permeability,

there is a large difference in ion concentrations inside and outside the cell and a high concentration gradient across the membrane. This difference in ion concentrations also causes a net imbalance of charges, resulting in a transmembrane potential difference and an electric field in the membrane [2].

Ion flow across the membrane is determined by the diffusion forces on ions due to the concentration difference between the two spaces, and electric field forces. Each ion has a different equilibrium potential, defined as the potential at which these two forces will balance each other to give a net zero ion flux. The difference between the transmembrane potential and ion equilibrium potential is also called the driving force for an ion [1, 2].

An action potential is the process through which the transmembrane potential rapidly increases and then decreases as membrane permeability to different ions changes. This change in ion permeability in modulated by ion channels embedded in the membrane. The generation of an action potential proceeds through multiple phases. Starting at the end, phase 4 is the resting state and is a stable, but active, state at which the cell expends energy to maintain a negative transmembrane potential. In cardiac cells, this is typically between -90 mV to -70 mV (intracellular negative to extracellular) depending on the region of the heart and species. To maintain this negative potential, which is typically close to the equilibrium potential for K^+, a Na^+-K^+ ion pump uses energy to export 3 Na^+ ions out of the cell and pump in 2 K^+ ions (a net negative inward flux) [1, 4].

Phase 0 of the action potential is the rapid initial upstroke which is at the wave front of electrical waves propagating through cardiac tissue. It is caused when a rise in the transmembrane potential is sufficient to allow it to reach the 'threshold' potential (typically around -50 mV) at which the fast Na^+ channels open (in non-pacemaker cells). The opening of these channels leads to a rapid influx of Na^+ into the cell and a rapid rise in the transmembrane potential, usually until the transmembrane potential becomes positive. Shortly after opening, these fast Na^+ channels also close rapidly, but the rising transmembrane potential sets off a cascade of successive ion channel activity [4].

Phase 1 of the action potential is a short rapid decrease in transmembrane potential caused by transient outward K^+ channels opening. This is followed by phase 2, where

delayed rectifier K^+ channels and L-type Ca^{2+} channels open. The resting concentration of Ca^{2+} inside the cell is orders of magnitude lower than in the extracellular space, so the Ca^{2+} ions flow into the cell, balancing the outflow of K^+ ions and causing a plateau phase of the action potential. The influx of Ca^{2+} activates Ca^{2+}-sensitive receptors on the sarcoplasmic reticulum (ryanodine receptors) which leads to a rapid release of Ca^{2+} from within the cell and closes the L-type Ca^{2+} channels on the membrane. Finally, in phase 3 of the action potential, various K^+ channels (primarily the rapid delayed rectifier and inward rectifier) continue to allow K^+ ions to flow out of the cell, lowering the transmembrane potential back to the resting state, phase 4 [1, 4].

The process that leads from electrical excitation to myocyte contraction is called excitation-contraction coupling [5]. As a cardiac cell is electrically excited, Ca^{2+} ion channels on the cell membrane open causing an inward Ca^{2+} current which subsequently causes a further release of Ca^{2+} from the sarcoplasmic reticulum. This results in a rise in intracellular Ca^{2+} concentration, leading to free Ca^{2+} ions binding to the myofilament protein troponin C and causing the cell to contract. As intracellular Ca^{2+} reduces, the cell relaxes once again [5].

The shape of the action potential is affected by the level of expression of different types of ion channels and changes depending on the region of the heart (see Figure 1.1). The interplay between Ca^{2+} influx and K^+ efflux during latter phases of the action potential is a key determinant in the time for a cardiac cell to complete one depolarisation/repolarisation cycle, known as action potential duration. After a cell has been excited, a period of time must pass before it can be excited again, known as the refractory period of a cell. The refractory period can be affected by the external environmental conditions and the cell's own previous activity [1, 4].

1.1.3 Gap junctions

For electrical waves to propagate through cardiac tissue, an action potential elicited in one cardiomyocyte must initiate an action potential in its neighbour(s). Conduction in the heart was originally thought to be a continuous phenomenon, however we now know that

at the microscopic level it is inherently discontinuous [6]. Cardiac myocytes in the human heart are rod-shaped, with length approximately 100-150 μm and diameter around 10-20 μm depending on the region of the heart they originate from [1, 7], and are connected end-to-end though intercellular pathways called gap junctions [8, 9].

Gap junctions are formed between cells when a hexameric connexon hemichannel on either cell, each formed of six proteins from the connexin family, meet to form a channel connecting the cytoplasmic space of both cells [8]. Three isoform connexins are expressed in the heart: Cx43, Cx40 and Cx45 (named for their molecular weight) [10]. They are expressed at different levels depending on the heart region [11], and different connexin isoforms can connect to form both homomeric and heteromeric channels [12].

Gap junctions in healthy myocardium are concentrated at the cell ends in a region called the intercalated discs [13–15], and a typical myocyte is, on average, coupled to 11 ± 3 surrounding cells in this manner [16]. This directional coupling leads to the anisotropic conduction properties of healthy cardiac tissue.

Though gap junctions allow electrical impulses and ions to pass directly between cells, their small cross-sectional area and limited number mean they are a much higher resistance pathway than intracellular fluid, though much lower resistance than the lipid bi-layer membrane. A 'rule of thumb' is that the resistance inside a single cell from end to end is on the same order as the resistance across the much smaller length of gap junctions connecting coupled cells [17]. As a result, gap junctions are an important component of microscopic conduction through cardiac cells as shown by the conduction delay at the junctions observed experimentally [18,19]. It is also well established that pharmacological inhibition of gap junctions slows conduction velocity [20,21]. On the other hand, reducing gap junction expression by genetic means is less conclusive with studies reporting both conduction slowing [22, 23] and no significant effect [24, 25].

Gap junctions have been shown to be important in pathological conditions which are arrhythmogenic such as cell remodelling [26]. Under these conditions, gap junction expression can be reduced or redistributed from the intercalated disks, leading to greater transverse coupling [27,28]. This results in localised conduction slowing and increases the

propensity of cardiac tissue to re-entrant arrhythmias [25].

1.1.4 Action potential propagation

Conduction through cardiac tissue is governed by three factors: the electrical activity of individual cells, their electrical connectivity to neighbouring cells, and the structure of the tissue itself (which includes both the micro-architecture and larger obstacles such as non-conductive scar tissue) [3]. Although the underlying process is inherently discontinuous (through the relatively high resistance gap junctions), using a continuous approximation is generally appropriate under specific conditions. Kléber and Rudy [3] give three conditions where the continuous approximation shows good agreement between experimental and theoretical results: (1) passive electrical properties of cardiac tissue at the macroscopic scale, (2) the relationship between the action potential upstroke velocity and propagation at scales greater than 1 mm, and (3) the relationship between conduction velocity and moderate changes in electrical coupling and interstitial volume [3].

An important concept in cardiac propagation is 'source-sink mismatch'. When an electrical wave propagates, the wave front caused by the upstroke of the action potential in individual cells provides the source, and this depolarising current must provide sufficient charge to depolarise adjacent tissue (the sink) or propagation fails [3, 29]. Conduction velocity can be slowed both through lowering excitability by reducing the current density of the fast Na^+ channel, and by lowering electrical coupling through gap junctions. In the former case, the source is diminished meaning propagation will more easily fail (as source-sink mismatch increases). Paradoxically, while electrical uncoupling lowers the velocity of propagation, the propagation itself actually becomes more robust as there is less electrotonic load from the excited cell into neighbouring cells, a concept known as the 'safety of propagation' [30, 31].

1.1.5 Self-sustaining activity

A normal propagating wave in the heart initiates from one location and then subsequently terminates in another. The heart can be disrupted from sinus rhythm when a wave,

rather than terminate, propagates around a region of tissue to re-enter tissue it had previously activated but has since had time to recover (recall the concept of the refractory period following an action potential). This activity is self-sustaining in the sense that no further external stimulus is required to initiate new wave fronts. Self-sustaining activity can override the heart's natural rhythm, leading to arrhythmia such as tachycardia (an organised propagation pattern but at a higher rate than sinus rhythm) or fibrillation (disorganised activity with no clear driving mechanism). In particular, atrial fibrillation is the most common sustained arrhythmia and is associated with increased risk of stroke and increased morbidity and mortality [32].

Self-sustaining activity can be caused by functional and/or structural features of the underlying cardiac tissue. In the simplest case, if there is a fixed anatomical obstacle through which the activation wave cannot propagate, then it is possible for the wave to rotate around the obstacle (originally posited as 'circus' re-entry) [33,34]. In this case, the requirement for self-sustaining activity to occur is for the tissue to have recovered from its refractory state before the returning wave front reactivates it. It is possible for excitable tissue to exist between the head and refractory tail of the wave, which is known as the excitable gap. To initiate circus re-entry requires a region through which a propagating wave can travel in only one direction, or unidirectional conduction block. Then a stimulus at one location around the obstacle will only propagate in one direction and, provided the refractory period of the tissue is sufficiently short and/or the wave front sufficiently slow, the wave will continue to propagate around the obstacle.

A functional concept of self-sustaining activity which does not depend on an anatomical obstacle is the 'leading circle' hypothesis. In this case, the wave front impedes on its refractory tail and there is no excitable gap as in circus re-entry. The leading circle re-entry develops when the stimulating effect of the wave front is *just* sufficient to initiate a new action potential in the partially refractory tissue [35–38]. The area of tissue which is rotated around is held in a constant refractory state by impeding wave fronts rendering it unexcitable, and therefore the self-sustaining activity remains fixed in one location.

Another form of functional re-entry that may occur is spiral wave, or rotor, re-

entry [39–42]. As opposed to the previous cases, spiral wave theory incorporates the wave front curvature. This non-planar wave front does not have a constant conduction velocity and instead it varies with the curvature due to changing source-sink mismatch [32]. The curved wave front and refractory wave tail meet at a singularity point (the 'rotor') [43,44]. At the core, the wave front curvature is extremely high and the conduction velocity very low so that the wave front cannot impede on the cells at the core. However, contrasting leading circle re-entry, this core is not held in a refractory state and so, instead of being unexcitable, it is just difficult for the wave front to excite this group of cells [32]. As a result, under some conditions, the rotor can meander through tissue, or anchor to small imhomogeneities [43].

1.1.6 *In vitro* models of arrhythmia

In vitro, *ex vivo* and *in vivo* experimental models of arrhythmia all have specific advantages and disadvantages [45, 46]. While *ex vivo* and *in vivo* models are closest to the clinical reality, they also have the highest biological variability and cost associated with experiments, making it challenging to standardise results. *In vitro* models typically consist of a layer of cardiac cells seeded to create an excitable synctium [47] which can be exposed to pharmacological interventions and may be genetically modified, and in which electrical activity can be recorded using electrodes or visualised with optical mapping [48–50]. A major downside of *in vitro* models is that they lack the complex three-dimensional macro- and micro-structure of cardiac tissue (though methods to reproduce some characteristics do exist, e.g. [51]), and the presence of neuronal cells or vasculature [46]. Cell monolayers typically consist of either primary cells, stem-cell derived cardiomyocytes or immortalised cell lines.

Primary cell monolayers, where cells are enzymatically dissociated from fresh neonatal animal hearts, are historically the most common monolayer model [46]. A large number of studies have investigated the basic mechanisms of self-sustaining activity and localised conduction block in these models (e.g. [52–58]). However, a downside of using primary cell monolayers is the challenge in achieving a high purity monolayer without the presence of

non-cardiomyocyte cells when not desired. Primary cells from post-neonatal hearts do not divide in culture, placing a limit on the source of new cells, and there are ethical arguments to consider regarding the use of animals in research. More recently, pluripotent stem cell monolayers have been explored as they can proliferate in culture and be differentiated into different cell types (for recent reviews see [46, 59]).

Immortalised cell lines can proliferate indefinitely in culture and be seeded into excitable monolayers. The HL-1 cell line [60, 61] was derived from murine atrial cells and retains characteristics of adult cardiomyocytes such as the ion channels necessary to generate action potentials [60–65]. They exhibit spontaneous activity when cultured in monolayers and have been used to study self-sustaining activity [66–68]. One downside of this cell line is the heterogeneous phenotypes of cultured cells at different stages of differentiation. Dias et al. [69] created more homogeneous sub-clones of the HL-1 cell line, among them HL1-6 cells. HL1-6 cells maintain their cardiac differentiation, can be passaged indefinitely in culture and frozen/thawed from stock. Being derived from the HL-1 cell line they possess the ion channels typical of atrial-derived cardiomyocytes and express Cx40, Cx43 and Cx45 for gap junctional coupling [69]. Like primary neonatal cardiomyocytes, they propagate electrical impulses in seeded monolayers, though with a lower conduction velocity ($\sim$41 mm/s in HL1-6 [69], compared to $\sim$340 mm/s in primary cultures [70]). This makes it possible to capture electrical activity at cell-scale spatial resolution without limiting the field of view or time resolution in optical mapping. Monolayers of HL1-6 myocytes also exhibit spontaneous triggers leading to self-sustaining activity [71].

1.2 Computational background

Computational models of action potential propagation provide advantages over biological models in that the environment and inputs of an experiment can be manipulated precisely, outputs can be recorded in the absence of experimental noise and (once developed) it is possible to run many experiments at relatively high speed and low cost. Significant downsides of computational models are they are by necessity a simplification of reality and substantial work must go into their development and validation to ensure they faithfully

represent the subject being studied.

A computational model of action potential propagation requires a model of the reaction process (action potential generation in each cell) and the diffusion process (electrical propagation to adjacent cells).

1.2.1 Modelling an action potential

Action potential models describe how the transmembrane potential, and other physiological properties, of a cardiac cell vary through time due to changing environmental conditions or applied stimuli. Since the development of the initial, relatively simple, model of a neuron [72], action potential models have grown in scope and complexity as new experimental data have become available [73]. Both phenomenological models, which aim to reproduce basic characteristics of an action potential that are solved in an efficient manner for use in large-scale simulation studies, and biophysical models, which aim to reproduce ion channel currents and intracellular processes at varying levels of detail, have been developed. They are generally composed of one or more currents with conductance regulated by the opening and closing of one or more 'gates', formulated as a set of nonlinear ordinary differential equations.

A range of models exist for cardiac cells from the atria [74, 75], ventricles [76], sinoatrial node [77] and purkinje fibre system [78] in humans, as well as across a range of species widely used in cardiac research including mouse [79–81], rabbit [82, 83], rat [84] and guinea pig [85, 86]. More recently, models to represent action potentials of induced pluripotent stem cells [87] have also been developed.

1.2.2 Continuum models of cardiac propagation

The most common method of modelling multicellular electrical activity, particularly at the tissue or whole organ scale, is the classical bidomain or monodomain approach [88–90]. This approach generalises Ohm's law leading to a system of partial differential equations, with the action potential incorporated as a reaction term. In these models, the fine microstructure of cardiac cells are homogenised to represent cardiac tissue as a synctium.

The geometry, which may be idealised or derived from experimental data such as MRI images, is divided into a mesh in which the equations can be solved using a numerical scheme such as finite difference, finite elements or finite volume. Extracellular and intracellular domains exist throughout the geometry, and are coupled at all points. As a results, discrete features, such as gap junctional coupling, are averaged over larger areas and represented by homogenised conductivity terms. The continuum approach has been successfully applied to a range of studies of cardiac propagation (see e.g. [91]). However, changes to conduction properties at the microscopic scale are difficult to represent in a meaningful way in these models.

1.2.3 Discrete models of cardiac propagation

Early discrete-cell models were developed in response to biological experiments highlighting the effect of gap junctions on propagation, the results of which could not be predicted by continuum approximations. In particular, for high gap junctional resistances it was shown that the conduction velocity prediction from cable theory breaks down, and the action potential time to peak increases as gap junctional resistance increases [92]. New models developed traditional cable theory by incorporating discrete discontinuities at the abutting cell ends in one-dimensional strands of cells [93–98], and were able to reproduce these features of high gap junctional resistance observed experimentally.

Spach et al. were one of the first to expand the concept of discrete cardiac propagation in two-dimensional computational models of adult- and neonatal-like cells through a number of studies [99–104]. Across these studies, the authors investigated how cardiac propagation was affected at the cellular scale by changes to three effects of cardiac remodelling: changes in the geometry of cells; changes in the distribution and resistance of gap junctions; and changes in the volume and distribution of the interstitial space between cells. Linking the work back to clinical applications, the role of interstitial collagen was highlighted as a potential target to reduce the effects of microfibrosis and improve transverse coupling of aging myocytes [104].

Stinstra et al. developed a three-dimensional model of discrete cardiac conduction,

which they called the 'microdomain' model [105–110]. The authors use computer-generated geometrical models of cardiac cells, interstitial space and capillaries which resemble realistic myocyte shape in a bundle of fibres. Each domain is treated as a separate volume conductor with a specific conductivity value. Gap junctions couple adjacent cells through any surfaces perpendicular to the fibre direction, which allows both longitudinal and lateral coupling. This model was initially applied in a passive sense, with no active action potential model on the cell membranes, to estimate bulk values of intracellular and extracellular conductivities in both healthy [105] and ischaemic tissue [106]. An electric field was applied across a finite element model of 64 generated cells along with capillaries and interstitial space, and the resulting current density measured to infer bulk tissue conductivity.

In later work, this microdomain model was extended to include the active component across the cell membranes [108–110]. In [108], action potential propagation along a fibre of 50 brick-shaped cells was simulated using a finite volume scheme, with different volumes and electrical properties in the interstitial space. The authors concluded that the nature of propagation and shape of transmembrane potential was very different between their simulations and the classical bidomain approach when non-uniform interstitial space was included. This approach was later extended to realistic myocyte morphology generated from histological images of myocyte bundles [109, 110], and compared to the idealised brick-like fibre. In the latter work, the authors concluded that in the simple case of a planar propagating wave, the use of a more realistic geometry had a "moderate" effect on measured conduction velocity at the microscopic scale [110].

More recent studies have returned to focus on two-dimensional discrete cardiac propagation in cell monolayers. The effect of how the cardiac microstructure is represented in these models has been investigated by comparing ideal brick-like cells with more realistic morphologies, directional anisotropy, varying gap junctional distribution and cleft spaces [111, 112]. Kim et al. conclude that in healthy cardiac tissue, with normal cellular coupling, the continuum (bidomain, etc) modelling approach can be appropriate but that it begins to break down in areas of sudden changes in cell orientation [112] . Along with

microstructural changes, representing cardiac cells individually in a model facilitates investigating the effects of coupling to non-myocyte cells such as fibroblasts [113–115]. Cardiac monolayers are frequently used in *in vitro* models of self-sustaining activity, and this has also been an area where discrete-cell computational models have been applied [116, 117]. Hubbard et al. modelled a monolayer with heterogeneity in gap junctional coupling and interstitial resistivity introduced into half of the domain [116], and a region in the centre [117]. In both cases, they were able to demonstrate how wave breakthrough could occur at the boundary of source-sink mismatch from single cells in the heterogeneous region into the well coupled region of their models.

A growing number of studies are using models of discrete cardiac conduction to investigate the role of ephaptic coupling in cardiac conduction [118–121]. Ephaptic coupling is hypothesised to occur when a depolarising cell draws in Na^+ ions, lowering the electric potential of the thin extracellular space around the cell, and causing the membrane of a closely adjacent cell to depolarise without the requirement of gap junctional coupling [122]. Ephaptic coupling was proposed in response to experimental evidence that electrical signals continue to propagate even when gap junctional coupling is significantly reduced [118, 120]. In particular, clustering of fast sodium channels at the intercalated discs appears to be a critical factor in this form of propagation succeeding, which is difficult to represent in a meaningful way in continuum models [123]. The 'EMI' model developed by Tveito et al. [120, 123] captures this behaviour by using rectangular cells with only part of the cell surfaces extending to connect to neighbouring cells, thus leaving a gap over which they demonstrate ephaptic coupling can occur.

1.2.4 Uncertainty and variability in cardiac modelling

Uncertainty and variability are unavoidable aspects of scientific experiments, and can be particularly acute in the biological sciences. As experiments are frequently used to tune parameter values in computational models, they have an influence on the model output. Further understanding of uncertainty and variability in cardiac modelling has been designated a priority as models become more closely implicated in safety-critical

clinical applications [124].

Uncertainty is introduced into cardiac models from a number of sources. These can be separated into two broad categories: *epistemic* and *aleatory* uncertainty [125]. Epistemic sources are a consequence of some missing knowledge about the system being modelled. As all models are a necessary simplification of the real system they aim to represent, epistemic uncertainty can be introduced by deficiencies in the model formulation which do not account for, or incorrectly portray, aspects of the real system. Epistemic uncertainty can also arise in the case of imperfect data from recording systems (e.g. noise in electrogram measurements). Aleatory sources are a result of the variability inherent in the biological system. This could be, for example, differences between action potentials in different cells, or in subsequent action potentials from the same cell [124]. A defining difference between the two sources is that epistemic uncertainty can be, theoretically, reduced while aleatory uncertainty is a property of the system being studied and cannot be eliminated.

In cardiac modelling, uncertainty and variability can be incorporated into both the action potential model and the tissue model (in both continuous and discrete cases). Action potential models, particularly biophysically detailed models, can be composed of many parameters, rendering calibration (selecting the model parameters based on experimental evidence) a challenge due to identifiability concerns. Identifiability refers to the ability of a parameter to be uniquely selected and may be *structural* (i.e. the form of the equations results in redundant parameters that can be varied together to give the same result) or *practical* identifiability (i.e. the inability to select a value given the available experimental data). Recently, numerous studies have investigated uncertainty, variability and unidentifiability in action potential models (see e.g. [123, 126–131]). The uncertainty in action potential models can be propagated into the full cardiac model, alongside those introduced at the tissue scale [125].

1.3 Thesis outline

This chapter has described the biophysical processes underlying the genesis of arrhythmias in patients and discussed the modelling modalities which can be used to investigate such

processes. In particular, under pathological conditions, the continuum modelling approach cannot adequately represent changes and heterogeneity at the microscopic scale which may be important in the perpetuation of self-sustaining electrical activity in fibrillation. HL1-6 myocytes allow electrical activity to be recorded at high temporal and spatial resolution with a field of view not possible in other *in vitro* models.

The central hypothesis driving this work is that *heterogeneous electrical coupling plays a key role in the initiation and perpetuation of re-entrant arrhythmias and fibrillation.* To address this hypothesis, the goal of this thesis is to develop a biophysically and geometrically accurate computational model of action potential propagation in cardiac cells cultured in a monolayer, through direct comparison with biological experiments using HL1-6 myocytes. Towards this goal, the thesis has the following sub-hypotheses and related aims:

- *Heterogeneity of cell coupling in monolayers of HL1-6 myocytes create a substrate for the formation of self-sustaining activity.* To address this sub-hypothesis, the first part of this thesis aims to improve understanding of the self-sustaining activity observed in this *in vitro* model.

- *The Hodgkin-Huxley approach can be used to model the action potential of HL1-6 cells* and *uncertainty and variability can be captured in this model using a Bayesian calibration approach.* The second part of this thesis therefore aims to construct an action potential model of an HL1-6 myocyte, with consideration of uncertainty and variability.

- *A multi-domain model accounting for the geometry and biophysics of individual cells can be constructed to faithfully and efficiently simulate action potential propagation through HL1-6 cell monolayers.* To address this sub-hypothesis, the final part of this thesis aims to build a multi-domain computational model of action potential propagation through HL1-6 cell monolayers, and to validate the model against biological experiments.

The rest of the thesis proceeds as follows. Chapter 2 characterises the form of self-

sustaining activity observed *in vitro* in HL1-6 monolayers, and the conditions necessary for its initiation. Chapters 3 and 4 develop the HL1-6 action potential model. In Chapter 3, the calibration methodology is explored through a retrospective uncertainty and variability analysis of previously published action potential models, and this approach is then used to build a new action potential model of the HL1-6 myocyte in Chapter 4. Chapter 5 describes the methodology for the multi-domain computational model, and shows theoretical results and performance considerations. Chapter 6 then presents and discusses results from simulations of action potential propagation in monolayers of HL1-6 myocytes, and compares with biological observations. Lastly, Chapter 7 concludes the thesis and offers avenues for future research. ■

Chapter 2

Self-sustaining activity in HL1-6 cell monolayers

Parts of the following chapter have been published in [71, 132] (CC BY).

2.1 Introduction

Self-sustaining activity spontaneously occurs in cultured monolayers of HL1-6 cells. This chapter addresses the first aim of the thesis: to investigate the initiation and perpetuation of self-sustaining activity in this relatively simple biological model. The slow propagation velocity of HL1-6 monolayers [69] enables activity to be visualised at high spatial and temporal resolution while maintaining a multicellular field of view.

Previous studies have investigated self-sustaining activity in monolayers of the original HL-1 cell line [66–68, 133, 134]. Studies have optically mapped activity using voltage [67], Ca^{2+} [68,134] and "propagation-induced phase contrast" approaches [66]. When reported, self-sustaining activity in HL-1 monolayers generally had a dominant frequency $\sim$3 Hz [66, 68], and remained rotating around a single location over extended periods of time. Previous work has mapped self-sustaining activity in HL-1 cell monolayers with field of view $>1\times1$ cm, focusing on the macroscopic propagation properties. In this chapter, we map at higher spatial resolution with a field of view closer to 1×1 mm which makes it possible to study detailed features at the core of the stable activity.

The chapter proceeds as follows. Section 2.2 details the methods used to culture the cells, protocols for individual experiments, and how data analyses were conducted. Section 2.3 then presents the results. Firstly, we try to uncover the conditions required for self-sustaining activity to initiate, and test whether trigger cells or self-sustaining activity is a constant or transient feature of a given preparation by halting and restarting monolayer activity. Subsequent experiments take a closer look at the core of the stable self-sustaining activity to characterise the substrate that allows the activity to perpetuate. Finally, in Section 2.4, we discuss these results in the context of the existing literature, and draw conclusions.

2.2 Methods

2.2.1 Cell culture

All cell culture work was carried out in laminar flow safety cabinets to maintain sterile conditions. HL-1 subclone 6 (HL1-6) cells [69] were grown in Claycomb medium (Sigma-Aldrich, USA) supplemented with 10% fetal bovine serum (Gibco, USA), 100 U/ml:100 μg/ml Penicillin/Streptomycin (Sigma-Aldrich, USA), 2 mM L-Glutamine (Sigma-Aldrich, USA) and 0.1 mM Norepinephrine (Sigma-Aldrich, USA). For a list of additional reagents included in Claycomb medium see Table 1 in [61]. Cells were incubated in an environment with 5% CO_2 overlay at 37 °C.

Cells were maintained in either 100 mm diameter TC-treated culture dishes (Corning, USA), or T-75 flasks (Sarstedt, Germany). In either case, the surface of the dish/flask was coated with a 5 μg/ml solution of fibronectin (Sigma-Aldrich, USA) in Hank's Balanced Salt Solution (HBSS) (Thermo Fisher Scientific, USA) for 30 minutes prior to seeding. This solution was aspirated off before seeding.

Cells were passaged at ratios between 1:6 and 1:3 every 3-7 days, once cell monolayers reached ∼80% confluency. Dishes were first washed gently with HBSS 2-3 times to remove any growth medium. For a T-75 flask, 2 ml of pre-warmed 0.05% trypsin/EDTA (Sigma-Aldrich, USA) in HBSS was added to the flask, which was then incubated in 1% CO_2

at 37 °C for 2 minutes. The flask was removed from the incubator, the old trypsin and cellular debris aspirated off and replaced with 3 ml of fresh trypsin. The flask was then returned to the incubator. After 3 minutes, flasks were tapped gently to dislodge cells and observed under a phase microscope to check whether most cells had dissociated. The enzyme activity was halted by adding an equal volume (3 ml) of soybean trypsin inhibitor (Sigma-Aldrich, USA) directly to the flask. This solution was added into a 15 ml falcon tube. The flask was then washed with 3 ml of Claycomb medium to ensure good cell recovery and this solution also added to the falcon tube. The tube was centrifuged (300×g, 5 minutes at room temperature), the supernatant aspirated off and the resulting cell pellet re-suspended in the appropriate volume of supplemented Claycomb medium for the passage ratio. After dilution in Claycomb medium, the single cell suspension was re-seeded onto newly coated dishes/flasks.

2.2.2 Cryo-preservation

Cells in a flask at ∼80% confluency were detached as detailed above up to the step where a cell pellet is obtained after centrifuging. The cell pellet was re-suspended in 1.5 ml of 95% FBS and 5% DMSO solution and added to a cryovial. Cryovials were quickly transferred to a -80 °C freezer, before being moved to liquid nitrogen if frozen for long-term storage.

To thaw cells, the cryovial was rapidly warmed in a 37 °C water bath and the cell solution transferred to a falcon tube containing 10 ml of Claycomb medium pre-warmed to 37 °C. The cells were centrifuged as described above, and the resulting pellet re-suspended in 5 ml of pre-warmed medium and added to a culture flask.

2.2.3 Seeding round colonies of controlled area

A range of volumes of fibronectin solution were applied to 35 mm diameter uncoated low-walled μ-dishes (ibidi, Germany) to achieve cell colonies of consistent sizes. Drops of the solution formed circular shapes due to the hydrophobic nature of the dish surface. Drop volumes were set at 2.5, 5 and 10 μl. Multiple drops of each volume, along with a large drop of 150 μl to facilitate checking for cellular activity, were seeded in each dish.

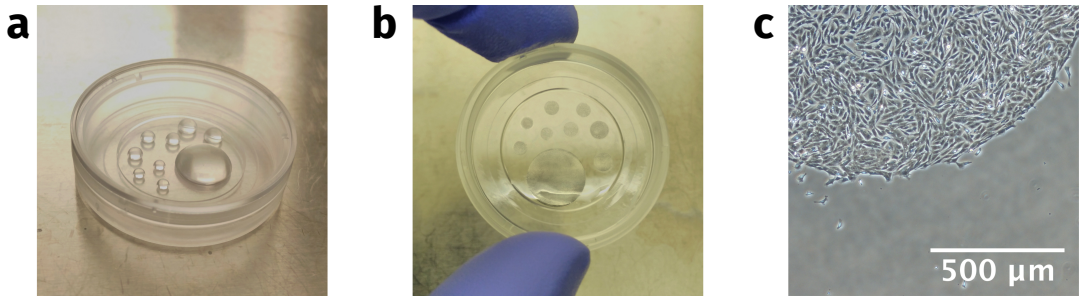


Figure 2.1: **a** Drops of fibronectin solution on the hydrophobic dish surface. **b** Resulting round colonies of cells after wash step. **c** Phase contrast image at edge of one colony.

After application, the fibronectin drops were left for approximately 30 minutes and then aspirated from the dish surface. Approximately 700,000 cells from a confluent dish were added directly to the μ-dishes and incubated in 5% CO_2 at 37 °C for approximately 30 minutes. An extensive wash with HBSS removed excess cells not adhered to the surface (i.e. outside the drop of fibronectin coated areas). Growth medium was added and dishes returned to the incubator. Cells in colonies would typically exhibit intrinsic activity after 4-8 days in culture. Figure 2.1 shows the resulting colonies in a μ-dish.

2.2.4 Anisotropic monolayers

When seeded as described above, HL1-6 monolayers do not align preferentially in a single direction. To generate anisotropic cell monolayers, the surfaces of μ-dishes were directly microabraded in one direction using 5 μm lapping paper [51] prior to seeding. The dishes were sterilised under UV light before small HL1-6 cell colonies were seeded directly onto the abrasions using the protocol above.

2.2.5 Optical mapping

In experiments mapping only Ca^{2+} transients, HL1-6 cell colonies in μ-dishes were loaded with 10 ng/ml Fluo-4 AM (Thermo Fisher Scientific, USA) diluted in 1 ml of HBSS containing 1 mM $CaCl_2$ for approximately 20 minutes. Ca^{2+} transients were used as a surrogate (for membrane potential changes) due to the much larger fluorescence amplitude recorded compared to conventional voltage dyes (e.g. di-8-ANEPPS). This makes it possible to visually track wave fronts to locate the core of self-sustaining activity within

monolayers, which was not possible using only voltage-sensitive dyes. After 20 minutes, the dye solution was aspirated off and an imaging solution of 1 ml HBSS containing 1 mM $CaCl_2$ added to the dish. In experiments with anisotropic monolayers, this imaging solution contained 1.5 mM $CaCl_2$ and 1 mM $MgCl_2$, as it produced more consistent activity in cell colonies. Cells were returned to the incubator for 20 minutes to de-esterify before imaging was carried out.

In two sets of experiments, Ca^{2+} transients were mapped simultaneously to, or immediately after, recordings using potentiometric dyes. For simultaneous imaging, cells were stained with 40 μM di-8-ANEPPS (Thermo Fisher Scientific, USA) diluted in 1 ml HBSS supplemented with 0.05% Pluronic F-127 (Life Technologies, USA) for 2 minutes. A new potentiometric dye with higher fluorescence compared to conventional dyes, BeRST-1 [135] (a kind gift from Professor Miller at University of California, Berkeley), was also tested. Cells were stained for 20 minutes with Fluo-4 AM solution (as above) mixed with BeRST-1 stock solution (prepared as described in [135]) diluted 1:1000 in HBSS. On our microscopy setup, it was not possible to capture simultaneous recordings using this dye combination, so they were captured sequentially with no delay between recordings.

For optical mapping experiments using Fluo-4 AM or Fluo-4 AM/BeRST-1, cell activity was recorded using an Axio Observer inverted widefield microscope (Zeiss, Germany). Video recordings were captured using a Flash 4 CMOS camera (Hamamatsu, Japan) through a 10×/0.5 Fluar objective lens (Zeiss, Germany) at 100 frames per second with an exposure time of 2 ms and 4×4 spatial binning (2.6 μm/pixel). The field of view of recordings was ∼1.6×1.6 mm. Images with no spatial binning (0.65 μm/pixel) and higher exposure time of 200 ms were captured immediately following each video recording. These images were used to align data from following experiments to the original video recording. All recordings on this system were captured using ZEN Pro imaging software (Zeiss, Germany) and stored in 16-bit proprietary *.czi* format.

Dual voltage and Ca^{2+} transient optical mapping using the di-8-ANEPPS/Fluo-4 AM dye combination was captured using a custom-built microscope setup (Cairn Research, UK). The system was built around an upright microscope (Eclipse FN1, Nikon Instru-

ments Europe B.V.). Excitation light (470 nm) was supplied by an OptoLED system (Cairn Research, UK). The emitted fluorescence was collected by a high aperture 20×/1.0 water dipping lens (Olympus, Japan). Using a 560 nm Brightline single-edge dichroic beamsplitter, located in an Optosplit II "LS" emission image splitter (Cairn Research, UK), the fluorescent light was divided into two beams that were passed through emission filters (525 nm and 628 nm). Recordings were captured with 10 ms time resolution, 4×4 spatial binning (1.15 μm/pixel) and 1 ms exposure time by a Zyla 10-tap sCMOS camera (Andor Technology, UK).

2.2.6 Imaging cell morphology

To capture cell morphology on the Axio Observer microscope setup, cells were live-stained while on the microscope stage to avoid losing saved coordinates of interest on the dish. The imaging solution was carefully aspirated off without disturbing the dish and replaced with 1 mg/ml Wheat Germ Agglutinin (Sigma-Aldrich, USA) diluted 1/40 in HBSS containing 1% bovine serum albumin for 10 minutes. Cells were then rinsed several times with HBSS before imaging. For anisotropic cell monolayers, cells were stained instead with 25 μM di-8-ANEPPS in HBSS for 5 minutes before returning to imaging medium. This live staining process ensured that (1) the dish was minimally disturbed during the staining process making it possible to return to approximately the same location where self-sustaining activity was previously observed, and (2) cell morphology was not affected by fixation of the cells. A z-stack of images with z-axis resolution of 0.5 μm was collected using the same objective on the Axio Observer microscope as above, and an exposure time of 200 ms. The z-stack of images was later deconvolved using Huygens software (Scientific Volume Imagine, Netherlands).

2.2.7 Quantifying occurrence of triggers and self-sustaining activity

In preliminary experiments, attempts were made to visually identify individual triggers in each size of colony. This process was challenging and unfeasible in the limited time

before photo-bleaching would occur. Instead, 30 s videos were recorded at the centre of each colony. Intrinsic pacemaker activity was then identified by wave fronts coming from different angles and with irregular frequency. The number of unique wave front angles was used as a surrogate for the number of unique pacemakers.

Each recording was additionally classified for the occurrence of self-sustaining activity in the colony. Self-sustaining activity (rotational activity or re-entry) was identified as > 4 regular consecutive wave fronts with the same incidence angle. When self-sustaining activity was observed, the colony was excluded from the pacemaker analysis (regardless of whether any trigger activity defined above was visible before/after the self-sustaining activity) as the self-sustaining activity could impede additional triggers.

2.2.8 Stability of triggers and self-sustaining activity

The aim of this set of experiments was to test whether triggers/self-sustaining activity were constant features of the underlying substrate, or transient and dependent on other activity. Triggers or cores of self-sustaining activity were first identified in individual colonies and recorded as described in Section 2.2.5. Imaging medium was then aspirated off, without removing the dish from the microscope setup, and replaced with either HBSS containing 20 mM KCl (to depolarise the cell membranes and maintain the fast Na^+ current in the inactivated state, thus halting activity), or containing 3 mM heptanol (to interrupt gap junctional coupling, also halting activity). Each colony was checked under the microscope to confirm that activity had ceased within a few seconds. The blocking solution was aspirated off, the cells rinsed with HBSS and returned to normal imaging medium. Further 10 s recordings were taken at each location where triggers or self-sustaining activity were previously observed.

2.2.9 Data processing and analysis

All images and videos were analysed using FIJI open source software (version 1.51f, `https://fiji.sc`). For experiments testing the effects of anisotropy, the directionality of images was measured using the OrientationJ plugin for FIJI [136]. The output of the algorithm is

a histogram of local directionality in each image, which will peak in dominant directions. A more pronounced peak indicates a more dominant direction.

Recordings from fluorescence microscopy experiments were processed prior to analysis to eliminate noise while retaining the underlying signal. A custom optical mapping toolkit was developed in Matlab (version 2017b, Mathworks, USA) within the group to facilitate processing of recordings [71, 132, 137]. The process follows established image processing techniques [138]. Recordings are first spatially filtered using a Gaussian kernel. The width of the kernel, defined by the standard deviation parameter σ, was selected according to the quality of the signal from the experiment, but was generally held close to $\sigma = 2.5$ pixels. Each pixel is then filtered in time using a low-pass temporal filter with low-pass level of 15 Hz. Corrections are made for drift of the signal if necessary by fitting each pixel signal to a fourth-order polynomial and subtracting the output to establish a new stable baseline.

Activation time maps were generated by defining activation time for each pixel as the point of steepest upstroke in the filtered signal [138], with additional checks as described for identifying a propagating wave front in [139].

One of the challenges of processing disorganised optical mapping data, particularly at the microscopic scale, is to isolate features of interest so that they may be studied in relation to specific hypotheses. To analyse recordings of self-sustaining activity at the single-cell level, a video-processing algorithm was developed to highlight areas of consistent conduction slowing or block over the time course of a recording. This makes it possible to generate 'heat maps' of conduction delay which can be studied in relation to features of the underlying substrate, such as cell size, ion channel density or gap junctional coupling.

Figure 2.2 outlines each stage of the proposed algorithm. Firstly, each raw recording is processed using conventional techniques: spatial binning, temporal filtering and drift correction as described above and in [132, 138]. A series of activation time maps are generated for the range of time points in the recording (Figure 2.2a, second graphic). Each of these maps is generated to cover one rotation of the self-sustaining circuit (i.e.

the window of interest is set equal to one period of rotation determined from the dominant frequency of the recording).

In each of these activation maps, areas of high activation time difference, but close proximity, are then calculated (Figure 2.2b). For every pixel (i) in the activation time map, neighbourhood pixels are determined within a user-defined radius. For each neighbourhood pixel (j), the absolute activation time difference is calculated as $\Delta t_{\mathrm{act}} = |t_{\mathrm{act,i}} - t_{\mathrm{act,j}}|$ (Figure 2.2b, second and third graphics). This value is added to a running total at the *geometric midpoint* between pixels i and j in the conduction delay heat map. After the time difference values for each neighbourhood pixel have been calculated, the algorithm iterates onto the next pixel in the activation map and the process repeats. After all pixels have been iterated over, the conduction delay heat map is averaged (by the number of calculations applied to each pixel) to generate the final conduction delay map for the single activation map. The regions in the map at this stage generally highlight the wave front itself, including parts of the core being rotated around (Figure 2.2b, final graphic).

To generate a conduction delay map for the entire recording, the above process is repeated for each activation map generated through the recording. The maps generated are then averaged together, resulting in the mean activation time differences at each pixel (Figure 2.2a, final graphic). This has the effect of retaining only stable features of the recording (e.g. apparent conduction block at the core of the self-sustaining circuit) and dampening features that change from frame to frame (e.g. the propagating wave front).

2.2.10 Statistical analysis

All values are presented as mean ± standard error of the mean. n represents the number of times an experiment was repeated, and different colonies within the same μ-dish were considered separate repeats. All statistical analyses were completed using R open source software (version 3.6.1, `https://r-project.org`). Normality was tested using the Kolmogorov-Smirnoff test. Differences between proportions were tested using Fisher's exact test followed by a Bonferroni correction for multiple comparisons. Mann-Whitney U-test was used to test for significant differences between groups and corrected for mul-

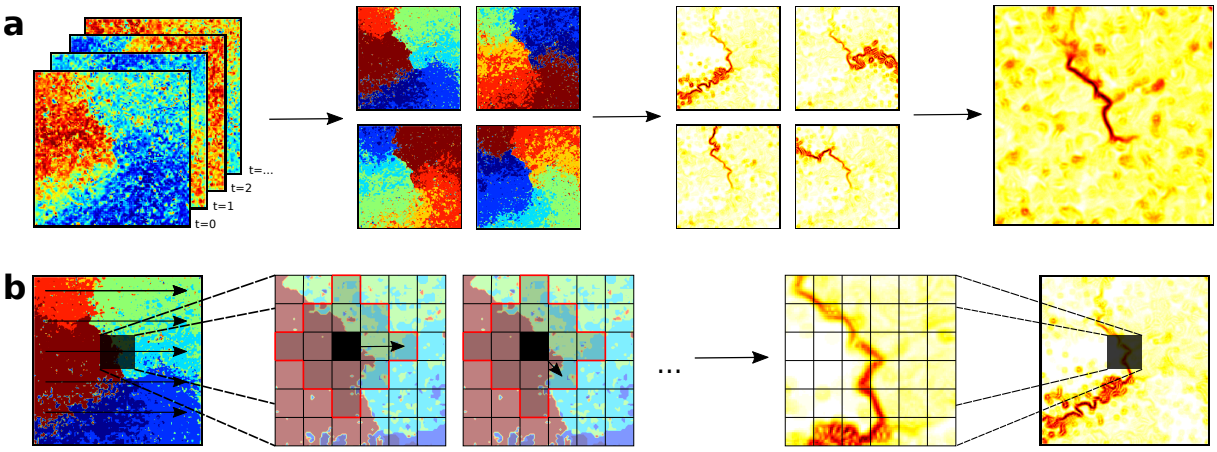


Figure 2.2: **a** Overview of the generate a conduction delay map for an entire recording of self-sustaining activity. Starting from processed frames of the recording, a series of activation maps are generated covering a full rotation of the circuit. Each activation map is processed into a single conduction delay map (detailed in the next subfigure). Averaging these maps produces a single conduction delay map for the recording, retaining consistent features and dampening features that change between frames. **b** Processing a single activation map into a conduction delay heatmap. For each pixel in the map, the neighbouring pixels are found, and the activation time difference between each calculated. The process is repeated for each pixel and averaged, giving a single conduction delay map. Figure adapted from [132] (CC BY).

tiple comparisons using Dunn's test. Relationships between two measurement variables were evaluated using regression analysis. Significance levels are indicated in the text.

2.3 Results

2.3.1 Prevalence of self-sustaining activity in microscopic colonies

The colony areas resulting from different volumes of fibronectin drops were established as 2.5 μl: 3.5±0.1 mm^2 ($n = 5$), 5 μl: 6.4±0.1 mm^2 ($n = 3$) and 10 μl: 9.8±0.2 mm^2 ($n = 3$) from measuring the curvature of the boundaries in phase images. These areas are adopted in the analyses that follow.

A total of 63 recordings with activity were captured and analysed in various sizes of colonies (3.5 mm^2: $n = 25$, 6.4 mm^2: $n = 22$, 9.8 mm^2: $n = 16$). Self-sustaining activity (or a series of wave fronts likely originating from this activity) was observed most often in 9.8 mm^2 colonies (38%, $n = 6/16$), a smaller proportion in the 6.4 mm^2 size (32%, $n = 7/22$) and only one identified in the smallest 3.5 mm^2 colonies (4%, $n = 1/25$). Figure 2.3 summarises the occurrence of self-sustaining activity with colony area. When

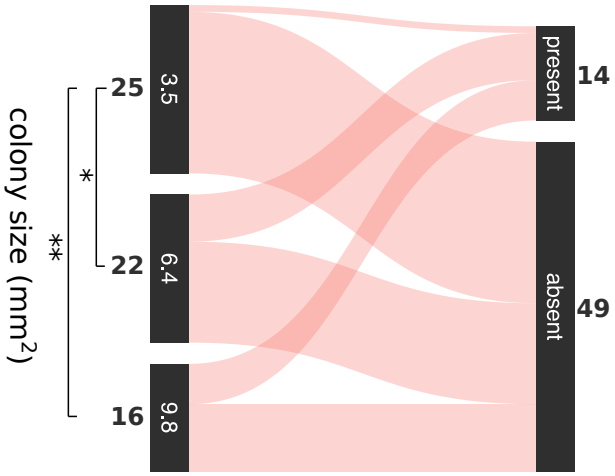


Figure 2.3: Presence/absence of self-sustaining activity by colony area. Numbers outside of boxes indicate the count for each category inside the boxes. Significance shown as measured using Fisher's exact test (* $p < 0.05$, ** $p < 0.01$).

tested with Fisher's exact test, there was a significant difference between the occurrence between the smallest and medium colonies ($p = 0.018$) and between the smallest and largest colonies ($p = 0.009$).

Wave fronts originating from self-sustaining activity would affect the count for triggers in the subsequent analysis. After excluding those recordings with self-sustaining activity, the number of natural triggers was quantified for each colony size. The results were 3.5 mm^2: 3.2±0.3 triggers ($n = 24$), 6.4 mm^2: 3.6±0.5 triggers ($n = 15$), and 9.8 mm^2: 5.7±0.5 triggers ($n = 10$). There was an increase in number of triggers between the 3.5 mm^2 and 9.8 mm^2 colonies ($p = 0.0014$) and between the 6.4 mm^2 and 9.8 mm^2 colonies ($p = 0.0166$). Figure 2.4a displays these results.

To determine the change in general activity with colony area, the total number of wave fronts irrespective of direction or frequency was also quantified for each 30 s recording. An increase in general activity was observed between the 3.5 mm^2 and 9.8 mm^2 colonies ($p = 0.003$) and between the 6.4 mm^2 and 9.8 mm^2 colonies ($p = 0.0264$). Figure 2.4b summarises these data.

2.3.2 Spatial stability of triggers and self-sustaining activity

Twenty locations with natural triggers were captured before and after depolarisation with KCl solution and 13 before and after inhibition of gap junctional coupling using heptanol.

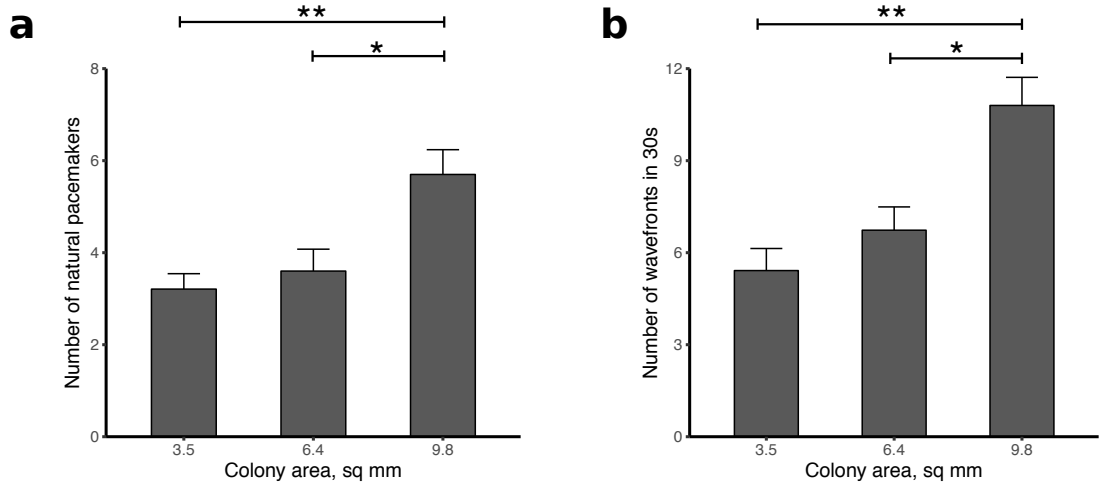


Figure 2.4: **a** Number of natural triggers in each colony size, with significance levels indicated. **b** Total number of wave fronts in 30 second recording in each colony size. Significance tested using Mann-Whitney U-test (* $p < 0.05$, ** $p < 0.01$). Figure adapted from [71] (CC BY).

Natural triggers were characterised by automatic activity at irregular frequencies. The location of the triggers was confirmed pre-treatment, then activity re-evaluated after treatment and return to normal imaging solution. Analysis of the recordings after depolarisation with KCl showed that 10% ($n = 2/20$) of recordings showed no trigger return, 55% ($n = 11/20$) showed activity from another location (i.e. another trigger cell) and 35% ($n = 7/20$) showed return of the original trigger. After uncoupling with heptanol, 38% ($n = 5/13$) showed no activity, 23% ($n = 3/13$) showed irregular activity from another location and 38% ($n = 5/13$) showed activity from the original trigger. No self-sustaining activity appeared after either depolarisation or uncoupling in any of these colonies (Figure 2.5a). There is not a statistically significant difference between the proportion of results for trigger stability between each intervention ($p = 0.087$).

Nine locations of self-sustaining wave circuits were recorded before and after depolarisation, and 18 before and after gap junctional uncoupling to assess whether the circuits would reappear in the same location. No self-sustaining circuit reappeared in the same location after either depolarisation or uncoupling. In 56% ($n = 5/9$) of the recordings after depolarisation and 28% ($n = 5/18$) after uncoupling, regular activity emanated from a different location, suggesting self-sustaining activity had developed elsewhere in the cell colony. 33% ($n = 3/9$) of recordings after depolarisation and 11% ($n = 2/18$) after uncoupling showed one or more impeding wave fronts from different directions, sug-

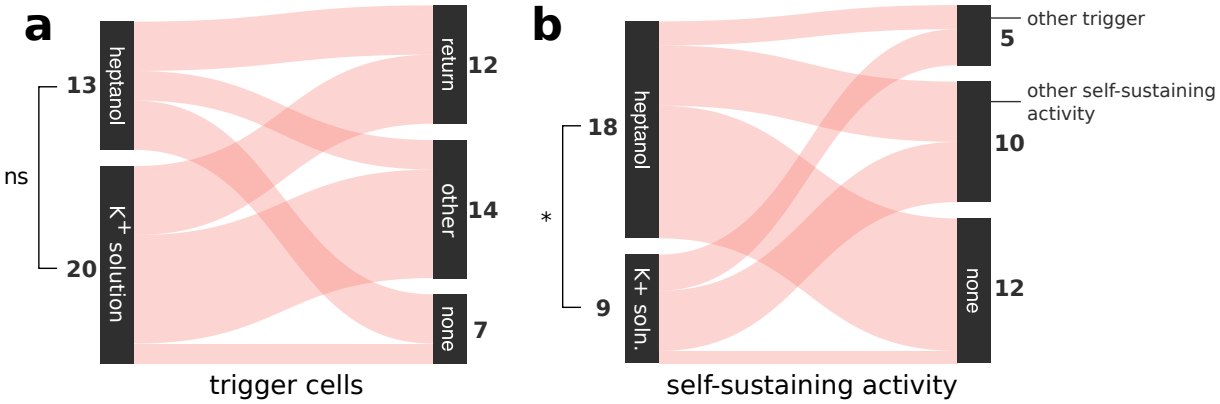


Figure 2.5: Results of testing spatial stability of activity in HL1-6 monolayers after either depolarisation using elevated K^+ solution or gap junctional uncoupling using heptanol. **a** Results for natural trigger cells, 'return' implies the same trigger was observed after washout, 'other' implies only trigger activity from another location was observed and 'none' implies no activity reappeared in the colony after washout. **b** Results for self-sustaining circuits.

gesting only activity from natural triggers. 11% ($n = 1/9$) after depolarisation and 61% ($n = 11/18$) after uncoupling showed no activity returning in the colony. When activity was present after depolarisation or uncoupling, the original location of the self-sustaining circuit did not display abnormal propagation, indicating cells in this location were not dysfunctional. There was a significant difference between the proportion of activity in each category ($p = 0.019$), suggesting a contrasting mode of action between the two interventions.

Figure 2.6 shows example activation maps captured before and after electrical uncoupling using heptanol of a trigger cell near a colony edge (a, b) and a self-sustaining activity circuit (c, d). The two time activation maps for the trigger cell are similar. The activation map generated at the same location as the self-sustaining circuit after uncoupling shows a wave passing the field of view, originating from a different location.

2.3.3 Characteristics of self-sustaining activity

Twenty-seven self-sustaining circuits were recorded in isotropic monolayers. Of the 27, all remained stable around the same 'core' path for the duration of the recording (10 s). While locating the circuit (up to 5 minutes), the wave fronts observed visually also appeared to emanate from the same location with the same regularity. The mean dominant frequency of the self-sustaining activity was 2.7±1.0 Hz.

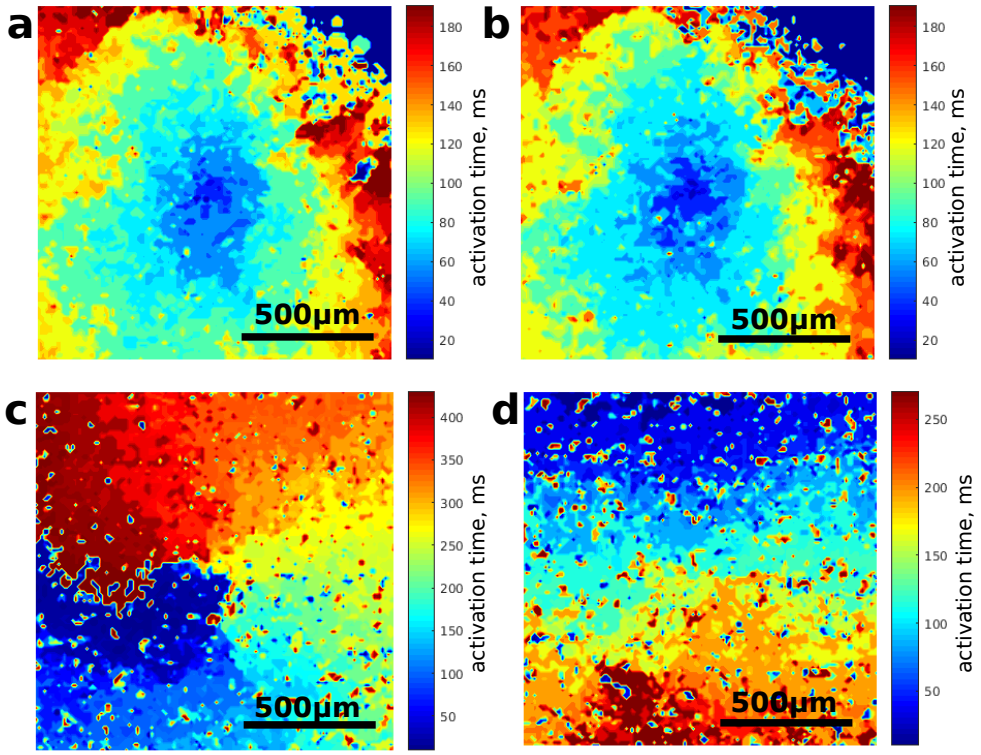


Figure 2.6: Example activation maps before and after electrical uncoupling with heptanol for **a, b** a trigger cell near a colony edge and **c, d** self-sustaining activity.

Recordings at the core of self-sustaining activity were processed using our algorithm to reveal regions of slow conduction or complete conduction block. The algorithm measures the local difference in activation time in space through each frame of the recording, and highlights the apparent 'core' being rotated around. The core generated appeared to manifest in three key forms (Figure 2.7). 59% ($n = 16/27$) showed self-sustaining activity was rotating around small areas of cells connected by thin lines which waves did not cross, 19% ($n = 5/27$) appeared to rotate around a single line which waves did not cross, and 22% ($n = 6/27$) around three or more connected lines.

The path of the self-sustaining activity was next analysed by estimating how far a wave would have to travel to complete one circuit. This perimeter was estimated for each recording by fitting a convex hull to a thresholded image of the conduction slowing heat map. A convex hull is defined as the smallest convex shape that contains a set of points (in this case the pixels of the thresholded image). Figure 2.8 shows an example of self-sustaining activity with corresponding activation time map and perimeter estimation.

Perimeters of the cores ranged from ∼0.8-3.1 mm when estimated using the convex hull

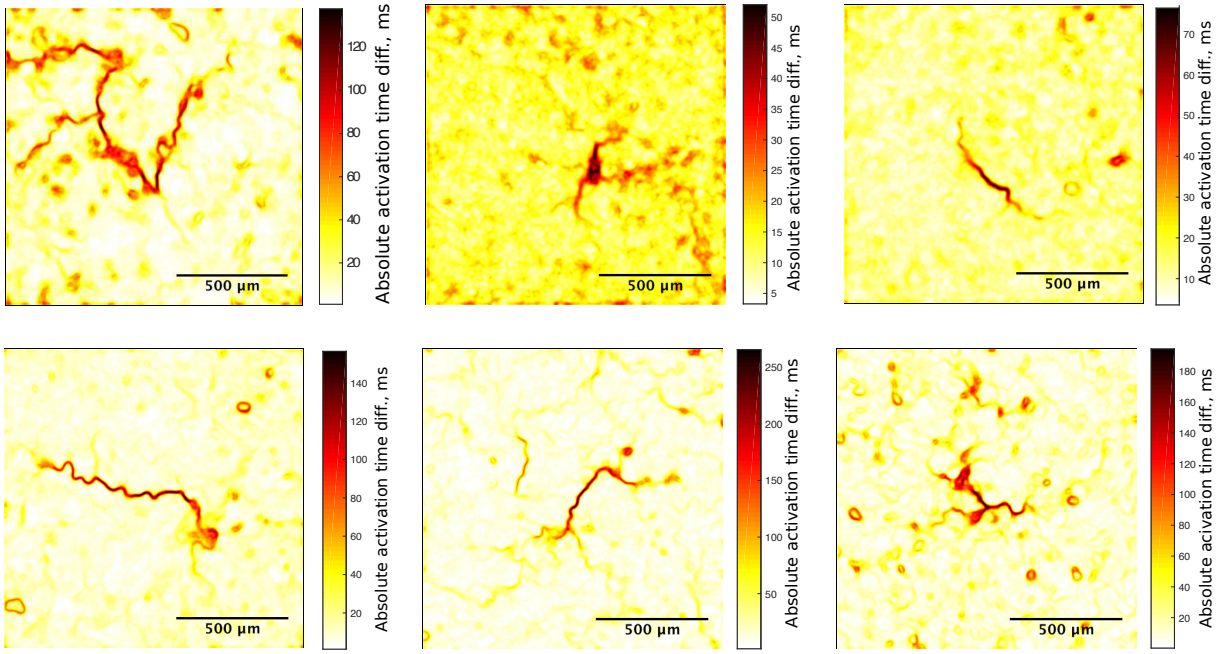


Figure 2.7: Examples of conduction delay heat maps showing the stable core of self-sustaining activity. Dark areas correspond to large conduction delay between activation on either side of the area. Colour bars are distinct to individual heat maps as the dominant frequency of the self-sustaining circuit was different. Adapted from [71] (CC BY).

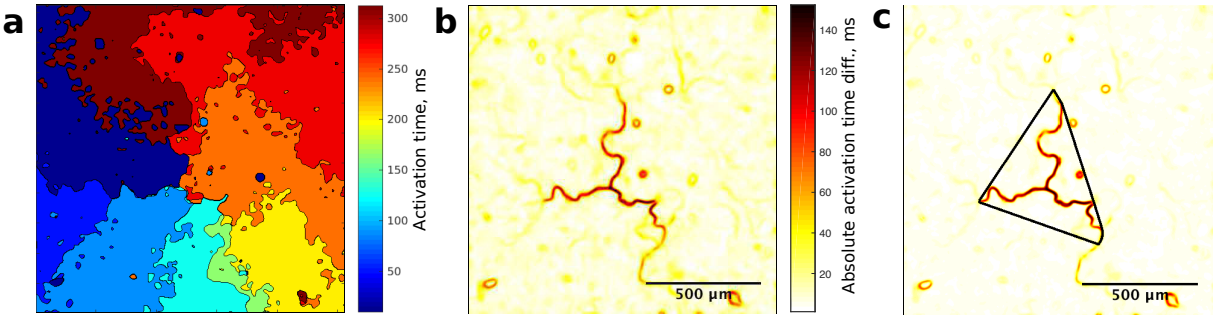


Figure 2.8: **a** Activation map of self-sustaining circuit, dominant frequency 2.9 ± 0.1 Hz. **b** Conduction delay heatmap generated from same recording highlighting the core of the rotational activity. **c** Calculated convex hull (black lines) overlaid on conduction delay heatmap. Adapted from [71] (CC BY).

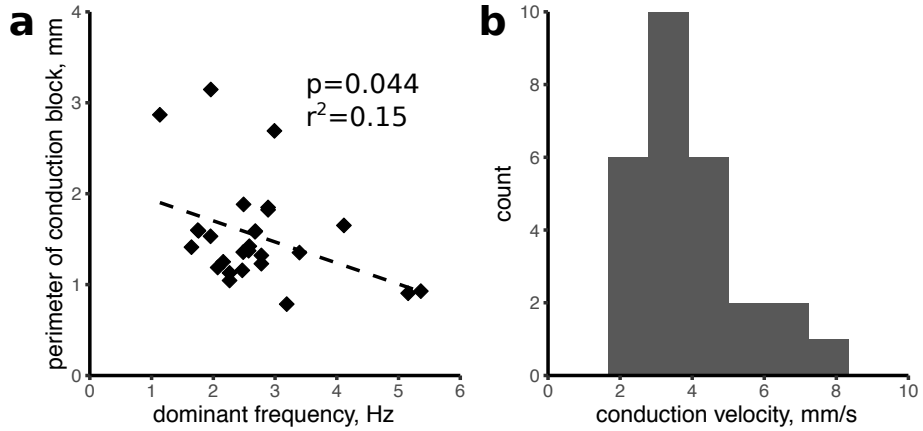


Figure 2.9: **a** Scatter plot showing perimeter of core of self-sustaining activity regressed on dominant frequency of the activity. Linear regression is shown as a dashed line, $p = 0.044$, $r^2 = 0.15$. Adapted from [71] (CC BY). **b** Histogram showing inferred conduction velocities at each core.

method. The mean and standard error of the perimeters were 1.5±0.6 mm. As we would expect (other variables held constant) an increasing perimeter to reduce the dominant frequency of the self-sustaining activity, the perimeter of the core was regressed on the dominant frequency of each recording. The resulting linear regression suggests that a reducing perimeter increases dominant frequency, but a low r^2 value indicates additional variables may also influence this relationship (Figure 2.9a).

The conduction velocity at the core was estimated from the perimeter values and period of rotation. Figure 2.9b shows a histogram of the resulting measurements. The mean conduction velocity at the core was 3.9±0.3 mm/s.

2.3.4 Closer look at the core of self-sustaining activity

The morphology and activity of individual cells near the core of self-sustaining activity in monolayers were analysed by overlaying the conduction slowing heat map on an aligned image of two-dimensional cell morphology from Wheat Germ Agglutinin staining. Figure 2.10a shows an example of an image from the self-sustaining circuit which generated the conduction slowing heat map in the lower left of Figure 2.7. Figures 2.10b shows a zoomed view from a region where a group of cells appears to be within the conduction slowing region, and Figure 2.10c shows a region along the line of apparent conduction block. The results for this single example were representative of 9 recordings analysed in the same fashion.

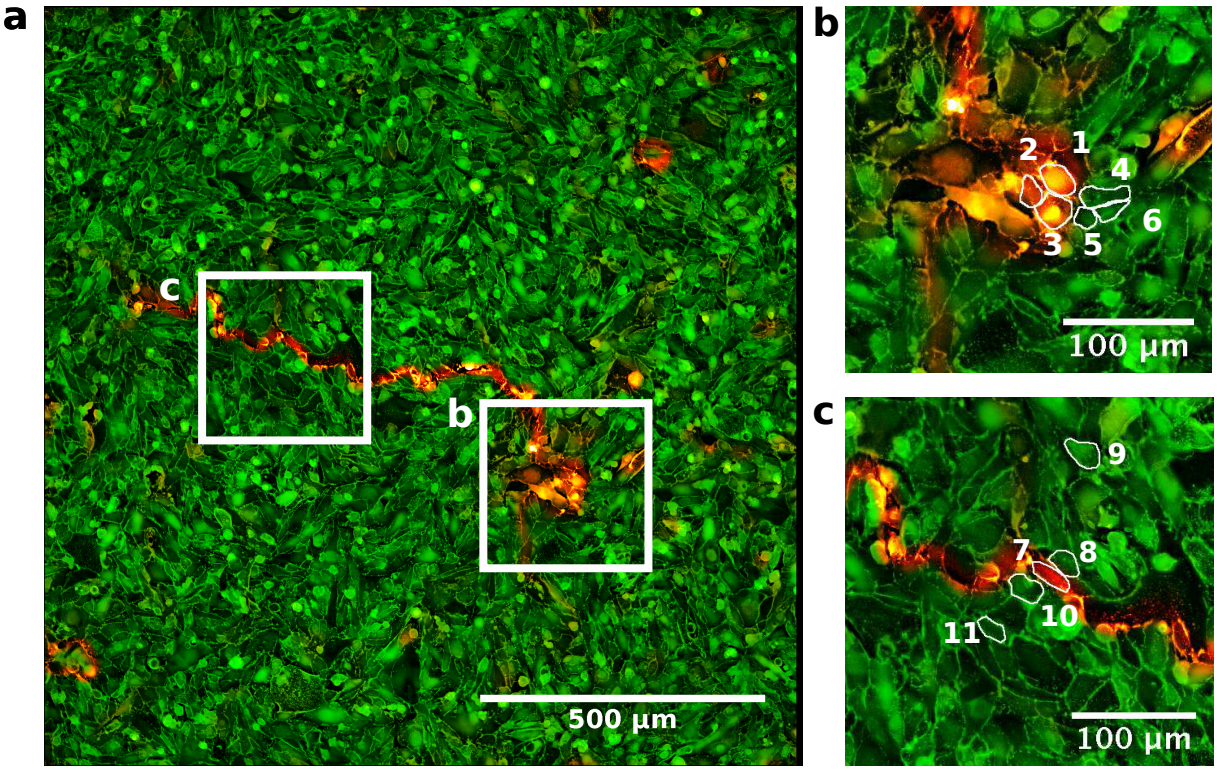


Figure 2.10: **a** Microscopy image of cell membrane staining in monolayer at location of self-sustaining circuit. The conduction block/slowing heat map which highlights the core of the circuit has been overlain on the image. The circuit corresponds to the conduction slowing heat map in the lower left sub-figure of Figure 2.7. White boxes indicate the locations of locations where cell activity has been analysed. **b, c** Zoomed images of regions with analysed cells. Activity was analysed in cells indicated, with numbers corresponding to graphs in Figure 2.11. Adapted from [71] (CC BY).

Six cells are highlighted in Figure 2.10b; three within the core region (cells 1, 2 and 3) and three outside (cells 4, 5 and 6). Ca^{2+} transient activity from these cells was analysed in the video recording and is shown in Figure 2.11a. The cells inside the core region show no clear pattern of intracellular Ca^{2+} activity. In contrast, the cells outside show regular firing at the frequency of the self-sustaining circuit.

When a conduction block line was observed at the core, it generally appeared to be on the order of one cell thick. However, it was not possible to confirm whether the block was indeed across the gap junctions between adjacent cells or through a particular line of cells. In Figure 2.10c, 5 cells were highlighted and measured in the original recording. Cell 7 appeared to reside 'inside' the conduction block region, cells 8 and 10 were adjacent to cell 7 on either side, and cells 9 and 11 were further away on either side of the line. Figure 2.11b shows Ca^{2+} transients measured in each of these cells (note the top row shows the same Ca^{2+} transient trace from cell 7 for vertical comparison with other traces). The left column shows activity in cells above the line of block, and the right column shows activity in cells below the line. Arrows have been added to mark the peak Ca^{2+} measurements at each rotation.

The traces exhibited by cells close (cells 8 and 10) and far (cells 9 and 11) from the line show the expected periodic Ca^{2+} transients associated with the self-sustaining circuit with a dominant frequency of 2.9 Hz. The two columns are out of phase with each other as they are on opposite sides of the line of block. Cell 7 (top row) exhibits different activity to other cells. It appears to fire Ca^{2+} transients at double the rotation rate of the self-sustaining circuit. The arrows indicate how this activity is consistent with activity on either side of the line. To ensure that this observation was not due to the recorded area for cell 7 overlapping other cells, the analysis was repeated with a smaller region within cell 7 and showed the same activity (with increased noise caused by fewer averaged pixels). Analysis of other cells along the line of block either showed similar 'double-firing' activity as cell 7, or unclear activity similar to cells 1-3 in Figure 2.11a.

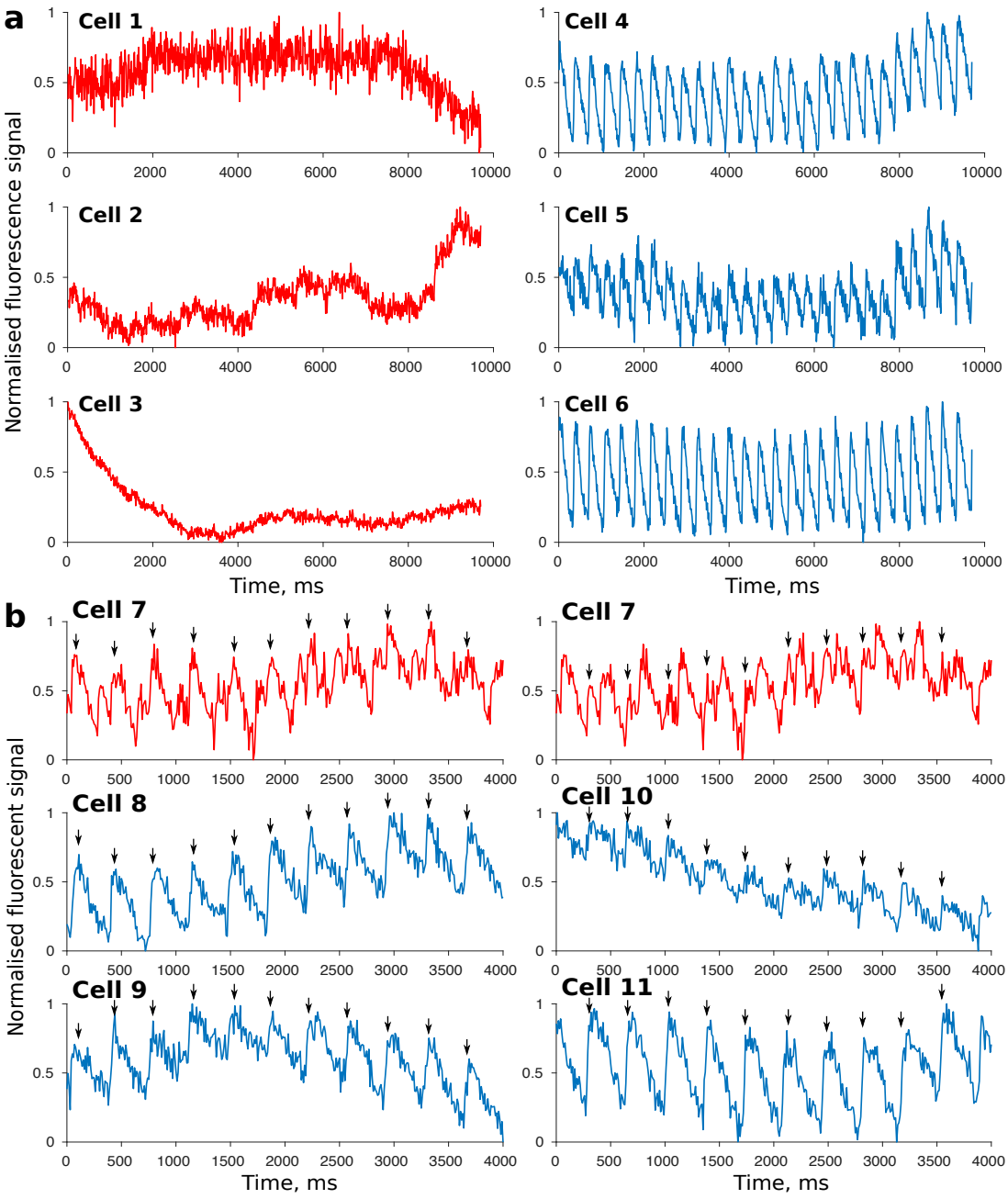


Figure 2.11: **a** Normalised fluorescence signals from regions encapsulating cells, highlighted in Figure 2.10b. Cells 1, 2 and 3 were within the region highlighted by the conduction slowing heat map. **b** Normalised fluorescence signals from regions encapsulating cells, highlighted in Figure 2.10c. Cell 7 is the top row of both columns is within the region highlighted by the conduction slowing heat map. Cells 8 and 10 are adjacent cells on either side. Cells 9 and 11 were cells further away from the conduction block line on either side. Normalised fluorescence signals are calculated as $(F - F_{\text{min}})/(F_{\text{max}} - F_{\text{min}})$ for each signal from the regions of interest outlined in Figure 2.10. Adapted from [71] (CC BY).

2.3.5 Comparing recordings of self-sustaining activity with voltage and Ca^{2+} dyes

The results above were obtained by recording Ca^{2+} transients in cell monolayers. The high fluorescence amplitude of the Ca^{2+} dye made it possible to visually track wave fronts to find the core of self-sustaining circuits. To check whether the Ca^{2+} activity in these regions is consistent with action potential propagation, two sets of dual-staining optical mapping experiments were also conducted. In the first, 3 simultaneous optical mapping experiments were carried out using di-8-ANEPPS and Fluo-4 AM. In the second, 10 recordings were captured using a new voltage dye, BeRST-1 [135], with Fluo-4 AM, where the Ca^{2+} transient activity was recorded immediately following the voltage recording. The new voltage dye has a higher fluorescence amplitude compared to conventional voltage dyes.

Figure 2.12 compares simultaneous recordings of a self-sustaining circuit using di-8-ANEPPS and Fluo-4 AM. Figures 2.12a and b show that activation maps generated from action potentials and Ca^{2+} transients are similar in this preparation. The maps were calculated using the same recording with a constant frame shift of 3 frames (30 ms) to account for the delay in upstroke of the Ca^{2+} transient compared to action potential (Figure 2.12g). Figures 2.12c and d display the conduction slowing heat maps for voltage and Ca^{2+} transients respectively. These maps show a similar morphology of the core region highlighted by large conduction delay. The core generated from action potential analysis appears larger than that generated from Ca^{2+} transients. This may be due to the much higher noise and lower signals produced by di-8-ANEPPS compared to Fluo-4 (compare traces in Figures 2.12e and f).

Figures 2.12e and f show traces taken from the indicated areas around the circuit core. On the dual optical mapping microscope setup, it was not possible to obtain the high resolution membrane images captured on the other microscope, so these areas (circles of diameter 10 μm) were selected to be less than the expected cross-sectional area of a cell. Outside of the highlighted core region (area 4), both fluorescent signals clearly show firing at the expected frequency of the self-sustaining wave. In areas 1, 2 and 3 (all 'within'

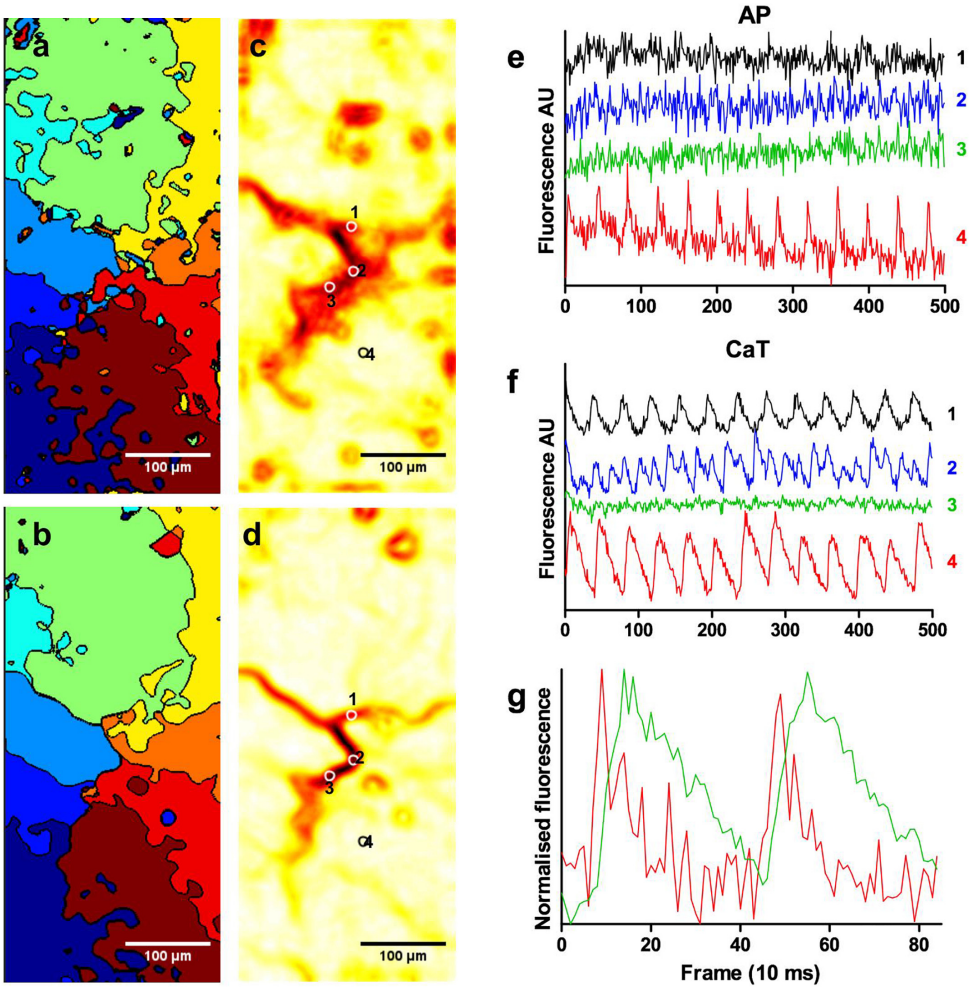


Figure 2.12: **a** Activation map of self-sustaining circuit generated by voltage recording. **b** Activation map of same circuit generated from simultaneous Ca^{2+} transient recording. **c, d** Corresponding conduction slowing heat maps highlighting the core of rotation. The maps for Ca^{2+} transients are generated from data three frames (30 ms) later than the voltage maps to account for the delay in upstroke between action potential and Ca^{2+} transient. Areas 1 to 4 are circles of 10 μm diameter used to record traces. **e** Unfiltered and non-normalised voltage fluorescence traces from 4 locations in c. **f** Unfiltered and non-normalised Ca^{2+} transient traces from same 4 locations in d. **g** Comparison of trace from area 4 showing the delay in upstroke between the two signals. Adapted from [71] (CC BY).

the core area), there is no clear firing pattern in the voltage trace (Figure 2.12e). Some rhythmic activity above the noise can perhaps be observed in trace 1, which may indicate a low amplitude Ca^{2+}-dependent action potential. Unclear signals in the voltage train were a common observation across all recordings in this experiment. Ca^{2+} transients can be observed (Figure 2.12f) at the frequency of the circuit (area 1), double the frequency (area 2) and with no apparent signal (area 3). This could indicate that some cells in the core are depolarised above the threshold for Na^{+} channel activation but not always above the threshold for Ca^{2+} channel activation and can therefore release intracellular Ca^{2+} stores triggered by influx of Ca^{2+} through transmembrane ion channels. This is consistent with observations in Figure 2.11 where some cells in the core (cells 1, 2 and 3) had no discernible Ca^{2+} activity whereas others showed activity (cell 7).

BeRST-1 is one from a new family of voltage dyes with higher signal-to-noise ratio and amplitude compared to conventional dyes [135]. 10 recordings of self-sustaining activity were captured in HL1-6 colonies dual-stained with BeRST-1 and Fluo-4 AM. Figure 2.13 gives a representative example from one experiment. In Figure 2.13a and b, the activation maps show clear similarities in the propagation path of the wave around the core of the self-sustaining activity. Figure 2.13c and d, show the corresponding conduction delay heat maps which highlight the stable core for each dye. The single line of apparent conduction block at the core has a similar, though not identical, shape in the two maps. The Ca^{2+} transient map has noticeably more cell-sized regions with a high activation time difference (one is highlighted with a black arrow).

The signal traces in Figure 2.13e and f are from an alike point on each map. Both the unfiltered and filtered signals are shown. The filtered signals are processed as described in Section 2.2.9. The voltage and Ca^{2+} transient signals have comparable fluorescence amplitudes, as opposed to observed previously using di-8-ANEPPS (Figures 2.12e and f). There is slow drift in the Ca^{2+} transient signal while the voltage signal maintains a stable baseline. The traces in Figure 2.13g and h are taken from a region with a notable difference in the voltage and Ca^{2+} transient core maps (highlighted by the black arrow in Figures 2.13c and d). The unfiltered trace shows the Ca^{2+} transient signal has low

fluorescence amplitude and drift in this region. Thus the filtered signal cannot accurately infer activation times, leading to the disparity observed in the Ca^{2+} transient core map while the voltage map does not exhibit this effect.

2.3.6 Self-sustaining activity in anisotropic monolayers

All experiments above were conducted in isotropic colonies of HL1-6 myocytes, with no clear alignment of cells in the monolayer. *In vivo*, cardiac cells are aligned in the fibre direction, giving cardiac tissue anisotropic conduction properties. The next experiments served to demonstrate that the same self-sustaining activity exists in anisotropic monolayers of HL1-6 myocytes, and determine the effect of anisotropy on features at the core of the circuit. In total, 45 recordings of activity were analysed from anistropic HL1-6 colonies. Of these recordings, 19 were of a self-sustaining circuit and the remainder were generic activity (wave propagation through the monolayer).

Figure 2.14a-c shows examples of images captured from anisotropic monolayer experiments. The phase image in Figure 2.14a clearly shows the microabrasions on the dish surface, while the membrane image in Figure 2.14b delineates the shape of the cells without interference of the dish surface. Figure 2.14c shows the processed conduction slowing map for the recording of self-sustaining activity at this site, captured prior to the previous images. In this case, it is particularly apparent that the conduction slowing line aligns with the direction of microabrasions.

Figure 2.14d compares the directionality histograms of each of the previous images using the OrientationJ plugin for FIJI. The phase histogram has a clearly defined dominant direction at approximately 10° anticlockwise positive to the horizontal. The histograms representing the cell morphology and core map appear to peak around the same direction, but their reduced prominence indicates the more diffuse local directionality in these images.

To firstly validate the methodology that the microabrasion protocol has a measurable effect on cell morphology, the dominant direction of membrane images (i.e. cell morphology) was regressed against the dominant direction of phase images (i.e. the direction of

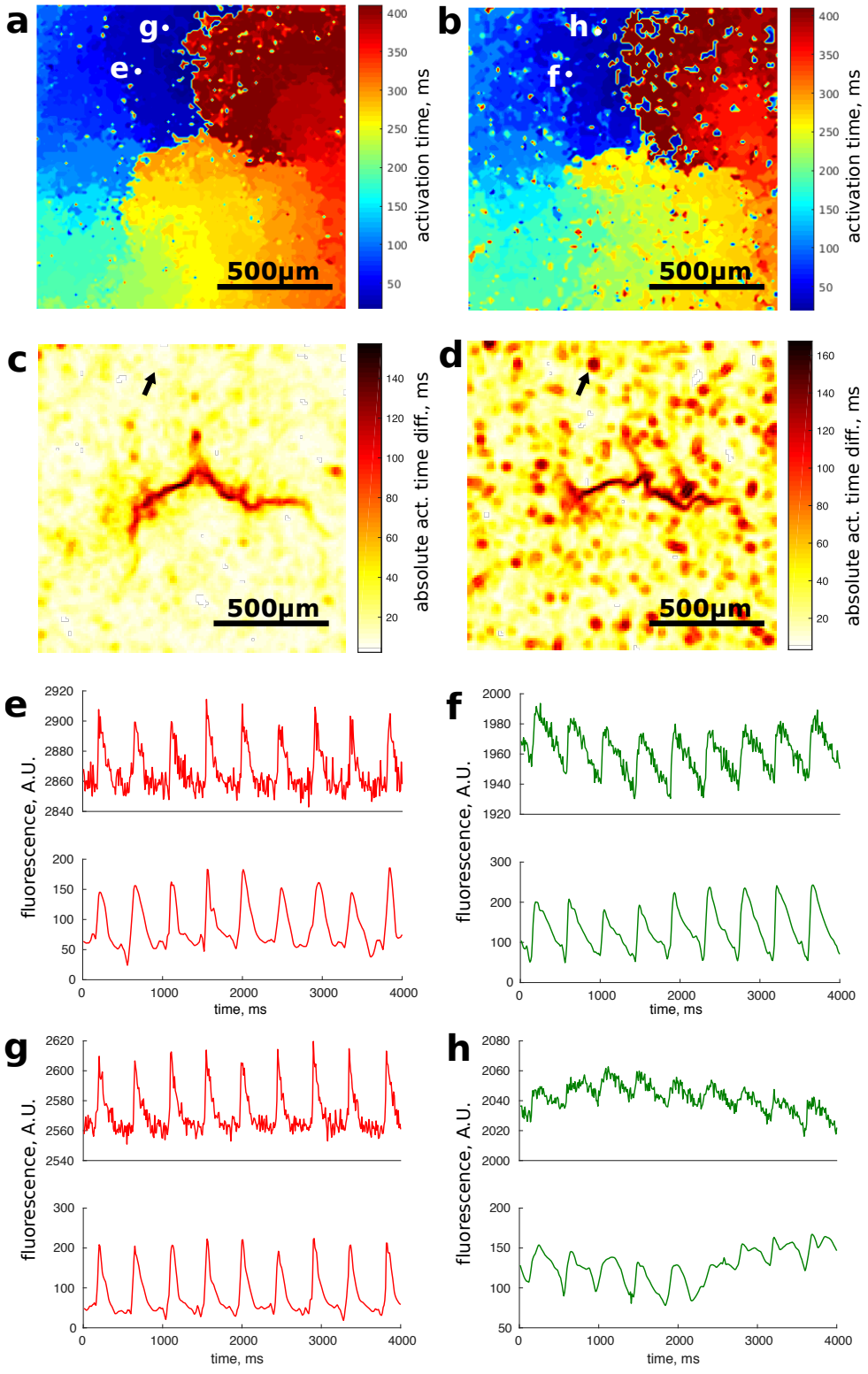


Figure 2.13: Comparing recording using BeRST-1 for voltage (left) to Fluo-4 AM for Ca^{2+} transients (right). **a** Activation map of self-sustaining activity recorded using voltage dye. **b** Same activity recorded using Ca^{2+} dye immediately following voltage recording. White dots mark sites where later traces are extracted. **c, d** Corresponding conduction delay heat maps from both recordings. Black arrow highlights one of the clear differences outside of the core. **e, f** Unfiltered (above) and filtered (below) signals for voltage and Ca^{2+} transient recordings from a 'normal' signal site. **g, h** Unfiltered (above) and filtered (below) signal for voltage and Ca^{2+} transient recording from a site with marked difference in the conduction delay heat maps. Unfiltered traces are non-normalised.

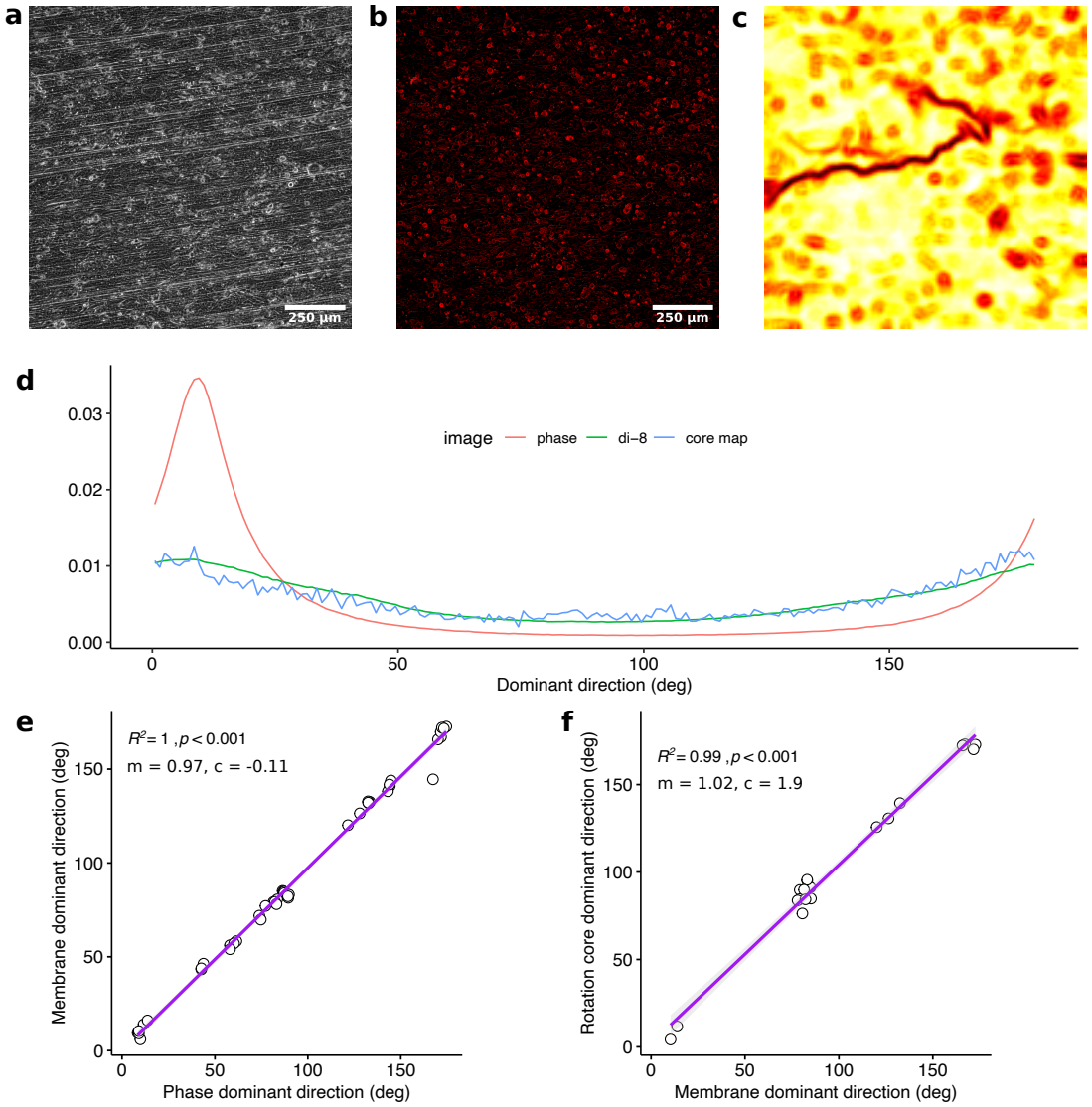


Figure 2.14: Results from anisotropy experiments. **a** Representative phase image clearly showing microabrasions on the dish surface. **b** Corresponding membrane image (stained using di-8-ANEPPS). **c** Corresponding conduction slowing heatmap processed from Ca^{2+} transient propagation recording acquired prior to previous images. **d** Directionality histograms of images in a-c generated using OrientationJ plugin in FIJI. **e** Membrane image dominant direction plotted against phase image dominant direction as confirmation that experimental protocol affects cell morphology in the monolayer. Linear regression line is plotted in purple. **f** Conduction slowing heatmap (showing core morphology of self-sustaining activity) dominant direction plotted against membrane image dominant direction to show effect of anisotropic monolayer on propagation activity. Linear regression line plotted in purple.

microabrasions) for all 45 captured images. Figure 2.14e shows the resulting relationship. Linear regression gives a line of unit slope indicating similar dominant directions in both images, suggesting that cells are aligning in the direction of microabrasions ($p < 0.001$, $R^2 = 1$).

Next, a similar analysis was carried out to test for an effect of monolayer anisotropy on the morphology of the core of the 19 recordings of self-sustaining activity. The dominant direction of the core map image was regressed against the membrane dominant direction (i.e. cell morphology). Figure 2.14f shows that a similar linear relationship exists between the two variables ($p < 0.001$, $R^2 = 0.99$).

2.4 Discussion

The aim of this chapter was to obtain insight into the formation and mechanisms of self-sustaining activity in monolayers of HL1-6 myocytes. There were six key findings from the results:

1. The occurrence of self-sustaining activity depends on colony size, possibly mediated by the number of interacting triggers in colonies;

2. Trigger activity is a feature of the underlying substrate and remains locationally stable while self-sustaining activity was never observed to re-occur in the same location;

3. The core of the self-sustaining activity is not only small groups of cells but also connected line(s) which appear to slow or block propagation;

4. There is an inverse relationship between the perimeter of this core region and the dominant frequency of the activity;

5. The cells within the core area appear to either be inactive or able to display Ca^{2+} transients, but action potentials could not be detected;

6. Adding anisotropy to the monolayer aligns lines of apparent conduction block at the core of self-sustaining activity.

Each of these findings will now be discussed in more detail.

2.4.1 Self-sustaining activity can be initiated from few triggers but requires a minimum area

The aim of the trigger quantification experiment was to determine if a minimum threshold for number of triggers or colony area exists for formation of self-sustaining activity in HL1-6 monolayers. The results showed that there were significantly more trigger cells and wave activity in the largest colony size (9.8 mm^2) compared to the smaller sizes (3.5 mm^2 and 6.4 mm^2). This is an unsurprising result, as one would expect that the number of automatic focal activities would increase along with the increased number of cells in larger colonies.

Despite the low incidence of natural triggers, it was possible to observe and record a single self-sustaining rotational circuit in the smallest colony area. This suggests that only a small number of point sources are required to initiate self-sustaining activity. Previous studies have shown that it is possible to induce re-entry in cell monolayers using stimulation by S1-S2 protocol or rapid pacing from a point source [43,140,141]. In our study, the smallest colonies had over three triggers on average yet showed almost no occurrence of self-sustaining activity. The significant increase in occurrence of self-sustaining activity between the smallest and largest colonies indicates that sufficient area is a likely condition for the activity to develop, provided that triggers are present. This could be due to an increasing area increasing the likelihood of an appropriate morphology substrate existing in a particular colony.

In HL1-6 monolayers, as colony size increases it appears that the minimum trigger number condition is satisfied before the minimum area, but this may not be the case for other cell types with differing degrees of natural automaticity and/or conduction velocities. For example, if a multicellular model had a lower incidence of automatic activity, it could be possible to seed a colony size large enough for self-sustaining activity to perpetuate, but without the necessary number of triggers to initiate the activity. Given that the smallest HL1-6 colony size showed almost no incidence of self-sustaining activity, while

the medium size exhibited this activity in 32% of recordings, it can be inferred that there is a steep increase in the likelihood of self-sustaining activity in these monolayers between 3.5 mm^2 and 6.4 mm^2.

2.4.2 Natural triggers remain spatially stable while self-sustaining activity can form in multiple locations

After depolarisation with KCl or electrical uncoupling by heptanol followed by reactivation in normal HBSS, triggers from cells that exhibited automaticity returned in the same location in 35% of cases using depolarisation and 38% after uncoupling. In the remaining recordings, activity from different triggers was observed to return, originating from one or more other locations. This observation is potentially caused by changing firing frequency of other triggers in the colony impeding the original triggering cells. Similarly, these other triggers would likely have been 'silenced' by the original trigger before depolarisation. It would be expected for automaticity to remain a constant property of the individual cell(s) as it is a molecular mechanism that should not be affected by temporary depolarisation of the cell membrane or by uncoupling [62, 142].

Self-sustaining activity recorded in the HL1-6 monolayers remained stable, rotating around the same apparent conduction block, but was never observed to return to the same location after either treatment. In 56% of cases for depolarisation and 28% for uncoupling, regular wave fronts emanated from outside of the recorded area. These were assumed to propagate from self-sustaining activity which emerged in a new location and remained spatially stable, though it was not possible in the time frame of the experiment to confirm. However, if this were the case, it would suggest that different sites exist as substrate that are conducive to self-sustaining activity formation within small areas. The interaction of wave fronts from trigger activity appears to arrange into an organised circuit that can manifest in any one of these locations. The consequence of this finding to clinical practice is that there may not be a single specific site that can be ablated to prevent initiation of re-entrant activity [143].

There were some differences between depolarisation using KCl and using heptanol.

After washout of heptanol, generally less activity was observed across experiments. For the trigger analysis, 38% of colonies displayed no activity after heptanol washout compared to 10% following repolarisation from elevated K^+. Similarly, for the analysis of self-sustaining activity, repolarisation led to no activity in 11% of colonies while uncoupling by heptanol resulted in 61% of colonies showing no activity following washout. This may have been caused by heptanol acting on other channels and receptors since its mode of action relies non-specifically on membrane fluidity [144, 145], whereas an elevation of K^+ can be compensated relatively rapidly by the cells upon return to a physiological solution.

2.4.3 The 'cores' of the stable self-sustaining activity have distinct shapes

The conduction delay algorithm developed in this chapter made it possible to investigate the shape of cores of self-sustaining activity in video recordings, and make comparisons to the underlying two-dimensional cell morphology. Thin lines which were not penetrated by the propagating waves in instances of self-sustaining activity were a prominent and unexpected outcome of these experiments.

The heat maps of conduction slowing were generated from recordings of Ca^{2+} transient imaging. This was necessary to visually track propagating wave fronts during experiments to locate the centre of rotational activity. Use of di-8-ANEPPS, in comparison, necessitates a high level of signal processing due to the poor signal-to-noise ratio and limited recording time of this dye due to toxicity and photo-bleaching. The results from dual-optical mapping suggest that Ca^{2+} transients are a reasonable surrogate for action potential propagation under the experimental conditions.

Compared to the dual-optical mapping with di-8-ANEPPS, BeRST-1 has a higher relative fluorescence amplitude (BeRST-1: 25% F/F_0 per 100 mV, di-8-ANEPPS: 10% F/F_0 per 100 mV) [146]. In experiments comparing sequential BeRST-1 and Fluo-4 AM recordings, the voltage dye gave a clearer signal than the Ca^{2+} dye. As in dual-optical mapping, maps of the core of self-sustaining activity were similar, but not identical. This could be caused by inherent differences in action potential and Ca^{2+} transient activity in

the cells, or due to changes in the shape of the circuit core between the recordings (which could not be carried out simultaneously in this case). Unfortunately, extended imaging using BeRST-1 appears to increase the action potential duration of HL1-6 cells, indicating it may have a non-negligible physiological effect on repolarising K^+ channels (Dr Pitcher, Imperial College London, personal communication).

Hong et al. [66] were the first to map self-sustaining activity in the original HL-1 cell line. They reported that rotational activity observed in their cell monolayers was very stable. Similarly, Umapathy et al. [67] showed that 32 of their 45 recordings of HL-1 cellular monolayers exhibited stable self-sustaining circuits, while the remainder displayed only wave break and collision. These findings agree with the general occurrence of self-sustaining activity investigated in this chapter in the HL1-6 cell line, which all exhibited stable rotation around a fixed location.

The dominant frequency of self-sustaining circuits observed in this work is also comparable to previous studies. Hong et al. [66] reported a decreasing trend of rotation frequency in HL-1 cells with time in culture. They observed circuits with dominant frequencies between ∼1.4-3.3 Hz (determined from Figure 1b in [66]). 22 out of 27 recordings in isotropic monolayers in this chapter fall within that range. The outlying values are potentially a result of differences between the original HL-1 cell line and the more homogeneous sub-clone 6 used in these experiments [69], recordings taken after less time in culture, or the seeding protocol used in this work that produces rapidly confluent colonies.

There appears to be a weak relationship between the dominant frequencies of self-sustaining activity and the perimeter of the conduction slowing region at the core (as measured using the convex hull approach). Increasing perimeter sizes were related to lower rates of rotation. This is an intuitive result as, in a self-sustaining circuit with a larger core perimeter, waves of excitation must travel a greater distance to complete a circuit which would give a longer time of re-entry (assuming conduction velocity remains the same). The consequence of this finding is that rotation frequency of self-sustaining activity may be determined by microscopic features at the fixed core location of the activity.

HL1-6 is more homogeneous in terms of electrophysiological properties compared to the original cell line [69], but not in terms of cell volume which affects the effective refractory period of cells. Smaller cells in the core regions will have longer effective refractory periods if connected to larger cells that depolarise them at each rotation. This difference in cell sizes and effective refractory period could be responsible for the difference in the shape of the circuit cores.

In neonatal rat cardiomyocytes, which have similar morphology to the HL1-6 cell line, self-sustaining re-entrant circuits have been studied at lower resolution than this work [141]. The core of the rotation was approximated as an ellipse with perimeter of approximately 1.7 mm (calculated from the values reported in results of [141]). This is close to the mean value of perimeter from this work (1.5 mm) despite the slower conduction velocity in HL1-6 subclone [69]. However, in this case, the core of the self-sustaining circuit was not found to be elliptical in shape necessitating the development of a different interpretation of 'core perimeter'. It is possible that at a lower resolution, propagation around lines of conduction block could have the appearance of an elliptical area of cells (e.g. with the major axis of the ellipse aligned with the conduction block line).

2.4.4 Cells within the core of the self-sustaining circuit may exhibit activation activity

Most of the cells inside areas of apparent conduction block show no activity despite neighbouring cells exhibiting Ca^{2+} transients at the expected frequency of the self-sustaining circuit. The observation that some cells may still fire Ca^{2+} transients but without detectable action potentials suggests that cells are depolarised above the Na^{+} channels threshold but below the threshold for Ca^{2+} channels. This could be a consequence of the cells being unable to transfer enough charge to their neighbours, resulting in the apparent conduction block, but are still functional. Other cells in these regions may be held in a constant refractory state caused by depolarisation above the threshold of both Na^{+} and Ca^{2+} channels and thus unable to propagate activity.

Schalij et al. demonstrated functional re-entry around a line of block in two-dimensional

tissue slices stimulated by rapid pacing [147]. Although at a much larger scale than the results in this chapter, they showed that the cells constituting the core line were held in a constant depolarised state due to electrotonic currents constantly imposed from a circulating wave. Cells in the core responded in a 2:1 or 3:2 fashion with the circulating wave, similar to observations in the cell monolayers studied in this chapter.

The two main concepts of functional self-sustaining activity are 'leading circle' and 'spiral wave' [3, 148]. In the leading circle concept, the excitation wave circulates around a group of cells which are held in the refractory state, and are therefore unexcitable, due to continuously impeding centripetal wave fronts [148]. By comparison, in the spiral wave concept, the increasing curvature towards the core of the rotating wave causes an increasing source-sink mismatch at the front of the wave. This leads to a core of cells which are unexcited (the electrotonic currents do not cause cells to reach their Na^+ channel threshold and so they do not fire action potentials) but are theoretically excitable. Self-sustaining activity observed in HL1-6 monolayers does not cleanly fit into either of these concepts.

High curvature of the wave front as it circles the group of cells in Figure 2.10b could explain why these cells appeared to be unexcited during the recording, and imply a factor of spiral wave theory. However, spiral wave theory alone cannot readily explain the line of conduction block, with little wave curvature along its length, or why a similarly sized group of cells is not present at the other pivot point. Conduction velocity around the core region was estimated to be $\sim 10\times$ lower than planar conduction velocity in HL1-6 cell monolayers of 41 mm/s [69] (Figure 2.9b). Both leading circle and spiral wave concepts predict that conduction velocity slows in self-sustaining activity; in leading circle theory this is due to the wave front impeding on the refractory tail, and in spiral wave theory due to the high degree of curvature of the reentry core.

Leading circle theory predicts that the self-sustaining activity remains in a fixed location as the core is in a constant refractory state and cannot propagate action potentials. All self-sustaining activity observed in this work remained fixed for the duration of the recording and appeared to also be fixed for the time taken to locate the core of the circuit.

However, it is also possible that meandering spiral waves exist in this substrate but were not detected due to termination at the boundaries of the small cell colonies, or that spiral waves have only been recorded once they anchored to a region of heterogeneity in the tissue [3]. The distinct line shapes at the cores indicate that source-sink mismatch due to cell size/volume or gap junctional coupling (which is relatively heterogeneous along the HL1-6 cell membranes [69]) could be a determining factor in the formation of this activity. This 'pinning' of spiral waves to local heterogeneities in cell monolayers has been previously observed using neonatal rat cardiomyocytes [149].

Some of the differences between interpretations of what happens at the core of self-sustaining activity may be explained by the disparate scales at which they are studied. Clinically-based cardiac mapping of re-entry is carried out at much lower spatial resolution than possible in a cell culture model, and tends to focus on larger areas and macroscopic features [150–152]. What may be viewed as spiral waves in clinical studies could potentially be driven by microscopic re-entry similar to the kind observed in this work.

2.4.5 The core of self-sustaining activity aligns with the direction of anisotropy in the monolayer

Self-sustaining activity was optically mapped in HL1-6 monolayers seeded on microabraded surfaces [51]. Local directionality analysis of phase and membrane stained images showed that the dominant direction of the cell membranes aligned with the direction of abrasion. Comparing conduction slowing heat maps at the core of the self-sustaining circuit also showed a correlation between the dominant direction of the conduction block and the cell membranes. These results would suggest that the core of rotational activity tends to align with the local directionality of the underlying substrate in HL1-6 monolayers.

Bursac et al., who developed the protocol used in this experiment, studied functional re-entry in monolayers of rat neonatal cardiomyocytes seeded in anisotropic monolayers [153]. The authors tracked the path of phase singularities in spiral waves (where the wave front meets the wave tail). Although not quantified in their study, their phase

maps of single loop reentry (Figure 1 in [153]) appear to also align with the direction of anisotropy.

Anisotropy in cardiac tissue results in conduction velocity being higher in the direction of anisotropy (i.e. along the fibre) than transverse to it (i.e. across the fibre). This is due to the increased number of high resistance gap junctions which must be passed through in the transverse direction for an excitation wave to propagate. This difference in conduction velocities could lead to the preferential alignment of conduction block lines observed here, as the slower transverse conduction velocity makes it easier for excitation waves to rotate around the high curvature pivot points to propagate back in the opposite direction.

2.4.6 Limitations

The use of Ca^{2+} transients as a surrogate for action potentials was a necessary limitation of the work which made it possible to visually track propagating wave fronts during experiments. While simultaneous optical mapping of Ca^{2+} transients and voltage has been studied previously in an HL-1 monolayer, the authors used a higher magnification lens and shorter timescale that would be impractical to analyse the features of self-sustaining activity at the scale and detail of this chapter [154]. The experiments conducted with voltage dyes (limited by photo bleaching effects and toxicity to the cells) suggest that propagation patterns of voltage and Ca^{2+} transients are similar in this experimental setting. Regardless, it is important to state that the conclusions from the results in this chapter are drawn predominantly from Ca^{2+} transient activity.

The assumptions made to differentiate triggers (low frequency wave fronts from multiple directions) from self-sustaining activity (high frequency wave fronts from a single direction) may have biased results as triggers could occasionally be regular and with a firing rate within the frequency of self-sustaining activity. The presence of self-sustaining activity may also have skewed the number of triggers required, as no trigger can be detected when there is an 'overriding' activity in the colony.

A different imaging solution was used in experiments measuring anisotropic propagation (1.5 mM $CaCl_2$, 1 mM $MgCl_2$) compared to other experiments (1 mM $CaCl_2$) as it

resulted in more reliable occurrence of self-sustaining activity in cell colonies. Different concentrations of ions in the extracellular solution will affect the action potential of cells and thus conclusions drawn may not be applicable to cells in other environments.

The two-dimensional monolayers in HL1-6 cell culture are a necessarily simplified model of three-dimensional features that exist *in vivo*. While the precise mechanisms of initiation and maintenance of self-sustaining activity may differ, action potentials propagate through gap junctions in this model in the same manner as more complex models. It is possible that the activity observed in this simplified preparation is generated by different mechanisms than in human cardiac tissue, where effects including heterogeneity in the structure (e.g. fibre orientation, fibrotic tissue) and function (e.g. changing cell phenotypes across the atria) could play a key role not investigated here.

The HL1-6 cell line display very low conduction velocities due to a lower Na^+ current density and lower gap junctional conductance than atrial myocytes. A lower conduction velocity may favour the formation of self-sustaining circuits. HL1-6 cells show similar protein expression patterns for connexins compared to mouse atria, but have approximately eight times lower gap junctional coupling compared to ventricular myocytes as assessed by dual voltage clamp on cell pairs (11.2±3.1 nS vs. 74±17 nS) [69, 155]. Patch clamp experiments show that the peak Na^+ current density is also ∼4× lower (-85.1 pA/pF vs -324.7 pA/pF) [69, 156]. ■

Chapter 3

Likelihood-free inference of action potential model parameters

Parts of the following chapter have been published in [157] (CC BY).

3.1 Introduction

In the previous chapter, optical mapping of self-sustaining activity in HL1-6 monolayers revealed unexpected and distinct shapes of conduction block/slowing at the cores. To further investigate the genesis of this activity, we sought to construct a computational model of action potential propagation in HL1-6 monolayers. A first step to developing this multicellular model is to build a model of the action potential of an individual cell. The goal of this chapter is to develop a computational framework to calibrate an action potential model using existing experimental data in a way that can capture sources of uncertainty and variability. This will subsequently facilitate the creation of a new model of the action potential in an HL1-6 cardiomyocyte which can produce a range of outputs by assigning probability distributions, rather than point estimates, to parameter estimates.

Action potential models have generally been developed to describe the average behaviour for a representative cell in a multicellular synctium [73]. In tissue scale simulations (i.e. bidomain or monodomain), passive and active properties of the cardiac tissue are modelled over regions that may contain many thousands of individual cells. They

generally aim to capture the average properties (conductivity, action potential, etc.) of a region of tissue at the expense of the variability between individual cells. In cell-scale simulations, each cardiomyocyte is modelled individually and so it is less meaningful to 'blur' the intrinsic variability between cells. This variability can be particularly relevant for cell types which have more heterogeneous phenotypes [87].

An important consideration for cardiac modelling is the uncertainty and variability in parameters of the model. The main sources of uncertainty in parameters of action potential models originate from variability intrinsic to the system being studied, and measurement uncertainties introduced through imperfect recording systems [124, 125]. If the uncertainty in model parameters can be estimated, then it is possible to propagate this uncertainty through to model output to establish confidence levels in model prediction through a process known as uncertainty quantification [131].

Uncertainty can also be introduced from the mathematical structure of the model itself. It is common for action potential models to use equations with a large number of parameters to describe the flow of ions across the cell membrane. When developing a model of a new cell type, the most common approach is to inherit gating kinetic formulations from existing models and tune channel conductances to data from multiple sources [158]. However, equations describing gating kinetics of ion channels can be extremely complex and often contribute the majority of the parameters in action potential models. In contrast to channel conductances, which can be adjusted to measurements of action potentials, gating kinetics are typically calibrated to data from voltage patch clamp experiments. In these experiments, channels are isolated, by pharmacological means or the use of specific voltage step protocols, to take measurements of individual current traces.

The consequence of the uncertainty and high number of parameters is that multiple different parameter combinations may produce the same residual to experimental data; a unique optimum parameter set may not exist. This case is known as *unidentifiability*. Unidentifiability may be either structural, caused by an overly complex model where parameters can be varied simultaneously without a change in model output, or practical, where insufficient data is available to determine a parameter's value.

Every model is a necessary simplification from reality. As a result, even if parameters are identifiable in the current context, the parameter values estimated may not be representative of the underlying biophysical system due to *discrepancy* between the model itself and the true system. This is a growing, and relatively unexplored, area of interest in cardiac modelling [159], and important to understand particularly if model equations are simplified in an attempt to ensure parameters are identifiable.

Traditional fitting techniques, such as simple least squares regression, implicitly assume that a single point estimate exists for each parameter in a model [130]. In cardiac modelling, this is unlikely to be the case as, even with perfect recording methods, cardiac cells typically exhibit substantial variability. Bayesian methods can quantify uncertainties in parameter estimates by determining a posterior distribution over parameter values given the available data [126]. These distributions can highlight unidentifiable parameters (i.e. those without a single unique optimum), and make it possible to capture the effect of experimental and biological variability on model parameters. In cardiac cell modelling, it can be difficult to obtain an exact likelihood function necessary for exact Bayesian inference when summary statistics are used, as is commonplace in studies of cardiac ion channels. This is further complicated by the high-dimensional parameter space, nonlinear nature and indirect observation properties of action potential models [160]. Instead, one can employ approximate Bayesian methods, such as approximate Bayesian computation (ABC), which provide a reasonable estimate to the posterior distributions of parameter values [161].

Previous studies [123, 130, 162–164] have been valuable in developing approaches to investigate parameter identifiability in both generalised Hodgkin-Huxley models and more biophysically detailed ion channel models. Here, we build on this field of work to include consideration of the available experimental data across a range of simple and complex channel models of a human atrial cell. The framework is developed and evaluated in a retrospective analysis of two human atrial cardiomyocyte cell models, namely the Nygren et al. [165] and Courtemanche et al. [166] models, to study the effects of recalibrating key ion currents in a stochastic fashion. These were the first two biophysical models developed

to simulate the action potential of a human atrial myocyte, and have proved influential in the development of subsequent models and whole-heart tissue-scale modelling. The Nygren and Courtemanche models are detailed cell models, each including descriptions of twelve ion currents which contribute to the action potential in human atrial myocytes. We thus only focus our study on the four major ion currents which are prominent determinants of their action potential morphology [123, 167]: the fast Na^+ channel (I_{Na}), L-type Ca^{2+} channel (I_{CaL}), transient outward K^+ channel (I_{to}) and ultra-rapid delayed rectifier K^+ channel (I_{Kur}).

We first recalibrate parameters in each channel model to experimental data sets used in the original publications to investigate the existing level of uncertainty and unidentifiability in parameters. To explore whether these issues can be alleviated from inclusion of more data, which would suggest practical unidentifiability, a 'unified' data set is formed and the models recalibrated to these data. To investigate whether these models suffer from structural unidentifiability, a model of reduced complexity [168] is calibrated to the same unified data set, and parameter posterior distributions and the overall goodness-of-fit of the model compared to the recalibrated Nygren and Courtemanche models. These recalibrated channel models are then inserted into the complete action potential models to study the effect of the recalibration on action potential morphology. Lastly, we demonstrate an extension to traditional ABC to incorporate model discrepancy into the calibration process on a single channel gate in the Nygren model. We conclude by discussing the relative advantages and drawbacks of these approaches.

3.2 Methods

3.2.1 Action potential models

The action potential models studied in this chapter follow the commonly-used Hodgkin-Huxley gating form [72]. Henceforth, the Nygren and Courtemanche models will be referred to as the 'N' and 'C' models respectively. The changing transmembrane voltage is calculated from the solution of several coupled ordinary differential equations describing

individual ion currents. Each current is of the common form

$$I_i = g_i \prod_j x_j^{k_j} f(V_m), \qquad \frac{dx_j(t)}{dt} = \alpha_{x_j}(V_m; \boldsymbol{p})\,[1 - x_j] - \beta_{x_j}(V_m; \boldsymbol{p}) x_j, \tag{3.1}$$

where g_i is the maximum channel conductance which scales the current amplitude (μS/μF); x_j are gates of the channel determined by voltage-dependent forward and backward transition rates between open and closed states, α and β, characterised by gating parameters $\boldsymbol{p}$; k_j is an exponent term that may be applied to represent multiple identical gates in parallel; V_m is the transmembrane potential (mV); and f is some voltage-dependent forcing function (most commonly the difference between V_m and the ion Nernst potential). The gating equation may equivalently be transformed into a form explicitly specifying steady-state values, γ_x ,and time constants, τ_x:

$$\begin{aligned} \frac{dx(t)}{dt} = \frac{\gamma_x(V_m) - x}{\tau_x(V_m)}, \qquad & \tau_x(V_m) = \left[\alpha_x(V_m; \boldsymbol{p}) + \beta_x(V_m; \boldsymbol{p})\right]^{-1}, \\ & \gamma_x(V_m) = \alpha_x(V_m; \boldsymbol{p})\tau_x \qquad \text{if activating gate}, \\ & \gamma_x(V_m) = \beta_x(V_m; \boldsymbol{p})\tau_x \qquad \text{if inactivating gate}, \end{aligned} \tag{3.2}$$

(where we omit the indexing subscript for clarity). There are no standard formulations for the voltage-dependent transition rates $\alpha_x(V_m; \boldsymbol{p})$ and $\beta_x(V_m; \boldsymbol{p})$, and each model implements a different set of equations [165, 166]. For I_{Na}, and for the C model also I_{CaL}, the structure of these equations was inherited directly from the parent model (of a rabbit atrial cell [82] and guinea pig ventricular cell [86] for the N and C models respectively), while I_{to}, I_{Kur} and, for the N model, I_{CaL} were introduced as new formulations in each model. The full equations for each model are included in Appendix A.1. In this work, we are interested in the ability of the gating kinetics to reflect the experimental data, and the variability and identifiability of parameters $\boldsymbol{p}$ with respect to this data.

The standardised formulation, henceforth referred to as the 'S' model, is used as a simpler structure to compare to the more complex formulations in the N and C models. In this formulation, the transition rates between open and closed states have a structure based on free energy arguments [2,169], which has been shown as sufficient to capture the

kinetics of a rapid delayed rectifier K^+ current [168]. The transition rates are given by

$$\alpha(V_m) = p_1 \exp(p_2 V_m), \qquad \beta(V_m) = p_3 \exp(-p_4 V_m), \tag{3.3}$$

where the parameters requiring calibration are $p_1, ..., p_4$ for each gate in the channel model. For I_{Na} and I_{CaL}, which each have two components of inactivation, we add another inactivation gate in parallel for the S model which is related directly to the existing inactivation gate by a scale parameter on its time constant (i.e. $\tau_{x2} = a\tau_{x1}$ where a is the scale parameter). Only the activation gate of the S model for I_{Na} has a cubic power to remain consistent with both N and C models.

3.2.2 Data sets and calibration

Parameters underlying gating kinetics are calibrated to experimental data from voltage patch clamp experiments conducted on isolated cardiomyocytes. Though more complex protocols may be better able to explore the entire range of kinetics exhibited by different ion channels [168], the majority of available data are generated through the use of 'traditional' voltage stepping protocols. In these experiments, the transmembrane potential is held fixed and subsequently clamped to a series of voltage steps while the current across the membrane is recorded. Specific features of the recorded current can then be calculated and summarised across different cells or experiments.

Data from voltage patch clamp experiments in human atrial myocytes for I_{Na} [170, 171], I_{CaL} [172–174], I_{to} [175–177] and I_{Kur} [176, 177] were digitised (including any error measurement). Table 3.1 contains a complete list of all experimental data sources for both original and unified data sets. A virtual voltage clamp protocol was created to replicate *in silico* each of the *in vitro* experiments. A precise description of each voltage clamp protocol can be found in Appendix A.2.

The N model did not include calibration data for any time constants in I_{Na}, for activation time constants in I_{to} and for deactivation of I_{Kur}. The C model did not calibrate to voltage-dependent recovery data in I_{CaL} and I_{Kur}. Neither model included an activation

Channel	Gate		Data	N [165]	C [166]	Unified
I_{Na}	activation, m	m_∞	Fig. 2 [170]	✓	✓	✓
		τ_m	Fig. 3C [171]	✗	✓	✓
	inactivation*, $\{h, j\}$	$\{h, j\}_\infty$	Fig. 7 [170]	✓	✓	✓
		$\tau_{\{h,j\}}$ (inact.)	Fig. 5B [170]	✗	✓	✓
		$\tau_{\{h,j\}}$ (recov.)	Fig. 9 [170]	✗	✓	✓
I_{CaL}	activation, d	d_∞	Fig. 5C [172][a] Fig. 2B [173][b]	✓[a]	✓[b]	✓[b]
		τ_d	Pg. H233 [173]	✗	✗	✓
	inactivation†, f	f_∞	Fig. 2B [173]	✓	✓	✓
		τ_f (inact.)	Fig. 3B [173][a] Fig. 4B [174][b]	✓[a]	✓[b]	✓[a]
		τ_f (recov.)	Pg. H230 [173]	✓	✗	✓
I_{to}	activation, r	r_∞	Fig. 3A [175][a] Fig. 2A [176][b]	✓[a]	✓[b]	✓[b]
		τ_r (act.)	Fig. 5D [166][‡]	✗	✓	✓
		τ_r (deact.)	Fig. 5D [166][‡]	✗	✓	✓
	inactivation, s	s_∞	Fig. 3C [177][a] Fig. 2C [176][b]	✓[a]	✓[b]	✓[b]
		τ_s (inact.)	Fig. 4C [165][a,‡] Fig. 5D [166][b,‡]	✓[a]	✓[b]	✓[b]
		τ_s (recov.)	Fig. 4C [165][a,‡] Fig. 5D [166][b,‡]	✓[a]	✓[b]	✓[b]
I_{Kur}*	activation, a	a_∞	Fig. 8E [176]	✓	✓	✓
		τ_a (act.)	Fig. 8F [176]	✓	✓	✓
		τ_a (deact.)	Fig. 5B [166][‡]	✗	✓	✓
	inactivation, i	i_∞	Fig. 3C [177][a,§] Fig. 7A [176][b,§]	✓[a]	✓[b]	✓[a]
		τ_i (inact.)	Fig. 4D [165][a,‡] Fig. 5B [166][b,‡]	✓[a]	✓[b]	✓[a]
		τ_i (recov.)	Fig. 4D [165][‡]	✓	✗	✓

Table 3.1: Summary of patch clamp experimental data sets used in modelling papers in human atrial myocytes for each channel studied. Ticks and crosses are used to indicate which data sets are included in the original model calibration and which compose the unified data set. *There are some differences in the terminology used in each model. The N model refers to the inactivation gates of I_{Na} as h_1 and h_2, and the I_{Kur} channel as I_{sus}. †The L-type Ca^{2+} current has a Ca^{2+}-dependent inactivation process which is not calibrated in this experiment. ‡In some cases it was not clear from the modelling paper where the comparison data plotted were obtained from. In these cases, the data points from the modelling paper itself are used and a protocol assumed based on the experimental paper cited. §In some cases it was not explicit which figure among a number of possibilities within a cited data source was used; the choice was inferred from the modelling paper.

time constant measurement available for I_{CaL}.

3.2.3 Approximate Bayesian computation

Approximate Bayesian computation (ABC) is a class of computational approaches to likelihood-free statistical inference. As a consequence of the likelihood-free approach, ABC methods are particularly advantageous in calibrating complex models. They have become increasingly popular in a range of scientific fields [178–183], and more recently in calibrating ion channel models [130, 160].

As a Bayesian method, ABC methods are rooted in the application of Bayes theorem:

$$\underbrace{P(\theta|D)}_{\text{Posterior}} \propto \underbrace{P(D|\theta)}_{\text{Likelihood}} \underbrace{P(\theta)}_{\text{Prior}}$$

where the posterior distribution gives the probability of model parameter values, θ, being the 'true' values given observed data, D, the likelihood function is the probability of observing a set of data assuming a model has a certain parameter value and the prior distribution is the probability of a parameter being selected for the model without consideration of the data. Note that θ and D can both be vectors of parameters and data respectively.

The ABC approach to model calibration is advantageous where computation of the likelihood function is intractable or prohibitively expensive, but the model itself can be easily simulated [161, 184]. ABC methods avoid determination of the likelihood function by sampling parameter values from a prior distribution and simulating model output, $\hat{D} := f(\theta)$. The simulated data may be processed into a smaller number of summary statistics (e.g. taking measurements of an action potential trace such as peak potential and action potential duration), $\hat{s} := S(\hat{D})$ where $S(\cdot)$ is some summary statistic function. The model output, or summary statistics, are then compared to experimental data using a chosen distance function, $\rho(\cdot, \cdot)$. A low distance value generated by the distance function indicates that a particular sample from the parameter space is more likely to be from the 'true' distribution. Samples with outputs within some threshold, ϵ, of the experimental data are accepted. As a result, ABC methods approximate the true posterior $P(\theta|D)$ by some $P(\theta|\rho(\hat{D}, D) \leq \epsilon)$. The final output of ABC methods is a sample of parameter

values which should be approximately distributed according to the target posterior [161].

There are different variants of ABC ranging from basic rejection sampling to combinations with Markov chain Monte Carlo methods [161]. Here, the Toni ABC sampler based on sequential Monte Carlo is used to infer parameter posterior distributions [185]. In the Toni sampler, the ABC process above is repeated through a number of iterations k, with reducing ϵ_k at each iteration. A population of parameter samples, referred to as 'particles', are propagated through each iteration and represent a discrete surrogate to the continuous posterior distribution.

In the first iteration, model parameters are sampled from uniform prior distributions, $P_0(\theta)$, as a first approximation to the posterior. In subsequent iterations, model parameters are sampled from the previous iteration's posterior distribution

$$P_k(\theta) := P_{k-1}(\theta|\rho(\hat{D}, D) \leq \epsilon_{k-1}), \tag{3.4}$$

and perturbed slightly by a kernel, $K_k(\cdot)$. The distance acceptance threshold, ϵ_k, is sequentially refined by selecting the median of particle population distances from the previous iteration [186]. Algorithm 1 shows the pseudo-code [185].

The algorithm requires the choice of a pertubation kernel $K_k(\cdot)$, sampling statistic function $S(\cdot)$, distance function $\rho(\cdot, \cdot)$, the number of ABC particles N and an appropriate termination criterion. We use a multivariate normal kernel as a pertubation kernel with covariance estimated from a kernel density estimate of the previous generation of parameter values: $K_k(\cdot|\theta_{k-1}) := \mathcal{N}(\mu_{k-1}, \Sigma_{k-1})$ [187,188], where μ_{k-1} is the estimated mean and Σ_{k-1} is the estimated covariance. The bandwidth of the kernel density estimate follows Silverman's rule of thumb [189].

The particle population number is set according to the number of parameters being constrained in the experiment by considering the size of the parameter sampling hyperspace and assuming at least two particles in each dimension. The algorithm terminates when less than 1% of parameter samples are accepted in a given iteration indicating the algorithm is struggling to improve on the current optimum. This criterion is chosen over termination at an absolute value of the distance metric used in other studies due to differ-

Algorithm 1 ABC-SMC algorithm

$k := 0$
$\epsilon_0 := \infty$
$N :=$ number of particles
repeat
  if $k = 0$ **then**
    $P_k(\theta) := P_0(\theta)$
  else
    $P_k(\theta) := \sum_{i:=1}^{N} w_{k-1}^{(i)} K_k(\theta|\theta_{k-1}^{(i)}) / \sum_{i:=1}^{N} w_{k-1}^{(i)}$
  repeat
    repeat
      $\hat{\theta}_k^{(i)} :=$ sample from $P_k(\theta)$
    until $P_0(\hat{\theta}_k^{(i)}) > 0$
    $\hat{D}_k^{(i)} :=$ simulate $f(\hat{\theta}_k^{(i)})$
    $\hat{s}_k^{(i)} := S(\hat{D}_k^{(i)})$
    $\hat{\epsilon_k}^{(i)} := \rho(\hat{s}_k^{(i)}, s)$
    accept if $\hat{\epsilon_k}^{(i)} \leq \epsilon_k$
  until N particles ($\boldsymbol{\theta_k} = \{\theta_k^{(i)}\}_{0 \leq i < N}$) have been accepted
  for $i := 0$ **to** $N - 1$ **do**
    $w_k^{(i)} := P_0(\theta_k^{(i)}) / P_k(\theta_k^{(i)})$
  $\epsilon_{k+1} :=$ median($\hat{\boldsymbol{\epsilon}}_{\boldsymbol{k}}^{(\boldsymbol{i})}$)
  $k := k + 1$
until minimum acceptance rate reached

ences in the number of model parameters and availability of data between experiments.

To compare our model summary statistics to the experimental data (which include error measurements at each point), we use a weighted Euclidean distance function:

$$\rho(\hat{s}, s) = \left[\sum_{i:=0}^{M} \left(\frac{\hat{s}_i - s_{\mathrm{i}}}{v_i} \right)^2 \right]^{1/2}, \qquad (3.5)$$
$$v_i = \max\left(\sigma_i, \delta\right) n_{\mathrm{exp}|i},$$

where v_i are the weights for each data point, σ_i is the standard deviation associated with the error at each data point, δ is a regularisation factor applied when weights are close to zero, $n_{\mathrm{exp}|i}$ is the number of data points within the experiment and there are M data points. Once generated, weights are mean-normalised which improves convergence of the ABC algorithm [185, 188]. δ was set to 0.05. The choice of distance function reduces the weighting of data points based on the magnitude of experimental uncertainty. This allows us to use information of which experimental data points we are relatively more confident about during the model calibration, propagating the experimental uncertainties and biological variability through to this stage in the model development [124]. Additionally, we account for the fact that we are simultaneously calibrating to multiple data sets by weighting according to the number of data points in a specific experiment (using $n_{\mathrm{exp}|i}$). This provides balance between the different types of channel behaviour, rather than favouring an experiment with a greater number of data points. Each data set is normalised to the maximum value in that experiment to avoid preference towards data sets with measurements at a larger scale in the ABC loss function.

A uniform prior distribution is used for each model parameter in the first iteration. The width of this prior is set to be sufficiently wide to cover the range of physiological possibilities. The summary statistics are calculated from the output of a function which makes specific measurements, for example peak current or decay rate from fitting an exponential equation, of the current trace in response to the voltage clamp protocol replicated from the experimental publication. Full details of all summary statistic functions are given in Appendix A.2.

3.2.4 Extending approximate Bayesian computation to quantify model discrepancy

In the *classical* ABC algorithm described above, the likelihood density is approximated by some distance measure, $\rho(\cdot, \cdot)$. The likelihood recovered by ABC has therefore become

$$P(D|\theta) := \mathbb{1}(\rho(f(\theta), D) \leq \epsilon), \tag{3.6}$$

where $\mathbb{1}$ is the identity function and we ignore any use of summary statistics for ease of exposition. Wilkinson [190] recognised that, in certain cases, ABC gives exact results under the assumption of additive model error. The source of this error can be attributed to experimental uncertainties and uncertainty due to model discrepancy. If $\rho(\cdot, \cdot)$ is the Euclidean distance function, the classical acceptor is the same as assuming uniform model error around each experimental data point.

This idea can be generalised so that the likelihood approximation can be described by any distribution:

$$P(D|\theta) := P(D|f(\theta), \eta), \tag{3.7}$$

where η here represents some variance of the distribution. For example, independent Gaussian distributions could be centred on each experimental data point with variance equal to the measurement variance of the experimental data. If the variance is unknown, then this parameter can be included in the ABC calibration [190].

3.2.5 Calibration algorithm settings

The majority of results in this work apply ABC in the classical sense, using the distance function acceptor. For the N and C models, the width of the uniform prior is set based on the published value of the parameter and its position in the model structure. The width was increased if it was noted that during calibration the distribution was being restricted by the upper or lower prior limit. For the S model, the prior ranges were set as previously [168, 191]. After convergence, the parameter posterior distributions are

inspected and, if observed to be restricted by the lower or upper limit of the prior, the calibration is restarted with a wider prior.

In some cases for I_{to} and I_{Kur}, it was not clear in the modelling paper where the data were obtained. In these cases, the points displayed in the figure from the modelling paper were digitised and 10% standard deviation error assumed (based on the error of similar measurements given in [176]).

The summary statistic functions are assumed to be invariant to the magnitude of current, and thus channel conductance is not included as a calibration parameter.

In the final section of results, ABC calibration is reapplied to the inactivation gate of the fast Na^+ channel (I_{Na}) in the N and S models using the generic probability distribution acceptor described in Section 3.2.4. We replace the uniform ABC distance with independent Gaussian distributions centred on each data point, with variance equal to the (known) experimental uncertainty and the (unknown) model discrepancy. The model discrepancy is not known *a priori*, and so is inferred along with the model parameters as a separate parameter per experiment [190].

3.2.6 Implementation

Voltage clamp experiments were simulated using the *myokit* Python library (version 1.30.6) [192]. The ABC-Sequential Monte Carlo sampling process uses the *pyABC* Python library (version 0.9.23) [188]. We created the *ion-channel-ABC* Python library for applying ABC in this context which integrates pyABC and myokit for voltage patch clamp ABC calibration (`https://github.com/charleshouston/ion-channel-ABC`).

When comparing the relative computational speed to solve different channel models, we apply a voltage pulse train protocol of 100 pulses (using channel-dependent voltage steps indicated in the text). We record the time taken for a simulation from each of the 100 samples from the posterior parameter distributions to account for variability.

3.2.7 Action potential simulations

To simulate the effect on the action potential of recalibrated channels, each new parameterisation was inserted into either the entire N or C model. Channels were tested one at a time, and parameters in other channels left at their published values. 100 samples were taken from the unified posterior distribution and a pulse train protocol applied to generate action potential samples from the full model. The pulse train consisted of 1 ms current stimuli at a rate of 1 Hz and with amplitude 40 pA/pF. The action potential elicited during the 100th pulse was recorded for analysis.

S channel models were then used in place of the published formulae to study the effect of a reduction in complexity on the overall action potential. In all cases, the conductance of the channel was set by matching the peak current magnitude from each sample to the peak from the published channel model (peak current was assumed to occur at 60 mV for I_{to} and I_{Kur} models).

This experiment could not be conducted for I_{Na} as both the N and C modellers positively shifted the steady-state curves according to macro measurements of the action potential (such as velocity of the upstroke), and in the previous section this channel was calibrated to the original experimental data. As in this study voltage clamp protocols were replicated exactly as described in the experimental publications, it is not clear how these would be adapted to fit the artificially-shifted data, or how to manually shift the steady-state curves.

All figures display experimental measurements as mean ± standard deviation reported in the experimental publication. The calibrated model is displayed by taking 100 samples from the posterior distribution of parameters and plotting the output from simulations as median ± 89% highest posterior density interval (HPDI) [193].

3.3 Results

3.3.1 Existing gating parameter uncertainties

We first sought to study uncertainty and unidentifiability present in gating parameters of the existing models using the data sets originally cited for calibration [165, 166]. Only I_{Na} and I_{to} channels of the C model were calibrated to the full range of data available in the original publications (Table 3.1). It would be expected that a higher level of uncertainty is present in the kinetics of a channel within voltage ranges that have not been explicitly tested. High uncertainty in a parameter value may be a consequence of high variability in kinetics of a channel measured during experiments. It may also be indicative of potential structural or practical unidentifiability.

To demonstrate unidentifiability, we first look at the I_{Na} channel in the N model. In the original publication, this channel was only directly compared to steady-state experimental data [170]. Figures 3.1a and 3.1b show representative posterior distributions and kernel density estimates of those distributions following ABC calibration of the channel to only this steady-state data. Parameters underlying steady-state parts of the channel formulation (e.g. $q1$ and $q2$ shown in Figure 3.1a) exhibit narrow posterior distributions after calibration, indicating they are well-constrained by the data. In contrast, parameters underlying time constants (e.g. $q4$ and $q6$ shown in Figure 3.1b) have relatively wide posterior distributions implying they are poorly constrained and suggesting there is a higher level of uncertainty surrounding their value in the model. The equations showing how these parameters influence the gating kinetics in this model are in Appendix A.1.

The effect of the poorly constrained time constant parameters can be seen in Figure 3.1c. This figure shows the normalised current response of this calibration of the I_{Na} model to the voltage clamp protocols from the calibrating experiments (shown in the inset plots). The wide shaded regions around the median lines indicate that the decay rate of the current is highly variable, consistent with the observation of poorly constrained time constants.

Figure 3.1d shows how this uncertainty is 'hidden' by the steady-state summary statis-

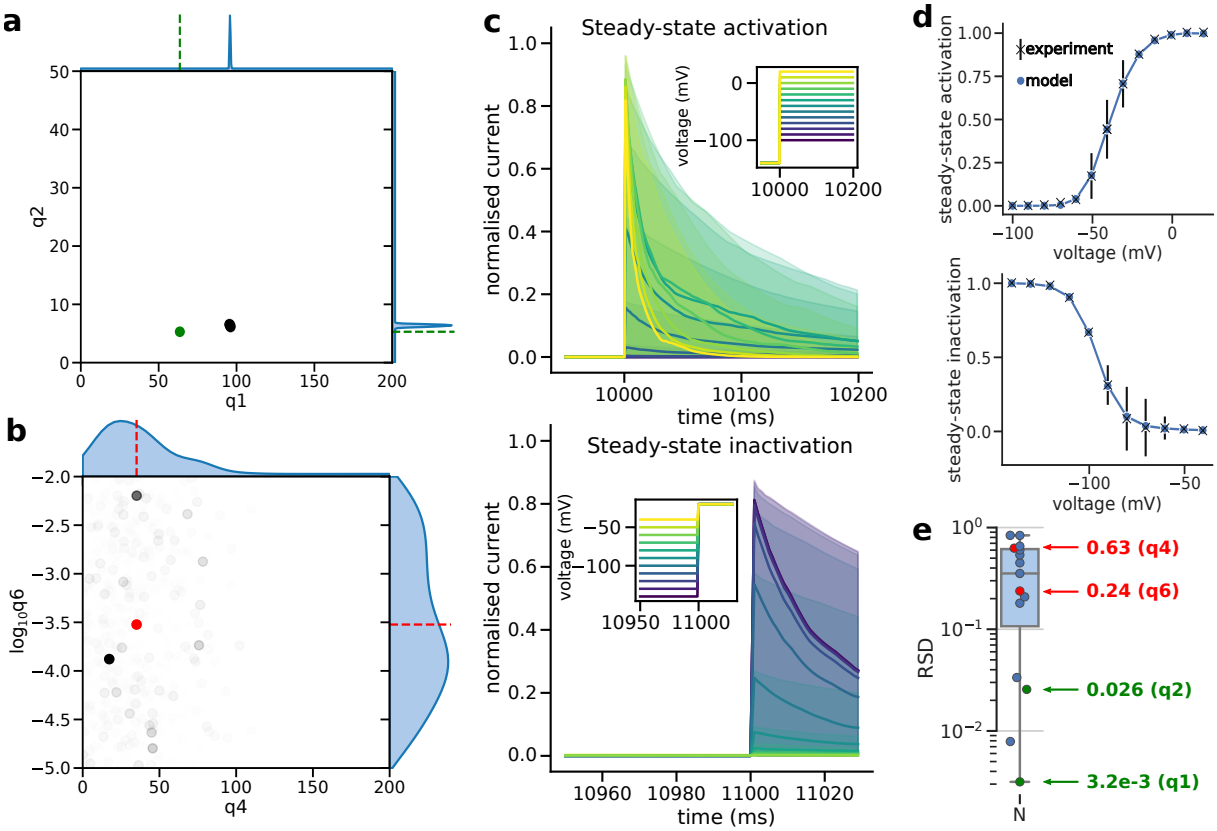


Figure 3.1: **a, b** Examples of parameter posterior distributions from the N model of I_{Na} after calibration to the original data set which only included steady-state data. Scatter plots show the population of posterior ABC particles with weights indicated by opacity. One-dimensional kernel density estimates of each parameter posterior distribution are displayed along the corresponding axes. The original parameter values from the model are indicated as dots and dashed lines. **c** Normalised current traces of posterior model response to inset voltage protocol displayed as median line with shading indicating 89% HPDI from 100 samples from parameter posterior distributions. The high variability in decay rate is the result of no time constant data included in the data set used for calibration. Note that due to normalisation the I_{Na} current trace unconventionally appears as if an outward current. **d** Summary statistics generated from results in c. Non-physiological error bars of the experimental data are a result of plotting as mean ± standard deviation **e** Relative standard deviation (RSD) values of all parameter posteriors with representative parameters from a and b highlighted. Adapted from [157] (CC BY).

tics function. The summary statistics, not the current trace, is compared to data during the calibration process. In this case, the summary statistics function for the steady-state experiments processes the traces into a single measurement of the peak (which is then normalised). As the function only outputs the peak value, it is less sensitive to how long the trace takes to reach the peak or the time taken to decay following the peak. This results in the steady-state parameters being tightly constrained and the time constant parameters only constrained within a 'viable' region (i.e. constrained to allow the current to sufficiently decay before the next voltage step in the protocol).

Relative standard deviation (RSD; defined as $\sigma/|\mu|$) is a scale invariant measure of the width of the parameter posterior distributions and can be used to provide a comparison of the posterior parameter uncertainty between models. Higher RSD values can indicate that a particular parameter is unidentifiable with respect to the model structure or available data, or that the biological process this parameter describes is highly variable.

Figure 3.1e shows the RSD values for all parameter posterior distributions in this N model calibration, and highlights the values for the specific parameter distributions plotted in Figures 3.1a and b. Parameters with narrower posterior distributions have RSD values orders of magnitude lower than those with wide posteriors. In this case, the four parameters with an RSD less than 10^{-1} can be interpreted as governing the shift and steepness of the steady-state activation and inactivation curves in Figure 3.1d (see Appendix A.1). It is thus not surprising that these were more identifiable than parameters involved in rise and decay rates of the current.

3.3.2 Recalibrating to a unified data set

Having observed a range of poorly and well-constrained parameters when calibrating to the original data sets, we next sought to investigate the effect of recalibrating each model to a different 'unified' data set. This data set is assembled from a union of the original experimental data sources (see Table 3.1).

Figure 3.2a shows the RSD of parameter posteriors for all channels studied in the N and C models when calibrated to the original and unified data sets. In all models, a wide

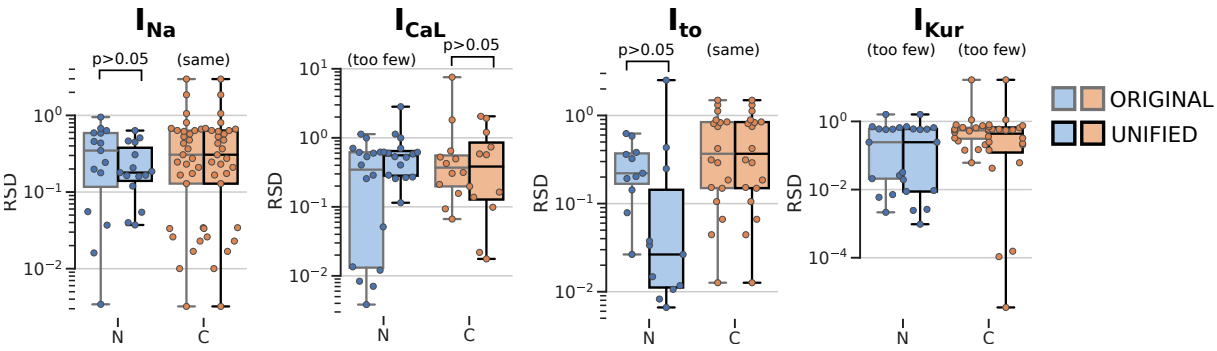


Figure 3.2: RSDs of each parameter in each channel model for original and unified experimental data sets in both N and C models. Significance tested with Wilcoxon signed rank test. Text 'too few' above a pair of box plots indicates that the sample size was too small to conduct the statistical test after eliminating differences of zero. Adapted from [157] (CC BY).

range of RSD values is observed for the original data sets which confirms each model has a combination of parameters that are well defined, and parameters that are highly variable and/or potentially unidentifiable.

In the N model, no significant differences in the parameter posterior RSDs were observed between original and unified data set calibrations for I_{Na} and I_{to} using a Wilcoxon signed-rank test. In the N models of both I_{Na} and I_{CaL}, the minimum RSD increased after calibrating to the unified data set. In I_{CaL} and I_{to}, there was also an increase in the maximum RSD.

No significant differences were observed for the C model. Note that a Wilcoxon signed-rank test was not carried out for I_{CaL} (for the N model) or I_{Kur} as this statistical test requires discarding differences between pairs of zero and the resulting sample size was too small for a normal approximation. This is a result of only recalibrating parameters of one gate to unified data in these models as the unified data for the other gate was the same as the original data set (thus the RSD values of parameters in the other gate remained constant between the original and unified data set).

Regions of high uncertainty in gating functions generally corresponded to behaviour or voltage ranges not tested by the experimental voltage clamp protocols. Adding the additional data in the unified data set generally reduced the variability in these regions, though this could also be at the expense of other aspects of the model.

For example, the N model of I_{Na} showed high uncertainty in the posterior estimates for time constant functions with the original data set, that was reduced on calibration to

the unified data set (compare the blue and orange shaded regions in the second column of Figure 3.3a). However, this reduction appeared to come at the expense of greater variability in the steady-state behaviour of the channel. A similar effect was noticed in the inactivation processes of the C model of I_{CaL} (Figure 3.4b).

For the N model of I_{to} and the inactivation of the C model of I_{Kur}, calibrating to the unified data set resulted in changes to the shift and steepness of the steady-state functions (Figures 3.3c and 3.4d). In I_{to} for the N model in particular, calibrating to the unified data set resulted in non-physiological steady-state functions as there is no significant overlap between the activation and inactivation gates.

3.3.3 Comparing to a standardised model

No statistically significant reduction in RSD values for parameter posterior distributions was observed when recalibrating the N and C models to unified data sets. This could imply that the additional data covering a wide range of kinetics for each channel was not sufficient to reduce unidentifiability observed in parameters. We hypothesised that this could be due to problems with structural unidentifiability caused by the complex form of the equations in the N and C models. To test this, we next studied whether the simpler model structure of the S model could be used to reflect the same experimental data with reduced parameter uncertainty for each channel.

Figure 3.5 summarises the results for all channels calibrated to the unified data set. Across all channels, the S model has fewest parameters of all models as expected from a simple formulation. With the exception of I_{CaL}, the C model has the greatest number of parameters; for I_{Na} it has almost double the number of the N model.

The RSD values of parameter posterior distributions for the S model compared to the N and C models varies depending on the channel considered. The RSD of the S model calibration is significantly lower than both models for I_{Na} ($p = 0.02$ vs. N, $p = 0.04$ vs. C) and lower than the C model for the K^+ channels (I_{to}: $p < 0.001$, I_{Kur}: $p = 0.007$). This suggests that in these cases the calibration of the S model results in parameters with lower uncertainty so we can be more confident in the model output. However, as we shall

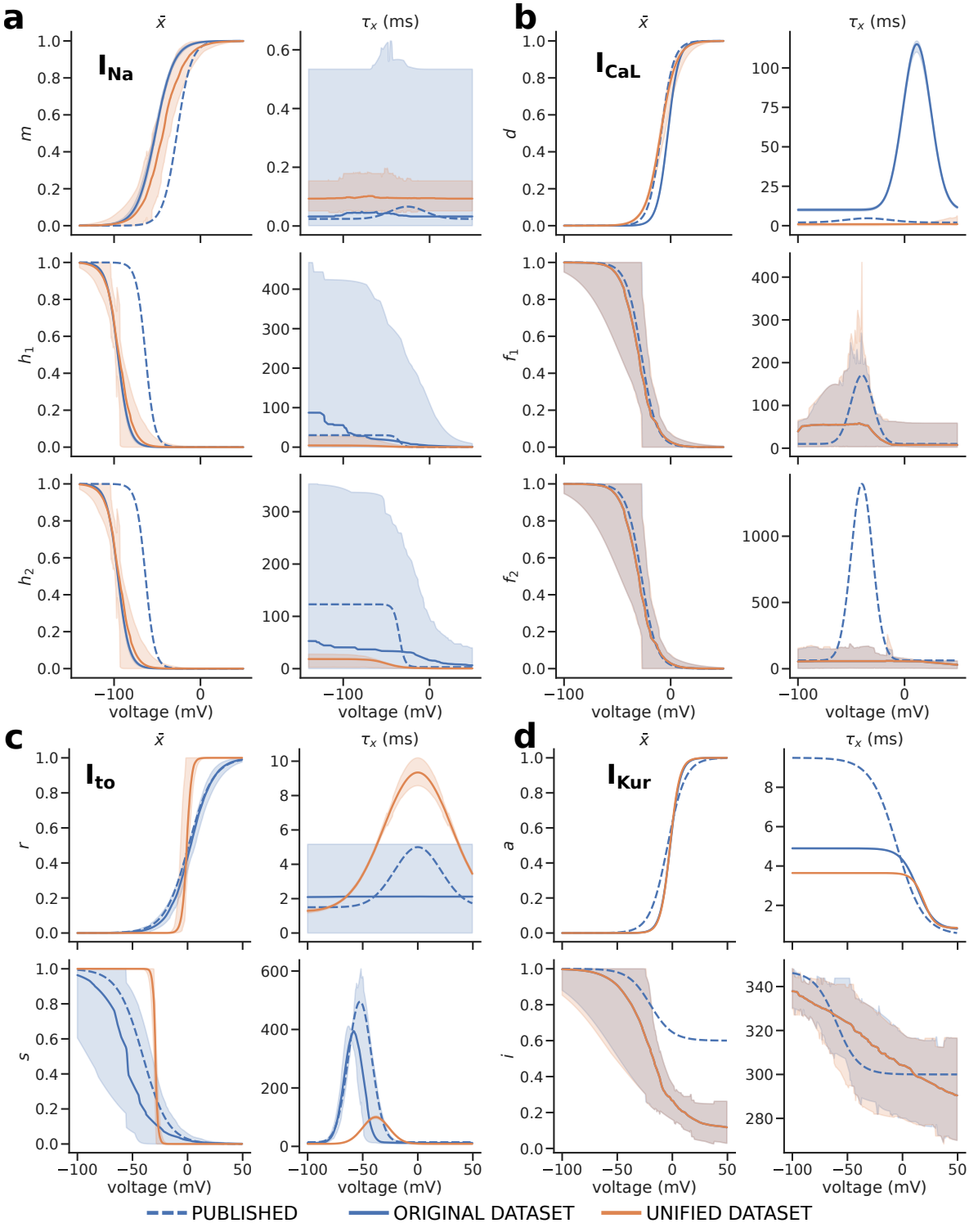


Figure 3.3: **a-d** Steady-state and time constant functions for each channel of the N model using original calibration data set and unified data set. Blue refers to original data set and orange to unified data set. Data displayed as median line with shading representing 89% HPDI of 100 samples from the parameter posterior distribution. Adapted from the Supplementary Information to [157] (CC BY).

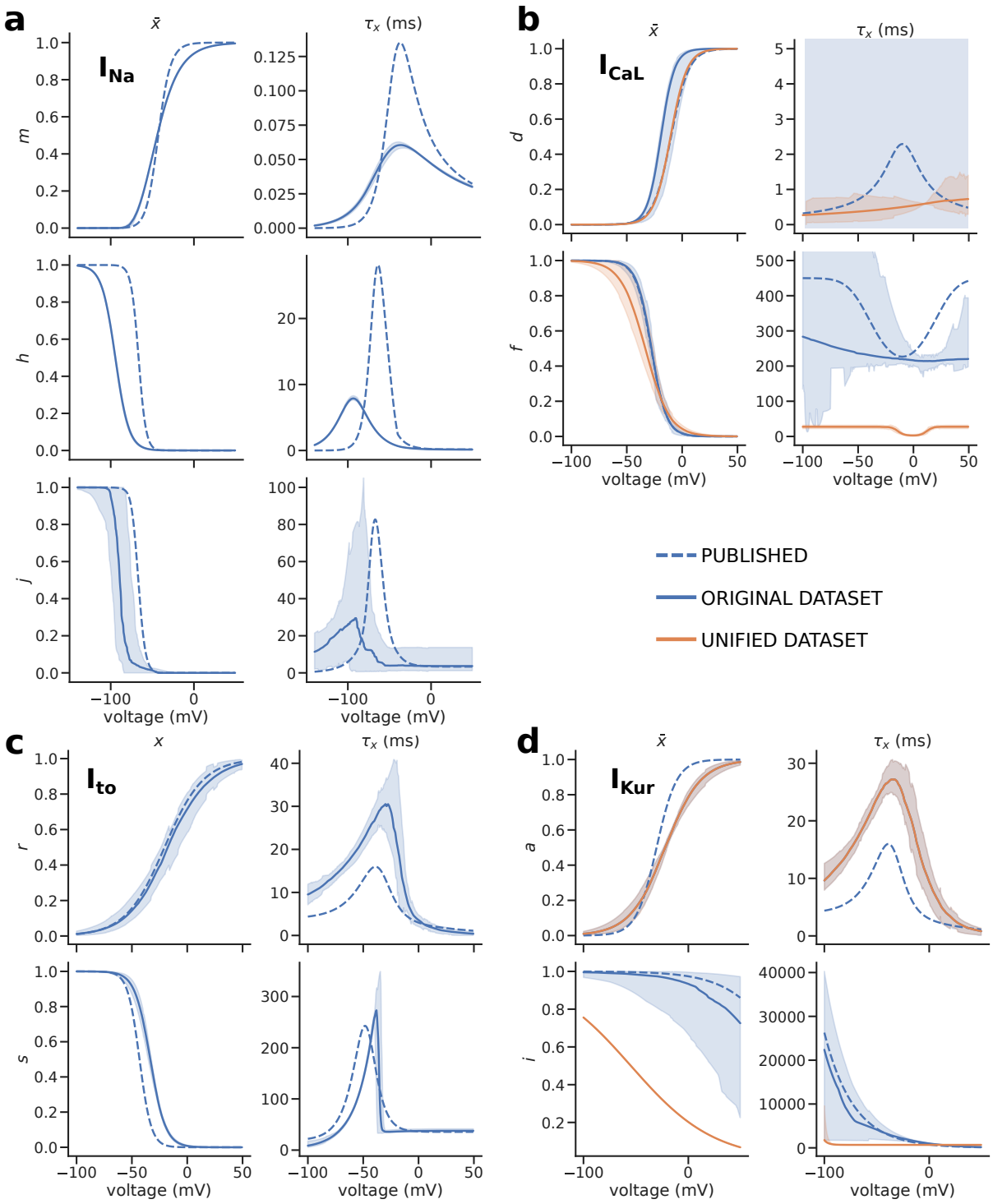


Figure 3.4: **a-d** Steady-state and time constant functions for each channel of the C model using original calibration data set and unified data set. Blue refers to original data set and orange to unified data set. Data displayed as median line with shading representing 89% HPDI of 100 samples from the parameter posterior distribution. Note for I_{Na} and I_{to} the original and unified data set are the same. Adapted from the Supplementary Information to [157] (CC BY).

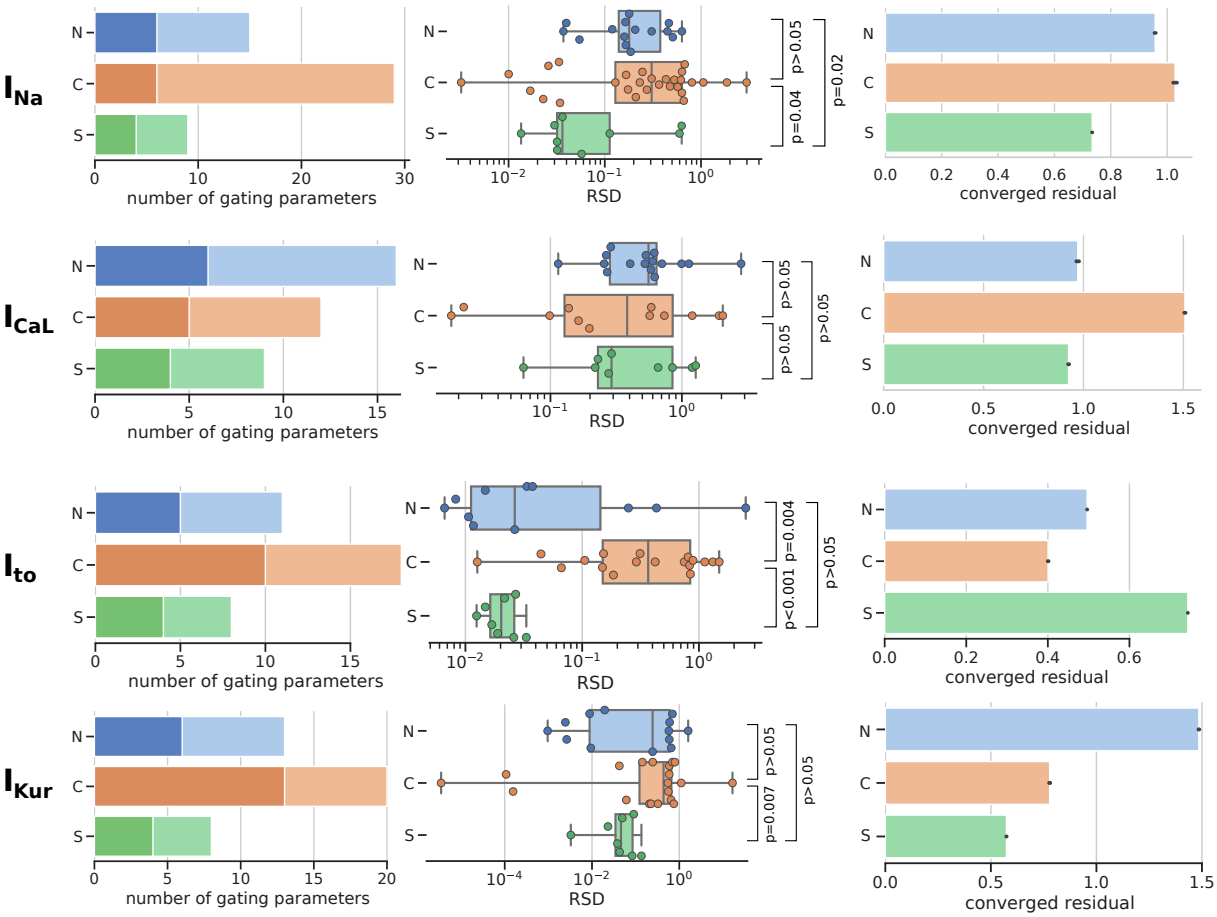


Figure 3.5: Each row shows the results for a different channel model calibrated to the unified data set (N=Nygren, C=Courtemanche, S=standardised). The left column compares the number of gating parameters in each channel. Dark and light shading correspond to activation and inactivation parameters respectively. The centre column compares the RSD of parameter posterior distributions for each calibration. Significance is tested using a Mann-Whitney U-test. The right column shows the goodness-of-fit of each model as assessed by the residual after convergence of the ABC calibration. Adapted from [157] (CC BY).

see, this is not the only consideration that needs to be made.

Goodness-of-fit is important in model calibration to understand how well a model reflects the experimental data. In this work, the goodness-of-fit can be assessed from the remaining residual of the model output to experimental data. The final column of Figure 3.5 shows the results for each calibration. For all channels except I_{to}, the S model calibration resulted in a lower converged residual than both the N and C models. As a result, despite having more defined parameters in a number of channels, only the S model calibration of I_{Na} has lower parameter RSDs and improved goodness-of-fit compared to both N and C models.

The results from Figure 3.5 provide an overview of the parameter variability and goodness-of-fit of each model. However, it is informative to also consider each channel individually to understand the particular strengths and deficiencies of each calibration. We now compare the summary statistics, gating functions and simulation performance of each channel in more detail.

Fast Na^+ channel. Figure 3.6 compares all I_{Na} models calibrated to the unified experimental data set. Figure 3.6a shows the summary statistic model outputs compared to experimental data. In most experiments, the S model qualitatively reflects the experimental data to a comparable degree as the N and C models, confirming the improved residual observed in Figure 3.5. For the fast and slow recovery τ experiments (last two plots in lower row of Figure 3.6a), both the S and C model are noticeably closer to experimental data than the N model. A particular deficiency of the S model calibration is in the activation τ experiment (second plot in top row of Figure 3.6a), where it deviates from experimental data in the upper voltage range by falling to zero rather than plateauing as in the other models and experimental data.

Figure 3.6b compares the underlying gating functions of each I_{Na} model. Note that the gating functions do not directly relate to the summary statistics recorded in experiments, as the summary statistic functions do not perfectly extract measurements of specific steady-state and time constant parameters of different interacting gates. The S model exhibits generally well constrained behaviour other than in the region of a gap in

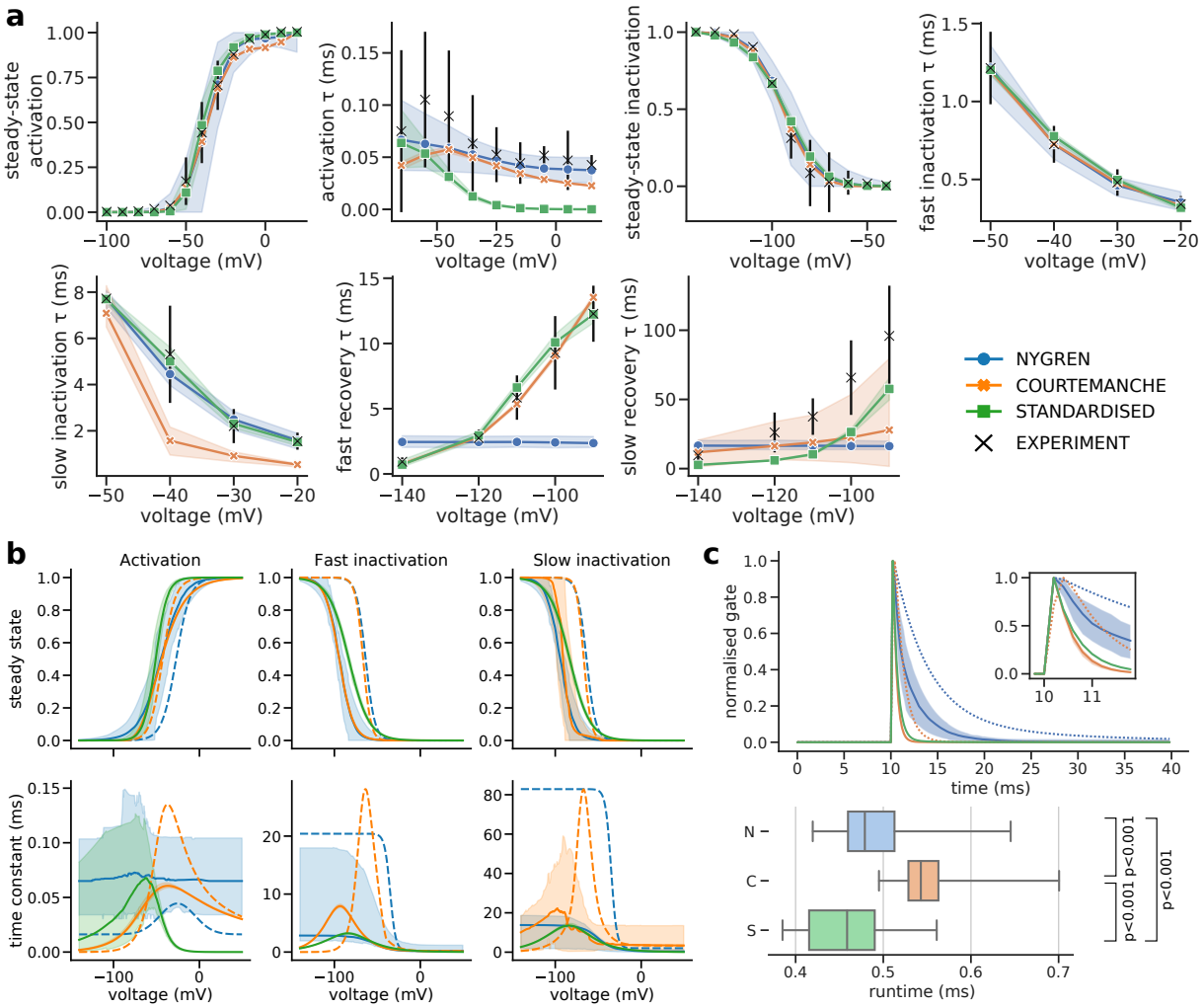


Figure 3.6: **a** Results of calibrating each I_{Na} model to the unified data set. Model output is plotted as median line and 89% HPDI from 100 parameter posterior samples. Experimental data is plotted as black crosses and bars representing mean and SD. **b** Steady-state and time constant functions for each gate from samples in a. Dashed lines indicate the published N and C models. **c** Example traces from each model generated from the last step of a pulse train of 100 steps from -140 mV to -30 mV for 100 ms at a rate of 1 Hz using samples from a. Normalised gate refers to the open probability of each channel model normalised between 0 and 1 by its maximum open probability in response to the pulse train. Dashed lines indicate the published N and C models. The box plot compares time taken to run the protocol for each model. Adapted from [157] (CC BY).

experimental data (deactivation data in lower voltages of the activation gate time constant). Only the C model exhibits low uncertainty in this region. In this case, the low uncertainty may not be beneficial as it could imply undue confidence in the C model's behaviour in model space without experimental data to compare.

There is a distinct difference in the form of the N model inactivation gate time constants which have a sigmoid shape rather than the peaked curve exhibited by both C and S models. Given the experimental data follows a peaked curve, this appears to be an instance of model discrepancy and leads to the difference between N model and experiment we observed in Figure 3.6a. This particular example will be explored in more detail in Section 3.3.5.

Comparing the current trace of each model at the end of a pulse train (Figure 3.6c), there is little difference between the fully calibrated traces of the C and S models, and the S model has a significantly reduced run time for this protocol. Note that this pulse train is not necessarily representative of how the channel would behave during an action potential when the transmembrane voltage is varying rather than imposed. The run time of the protocol for each model is smallest for the S model with the simplest structure, and greatest for the C model with the most parameters, as would be expected.

L-type Ca^{2+} channel. I_{CaL} has Ca^{2+}- as well as voltage-dependent components of inactivation. The N and C models differ in how they formulate this channel; the former includes two voltage-dependent inactivation gates and the latter includes a single voltage-dependent inactivation gate. Both include a single Ca^{2+}-dependent inactivation gate which was held at a constant value to isolate the voltage-dependent features of the channel. Given the data typically shows a fast and slow component of inactivation [173], we include two voltage-dependent inactivation gates in the S model of I_{CaL}. Thus comparisons are more meaningful between the N and S models in this case, as the structure of the C model differs substantially and relies more directly on intracellular Ca^{2+} concentration to modulate the rate of current decay.

Figure 3.7 summarises the results for I_{CaL}. None of the models appear able to calibrate to the slowest components of recovery from inactivation (final frame of Figure 3.7a). In

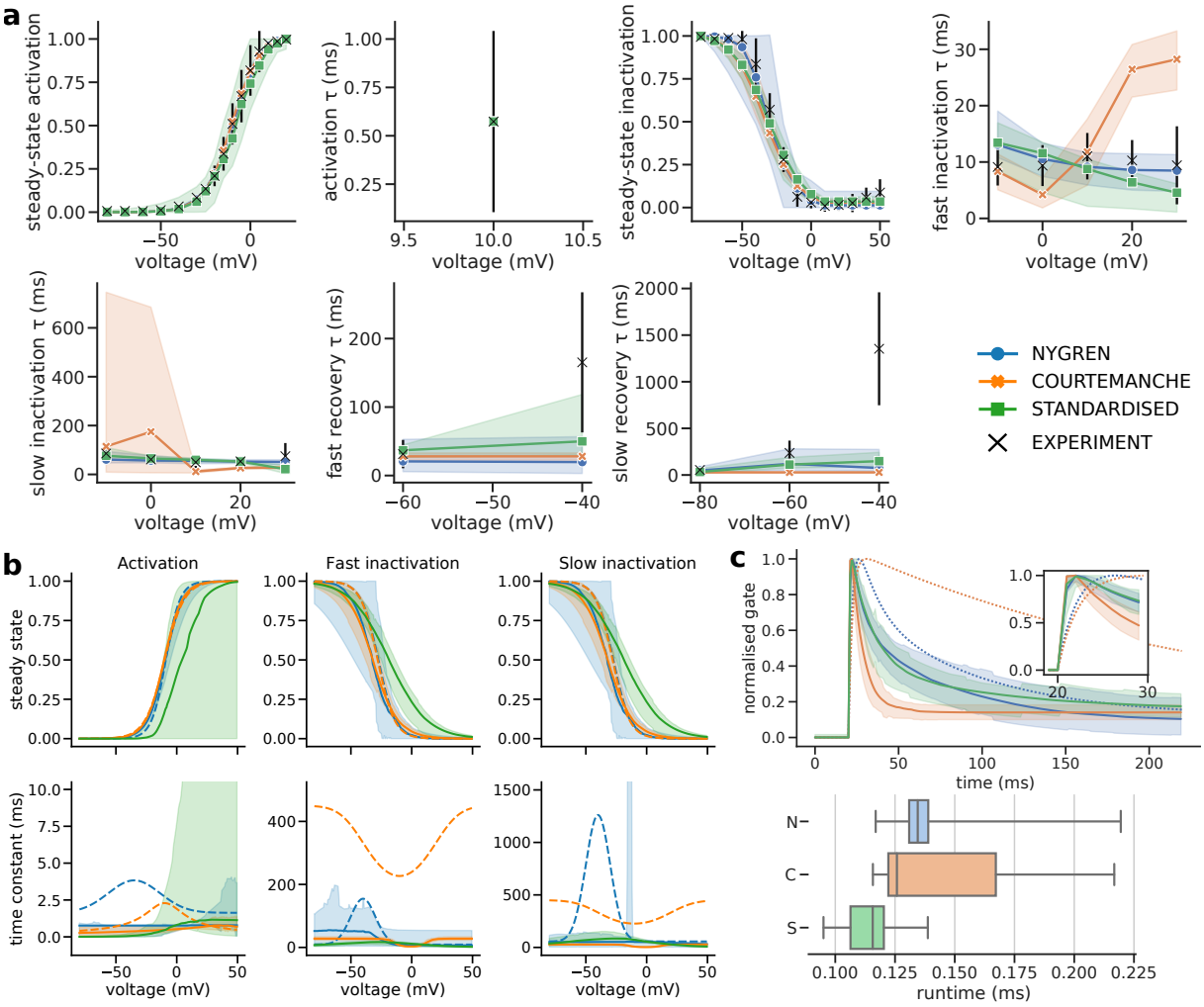


Figure 3.7: All sub-figures are plotted as described in Figure 3.6. **a** Results of calibrating I_{CaL} models to the unified data set. **b** Steady-state and time constant functions for each gate from the samples in a. **c** Example traces from each model generated from the last step of a pulse train of 100 steps from -80 mV to -10 mV for 200 ms at a rate of 1 Hz using samples from a. Adapted from [157] (CC BY).

Figure 3.7b, showing plots of gating functions, the same activation time constants are plotted for the C model in both the fast and slow inactivation columns, as this model had only one inactivation gate. The gating functions show high variability in the steady-state activation function of the S model, and this model also differs from the N and C models at higher voltages of the inactivation steady-state curve. However, this is not apparent from the summary statistic functions (Figure 3.7a), which suggests interaction between gating variables 'hides' this underlying variability. Each model has reduced variability around the voltages of time constants which are explicitly tested (inactivation and recovery τ measurements) with, particularly in the N model, wide uncertainty outside of these ranges.

We saw previously (Figure 3.5) that there were no significant differences in RSD values between the models for this channel, highlighting that each model calibration has similar parameter variability and potential unidentifiability. The N and S models provide better fits to the data, though this may be a consequence of the C model relying more heavily on the Ca^{2+}-dependent inactivation processes held constant in this experiment. This can also be observed by comparing the current traces in Figure 3.7c. While the N and S models both decay in a similar fashion, the C model initially decays at a faster rate before reaching a plateau, which is a result of the Ca^{2+}-dependent gate being held open. In the complete cell model, we would expect this current to continue decaying as the intracellular Ca^{2+} rises during the action potential.

Transient outward K^+ channel. We saw previously that the N and S models of I_{to} had similar posterior parameter RSD values significantly lower than the C model, but the S model exhibited the poorest goodness-of-fit amongst the models (Figure 3.5). We also observed in Figure 3.3 that calibration of the N model to the unified data set resulted in non-physiological steady-state gating functions, despite fitting to the data.

Figure 3.8 shows the summary statistics, gating functions and current traces of each model calibration for I_{to}. Despite low variability in model summary statistic output for the S model across experiments in Figure 3.8a, the reduced goodness-of-fit of this model can be explained by the calibration being unable to capture particular gating kinetics such as the peak of the activation time constant (top row, second plot in Figure 3.8a) and the plateau region of the inactivation time constant (bottom row, second plot in Figure 3.8a). Both the N and C models are able to better reflect this aspect of the experimental data.

Despite mostly similar behaviour of each model's output when processed into summary statistics, the underlying gating functions plotted in Figure 3.8b reveal striking differences between how each model behaves. Particularly for the activation gate, there are differences in the steady-state mid-point and slope. The form of the equations (Appendix A.1) enforces that peak time constants of each model are approximately at the midpoint voltage of activation and thus also differ from each other.

Both the N and S model calibrations have non-physiological steady-state activation

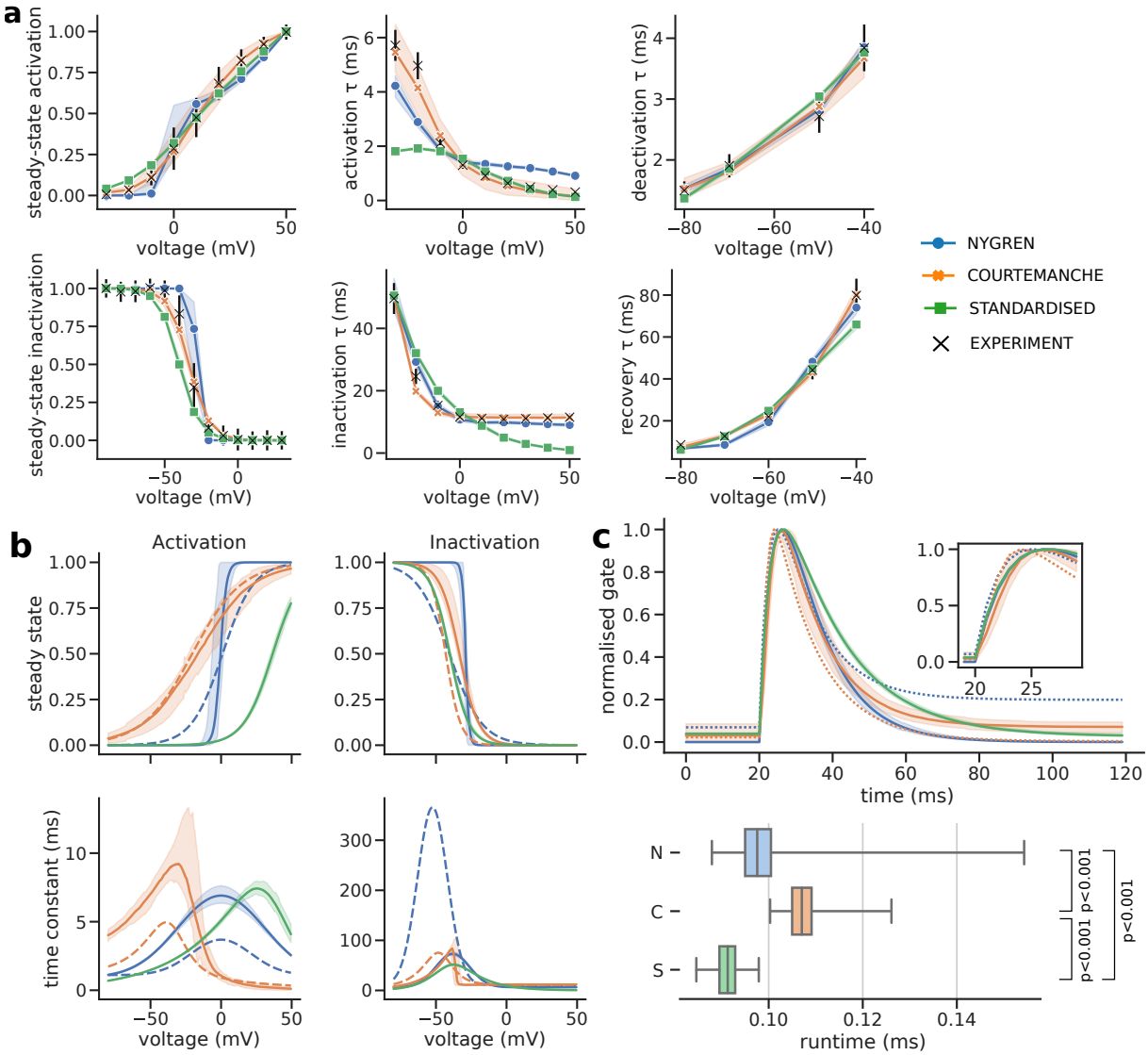


Figure 3.8: All sub-figures are plotted as described in Figure 3.6. **a** Results of calibrating each I_{to} model to the unified data set. **b** Steady-state and time constant functions for each gate from the samples in a. **c** Example traces from each model generated from the last step of a pulse train of 100 steps from -50 mV to -10 mV for 100 ms at a rate of 1 Hz using samples from a. Adapted from [157] (CC BY).

and inactivation curve combinations. This can be seen (for example) by comparing each gate's steady-state value at 0 mV, showing there is no, or very little, overlap region. In the summary statistic output, both models reflect the experimental data in a visibly reasonable way (Figure 3.8a). Despite the underlying difference in gating functions, the models all produce comparable current traces (Figure 3.8c).

Ultra-rapidly activating delayed rectifier K^+ channel. We previously saw that the S model calibration of I_{Kur} had a improved goodness-of-fit over either other model, and significantly lower RSD values compared to the C model (Figure 3.5). I_{Kur} exhibits a very slow voltage-dependent component of inactivation and only partially inactivates in the available voltage clamp experimental data [177].

Similar to I_{to}, each model showed distinct differences in gating functions (Figure 3.9b). However, in this case, the difference was also more clearly reflected in the model summary statistics output (Figure 3.9a). All models deviate from experiment data points at lower voltage ranges of steady-state activation (first plot in Figure 3.9a). As we saw previously for I_{Na}, the poor fit of the N model deactivation τ (top row, last plot in Figure 3.9a), is caused by model discrepancy due to the sigmoid shape of the time constant function for the activation gate, rather than the peaked shape exhibited by the C and S models.

A unique (in this study) feature of the experimental data for I_{Kur} is that the steady-state inactivation gate does not fully close (notice scale in bottom row, first plot of Figure 3.9a). The simple structure of the S model does not allow for this outcome, and as a result we see that the steady-state inactivation gate has a non-physiological value (Figure 3.9b). The N and C models have also handled this possibility in different ways; the former plateaus at a non-zero value while the latter has a much shallower slope across the voltage range (Figure 3.9b). As we have seen previously, despite the substantially different gating functions, all models result in a similar current trace for this pulse train protocol (Figure 3.9c).

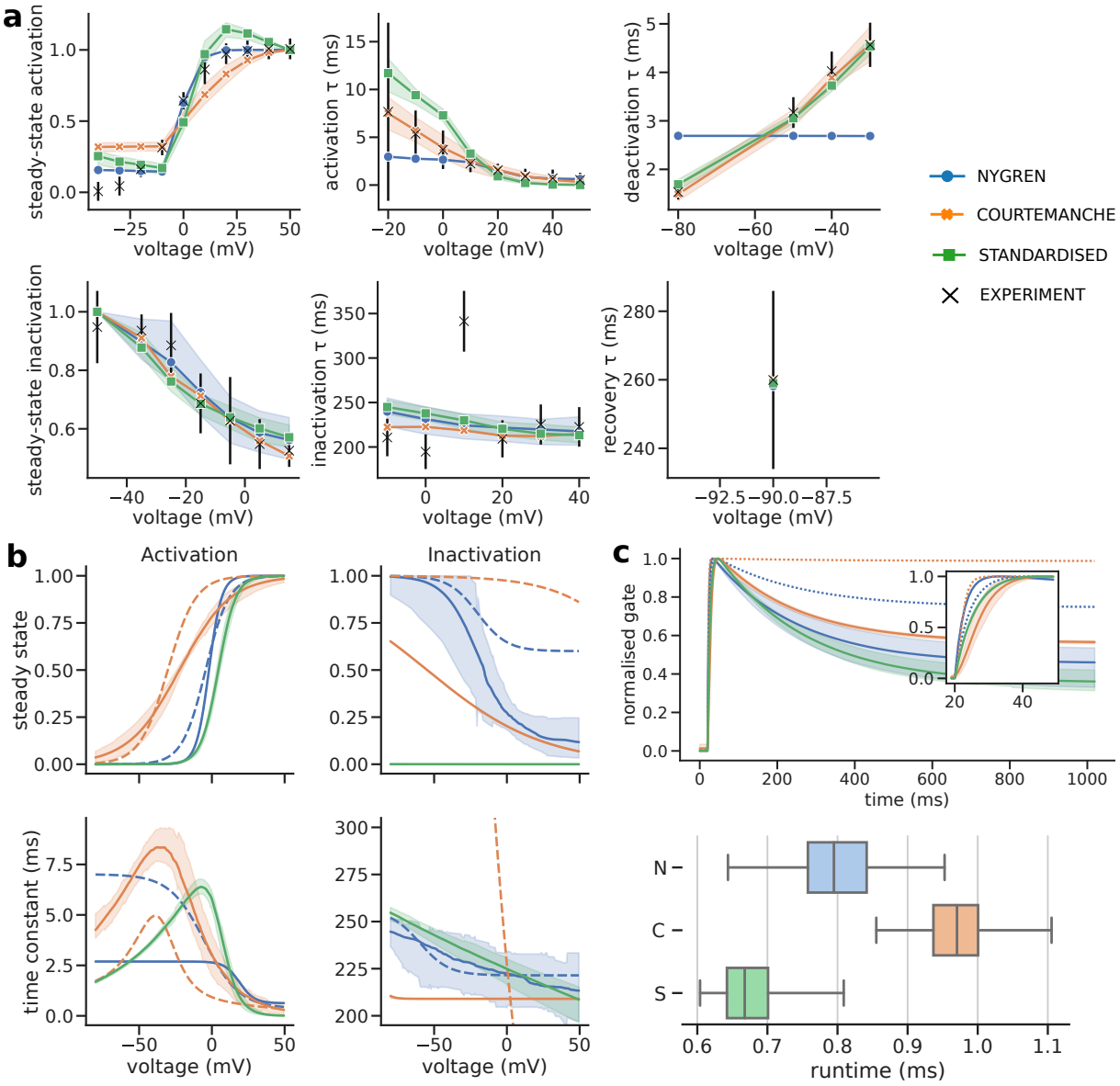


Figure 3.9: All sub-figures are plotted as described in Figure 3.6. **a** Results of calibrating each I_{Kur} model to the unified data set. **b** Steady-state and time constant functions for each gate from the samples in a. **c** Example traces from each model generated from the last step of a pulse train of 100 steps from -50 mV to -10 mV for 1000 ms at a rate of 0.1 Hz using samples from a. Adapted from [157] (CC BY).

3.3.4 Effect on action potential

Having studied each calibrated channel in isolation, we next sought to investigate how inclusion of uncertainty and variability in the gating of these channels would impact the action potential when combined back into the complete cell models. Figure 3.10 shows how measurements of the action potential changed for the recalibrated N channels, recalibrated C channels, and when the calibrated S model replaced the original channel in either model (referred to as N+S and C+S). Corresponding action potential traces are shown in Figure 3.11. Graphs showing current traces underlying these action potentials can be found in the Supplementary Information to [157].

This experiment could not be completed for I_{Na} due to the steady-state shifts applied by the original authors when this channel was combined back into the complete cell, which was different for each model [165, 166]. It would not be trivial to shift parameters in a valid manner post-calibration, or to shift the data sets and recalibrate. We instead chose to focus on channels which activate later in the action potential for which data was not shifted by the original authors. Conductance parameters were not included in the calibration steps above, and so were set for each model as described in Section 3.2.7.

For I_{CaL}, a portion of posterior samples in the N model resulted in an elevated resting potential, indicative of incomplete repolarisation, though the median result was still close to the published value. This causes the wide 89% HPDI observed in the corresponding trace (top row of Figure 3.11), while the median line is much closer to the dashed line of the original model. This also occurred to a lesser degree when the S model was inserted into the C cell model for this channel. The recalibrated C model was more stable with the action potential duration being mainly reduced from the published value as a result of quicker and more complete inactivation of the channel during the action potential (Figure 3.11).

Traces generated by using the posterior parameterisations for I_{to} generally showed small differences from the published values for resting potential and action potential amplitude, though larger changes in the action potential duration. For the full N model (both with the original channel form and S form), an increased action potential duration

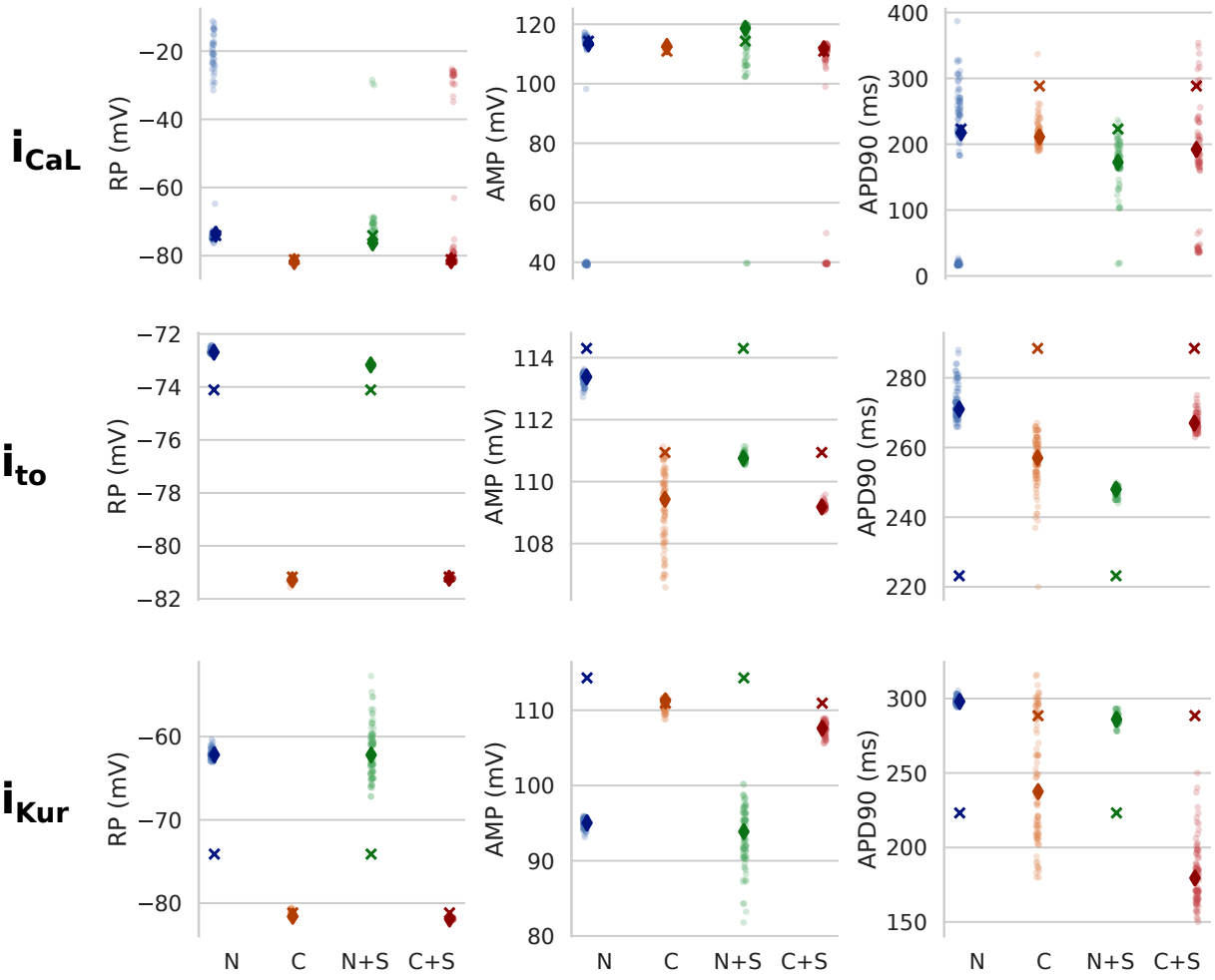


Figure 3.10: Strip plots showing measurements of resting potential (RP), action potential amplitude (AMP) and action potential duration to 90% repolarisation (APD90) from action potentials elicited from the full N and C models. Crosses indicate values from the models run at published settings. Each point is a measurement from an action potential generated from a sample from the posterior parameter distribution of the channel indicated in bold. The diamond is the median of the samples. N: using N unified posterior distribution in the full N model, C: using C unified posterior distribution in the full C model, +S: indicates the standardised model replaced the corresponding channel in the full model and used the S posterior distribution. Adapted from [157] (CC BY).

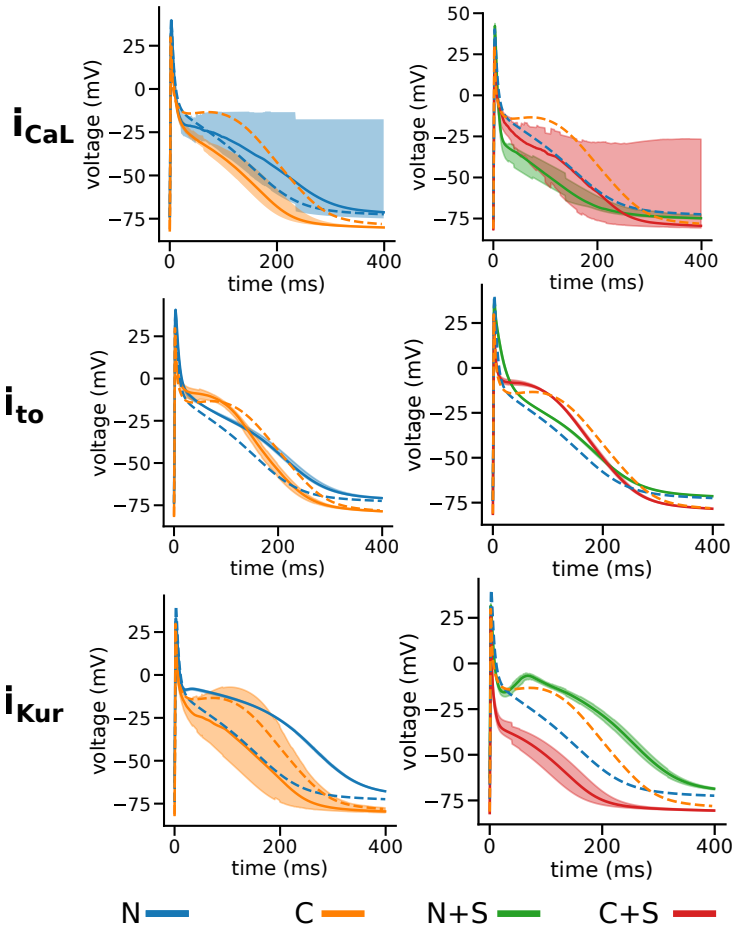


Figure 3.11: Line plots showing a summary of the action potential traces. Traces are displayed as median lines with shading representing 89% HPDI from 100 posterior samples. The published N and C models are plotted as dashed lines in all plots for comparison. Adapted from [157] (CC BY).

is observed, while the opposite was observed for the C model. This makes the two action potential models, which have quite different published action potential morphology, more similar to one another. A small degree of variability is apparent from the posterior intervals around the traces and, in contrast to I_{CaL} all samples resulted in 'normal' action potentials.

Using the recalibrated form of I_{Kur} resulted in more noticeable changes to the action potential than I_{to}. For both the N and N+S experiments, this increases the resting potential and action potential amplitude accompanied by an increase in action potential duration to a similar level as the published C model. In both cases, the triangular morphology of the published N model was altered to have a more prolonged plateau phase. For the C model, the resting potential and amplitude of the action potential were close to the published values, while a large degree of variability is observed in the action potential duration. When using the C form of the channel, this variability encompasses the published value, which is apparent from the shading of the action potential trace including the dashed trace of the published C model. When using the S form of the channel, the cell repolarises more quickly as a result of an increased I_{Kur} current density.

3.3.5 Including model discrepancy

The results above were obtained by calibrating channel models using the classical form of ABC. This final results section presents a brief standalone study into the effect of including an estimate of model discrepancy as a calibrating parameter and the general probability ABC acceptor as described in Section 3.2.4.

We compare calibrations of the inactivation gate of the N model for I_{Na} to the simpler S model using the three experiments from the unified data set relevant to that gate. Along with the model parameters, one additional parameter is included in the calibration per experiment (three in total for each model) to represent the additional variance added due to model discrepancy at each data point. These parameters are used in the independent Gaussian probability acceptors at each data point. Each of these parameters are assigned uniform priors between 0 and 0.5. A tempering scheme is used to increase acceptance

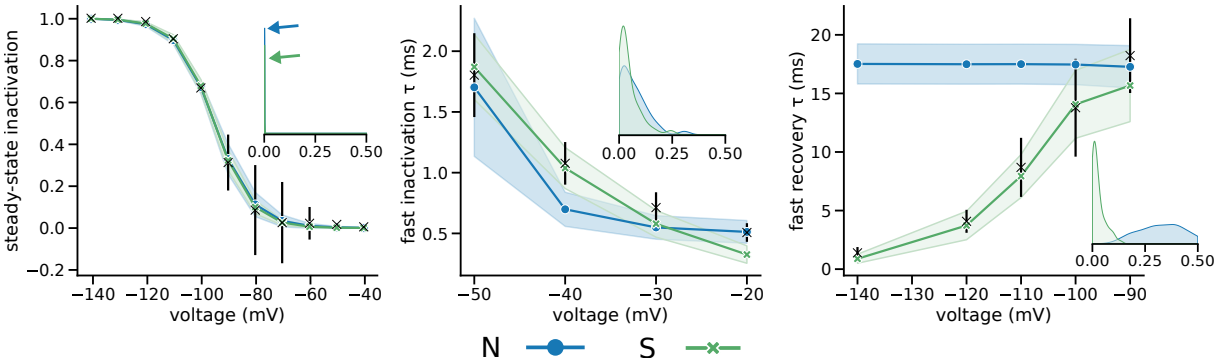


Figure 3.12: Output from calibrated models for the fast inactivation gate of the fast sodium channel, generated from 100 samples from the ABC parameter posterior distributions, compared to experimental data points. The samples are summarised as a mean line and shading indicating one standard deviation around this line. Inset graphs show the posterior distribution kernel density estimate for the model discrepancy variance in each experiment. Blue represents Nygren model and orange represents standardised form.

rates in early iterations of the ABC-SMC algorithm, and the calibration is halted once we are accepting based on the true likelihood function (see [188] for details of the algorithm).

Figure 3.12 shows the resulting calibrated models in each case. Both the calibrated N gate and the S form match the first two experimental data sets with a reasonable accuracy. Particularly the steady-state values are constrained with little variation between the samples from the parameter posterior distribution. The S formulation follows the fast recovery time constant data more closely than the N model. As mentioned in the previous results, this is likely a result of the structure of the equations used in either case. The N model uses a sigmoid function for the time constant behaviour of this gate, and so plateaus as $V \to \pm\infty$.

The inset plots in Figure 3.12 show the posterior distributions (displayed as kernel density estimates) for the additional variance attributed to model discrepancy for each experiment. For the steady-state inactivation experiment, which both models represent closely with little variance in their output, the posterior distributions both cluster on the lower zero limit of the prior (highlighted by arrows in the figure). For the fast inactivation time constant, both posterior distributions have a low non-zero modal value indicating neither reproduces the experimental data perfectly with similar discrepancy in either case.

A clearly very different distribution of the model discrepancy variance is visible in the fast recovery experiment. The N model posterior has a much wider distribution spanning the upper portion of the uniform prior while the S model shows a similar distribution as

the previous experiment. This reflects the ability of the S form of this gate to reproduce the fast recovery behaviour, and the significant difference between the calibrated output of the N model compared to the experimental observations.

3.4 Discussion

Understanding the uncertainty and unidentifiability of parameters in action potential models is critical to the development of trustworthy cardiac models for the era of personalised medicine [124, 126]. Prior to the development of a model of the HL1-6 myocyte, it was thus important to develop an approach which can assess these properties. These results will also subsequently influence which channel formulations are suitable for the development of an HL1-6 cell model.

In this work, we have applied ABC to recalibrate the gating kinetics in detailed ion channel models of human atrial myocytes. We calibrated these models to the experimental data sets used in the published calibration and showed a portion of parameters exhibited wide posterior distributions indicative of unidentifiability. Calibration to more complete experimental data sets did not reduce the unidentifiability present, which suggested that it may be structural and/or practical. Reducing the structural complexity of the model through a common gating form was successful in reducing unidentifiability in I_{Na} without sacrificing goodness-of-fit. Experiments with other channels suggested that a trade-off exists between tailoring a model to provide a good fit to experimental data, and identifiability of parameters as models become more complex. We then looked at changes of the action potential introduced by using the recalibrated I_{CaL}, I_{to} and I_{Kur} channels in the full cell models. Finally, a brief example demonstrated how model discrepancy can be incorporated into the ABC calibration process.

Five conclusions can be drawn from the results presented:

1. A model is only as good as the data used to calibrate it; an incomplete data set results in low confidence of model parameters;

2. Using a 'complete' data set does not necessarily reduce uncertainty in model pa-

rameters, particularly for complex models;

3. A simpler model formulation may improve parameter identifiability, but more detailed models may be required for some ion channels;

4. Channel models do not stand in isolation and should be studied in relation to action potentials generated by the complete cell model;

5. Model discrepancy can be quantified to a limited degree in approximate Bayesian computation.

Each of these conclusions will now be addressed in greater detail.

3.4.1 Incomplete data sets reduce the ability to identify parameter values

Figure 3.1 shows uncertainty in parameter estimates for the I_{Na} channel current in the N model manifest in a range of possible outputs of the current trace in response to voltage steps. The medians of the posterior parameter distributions related to time constant behaviour were close to the original reported values but showed a high degree of uncertainty. This was the expected result as only steady-state data were used to calibrate I_{Na} of the N model. As a consequence, the time constant parameters in this example likely exhibit practical unidentifiability, as they cannot be constrained given the provided experimental data. It should be noted that the well-constrained parameter q_1 in Figure 3.1a is different from the published value due to a constant offset applied to the steady-state curve in the N model justified by time- and/or temperature-dependent drifts in steady-state characteristics of the current [165].

In comparison, the C model used a more complete data set to calibrate kinetics for this channel. Nevertheless, this model also exhibits parameters with high RSD values suggesting unidentifiability (Figure 3.2). In contrast to the practical unidentifiability observed in the case of the N I_{Na} model, this is likely due to structural identifiability issues. The high number of parameters in the C I_{Na} model (Figure 3.5) facilitates overfitting to experimental data and leads to redundancy of some parameters.

Daly et al. previously applied approximate Bayesian computation to investigate the uncertainty in parameter estimates of the Hodgkin-Huxley action potential model [130]. The authors reported wide posteriors around the estimates of certain parameters in the Na^+ and K^+ channels of that far simpler action potential model. It therefore is unsurprising to observe these results in more complex models of a Na^+ channel where there is more opportunity for parameters to covary within the structure of the model. Additionally, the use of conventional voltage clamp protocols further aggravates this issue as it only provides an indirect measure of the underlying gating kinetics [194].

3.4.2 Complete data sets do not necessarily reduce the uncertainty around all parameters in more complex models

We next recalibrated the N and C models to unified data sets. In Figure 3.2 it was apparent that the addition of data sources, most often relating to the time constants of gates, would reduce the uncertainty around the gating functions though often at the expense of increased uncertainty in other regions of model behaviour.

In the case of the N model of I_{Na}, the addition of time constant data led to a reduction in the RSD value of time constant parameters at the expense of increased RSD values of the steady-state parameters. This may be a result of the structure of this model (using sigmoid functions for inactivation time constants, see Appendix A.1) not providing a proper fit to experimental data. As a result, ABC calibration reaches the sampling rate stopping criteria earlier because the steady-state experimental data now represents a smaller portion of the overall calibration data set.

The C model of I_{Na} has 29 parameters to constrain across three gates, the most of any of the channels investigated. Although using a complete data set for calibration, the high RSD values of parameters suggest that this model still suffers from parameter unidentifiability. The complex form of the equations makes over-fitting possible when using conventional calibration processes such as simple least-squares, which would not highlight the consequences of doing so as compared to a Bayesian method such as ABC. Often these complex forms of equations are initially based on direct comparisons between

the gating functions and the experimental data and may be tailored to the specific data sources selected for calibration, rather than through forward evaluations of the model. Carro et al. highlighted the importance of replicating the experimental conditions and voltage protocols as closely as possible when calibrating action potential models, despite the inherent difficulties of doing so [194]. The complex form of model gating functions, which are often combined in parallel, means that the behaviour of the gating function itself may not be representative of the behaviour of the full channel model when tested with experimental protocols.

3.4.3 Reducing structural complexity is a trade-off between parameter identifiability and tailoring for specific currents

Reducing the structural complexity of the model equations by adopting a standardised gating formulation showed channel-dependent success. For I_{Na}, the S formulation resulted in a significant reduction in RSD values for parameter posterior distributions (p=0.02 compared to N model, p=0.04 compared to C model) which suggests it is partly alleviating unidentifiability concerns. The output from the S model of I_{Na} also resulted in an improved goodness-of-fit measure compared to either other model (Figure 3.5). Despite this, for some experiments the goodness-of-fit was clearly worse than either N or C model, such as for activation and slow recovery time constants (Figure 3.6a). In addition, there was variability around the lower voltage range of the activation gate time constant for which there is an absence of experimental data, highlighting this model is not immune to practical identifiability issues.

For I_{Na} at least, there appears to be an advantage to the less complex formulation which provides more confidence in the identifiability of its parameters without sacrificing representation of the experimental data. Fewer parameters also allow more direct reasoning about the impact different gating parameters have on the channel behaviour. As with any model, considerations should be given to the specific goals of the modelling study, though the S model of I_{Na} presents a less complex foundation which could be built upon as necessary with additional, context-specific data.

For I_{CaL}, the S model produced approximately the same goodness-of-fit as the more complex N model. However, in this case, the similar RSD values across each model imply that the use of a simpler model structure did not alleviate issues relating to parameter unidentifiability. This is particularly noticeable in the steady-state activation gate of the channel, where there is a greater variation in the posterior behaviour compared to the other two models (Figure 3.7b). This is potentially a result of the way steady-state summary statistics are calculated through normalising to a reference value in the output. As a consequence, the gate is less constrained to be fully open at the maximum activation as the normalisation hides this behaviour. The unidentifiability of parameters across all models for this channel is likely a consequence of the relative paucity of experimental data relating to the voltage-dependent time constant behaviour of I_{CaL}, which has fewer voltages tested in the unified data set compared to the other channels studied.

For both K^+ channel models (I_{to} and I_{Kur}), simplifying the model structure is a balance between unidentifiability of parameters and goodness-of-fit to experimental data. The inactivation τ plot of Figure 3.8a shows an example where both the N and C models are able to capture the plateau region at upper voltages ranges while the S model tends to zero. Similarly, the form of the S model leads to the peak of the time constant curve occurring at approximately the mid-point of activation or inactivation which appears inappropriate for the activation gate of this channel. This is reflected in the higher converged residual of the S model compared to the N and C models (Figure 3.5).

For I_{to}, the parameters of the less complex S model have lower RSD values than the C model ($p < 0.001$) and a smaller range than the N model. This suggests that the closest fit of this model to the experimental data is identifiable despite being a poorer fit, and highlights that low uncertainty in posterior parameters does not necessary imply a model fits the data well (and vice-versa). A trade-off exists which may depend on the goals and particular use-case of a modelling study.

Beattie et al. [168] used the same standardised gating formulation to model the behaviour of a rapid delayed rectifier K^+ current (the hERG current) using an information-rich voltage protocol. In their case, the studied current appears to satisfy the requirement

of peak time constant of the gate at mid-point of the steady-state curve (e.g. see Figure 5 in [168]). Based on these observations and our results, this standardised approach may therefore be appropriate in cases when experimental data suggests particular requirements, such as this one, are met.

Using a standard gating formulation alleviates problems associated with the high number of parameters in very detailed models, without sacrificing the biophysical basis for the model. In contrast to purely phenomenological models, the form of the S model is based on Eyring-derived transition rates giving its parameters a physical interpretation [168, 169].

For the N and S models of I_{to} and the S model of I_{Kur}, non-physiological steady-state gating functions were observed when calibrating to the unified data set. However, these models still reflected the experimental data in the summary statistics output to a reasonable degree. This may have been caused by not including the conductance parameter in the ABC calibration step, as the summary statistic function used (adopted directly as reported in the experimental papers) normalises the current peak. Therefore even a very small current could produce a reasonable activation or inactivation curve once processed into summary statistics. Including the conductance parameter in calibration with a physiological prior range, along with additional data available for the current density rather than just open probability, could potentially alleviate this issue.

A final note was that, across all channels studied, the S model leads to a reduction in run time (at least for the channel in isolation as tested in this solver). This is an important consideration as patient-specific modelling is further explored in whole-heart tissue simulations. However, in contrast to even simpler models which have been shown to reproduce patient-specific action potential morphologies [195], the standardised formulation retains information about specific ion channel currents which provides a stronger body of evidence in terms of model validation. It would be encouraging if future ion channel modelling promoted the use of common forms of equations in cell models rather than the current heritage of complex equations. Another promising proposition is a model reductionist approach to reduce uncertainty in parameter estimates by eliminating parameters which have little effect on the model output (e.g. manifold boundary approximation [167]).

3.4.4 Channel models should be calibrated with both patch clamp data and observing changes in action potentials

When testing the new parameterisations in the complete cell models, it was apparent that a proportion of samples led to non-physiological behaviour. This was also the case when combining samples from all new parameterisations, which generally caused simulations to become numerically unstable. This highlights the importance of a feedback process in the development of action potential models, where the form of the full action potential also informs the design of the underlying currents.

A future step for this work could follow a similar approach to Kernik et al. [87] with multiple stages of calibration. For example, the full action potential samples in these results could be used to further constrain the posterior distribution of the channel model parameters by eliminating non-physiological cases. This approach in the context of ABC will be explored in the next chapter through the development of a full cell model.

These results also demonstrate an important consideration in the development of full action potential models that tends to be omitted from modelling papers: the sheer challenge of combining a variety of nonlinear models of individual ion channels usually developed in isolation into a single model of a cardiac cell and tuning to produce a physiological action potential.

3.4.5 Model discrepancy can be included as additional parameters in approximate Bayesian computation

In the main set of results, it was noted in some cases that there was a clear difference between the model structure and the experimental data. In particular, for the N model of I_{Na} and I_{Kur} time constant equations, the sigmoid function used differed from the peaked experimental data. This model discrepancy could result in an overconfidence in the calibrated parameters and increased uncertainty due to model structure.

In the final results section, we investigated how the acceptance step of ABC might be generalised, as described by Wilkinson [190], and used to quantify some measure of model

discrepancy. The inactivation gate of I_{Na} was used as an example, with both the N and S model formulations calibrated to only the inactivation data. An additional variance term was calibrated for each experiment which increased the width of the Gaussian acceptor on each data point.

The model calibrations highlighted discrepancy in inactivation time constant of the N model at lower ranges, which was not present in the S model. These results are promising as an additional avenue for ABC though, in the current context, limited. It would obviously be desirable to have a separate measure of model discrepancy at each data point, not just per-experiment. However, a significant limitation of this approach is that each additional model discrepancy parameter increases the dimensionality of parameter search space. It is therefore challenging to see how this could be scaled up in all but the simplest models. A more robust approach may be to model the discrepancy using Gaussian processes or autoregressive-moving-average models, when time series experimental data is available [159].

3.4.6 Limitations

RSD was used as a measure of the width of parameter posterior distributions and as an indicator of parameter unidentifiability in this study. This measure tends to become inflated when the mean value in the denominator is close to zero. This approach does not allow us to separate structural and practical unidentifiability and the likely form was inferred from the availability of experimental data and structural form of the model in experiments.

Our ABC stopping criterion for all experiments was set to halt execution once an iteration had dropped below a 1% particle acceptance rate. This was based on preliminary experiments on the C model where it was assumed the algorithm is close to the optimum solution once sampling became too difficult. However, in some cases this criterion may be excessive or insufficient, as was observed for example for the original N and S model of the I_{CaL} channel. Investigations into more appropriate stopping criterion were outside the scope of this thesis. Parameters involved in the Ca^{2+}-dependent gate in I_{CaL} of all

models were omitted from calibration and the gate set to a constant value due to the lack of specific data and difficulty in isolating calcium handling components of the cell model. Particularly for the C model, which relies on the calcium transient to modulate the inactivation rates, it is perhaps inappropriate to attempt calibration using this approach.

The calibration process relied on summary statistics of the model responses to the virtual voltage clamp protocols. Reducing the data in this fashion was necessary to obtain the same form as in the experimental data set. However, as highlighted in [161], it is generally not possible to obtain a finite dimensional set of summary statistics that are sufficient to fully capture all relevant information obtained from a voltage clamp protocol.

Channel models with greater than 14 parameters (N: I_{CaL}, I_{Kur}; C: I_{Na}, I_{to}, I_{Kur}) could not be calibrated as a complete model due to the large number of particles required to sample the high-dimensional parameter hyperspace. In these cases, we calibrated parameter subsets for each gate separately to the relevant experimental data while leaving the remainder at their published values. It is possible that the original gates could affect the calibration of the chosen gate, for example in exponential fitting to decay traces for channels with fast and slow inactivation. Despite this, it should be noted that conventional calibration techniques (e.g. least squares regression) do not restrict the modeller from applying the method in the case of this kind of sparse sampling space and will not explicitly convey the implications of doing so.

Experimental data in the conventional form of patch clamp experiments summarised as mean values with standard deviations was used to calibrate the models in this chapter. This was used as it was the same data calibrated to by the original modellers. Recent studies have noted that the use of a normal distribution to summarise data from cellular electrophysiology likely overestimates the mean, as closer inspection of experimental distributions reveals positive skew compared to a normal distribution [196]. ■

Chapter 4

An HL1-6 action potential model accounting for biological variability and uncertainty

4.1 Introduction

In the previous chapter, a calibration methodology using approximate Bayesian computation was explored through a retrospective analysis of two human atrial cell models compared to a standardised formulation. The goal of that chapter was to develop the computational methods and insight from the results to inform the design of a new model of the HL1-6 myocyte.

One conclusion from the previous chapter was that the use of a standardised channel formulation (e.g. [168, 191]), can result in parameters that are better constrained than more complex formulations. In an ideal case, one would be able to reduce these parameter uncertainties to the level where they are representative of only the underlying variability of the biological system. It was also noted that some channels may require more specific forms depending on their current response at different voltage levels. Therefore, in this chapter, the HL1-6 cell model is developed using the same standardised formulation for ion channels where possible, and modified minimally when behaviour from experimental

data does not fit this model.

The HL1-6 myocyte is a more homogeneous sub-clone of the original HL-1 cell line [60]. Ion channels in the original cell line have been characterised through a number of electrophysiology studies [62–65, 197–201]. In the sub-clone, behaviour of both the fast Na^+ channel and L-type Ca^{2+} channel have also been measured [69]. HL1-6 is a murine cell line with similar spontaneous beating and immature morphology to neonatal cells. Cell models have been developed using traditional calibration approaches for adult mouse ventricular cells [79, 80], neonatal cells [84] and populations of stem cells with similar heterogeneity and spontaneous automaticity [87].

Takeuchi et al. [202, 203] recently developed a cell model of the original HL-1 cell line based on a human atrial cell model [204]. They modified the Grandi model by re-fitting channels to data from HL-1 myocytes, adding models for the hyperpolarisation-activated 'funny' current and T-type Ca^{2+} current which HL-1 cells are known to possess [62,65,198], and adding mitochondrial Ca^{2+} handling which was the specific interest of the study. The model spontaneously beats at 3.5 Hz, similar to their biological experiments [202]. The authors noted the biological variability between electrophysiology measurements in individual cells, but did not attempt to explicitly account for this variability in their model as they noted its effect would be dampened in a cellular synctium. In the context of this thesis, studying action potential propagation on a cellular level, this variability may play a more important role. The authors also showed that their channel models fit experimental data to a good degree, but they did this by plotting the underlying gating functions against the 'summary statistics' experimental data which, as we have seen from the previous chapter in this thesis, is not always representative of the combined channel output.

The goal of this chapter is to apply the methodology developed in the previous chapter to construct an action potential model of an HL1-6 myocyte, accounting for biological variability and uncertainty. This will subsequently be combined in a multi-domain model to simulate action potential propagation in HL1-6 cell monolayers. Section 4.2 describes the structure of the cell model, how multiple channel models were combined into the final

complete cell model, and steps taken to validate the model. Section 4.3 then shows the results of calibrating each channel in the HL1-6 cell model, the final calibrated model and compares the full model to 'unseen' data as validation. Finally, in Section 4.4 the newly developed model is discussed in the context of the goals of this thesis.

4.2 Methods

4.2.1 Model structure

The action potential model for the HL1-6 myocyte is described as:

$$\frac{dV_m}{dt} = I_{\text{ion}} - I_{\text{stim}}, \tag{4.1}$$

where V_m is the transmembrane potential (mV), t is time (ms), I_{ion} is the ion current across the membrane (pA/pF) and I_{stim} is any applied stimulus current (pA/pF). Units of current are relative to the cell membrane capacitance, C_m (μF), which is why it does not appear in the above equation. I_{stim} is set to zero during voltage clamp simulations. The sarcolemmal ion current is the sum of currents through ion channels, exchangers and pumps:

$$\begin{aligned} I_{\text{ion}} = {} & I_{\text{Na}} + I_{\text{Nab}} + I_{\text{CaL}} + I_{\text{CaT}} + I_{\text{pCa}} + I_{\text{Cab}} \\ & + I_{\text{Kr}} + I_{\text{to}} + I_{\text{ss}} + I_{\text{f}} + I_{\text{K1}} + I_{\text{NCX}} + I_{\text{NaK}}, \end{aligned} \tag{4.2}$$

Each channel is described in more detail in the results. Standardised gating kinetics were adopted for I_{Na}, I_{CaL}, I_{CaT}, I_{Kr}, I_{to}, I_{ss}, I_{f} and I_{K1} as described in Equation 3.3 in Chapter 3. For all other currents, equations from a previous cell model related to HL1-6 myocytes were used and their key parameters recalibrated to whole cell measurements.

HL1-6 myocytes have round, immature morphology [69], lacking the T-tubule structures of adult cardiomyocytes that bring L-type Ca^{2+} channels in close proximity to ryanodine receptors on the sarcoplasmic reticulum. To describe the intracellular Ca^{2+} handling, the formulation from a model of neonatal rat ventricular myocytes is used [84]

in a simplified form. This neonatal model accounts for diffusion of Ca^{2+} ions from the membrane to the sarcoplasmic reticulum due to the immature morphology of the cells using multiple cytosolic subspaces and a finite difference formulation [84]. This approach is adopted and simplified in our model by agglomerating the subspaces into a single cytosolic space, with a time delay parameter governing Ca^{2+} diffusion from the membrane to the sarcoplasmic reticulum as has been done previously in models of spontaneously beating cells [83].

The equations for Ca^{2+} buffers are also generalised to overall cytosolic and sarcoplasmic reticulum buffering to reduce unknown parameters, as in a recent model of induced pluripotent stem cells [87]. The sarcoplasmic reticulum is separated into release and uptake compartments to provide a realistic delay until Ca^{2+} becomes available for release after uptake [79, 84].

The Ca^{2+}-handling processes are described as

$$\frac{d[Ca^{2+}]_i}{dt} = \beta_i \left(J_{\mathrm{Ca,SL}} + J_{\mathrm{RyR}} \frac{V_{\mathrm{SR,rel}}}{V_i} - (J_{\mathrm{SERCA}} - J_{\mathrm{leak}}) \frac{V_{\mathrm{SR,up}}}{V_i} \right), \tag{4.3}$$

$$J_{\mathrm{Ca,SL}} = \left(2I_{\mathrm{NCX}} - I_{\mathrm{CaL}} - I_{\mathrm{CaT}} - I_{\mathrm{pCa}} - I_{\mathrm{Cab}}\right) \frac{C_m}{2FV_i}, \tag{4.4}$$

$$\frac{d[Ca^{2+}]_{\mathrm{SR,up}}}{dt} = J_{\mathrm{SERCA}} - J_{\mathrm{leak}} - J_{\mathrm{tr}} \frac{V_{\mathrm{SR,rel}}}{V_{\mathrm{SR,up}}}, \tag{4.5}$$

$$\frac{d[Ca^{2+}]_{\mathrm{SR,rel}}}{dt} = \beta_{\mathrm{SR}} \left(J_{\mathrm{tr}} - J_{\mathrm{RyR}} \right), \tag{4.6}$$

$$\beta_x = \left(1 + \frac{\mathrm{Buf}_{\mathrm{tot,x}} K_{\mathrm{m,Buf,x}}}{\left([Ca^{2+}]_x + K_{\mathrm{m,Buf,x}}\right)^2} \right)^{-1}, \tag{4.7}$$

where J terms are ion fluxes (μM/ms) between different intracellular spaces which are explained in more detail in the results, β_x accounts for Ca^{2+} buffering in the intracellular space 'x', and other parameters are described in Table 4.1.

Parameter	Definition	Value	Unit	Source
C_m	Membrane capacitance	$\mathcal{N}(13.7, 4.8)$	pF	[69]
F	Faraday constant	96.5	C/mmol	
R	Ideal gas constant	8.314	J/mol/K	
T	Temperature	296-310	K	
r_{nucleus}	Radius of nucleus	5.7934	μm	[84]
r_{SR}	Radius of sarcoplasmic reticulum	6	μm	[84]
r_{SL}	Radius of cell	10.5	μm	[84]
V_{cell}	Volume of cell	$^4/_3\pi r_{\text{SL}}^3 \times 10^{-3}$	pL	
V_{SR}	Volume of sarcoplasmic reticulum	$^4/_3\pi\,(r_{\text{SR}}^3 - r_{\text{nucleus}}^3) \times 10^{-3}$	pL	
$V_{\text{SR,up}}$	Volume of sarcoplasmic reticulum uptake	$0.9V_{\text{SR}}$	pL	[84]
$V_{\text{SR,rel}}$	Volume of sarcoplasmic reticulum release	$0.1V_{\text{SR}}$	pL	[84]
V_{i}	Volume of cytosolic space	$^4/_3\pi\,(r_{\text{SL}}^3 - r_{\text{SR}}^3) \times 10^{-3}$	pL	
$[\text{Na}^+]_o$	Extracellular Na^+ concentration	Experiment-specific	μM	
$[\text{K}^+]_o$	Extracellular K^+ concentration	Experiment-specific	μM	
$[\text{Ca}^{2+}]_o$	Extracellular Ca^{2+} concentration	Experiment-specific	μM	
$\text{Buf}_{\text{tot,i}}$	Total concentration of buffer in cytosol	Calibrated	μM	
$K_{\text{m,Buf,i}}$	Half-saturation constant of cytosolic buffering	Calibrated	μM	
$\text{Buf}_{\text{tot,SR}}$	Total concentration of buffer in sarcoplasmic reticulum	15000	μM	[79]
$K_{\text{m,Buf,SR}}$	Half-saturation constant of sarcoplasmic reticulum buffering	800	μM	[79]

Table 4.1: HL1-6 cell model pre-defined parameters with values, units and sources.

Buffer concentration and half-dissociation constant in the sarcoplasmic reticulum are adopted from a model of mouse ventricular myocytes [79], while cytosolic buffering parameters are included in the whole cell calibration routine. Cell morphology of HL1-6 myocytes is similar to the morphology of neonatal cells [69], so the radii of different compartments, and therefore the resulting cell volume, used in the neonatal cell model [84] is retained.

Intracellular Na^+ and K^+ are approximated assuming rapid equilibrium in the cytosolic space:

$$\frac{d[\mathrm{Na}^+]_i}{dt} = -\left(I_{\mathrm{Na(Na)}} + I_{\mathrm{Nab}} + I_{\mathrm{f(Na)}} + 3I_{\mathrm{NCX}} + 3I_{\mathrm{NaK}}\right)\frac{C_m}{FV_i}, \tag{4.8}$$

$$\frac{d[\mathrm{K}^+]_i}{dt} = -\left(I_{\mathrm{Na(K)}} + I_{\mathrm{Kr}} + I_{\mathrm{to}} + I_{\mathrm{ss}} + I_{\mathrm{f(K)}} + I_{\mathrm{K1}} + I_{\mathrm{stim}} - 2I_{\mathrm{NaK}}\right)\frac{C_m}{FV_i}, \tag{4.9}$$

$$E_X = \frac{RT}{z_X F}\log\left(\frac{[X]_o}{[X]_i}\right), \tag{4.10}$$

where currents are multiplied by membrane capacitance (C_m) as they are assumed to be given in units (pA/pF), and E_X is the Nernst potential for ion 'X' (one of Na^+, K^+ or Ca^{2+}) with z_X as the valence. Current terms will be explained in further detail in the results, and other terms are explained in Table 4.1.

4.2.2 Likelihood-free inference settings

Each ion channel model is calibrated using the approximate Bayesian computation (ABC) approach developed in Chapter 3 and described in detail in Section 3.2.3. Due to the limitations of the generalised ABC algorithm including estimation of model discrepancy discussed in Chapter 3, the classical form of ABC with decreasing threshold values was applied. As opposed to the previous chapter, which focused exclusively on gating kinetics, in this chapter channel conductances are also calibrated by including experimental data with current density measurements at different voltage steps (so called current-voltage or 'I-V' experiments).

The particle population size for ABC was set for each channel according to the number of parameters being calibrated. An initial estimation was made by attempting to sample

sufficiently in each dimension of the parameter hyperspace. Assuming that at least two ABC particles would be required in each hyperspace dimension yields:

$$M = 2^N, \tag{4.11}$$

where M is the number of ABC particles and N is the number of model parameters. This was used as a minimum value for channel model calibrations. When, after initial test runs, it appeared that posterior parameter estimates were 'collapsing' onto a single value, as would happen if the particle population was too low [161], the population size was increased. The final population size used in each channel is indicated in the results.

The regularisation factor for the error function (δ in Equation 3.5) was set to 0.05 in all channel model calibrations except for the fast Na^+ current (I_{Na}) and the L-type Ca^{2+} current (I_{CaL}). For these models, we found it was necessary to increase the regularisation factor to 0.2 to prevent underfitting to the I-V experiment data sets [69] due to their relatively large experimental uncertainty with respect to the other data sets used. These data sets are key to inferring a reasonable estimate of the channel conductance.

As in Chapter 3, all simulations are performed using the *myokit* (version 1.30.6) [192] and *pyABC* (version 0.9.23) [188] Python libraries, combined in our *ion-channel-ABC* library (`https://github.com/charleshouston/ion-channel-ABC`). Jupyter notebooks containing all calibration and validation code can be found in the *docs/examples/hl1* folder of that repository.

4.2.3 Ion channel calibration data sets

Experimental data for all channels in HL1-6 myocytes were not readily available to calibrate the cell model. Therefore, channels were also calibrated to data from the original HL-1 cell line, and mouse ventricular myocytes where more specific data was lacking. As HL1-6 myocytes are derived from the HL-1 cell line, which is itself a murine line, the current behaviour should not be too dissimilar, but this is a clear limitation of the study that will be discussed in more detail at the end of the chapter.

Channel(s)	Conductance Q_{10}	Source	Time constant Q_{10}	Source
I_{Na}	1.5	[206]	2.79	[207]
I_{CaL}, I_{CaT}	2.3	[208]	2.1	[208]
I_{Kr}, I_{to}, I_{ss}	4.4	[208]	4.1	[208]
I_{f}			2.3	[83]
I_{K1}	1.5	[208]		

Table 4.2: Q_{10} temperature adjustment values used for each channel.

Results from patch clamp experiments on individual channel currents in HL1-6 cells [69], HL-1 cells [62–65, 197–201] and mouse ventricular myocytes [205] were digitised. The corresponding voltage clamp protocols were translated into *myokit* code suitable for replicating the corresponding experiment *in silico*.

Conductance and gating kinetics of ion channels vary with temperature. When necessary, experimental data were adjusted to room temperature (assumed to be 23 °C or 296 K) using Q_{10} factors as indicated in Table 4.2. In the mathematical model, this process scales channel conductance by $Q_{10}^{\frac{T-T_{\mathrm{ref}}}{10}}$, and time constants by $Q_{10}^{\frac{-(T-T_{\mathrm{ref}})}{10}}$. Experimental extracellular and pipette solutions were replicated in the simulations. Table 4.3 shows all experimental data sources and conditions.

4.2.4 Whole cell calibration

As noted in Chapter 3, channel models must be considered in the context of the complete action potential model. Following calibration of the major sarcolemmal ion channel models to specific data for each current, a subset of remaining cell parameters were calibrated using ABC to measurements taken from action potentials and Ca^{2+} transients in HL1-6 cells [69].

The parameters calibrated in this step include the conductance of remaining pump and exchange currents and intracellular calcium handling kinetics. The prior of each parameter is set to cover a sufficiently wide physiological range around the published value from which the model was adopted. Table 4.4 describes the full list of 12 parameters calibrated in this step.

Channel	Source	Species	Experiment(s)	Temperature (K)	n	Extracellular (mM)			Pipette (mM)		
						Na^+	K^+	Ca^{2+}	Na^+	K^+	Ca^{2+}
I_{Na}	[69]	HL1-6	I-V, τ_{act}, τ_{inact}	room	12, 1, 1	140	4	2	10	130	1
	[63]	HL-1	γ_{inact}	room	19	145	0		10	0	
	[197]	HL-1	τ_{rec}	room		136	0		10	0	
I_{CaL}	[69]	HL1-6	I-V	room	7	140	4	2	10	130	1
	[64]	HL-1	γ_{inact}, τ_{inact}, τ_{rec}	room	8			5			
I_{CaT}	[65]	HL-1	I-V, γ_{inact}	room	9, 7			5			
	[198]	HL-1	τ_{rec}	room	19			5			
I_{Kr}	[199]	HL-1	I-V, τ_{act}, τ_{deact}	308	10		5.4			130	
			γ_{inact}, τ_{rec}	298	1, 4		5.4			130	
I_{to}	[200]	HL-1	I-V	room	9		4			145	
	[205]	mouse ventricle	τ_{act}, γ_{inact}	room	4, 7		4			135	
I_{ss}	[200]	HL-1	I-V	room	9		4			145	
	[205]	mouse ventricle	τ_{act}	room	4		4			135	
I_f	[62]	HL-1	I-V, τ_{act}	room	10, 50	140	25		10.8	120	
I_{K1}	[201]	HL-1	I-V	room			120			140	

Table 4.3: Experimental conditions for all data sources used in ion channel calibration. Blank entries were either not reported in the source, or were not required for simulation (i.e., the channel model did not depend on the value).

Parameter	Definition	Prior	Units
$K_{\mathrm{m,CaL}}$	Ca^{2+} dissociation constant for I_{CaL}	$\mathcal{U}(0,2)$	μM
$a^*_{\mathrm{inact,Ca}}$	Ca^{2+} dissociation rate for I_{CaL}	$\mathcal{U}(-3,0)$	1/ms
k_{NCX}	Scaling factor for Na^+-Ca^{2+} exchanger	$\mathcal{U}(0,20)$	pA/pF/μM^4
η	Voltage dependence of Na^+-Ca^{2+} exchanger	$\mathcal{U}(0,1)$	1
$I_{\mathrm{max,NaK}}$	Maximum current through Na^+-K^+ pump	$\mathcal{U}(0,5)$	pA/pF
V_{max}	Maximum SERCA flux	$\mathcal{U}(0,5)$	μM/ms
k^*_{RyR}	Scaling factor for ryanodine receptors	$\mathcal{U}(-2,1)$	1/ms
k_{open}	Opening rate for ryanodine receptors	$\mathcal{U}(0,10)$	1/ms
k_{close}	Closing rate for ryanodine receptors	$\mathcal{U}(0,1)$	1/ms
g_{pCa}	Conductance of Ca^{2+} pump	$\mathcal{U}(0,5)$	mS/μF
g^*_{Nab}	Conductance of background Na^+ current	$\mathcal{U}(-3,-1)$	mS/μF
g^*_{Cab}	Conductance of background Ca^{2+} current	$\mathcal{U}(-4,-2)$	mS/μF
$\mathrm{Buf}_{\mathrm{tot,i}}$	Concentration of cytosolic Ca^{2+} buffers	$\mathcal{U}(0,100)$	μM
$K_{\mathrm{m,Buf,i}}$	Half-dissociation constant of cytosolic Ca^{2+} buffers	$\mathcal{U}(0,2)$	μM

Table 4.4: Parameters calibrated in whole cell calibration step. * indicates that the prior was searched in $\log_{10}$-space.

In the whole cell calibration step, we incorporate the previously calibrated parameter posterior estimates for ion channels, but do not explicitly further refine them. Instead, in this stage, there are two sets of parameters: the parameters being calibrated, and ion channel parameters which are sampled but not included in the conventional ABC calibration process (see Section 3.2.3).

For each forward evaluation of the complete cell model during ABC, the final posterior particle population for every pre-calibrated channel is sampled and the resulting set of parameters combined with the whole cell parameter sample from Table 4.4. An additional parameter for membrane capacitance (C_m) is also sampled from a normal distribution according to experimental measurements in patched HL1-6 cells [69] (see Table 4.1).

The previously calibrated ion channel parameters (and capacitance parameter) are not constrained in this ABC step, instead being resampled from their respective distributions upon each model evaluation with the ABC algorithm. If during an iteration, a particle does not pass the acceptance criteria, these parameters are resampled from their distributions alongside the whole cell parameters (i.e. the iteration is not continuously attempted with the same sample of previously calibrated ion channel parameters).

The response of the whole cell model to two stimulus protocols was simulated to replicate conditions during experiments in HL1-6 myocytes [69]. In the first protocol, the cell

is left to reach steady-state for 100 s and the resting potential (V_{rp}) recorded. A series of 2 ms current stimulus pulses are then applied at a rate of 1 Hz, from 5 pA/pF to 40 pA/pF in steps of 5 pA/pF [69]. The final elicited action potential is recorded and measurements taken of action potential amplitude (V_{AMP}), maximum upstroke gradient ($\left(\frac{dV}{dt}\right)_{\mathrm{max}}$) and action potential duration to 90% repolarisation (APD_{90}). APD_{90} was measured as the time between the time of maximum upstroke gradient to the time when the transmembrane voltage had reduced from its peak by 90% of the action potential amplitude. It was also found necessary to include estimates of diastolic Ca^{2+} and amplitude of the Ca^{2+} transient in this protocol to constrain Ca^{2+} handling processes within physiological ranges. These estimates were taken from a mouse cell model [79], and their experimental uncertainty set equal to the largest experimental uncertainty (by proportion) to avoid overweighting these estimated values compared to real experimental measurements.

In the second protocol, the cell was again left to reach steady-state for 100 s after which the resting Ca^{2+} level was measured. A series of 101 current stimulus pulses of 40 pA/pF for 2 ms were applied at a rate of 1 Hz. The Ca^{2+} transient elicited during the final pulse was recorded and measurements taken of the Ca^{2+} transient time to peak ($\mathrm{CaT}_{\mathrm{t2p}}$), the amplitude ($\mathrm{CaT}_{\mathrm{amp}}$) and the time to 50% and 90% recovery ($\mathrm{CaT}_{\mathrm{r50}}$, $\mathrm{CaT}_{\mathrm{r90}}$). The recovery times were again measured from the time of maximum upstroke gradient in a similar fashion to the action potential duration. Similar estimates of diastolic Ca^{2+} and Ca^{2+} transient amplitude were included in the same manner as the first protocol.

Each protocol was simulated using the same conditions as in experiments. The action potential measurements were recorded under patch clamp at 296 K [69], and thus both extracellular and intracellular ion concentrations were prescribed. Intracellular Ca^{2+} was not fixed to allow sarcoplasmic reticulum release of Ca^{2+} in this experiment. The experiment measuring Ca^{2+} transients was carried out on a microelectrode array (to provide stimulation) with the cells in solution kept at 310 K [69] and therefore only extracellular concentrations were prescribed. The concentration of the Tyrode's solution for this experiment was taken from [209]. Table 4.5 summarises the conditions for each experiment.

In the whole cell calibration, conductance and kinetics of the model itself were adjusted

Experiment	T (K)	Extracellular (mM) Na^+	K^+	Ca^{2+}	Intracellular (mM) Na^+	K^+
Action potential [69]	296	140	4	2	10	130
Ca^{2+} transient [69]	310	140	4	2		

Table 4.5: Experimental conditions for whole cell calibration simulations.

Experiment	Measurement	Units	n	Mean	Standard deviation
Action potential [69]	V_{rp}	mV	25	-67	10
	V_{amp}	mV	11	105	6.6
	$\frac{dV}{dt}_{\text{max}}$	mV/ms	11	107	23.2
	APD_{90}	ms	7	42	23.8
	$\text{CaT}^*_{\text{diastole}}$	μM		0.1 [79]	
	$\text{CaT}^*_{\text{amp}}$	μM		0.5 [79]	
Ca^{2+} transient [69]	CaT_{t2p}	ms	6	59	4.9
	CaT_{r50}	ms	6	157	14.7
	CaT_{r90}	ms	6	397	34.3
	$\text{CaT}^*_{\text{diastole}}$	μM		0.1 [79]	
	$\text{CaT}^*_{\text{amp}}$	μM		0.5 [79]	

Table 4.6: Summary of experimental data for whole cell calibrations. * indicates an estimated value, where the standard deviation is set equal to the largest standard deviation from experimental measurements.

for temperature, rather than adjusting the data (as there would be no clear way to adjust the experimental measurements). To adapt the model for the different temperatures in each experiment, the conductance and time constants of ion channels were adjusted using Q_{10} values as described previously in Table 4.2.

Measures from the simulations were compared to experimental measurements summarised in Table 4.6. The same ABC distance function used in previous ABC calibration in this thesis was used with a regularisation factor (δ) of 0.2. This factor was found to be necessary to avoid significantly overweighting specific measurements due to the disparity in experimental uncertainty between measurements.

In patch clamp experiments of the hyperpolarisation-activated 'funny' current (I_{f}) in HL-1 myocytes, the current was measured in only ∼30% of cells [62]. As this current at least partially regulates automaticity in these cells [142], the pre-calibrated I_{f} current was not included in this whole cell calibration step. It was then reintroduced into 30% of the final samples of whole cell model posterior parameter estimates.

4.2.5 Sensitivity analysis

A sensitivity analysis was carried out to investigate the influence of key parameters on measurements of action potential and Ca^{2+} transients in the calibrated complete cell model. Parameters representing ion channel conductances (g_{Na}, g_{CaL}, g_{CaT}, g_{Kr}, g_{to}, g_{ss}, g_{K1}, g_{Nab}, g_{Nab}, k_{NCX}, $i_{NaK,max}$) and intracellular Ca^{2+} fluxes (k_{RyR}, V_{max}, k_{leak}) were included in the analysis. The analysis was completed for 50 random samples from the population of 1000 complete cell model parameterisations.

The sensitivity analysis is based on multivariable regression [210]. For each model parameterisation, the parameters above are varied by multiples drawn from a multivariable lognormal distribution with median of 1 and standard deviation of 0.05. The new model parameterisation is simulated under the same experiments used to calibrate the whole cell. After 500 repeats of this process with different samples from the lognormal distribution, the parameters and outputs are mean normalised and the output is regressed on the parameters resulting in a multivariable linear model. The regression coefficients provide a measure of the sensitivity of changes in a parameter value on a particular measurement from the experiment. For further details of the approach see [210].

4.2.6 Automaticity

The hyperpolarisation-activated 'funny' current (I_f) was not included in the initial whole cell calibration step. This was in order to generate a stable population of parameter variants with quiescent phenotype to avoid automaticity interfering with model measurements. In initial tests, it was found that including I_f at this stage would cause the calibration to converge on a parameterisation where the resting potential of the cell depends strongly on I_f.

The experimental data sets used in whole cell calibration [69] did not include specific characterisation of the occurrence of automaticity in the HL1-6 cell line. It is at least partly mediated by I_f, which 30% of cells in the original cell line were shown to express [62]. A specific study into automaticity in the original HL-1 cell line was used as the source of experimental conditions to test for automaticity [142]. In their study,

the authors noted that automaticity was more prevalent, and had a higher beat rate, in a cellular synctium. However, they also made measurements in single dissociated cells in the following experiment conditions: $[Na^+]_o = 145$ mM, $[K^+]_o = 4.0$ mM, $[Ca^{2+}]_o = 1.8$ mM, $[Na^+]_i = 14$ mM, $[K^+]_i = 120$ mM and $T = 296$ K.

An *in silico* protocol was generated to test for automaticity after the whole cell model had been calibrated. The protocol runs the cell model with no stimuli for 10 s to reach a steady state, and then a further 10 s of activity is recorded, again without any stimuli.

The I_{f} current in each of the 1000 model parameterisations from whole cell calibration was 'unblocked' and the model run using the protocol described above. The parameters for this channel were unchanged from whatever sample was selected from the whole cell calibration step.

The recording in the last 10 s of simulation was analysed to assess whether a cell model variant fired spontaneous action potentials. A parameterisation was rejected if action potentials were found not to fully repolarise ($\min(V_m) > -50$ mV), the minimum $[Ca^{2+}]_i$ exceeded 0.5 μM or the maximum $[Ca^{2+}]_i$ exceeded 1 μM, to keep results physiological.

4.2.7 Validation through ion channel blocking

The whole cell parameterisations, including those exhibiting automaticity, were validated by simulating the effects of blocking different sarcolemmal ion currents and intracellular Ca^{2+} fluxes. Simulations compared the effects of 20 μM TTX (I_{Na} current block), 10 μM Ivabradine (I_{f} current block), 1 μM Dofetilide (I_{Kr} current block), 10 μM Mibefrabil (I_{CaT} current block), 2 μM Nimodipine (I_{CaL} current block), 30 μM Ryanodine (J_{RyR} flux block) and 5 μM Thapsigargin (J_{SERCA} flux block). Simulations were compared to experiments conducted in spontaneously beating cells of the original HL-1 cell line [142] in the absence of more specific data for HL1-6. As the sub-clone is a less heterogeneous derivation of the original cell line, it would be expected that results between the two would be broadly similar.

Yang and Murray measured action potentials using current clamp on cells in a spontaneously beating synctium [142]. Under these conditions, the authors found two phenotypes

of beating cells: 'drivers' and 'followers'. The drivers constitute cells with a prolonged diastolic depolarisation, while the follower cells did not display this behaviour, and thus were likely beating due to propagating action potentials within the monolayer [142]. To replicate these conditions as closely as possible in the single cell model, cells were simulated using a protocol that applies no stimulating current for 20 s, followed by 20 s of stimulating at a rate of 1 Hz with a stimulus current 40 pA/pF with duration 0.5 ms. If action potentials were detected in the first 20 s after application of a blocking solution (i.e. the model exhibits spontaneous activity), action potentials in the last 5 s of this phase of the protocol were analysed. If the effect of the blocking solution inhibits spontaneous activity, the action potentials in response to the stimuli current are instead analysed. The second phase of the protocol serves to reproduce the fact that the non-beating cell in a monolayer may still be subject to stimulating currents from surrounding, beating cells.

4.3 Results

Results for the calibration of each ion channel model are shown as median lines with 89% highest posterior density interval (HPDI) indicated by shading [193]. Experimental data points plotted for comparison are given as mean with error bars (when available) indicating standard deviation.

4.3.1 Fast Na^+ current (I_{Na})

The model for the fast Na^+ current has three Hodgkin-Huxley gating variables for activation and fast/slow inactivation (x_{act}, $x_{inact,f}$, $x_{inact,s}$), as commonly used to model this channel since the work of Beeler and Reuter [211]. The activation and fast inactivation gates use the standardised formulae described previously. To reduce the dimensionality of the calibration problem, the steady-state equations of both inactivation gates are the same, and the time constant for the slow inactivation gate is a constant multiple of the fast inactivation time constant at all membrane potentials (i.e. $\tau_{inact,s} = A\tau_{inact,f}$ where A is a constant). This is consistent with handling of the standardised model of I_{Na} in

Chapter 3.

Three independent data sets are used to calibrate the fast Na^+ channel. The I-V curve is measured from HL1-6 cells [69] while the inactivation curve is measured in the original HL-1 cell line [63], as is the recovery curve [197].

To include data for time constants of activation and inactivation, a representative peak current trace is extracted from the I-V experiment (Figure 6a in [69]), and normalised. The activation and inactivation portions of each trace are fit to exponential functions (activation: $(1 - e^{-t/\tau})^3$, inactivation: $e^{-t/\tau}$ where t is time and τ is the time constant). In calibration, these values are then extracted from the peak current during the I-V experiment.

The I-V curve for the fast Na^+ channel in HL1-6 myocytes from [69] showed a reversal potential of the channel at approximately +25 mV. This was substantially different from the expected reversal potential of a Na^+-selective channel given the solution concentrations in the extracellular and pipette solution during the patch clamp experiments (extracellular: 140 mM Na^+, pipette: 10 mM Na^+, temperature: 296 K [69] would give a Nernst equilibrium potential of approximately +67 mV). In [69], the authors gave two possible reasons for their finding: the HL1-6 clone could express a splice variant of the SCN5A gene encoding $Na_{v1.5}$, or the clone possesses Na^+ channels which are not fully developed to adult phenotype and are closer to an embryonic phenotype. A loss of the highly Na^+-selective nature typical of cardiac Na^+ channels could be a consequence of either of these explanations. To account for the difference between the reversal potential and predicted Nernst potential, the channel model includes a parameter for relative permeability to K^+ ions and thus the reversal potential is mediated by a balance between the Nernst potentials of Na^+ and K^+ in each experiment.

The final model for the fast Na^+ current is

$$I_{\mathrm{Na(Na)}} = g_{\mathrm{Na}} x_{\mathrm{act}}^3 x_{\mathrm{inact,f}} x_{\mathrm{inact,s}} (V - E_{\mathrm{Na}}), \tag{4.12}$$

$$I_{\mathrm{Na(K)}} = g_{\mathrm{Na}} \frac{P_K}{1 + P_K} x_{\mathrm{act}}^3 x_{\mathrm{inact,f}} x_{\mathrm{inact,s}} (V - E_{\mathrm{K}}), \tag{4.13}$$

$$I_{\mathrm{Na}} = I_{\mathrm{Na(Na)}} + I_{\mathrm{Na(K)}}, \tag{4.14}$$

where g_{Na} is the conductance of the current (mS/μF), P_K is the relative permeability to K^+ (dimensionless) and E_{X} are the Nernst potentials for each ion X (mV).

Parameters for each gate, the slow inactivation gate time constant multiple, the channel conductance and the relative K^+ permeability are calibrated to experimental data using an ABC particle population of 2000 particles. The calibration was run until the acceptance rate dropped below 0.25%. To account for the high uncertainty in peak measurements in the I-V curve [69], the distance function regularisation parameter (δ) was increased to 0.2.

Figure 4.1 shows the calibrated I_{Na} model compared to the experimental data sets. The channel model reflects the experimental data well across all calibration experiments, with little variability apparent in the model output. The calibrated parameter distributions are summarised in Table A.21 in the Appendix. All parameter posterior distributions have low relative standard deviation (RSD) values (the metric used to assess the width of the posterior distributions in Chapter 3), indicating they are well constrained by the data.

4.3.2 L-type Ca^{2+} current (I_{CaL})

The model for L-type Ca^{2+} current has voltage-dependent activation and inactivation gates (x_{act}, x_{inact}). Both are described using the standardised Hodgkin-Huxley gating formulations. In contrast to the human atrial cells considered in Chapter 3, the L-type Ca^{2+} channel data for HL1-6 or HL-1 myocytes showed no evidence for a fast and slow component of inactivation, so only a single voltage-dependent inactivation gate is included. This current also exhibits Ca^{2+}-dependent inactivation ($x_{\mathrm{inact,Ca}}$) which is modelled using a simple formulation [83], and assumes that the two modes of inactivation are independent.

The L-type Ca^{2+} channel is highly-selective to Ca^{2+} ions. However, the observed reversal potential of the current is displaced from what would be expected given ideal Nernst equilibrium. Thus, most models either adopt permeability to other ions (e.g. [85, 87, 212]), set to a constant value (e.g. [79, 83, 165, 166]), or use more complex formulations (e.g. [207, 213, 214]). In this model, a constant value is set for the reversal potential

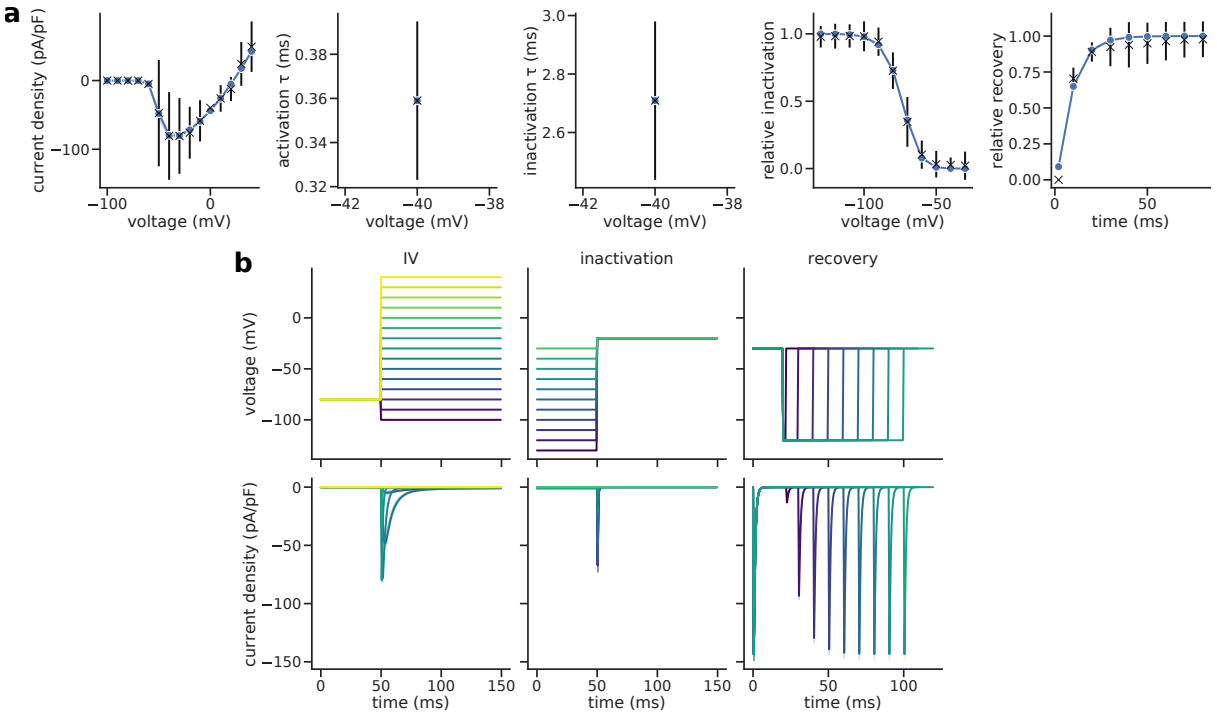


Figure 4.1: **a** Simulated output of fast Na^+ channel model compared to experimental results [63, 69, 197] adjusted for temperature as described in the text. **b** Current traces generated by the fast Na^+ channel model from each experiment. Upper row shows the voltage protocol (cropped to region of interest) and lower row shows the model current response. All model results are displayed as median lines with shading indicating 89% HPDI. Experimental results are shown as mean with errors bars indicating standard deviations.

assuming perfect selectivity for Ca^{2+} ions. It may be difficult to formulate the reversal potential as a relationship between ion concentrations due to the more complex interaction of the channel with ions and other ion channels [83].

The model for I_{CaL} is given as

$$I_{\mathrm{CaL}} = g_{\mathrm{CaL}} x_{\mathrm{act}} x_{\mathrm{inact}} x_{\mathrm{inact,Ca}} (V - E_{\mathrm{CaL}}), \tag{4.15}$$

$$\frac{dx_{\mathrm{inact,Ca}}}{dt} = \frac{\gamma_{\mathrm{inact,Ca}} - x_{\mathrm{inact,Ca}}}{\tau_{\mathrm{inact,Ca}}}, \tag{4.16}$$

$$\gamma_{\mathrm{inact,Ca}} = \left(1 + \frac{[\mathrm{Ca}^{2+}]_i}{K_{\mathrm{m,CaL}}}\right)^{-1}, \tag{4.17}$$

$$\tau_{\mathrm{inact,Ca}} = \frac{\gamma_{\mathrm{inact,Ca}}}{a_{\mathrm{inact,Ca}}}, \tag{4.18}$$

where g_{CaL} is the channel conductance (mS/μF), E_{CaL} is the reversal potential (mV), $[\mathrm{Ca}^{2+}]_i$ is the cytosolic Ca^{2+} concentration (μM), $K_{\mathrm{m,CaL}}$ is the dissociation constant for the channel (μM) and $a_{\mathrm{inact,Ca}}$ is the dissociation rate (ms^{-1}).

The channel is calibrated to two independent data sets. The I-V curve was measured in HL1-6 cells [69]. Although the authors did not specify which Ca^{2+} current was measured, it can be inferred from the holding potential of the voltage-clamp protocol to be L-type Ca^{2+} current (T-type Ca^{2+} currents would be inactivated at the voltage range used). The second data set is composed of voltage-dependent inactivation and recovery in the original HL-1 cell line, and includes measurements of inactivation time constants at three potentials [64].

Voltage-dependent gating parameters, conductance and reversal potential are calibrated to these data. Due to the paucity of available data for Ca^{2+}-dependent inactivation in HL1-6 or HL-1, the parameters underlying this gate were held fixed to the original values in [83] for the channel calibration. $a_{\text{inact,Ca}}$ and $K_{\text{m,CaL}}$ were subsequently calibrated in the whole cell calibration step. The ABC calibration for this channel was run using 2000 particles until the acceptance rate dropped below 0.5%. To account for the high uncertainty in the I-V curve data [69] relative to other experiments, the distance function used a regularisation factor of $\delta = 0.2$ in the error weighting.

Figure 4.2a shows the output of the calibrated model compared to experimental data. The model mostly follows the calibration within the experimental uncertainty. At higher voltages of the inactivation curve (second plot in Figure 4.2a) the model appears to plateau before reaching zero. This discrepancy would be diminished in the complete cell model as the Ca^{2+}-dependent inactivation process also inactivates the channel. Figure 4.2b shows there is more uncertainty around current traces than for I_{Na} which could be a consequence of higher experimental uncertainty.

The parameter posterior results for I_{CaL} are summarised in Table A.22. Parameter posterior distributions have low RSD values except for parameters underlying the activation gate. This reflects the lack of experimental data specific to the activation gate of this channel other than the I-V experiment.

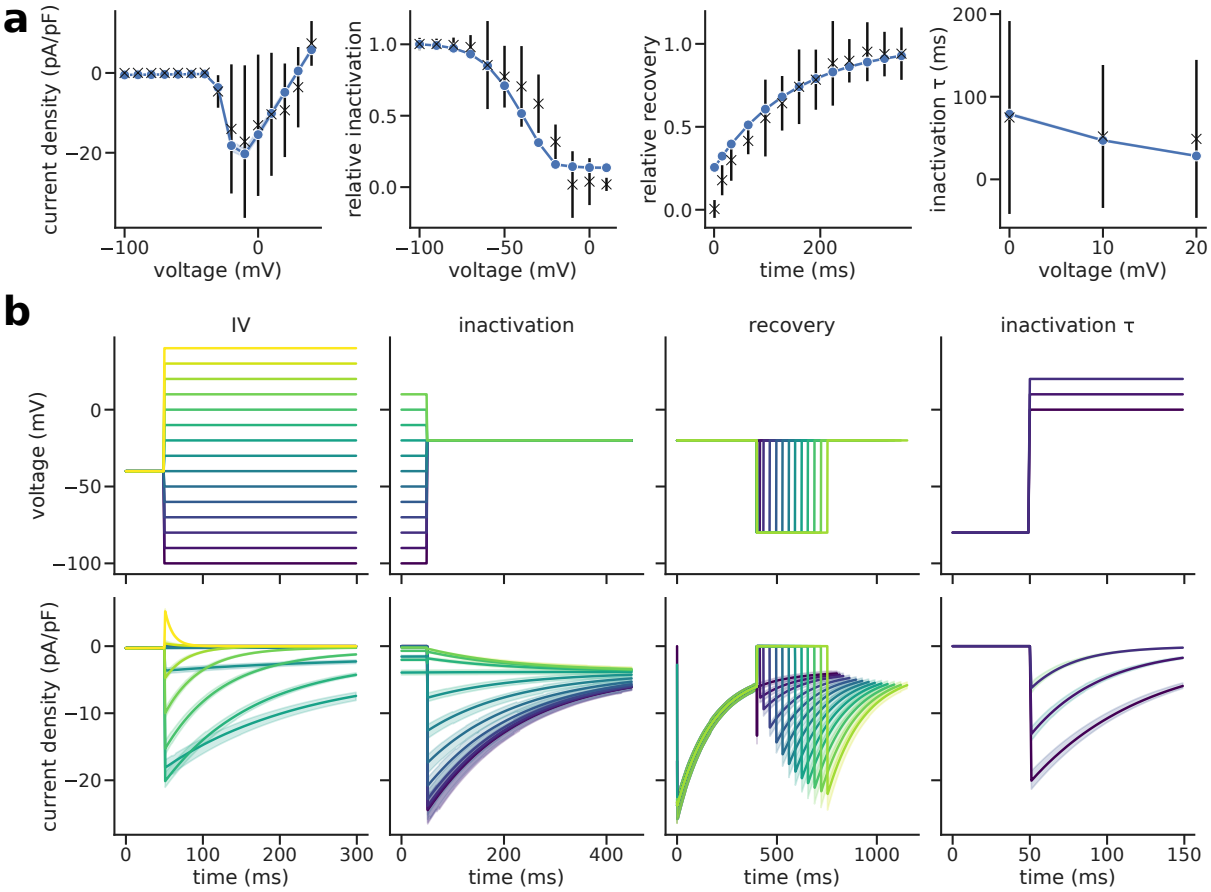


Figure 4.2: **a** Simulated output from the calibrated L-type Ca^{2+} current model compared to experimental results [64,69] adjusted for temperature as described in the text. **b** Current traces generated by the L-type Ca^{2+} current model from each experiment. Upper row shows the voltage protocol (cropped to region of interest) and lower row shows the model current response. All model results are displayed as median lines with shading indicating 89% HPDI. Experimental results are shown as mean with errors bars indicating standard deviations.

4.3.3 T-type Ca^{2+} current (I_{CaT})

The T-type Ca^{2+} current activates at a lower voltage and inactivates at a faster rate compared to the L-type Ca^{2+} current. It is predominantly expressed in cardiomyocytes originating from the atria or sino-atrial node, and expressed by atrial-derived HL-1 myocytes [198]. In HL-1 myocytes, it has been characterised as the dominant Ca^{2+} current [65, 215].

The channel is modelled with single voltage-dependent activation and inactivation gates (x_{act}, x_{inact}). As with the L-type Ca^{2+} channel, there is a large potential offset between the Nernst Ca^{2+} potential and the reversal potential for this channel. Following the same logic as above, a prescribed reversal potential is calibrated as an additional parameter rather than using an offset to the Nernst potential (e.g. [214]) or more complex formulation.

The I_{CaT} model is described as

$$I_{CaT} = g_{CaT} x_{act} x_{inact} (V - E_{CaT}), \tag{4.19}$$

where g_{CaT} is the channel conductance (mS/μF) and E_{CaT} (mV) is the prescribed reversal potential.

The channel model is calibrated to two experimental data sources, both of which were measured from the original HL-1 cell line. The first data set measured an I-V curve and relative inactivation of the channel [65], and the second included measurements of the recovery kinetics of the channel [198]. A population of 1000 particles was used in the ABC calibration and run until the acceptance rate dropped below 0.5%.

Figure 4.3 compares the calibrated model to experimental data. There is little variability in the output of the model in any experiment, and the underlying parameter posterior distributions are all tightly constrained (Table A.23).

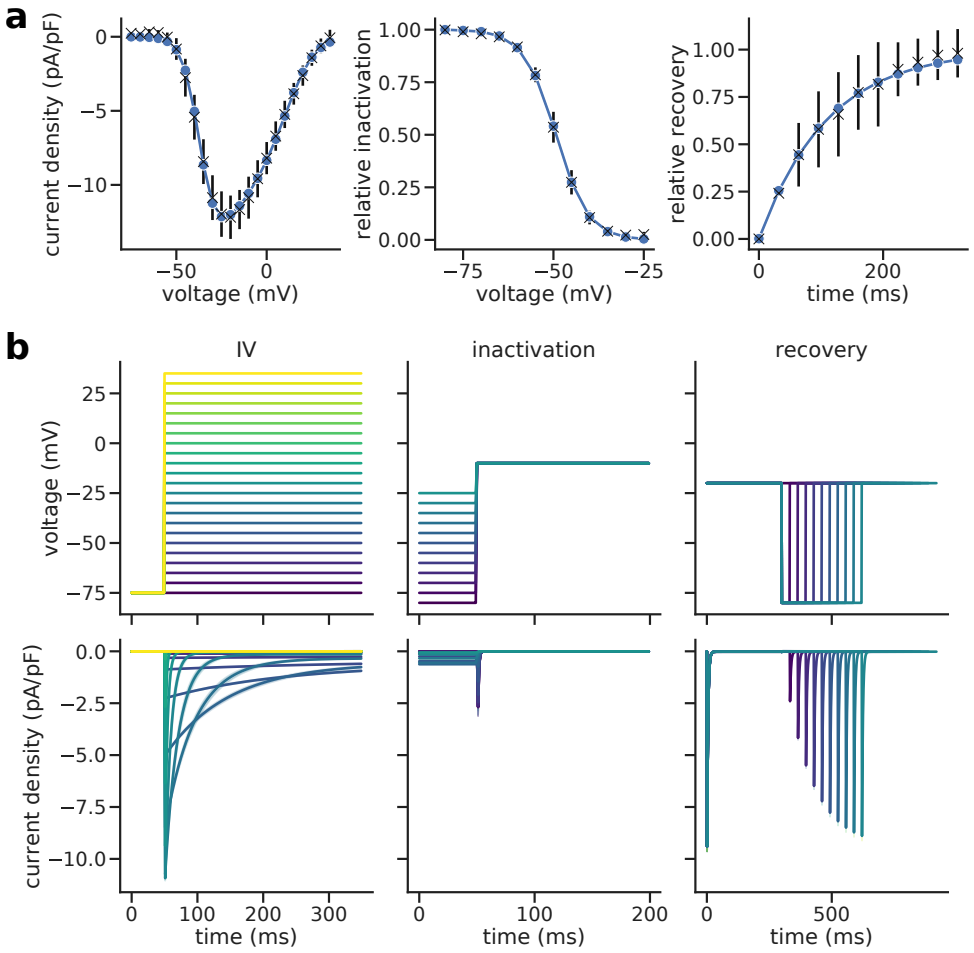


Figure 4.3: **a** Simulated output from the calibrated T-type Ca^{2+} current model compared to experimental results [65, 198]. **b** Current traces generated by the T-type Ca^{2+} current model from each experiment. Upper row shows the voltage protocol (cropped to region of interest) and lower row shows the model current response. All model results are displayed as median lines with shading indicating 89% HPDI. Experimental results are shown as mean with errors bars indicating standard deviations.

4.3.4 Rapidly-activating delayed rectifier K^+ current (I_{Kr})

Cardiac delayed rectifier K^+ currents are composed of two components in most mammalian cells, rapidly- and slowly-activating. HL-1 cells predominantly express the rapid component [199, 216]. Slowly-activating delayed rectifier K^+ current (I_{Ks}) was rarely seen in measurements of the original HL-1 cell line [199, 200], and is therefore not included in the model.

The rapid delayed rectifier current is modelled as

$$I_{Kr} = g_{Kr}\sqrt{\frac{[K^+]_o}{5400}}x_{act}x_{inact}(V - E_K), \tag{4.20}$$

where g_{Kr} is the channel conductance (mS/μF), $[K^+]_o$ is the extracellular K^+ concentration (μM) and E_K is the Nernst potential for K^+ (mV). The dependence on $[K^+]_o$ is retained from previous models of the channel [84, 87, 207, 214].

Toyoda et al. [199] thoroughly characterised the rapidly-activating delayed rectifier current in the original HL-1 cell line. The model is calibrated to their data consisting of an I-V curve, measurements of activation and deactivation time constants, inactivation curve, and recovery time constants. ABC calibration was run with a population of 2000 particles until the acceptance rate fell under 0.5%.

The calibrated model output is compared to experimental data in Figure 4.4. The model compares well to experimental data, with low variability across different behaviours of the channel. The model doesn't appear to peak at the same point as the data in the activation time constant experiment (second plot of Figure 4.4a), though there is large uncertainty in the data's peak value. The calibrated parameters are summarised in Table A.24.

4.3.5 4-AP-sensitive K^+ currents (I_{to}, I_{ss})

Two outward K^+ currents sensitive to 4-Aminopyridine (4-AP) are present in the original HL-1 cell line, a transient outward current (I_{to}) and a non-inactivating steady-state current (I_{ss}) [200, 217–219]. This is consistent with observations of mouse atrial cardiomy-

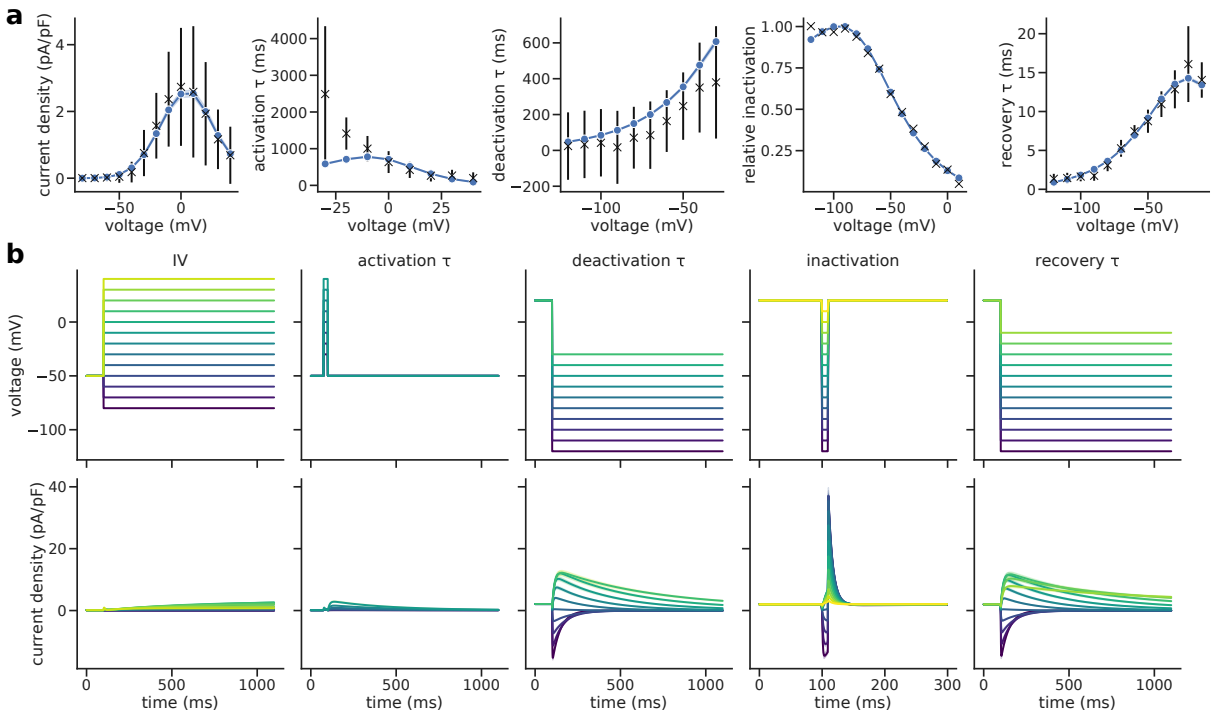


Figure 4.4: **a** Simulated output from the calibrated delayed rectifier potassium current model compared to experimental results [199] adjusted for temperature as described in the text. **b** Current traces generated by the delayed rectifier potassium current model from each experiment. Upper row shows the voltage protocol (cropped to region of interest) and lower row shows the model current response. All model results are displayed as median lines with shading indicating 89% HPDI. Experimental results are shown as mean with errors bars indicating standard deviations.

ocytes [220–222], from which the HL-1 cell line is originally derived [60].

The transient outward current model has one activation and one inactivation gate whereas the steady-state current only has an activation gate. The models are described as

$$I_{\text{to}} = g_{\text{to}} x_{\text{act}} x_{\text{inact}} (V - E_{\text{K}}), \tag{4.21}$$

$$I_{\text{ss}} = g_{\text{ss}} x_{\text{act}} (V - E_{\text{K}}), \tag{4.22}$$

where g are channel conductances (mS/μF) and E_{K} is the Nernst potential for K^+ (mV).

The models are individually calibrated to I-V curve data gathered in the original HL-1 cell line [200]. Due to a lack of data on rate of activation/inactivation in HL-1 cells, the models are also calibrated to time constant measurements of the channels in mouse ventricular myocytes [205], which exhibit the same phenotype as mouse atrial myocytes [220, 221]. ABC calibration was run with a particle population of 2000 for I_{to}

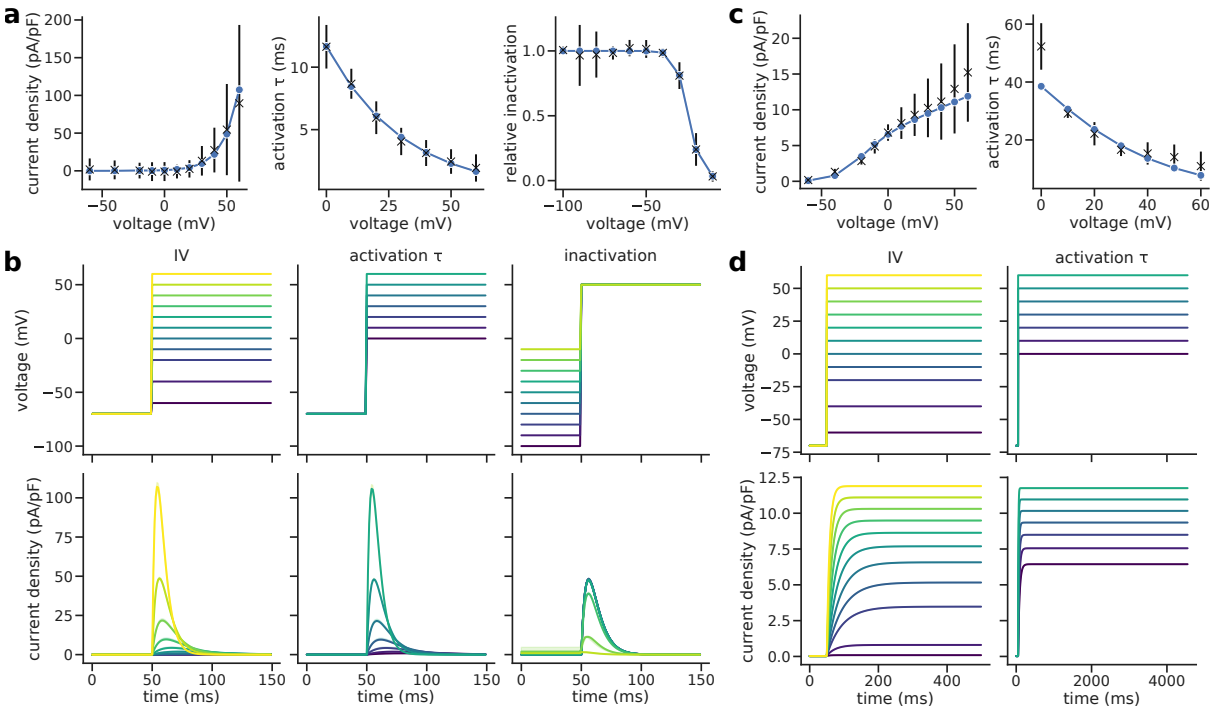


Figure 4.5: **a & c** Simulated output from the calibrated transient outward K^+ current (a) and steady-state current model (c) compared to experimental results [200, 205]. **b & d** Current traces generated by each model (b: I_{to}, d: I_{ss}) in response to each experiment. Upper row shows the voltage protocol (cropped to region of interest) and lower row shows the model current response. All model results are displayed as median lines with shading indicating 89% HPDI. Experimental results are shown as mean with errors bars indicating standard deviations.

and 1000 for I_{ss}, both until the acceptance rate dropped below 0.5%.

Figure 4.5 shows the calibrated models for both currents. Both currents follow the experimental data closely in the areas of behaviour tested and appear to have little variability in their output. Analysis of the posterior parameter distributions (Tables A.25 and A.26) reveal that a portion of parameters governing the activation of I_{to}, including the conductance, exhibit more variability than the model output in these experimental conditions suggest, whereas the I_{ss} model appears well constrained by the available data.

4.3.6 Hyperpolarisation-activated 'funny' current (I_f)

The original HL-1 cell line expressed the hyperpolarisation-activated 'funny' current [62] in approximately 30% of cells tested. In these cells, it appeared to be moderately involved in automaticity and slowed spontaneous beat rate when pharmacologically blocked [142].

The model is described with a single activation gate (that activates when hyperpolarised rather than depolarised) and permeability to both Na^+ and K^+ ions as common

in models of this channel [79, 83, 84, 87, 207, 214]:

$$I_{\mathrm{f(Na)}} = g_{\mathrm{f}} \kappa x_{\mathrm{act}} (V - E_{\mathrm{Na}}), \tag{4.23}$$

$$I_{\mathrm{f(K)}} = g_{\mathrm{f}} (1 - \kappa) x_{\mathrm{act}} (V - E_{\mathrm{K}}), \tag{4.24}$$

$$I_{\mathrm{f}} = I_{\mathrm{f(Na)}} + I_{\mathrm{f(K)}}, \tag{4.25}$$

where g_{f} is the channel conductance (mS/μF), κ mediates the proportion of Na^+/K^+ current through the channel (dimensionless) and E_{ion} are Nernst potentials for each ion (mV). The activation gate is described using the standardised Hodgkin-Huxley form for an *inactivation* gate as the current is activated in the opposite voltage direction to 'normal' sarcolemmal currents.

The model is calibrated to data obtained from the original HL-1 cell line [62]. The data set includes an I-V curve, steady-state activation and activation time constants measured across a range of voltages. The ABC calibration was run with a population of 500 particles until the acceptance rate dropped under 0.5%.

Figure 4.6a-b show the output of the simulated model compared to experimental data. The model follows the experimental data closely and remains within experimental error bars. The current density appears to reduce in comparison to experiments at low voltage ranges (first plot in Figure 4.6a), though the experimental data also exhibits greater uncertainty in this region. Analysis of the parameter posterior distributions (Table A.27) reveals that the RSD values are very low, suggesting the ABC calibration may have collapsed onto a single value. Repeated runs with increased particle population numbers (which may be expected to reduce this effect) gave a similar result, so this parameterisation was retained.

4.3.7 Inward rectifier K^+ current (I_{K1})

The inward rectifier K^+ current is modelled as

$$I_{\mathrm{K1}} = g_{\mathrm{K1}} \sqrt{\frac{[\mathrm{K}^+]_o}{5400}} \gamma_{\mathrm{act}} (V - E_{\mathrm{K}}), \tag{4.26}$$

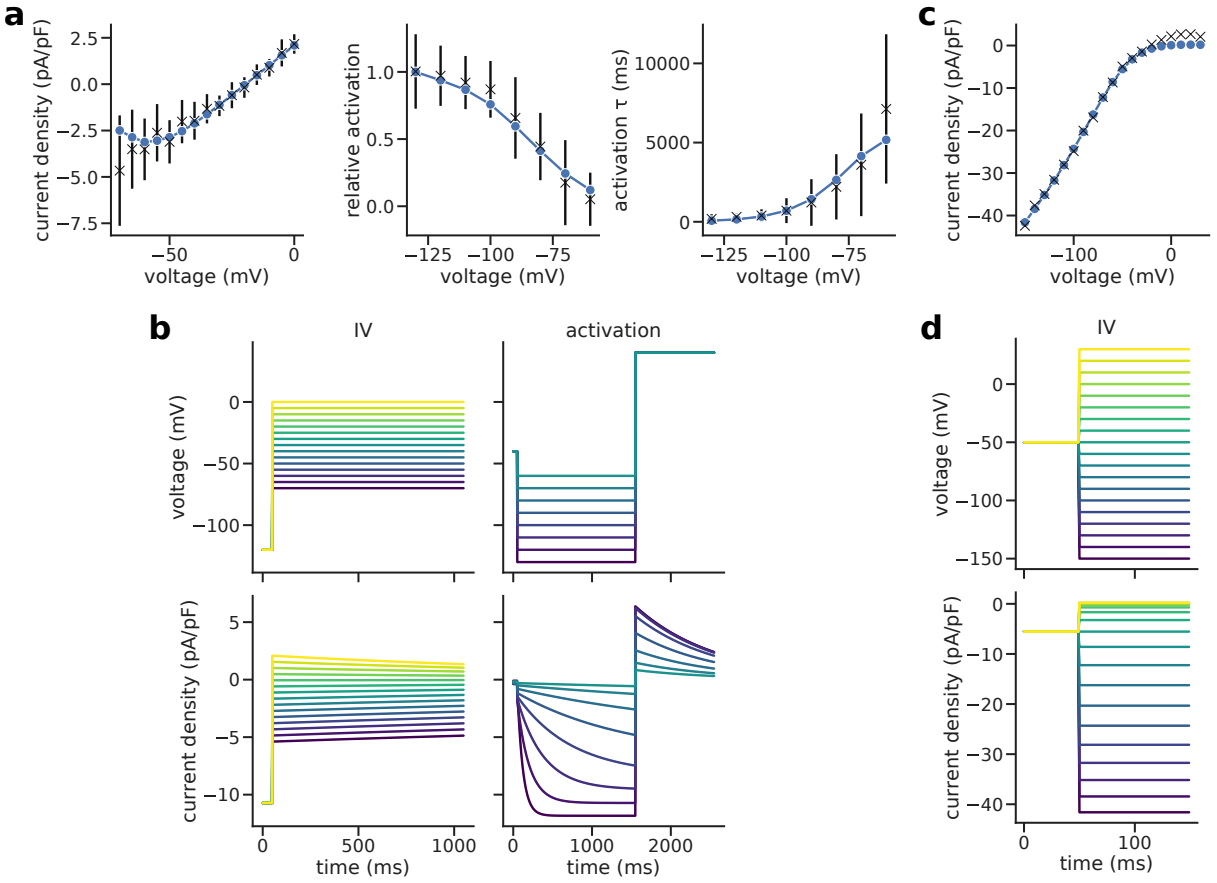


Figure 4.6: **a** Simulated output from the calibrated 'funny' current model compared to experimental results of I-V curve, steady-state activation and activation time constants [62]. **b** Current traces of the 'funny' current in response to each experiment. The activation curve and time constants are measured from the same experiment. **c** Simulated output of the calibrated model for the inward rectifying K^+ current compared to experimental data [201]. **d** Current traces of the inward rectifying K^+ current in response to the voltage protocol from the experiment. In b and d, the upper row shows the voltage protocol (cropped to region of interest) and lower row shows the model current response. All model results are displayed as median lines with shading indicating 89% HPDI. Experimental results are shown as mean with errors bars indicating standard deviations.

where g_{K1} is the channel conductance (mS/μF), $[K^+]_o$ is the extracellular K^+ concentration (μM), γ_{act} is the steady-state portion of a standardised activation gate (dimensionless) and E_K is the K^+ Nernst potential (mV).

The dependence on extracellular K^+ concentration is retained from previous models of this channel [87, 207]. The formulation assumes that the current reaches steady-state instantaneously, consistent with the very quick activation in HL-1 cells [201] and previous model formulations [79, 84, 87, 207, 214]. The conductance and gating parameters are calibrated to an I-V curve generated from recordings of the original HL-1 cell line [201]. These experiments were carried out with high K^+ concentration in the extracellular solution (120 mM), resulting in an elevated reversal potential for the current around -4 mV, evident from the data points in Figure 4.6c. The ABC calibration used a population of 1000 particles and was run until less than 0.5% samples were accepted in an iteration.

Figure 4.6c-d show output of the calibrated model compared to the single experiment. No error bars were provided in the experimental data though, regardless, the model follows experimental data points very closely. This appears to be a consequence of the well constrained conductance parameter as the other parameters exhibited higher RSD values (Table A.28).

4.3.8 Background currents (I_{Nab}, I_{Cab})

Na^+ and Ca^{2+} background currents regulate the resting potential of the cell, and are modelled as linear ohmic currents:

$$I_{Nab} = g_{Nab}(V - E_{Na}), \tag{4.27}$$

$$I_{Cab} = g_{Cab}(V - E_{Ca}), \tag{4.28}$$

The conductance of both currents (g_{Nab}, g_{Cab}) (mS/μF) were included in the whole cell calibration step.

4.3.9 Sarcolemmal pump and exchanger currents ($I_{\mathbf{NCX}}$, $I_{\mathbf{NaK}}$, $I_{\mathbf{pCa}}$)

The sarcolemmal Ca^{2+} pump (I_{pCa}) is simplified from a mouse ventricular model [79]:

$$I_{\mathrm{pCa}} = g_{\mathrm{pCa}} \left(1 + \frac{K_{\mathrm{m,pCa}}}{[\mathrm{Ca}^{2+}]_i}\right)^{-1}, \tag{4.29}$$

where g_{pCa} is the channel conductance (mS/μF), $K_{\mathrm{m,pCa}}$ is the dissociation constant of the channel (μM) and $[\mathrm{Ca}^{2+}]_i$ is the cytosolic Ca^{2+} concentration (μM). The Na^+-K^+ pump current is also modelled using a formulation from the same mouse ventricular model [79]:

$$I_{\mathrm{NaK}} = I_{\mathrm{NaK,max}} \frac{f_{\mathrm{NaK}}}{\left(1 + \left({}^{K_{\mathrm{m,Nai}}}/_{[\mathrm{Na}^+]_i}\right)^{n_{\mathrm{NaK}}}\right)\left(1 + {}^{K_{\mathrm{m,Ko}}}/_{[\mathrm{K}^+]_o}\right)}, \tag{4.30}$$

$$f_{\mathrm{NaK}} = \left(1 + 0.1245\mathrm{e}^{-0.1\frac{VF}{RT}} + 0.0365\sigma\mathrm{e}^{-\frac{VF}{RT}}\right)^{-1}, \tag{4.31}$$

$$\sigma = 1/7\left(\mathrm{e}^{{}^{[\mathrm{Na}^+]_o}/_{67300}} - 1\right), \tag{4.32}$$

where $I_{\mathrm{NaK,max}}$ is the maximum current (pA/pF), $K_{\mathrm{m,ion}}$ are dissociation constants for intracellular Na^+ ($[\mathrm{Na}^+]_i$) or extracellular K^+ ($[\mathrm{K}^+]_o$) (μM) and n_{NaK} is the Hill coefficient for intracellular Na^+ (dimensionless). The Na^+-Ca^{2+} exchange current is formulated using a simplified version of the mouse ventricular model [79] and the same as used in a model of neonatal rat ventricular myocytes [84]:

$$I_{\mathrm{NCX}} = k_{\mathrm{NCX}} \times 10^{-16} \frac{[\mathrm{Na}^+]_i^3[\mathrm{Ca}^{2+}]_o\mathrm{e}^{\eta\frac{VF}{RT}} - [\mathrm{Na}^+]_o^3[\mathrm{Ca}^{2+}]_i\mathrm{e}^{(\eta-1)\frac{VF}{RT}}}{1 + d_{\mathrm{NCX}}\left([\mathrm{Na}^+]_o^3[\mathrm{Ca}^{2+}]_i + [\mathrm{Na}^+]_i^3[\mathrm{Ca}^{2+}]_o\right)}, \tag{4.33}$$

where k_{NCX} is a scaling constant for the current (dimensionless), η controls the voltage dependence of the current (dimensionless) and d_{NCX} is a denominator constant (dimensionless).

Data was not available to calibrate directly to each of these currents, so a subset of their parameters were calibrated in the final whole cell calibration step: g_{pCa}, $I_{\mathrm{NaK,max}}$, k_{NCX} and η.

4.3.10 Sarcoplasmic reticulum fluxes ($J_{\mathbf{RyR}}$, $J_{\mathbf{SERCA}}$, $J_{\mathbf{leak}}$, $J_{\mathbf{tr}}$)

Ca^{2+} handling in the sarcoplasmic reticulum of HL1-6 cells has not been experimentally characterised. The cells have similar immature morphology to neonatal cells [60,69] without the T-tubule structure that would be found in more developed cells. The model therefore adopts a simplified version of Ca^{2+} handling from a model of neonatal rat ventricular myocytes [84].

The formulation for Ca^{2+} uptake to the sarcoplasmic reticulum through SERCA pump (J_{SERCA}), release through ryanodine receptors (J_{RyR}), leak flux from the uptake compartment of the sarcoplasmic reticulum (J_{leak}) and flux between the uptake and release compartments (J_{tr}) are adopted from that model:

$$J_{\mathrm{SERCA}} = V_{\max}\frac{([\mathrm{Ca}^{2+}]_i/K_{\mathrm{m,f}})^H - ([\mathrm{Ca}^{2+}]_{\mathrm{SR,up}}/K_{\mathrm{m,r}})^H}{1 + ([\mathrm{Ca}^{2+}]_i/K_{\mathrm{m,f}})^H - ([\mathrm{Ca}^{2+}]_{\mathrm{SR,up}}/K_{\mathrm{m,r}})^H}, \tag{4.34}$$

$$J_{\mathrm{leak}} = k_{\mathrm{leak}}\left([\mathrm{Ca}^{2+}]_{\mathrm{SR,up}} - [\mathrm{Ca}^{2+}]_i\right), \tag{4.35}$$

$$J_{\mathrm{tr}} = \frac{[\mathrm{Ca}^{2+}]_{\mathrm{SR,up}} - [\mathrm{Ca}^{2+}]_{\mathrm{SR,rel}}}{\tau_{\mathrm{tr}}}, \tag{4.36}$$

$$J_{\mathrm{RyR}} = k_{\mathrm{RyR}}P_{\mathrm{open}}\left([\mathrm{Ca}^{2+}]_{\mathrm{SR,rel}} - [\mathrm{Ca}^{2+}]_i\right), \tag{4.37}$$

$$\frac{dP_{\mathrm{open}}}{dt} = P_{\mathrm{closed}}k_{\mathrm{open}}\left(1 + \left(\frac{K_{\mathrm{m,RyR}}}{[\mathrm{Ca}^{2+}]_i}\right)^4\right)^{-1} - k_{\mathrm{close}}P_{\mathrm{open}}, \tag{4.38}$$

$$P_{\mathrm{closed}} = 1 - P_{\mathrm{open}}, \tag{4.39}$$

$$K_{\mathrm{m,RyR}} = 3.51\left(1 + \mathrm{e}^{\left([\mathrm{Ca}^{2+}]_{\mathrm{SR,rel}} - 530\right)/200}\right)^{-1} + 0.25. \tag{4.40}$$

The transfer time constant (τ_{tr}) is adjusted to 20 ms, the value used in a mouse ventricular myocyte model [79], instead of the original value in the rat neonatal myocyte model to better represent the same species HL-1 originates from. Maximum SERCA flux ($V_{\max}$), ryanodine receptor scaling constant (k_{RyR}) and the opening and closing rates of the ryanodine receptors (k_{open}, k_{close}) were included in the whole cell calibration.

4.3.11 Channel gating functions

Figure 4.7 shows the gating functions for the eight channel models calibrated using ABC. Figure 4.8 compares the relative standard deviations (RSD) for parameter posterior distributions of each channel.

For I_{Na}, I_{CaT}, I_{Kr}, I_{ss} and I_{f}, the small variability in the 'summary statistic' model output from the previous results is representative of the small variability in the underlying functions. In contrast, for I_{CaL} and I_{to}, the small variability in the 'summary statistic' model output masks the underlying uncertainty in gating functions. This is apparent from the wide shaded regions around τ_{act} in I_{CaL} and the activation gate of I_{to}, as well as the corresponding parameters having RSDs higher than comparable channels (Figure 4.8).

I_{K1} exhibits unique results amongst the channels considered in that there is little variability in either the model output or gating function despite the high RSDs in all but the conductance parameter for this channel. The structure of the standardised equations in this case may in turn be too complex to model a single steady-state activation gate.

4.3.12 Complete cell calibration

The remaining set of parameters (Table 4.4) in the complete cell model were next calibrated, using the individual channel parameter posterior distributions as 'extra' parameters during the calibration process. ABC was run until the acceptance rate dropped below 0.5%. Due to computational limitations by more expensive simulations of the full cell, ABC was run using 1000 particles.

To generate a population of model parameterisations for analysis after calibration, a final rejection sampling step was carried out by sampling from all parameter posterior distributions (channels and complete cell) and accepting only those simulations of the complete cell experiments which resulted in a residual from experimental data less than the final threshold in the complete cell ABC calibration. A population of 1000 model parameterisations was generated in this way for the analyses below.

Figures 4.9 and 4.10 compare simulated measurements to the experimental measurements used to calibrate the complete cell (summarised above in Table 4.6). The ex-

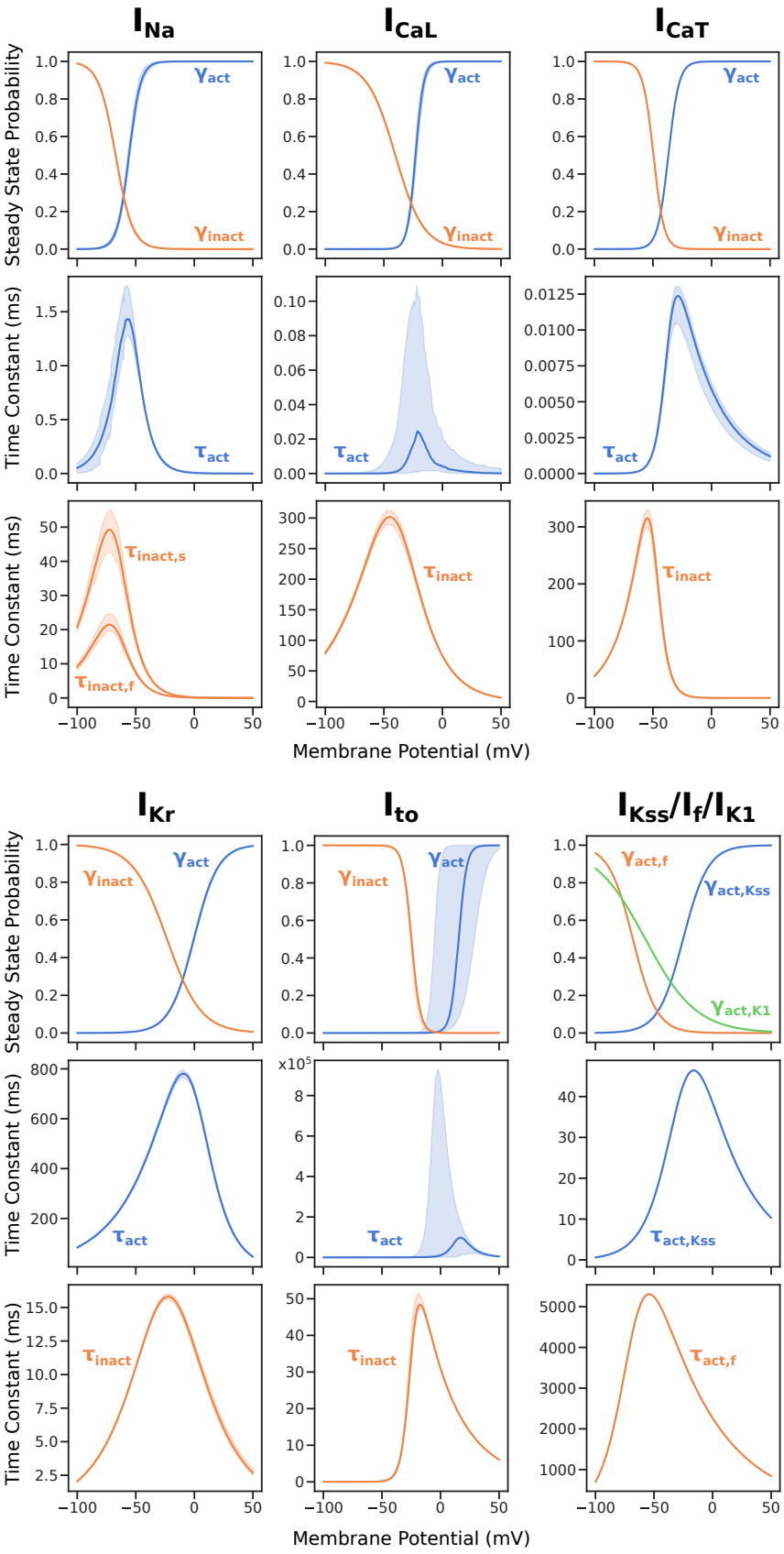


Figure 4.7: Steady-state probabilities and time constants for each calibrated channel. Results are generated from 100 samples from each parameter posterior distribution, and summarised as median line with shading indicated 89% HPDI.

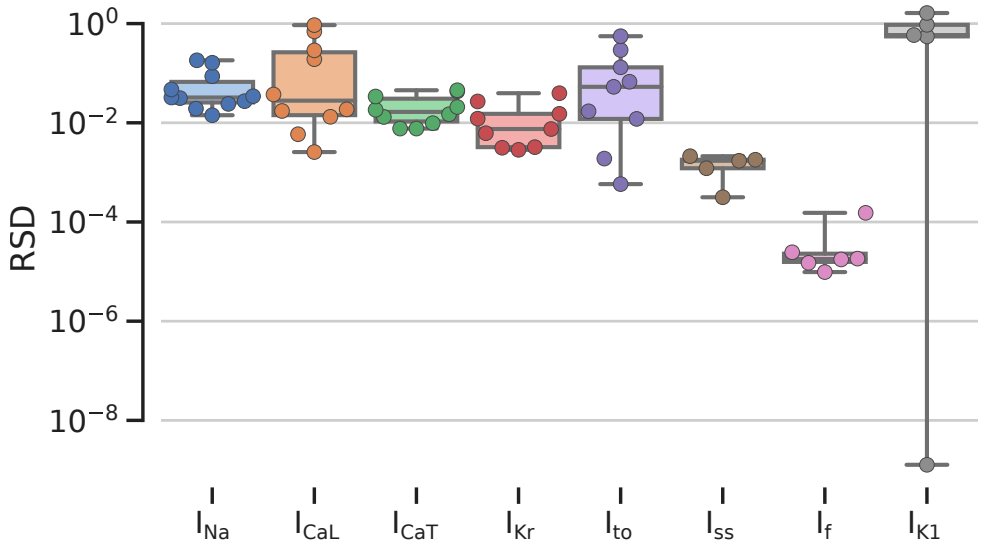


Figure 4.8: Box plots showing relative standard deviation of parameter posterior distributions for channels calibrated by ABC in the HL1-6 cell model.

perimental data is plotted as a normal distribution implied by the mean and standard deviation of the reported values. The diagonal plots show kernel density estimates for the model output, the upper triangular plots show scatter plots of each individual model parameterisation output and the lower triangular plots shows two-dimensional kernel density estimates for the distribution of the model outputs. A summary of parameter posterior distributions for the whole cell parameters is in Table A.29 (for an interpretation of the parameter symbols see Table 4.1).

In general, the calibrated cell model output distribution is predominantly within one standard deviation of the experimental mean. Most model outputs have a lower variability than the experimental measurements (the width of the blue distributions is less than the orange distributions in diagonal plots in Figures 4.9 and 4.10). However, this assumes a normal distribution is the appropriate description for the experimental data. In the case of some experimental measurements (e.g. APD90 in Figure 4.9), reporting results as mean with standard deviation implies it is possible to achieve a negative duration, which is clearly nonphysical. For timing measurements of the Ca^{2+} transient (Figure 4.10), the variability in the model output is similar to the experiment, particularly for the time to peak (Ca_{T2P}).

Figure 4.11 shows the correlation between the model outputs for the final calibration

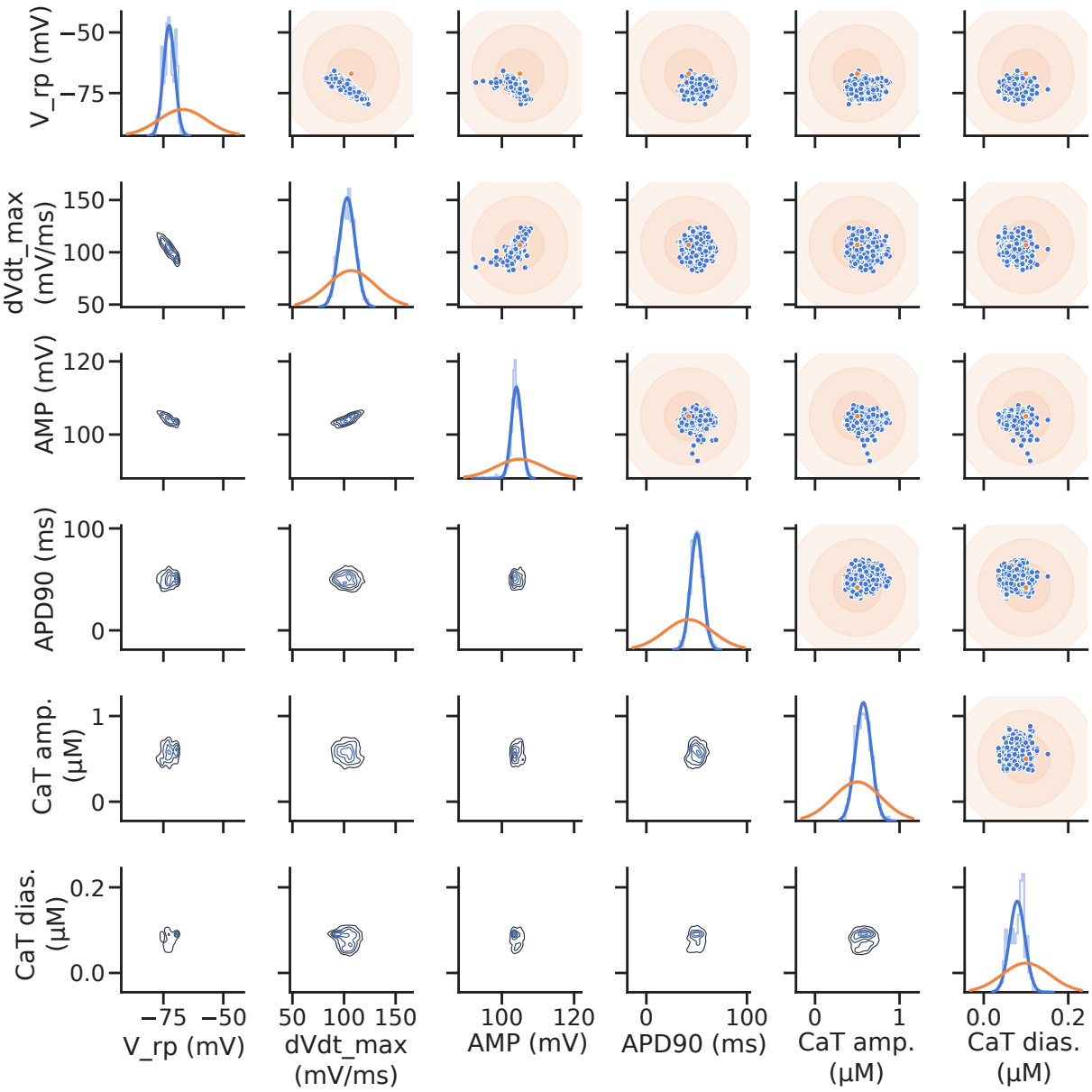


Figure 4.9: Simulated measurements from first whole cell calibration experiment compared to experimental results. The diagonal shows a histogram of each measurements with a fitted Gaussian curve for the simulations in blue. A Gaussian curve generated from the mean and standard deviations is shown in orange. The upper diagonal shows scatter plots of simulated measurements (blue) and the mean of the experimental measurements with shading indicating one, two and three standard deviations (orange). The lower diagonal are contour plots of two-dimensional kernel density estimates for the simulated measurements. Simulated results are shown for 1000 model parameterisations. 'V_rp' is the resting potential, 'dVdt_max' is the maximum upstroke of the action potential, 'AMP' is the action potential amplitude, 'APD90' is the action potential duration to 90% repolarisation, 'CaT amp.' is the amplitude of the Ca^{2+} transient and 'CaT dias.' is the minimum of the Ca^{2+} transient.

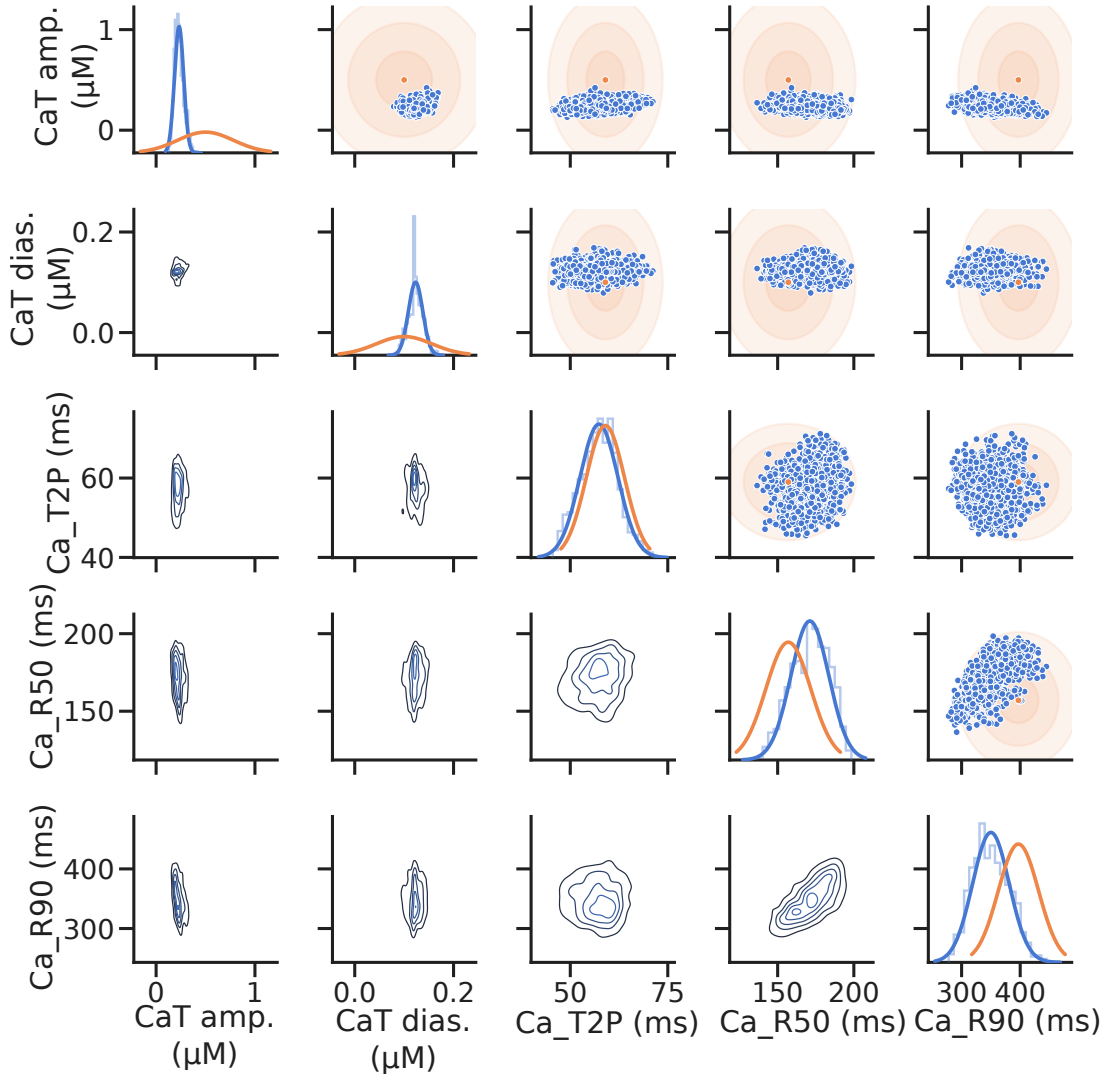


Figure 4.10: Simulated measurements from second whole cell calibration experiment compared to experimental results. Plotted as described in Figure 4.9. 'CaT amp.' is the amplitude of the Ca^{2+} transient, 'CaT dias.' is the minimum of the Ca^{2+} transient, 'Ca_T2P' is the time to peak of the Ca^{2+} transient, 'Ca_R50' is the time to 50% recovery of the Ca^{2+} transient and 'Ca_R90' is the time to 90% recovery of the Ca^{2+} transient.

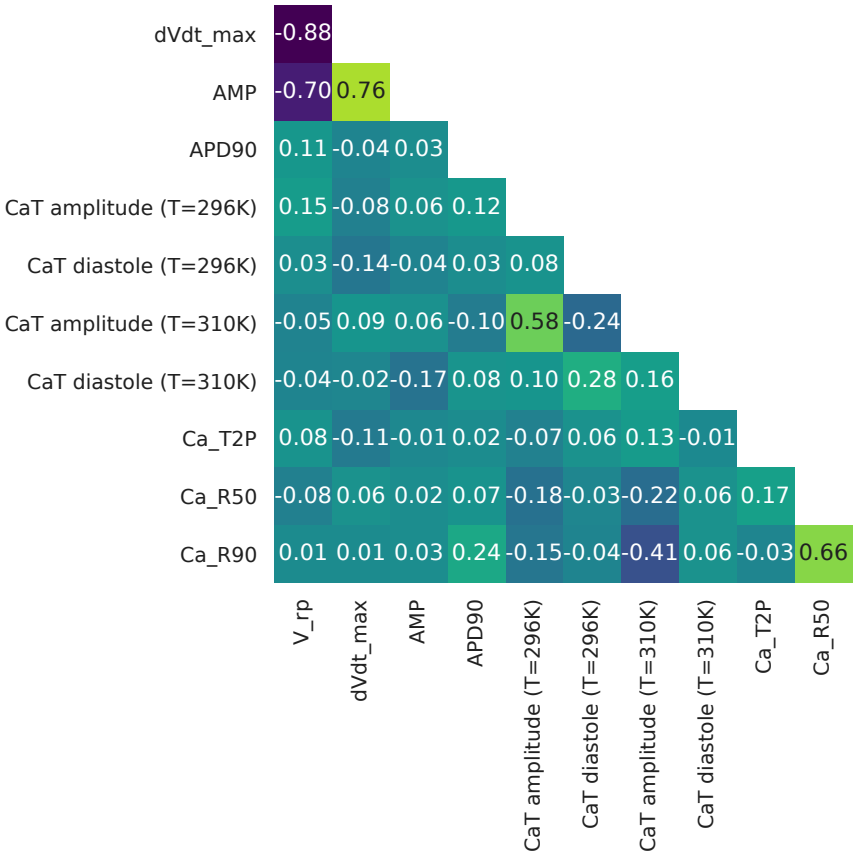


Figure 4.11: Heat map of Pearson correlation coefficients between action potential and Ca^{2+} transient (CaT) measurements in 1000 model parameterisations. Only lower triangle and diagonal values are shown (upper diagonal is symmetrical). For interpretation of measurements see Table 4.6.

step, calculated as Pearson correlation coefficients. Most measures show little correlation between outputs. There is a positive correlation (> 0.5) between the amplitude and maximum upstroke, between the Ca^{2+} transient amplitude at different temperatures and between the two measurements of Ca^{2+} repolarisation. A negative correlation (< -0.5) was found between the resting potential and maximum upstroke, and between the resting potential and amplitude.

The parameter posterior distributions for the whole cell model reveal that these final calibrated parameters generally exhibit higher RSDs than previously observed in single channel calibrations (Table A.29). Figures 4.12 and 4.13 show how this variability underlying the whole cell parameters contributes to variability in traces of the measured action potential and Ca^{2+} transient, along with major ion channel currents and fluxes, in the model output for each of the complete cell experiments. Currents in which the conductance parameter was included in the final complete cell calibration step show the

most variability indicated by wider shaded regions around the median line (e.g. I_{Nab}, I_{NaK}, I_{pCa} in Figure 4.12). These currents also have lower magnitude than currents calibrated individually and so do not have as substantial an impact on the overall action potential and Ca^{2+} transients. There are wide shaded regions around the level of sarcoplasmic reticulum Ca^{2+} during an action potential (Figure 4.13), potentially a result of no experimental data directly measuring this feature being included for calibration.

4.3.13 Parameter sensitivity

A parameter sensitivity analysis of key conductance and maximum flux parameters was carried out to investigate their influence on output of the complete cell model. Only regression coefficients from multivariable regression fits where $R^2 > 0.7$ were retained for analysis. Figure 4.14 shows the regression coefficients for parameters against the first complete cell calibration experiment (i.e. action potential measurements), and Figure 4.15 shows the same for the second experiment (i.e. Ca^{2+} transient measurements). Both also include the measurements of diastolic Ca^{2+} and Ca^{2+} transient amplitude at the temperature of each experiment. These graphs are plotted separately for clarity, but the analysis was conducted with both experiments simultaneously. The magnitude of the regression coefficient reflects the influence of a parameter on the output of the complete cell model. A positive value implies a reinforcing effect and a negative value implies a deleterious effect.

In general, the results show different subsets of channels and Ca^{2+} fluxes contributing to each model output, usually dominated by one or two of the currents. The resting potential (V_{rp}) of the cell model is controlled by a balance between background Na^+ current and inward rectifier K^+ current, as expected in cells derived from the HL-1 cell line [201]. Increasing the conductance of the fast Na^+ current has a reinforcing effect on the maximum upstroke gradient ($\left(\frac{\mathrm{dV}}{\mathrm{dt}}\right)_{\mathrm{max}}$) and action potential amplitude (AMP), but little to no impact elsewhere in the action potential. This is an expected result for a current that activates and inactivates rapidly at the beginning of the action potential.

The amplitude of the action potential is increased by increasing the dominant currents

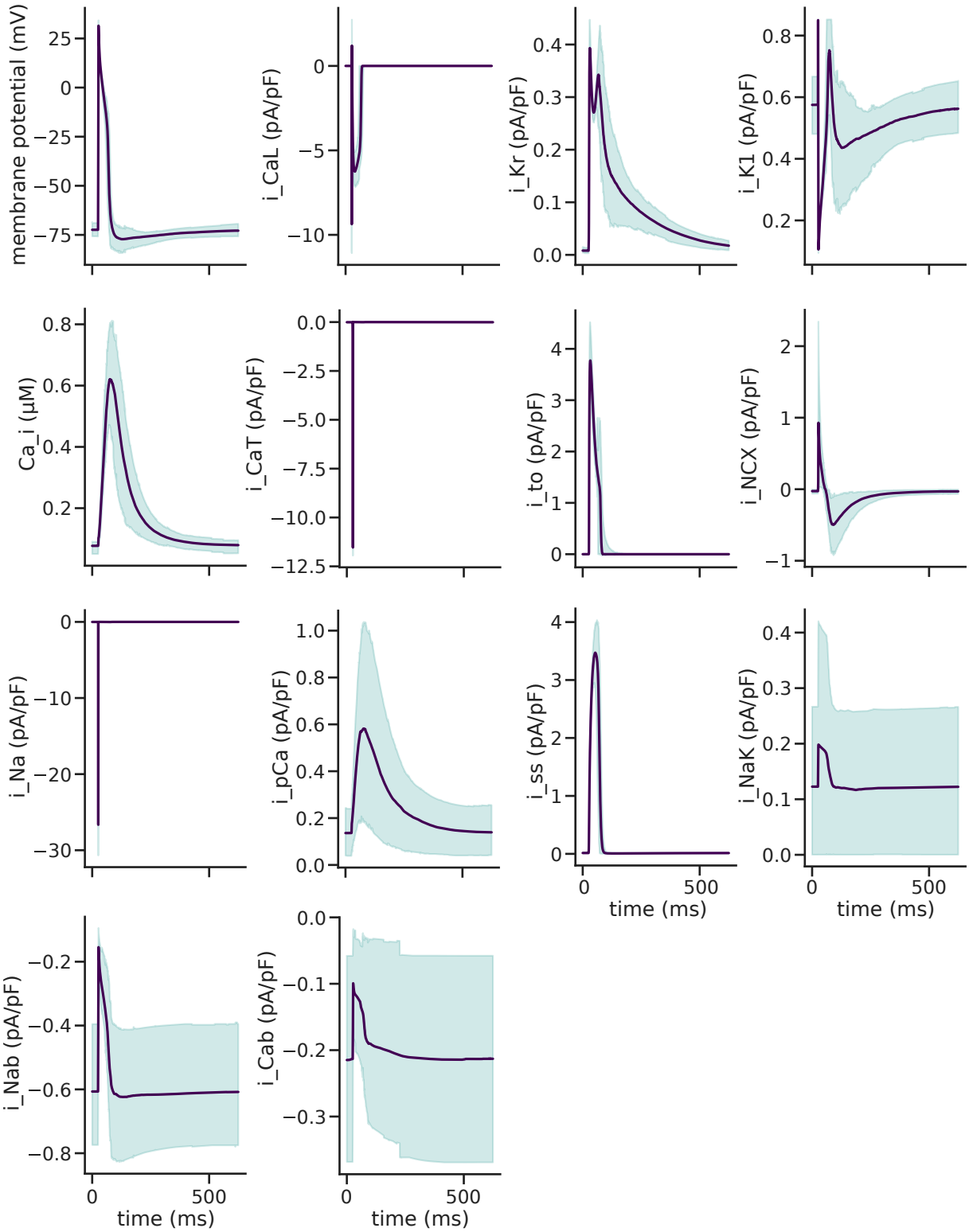


Figure 4.12: Traces of action potential, Ca^{2+} transient and ion currents generated during the final action potential of the first experiment from whole cell calibration. Results are plotted for 1000 model parameterisations as median lines with 89% HPDI represented by shading.

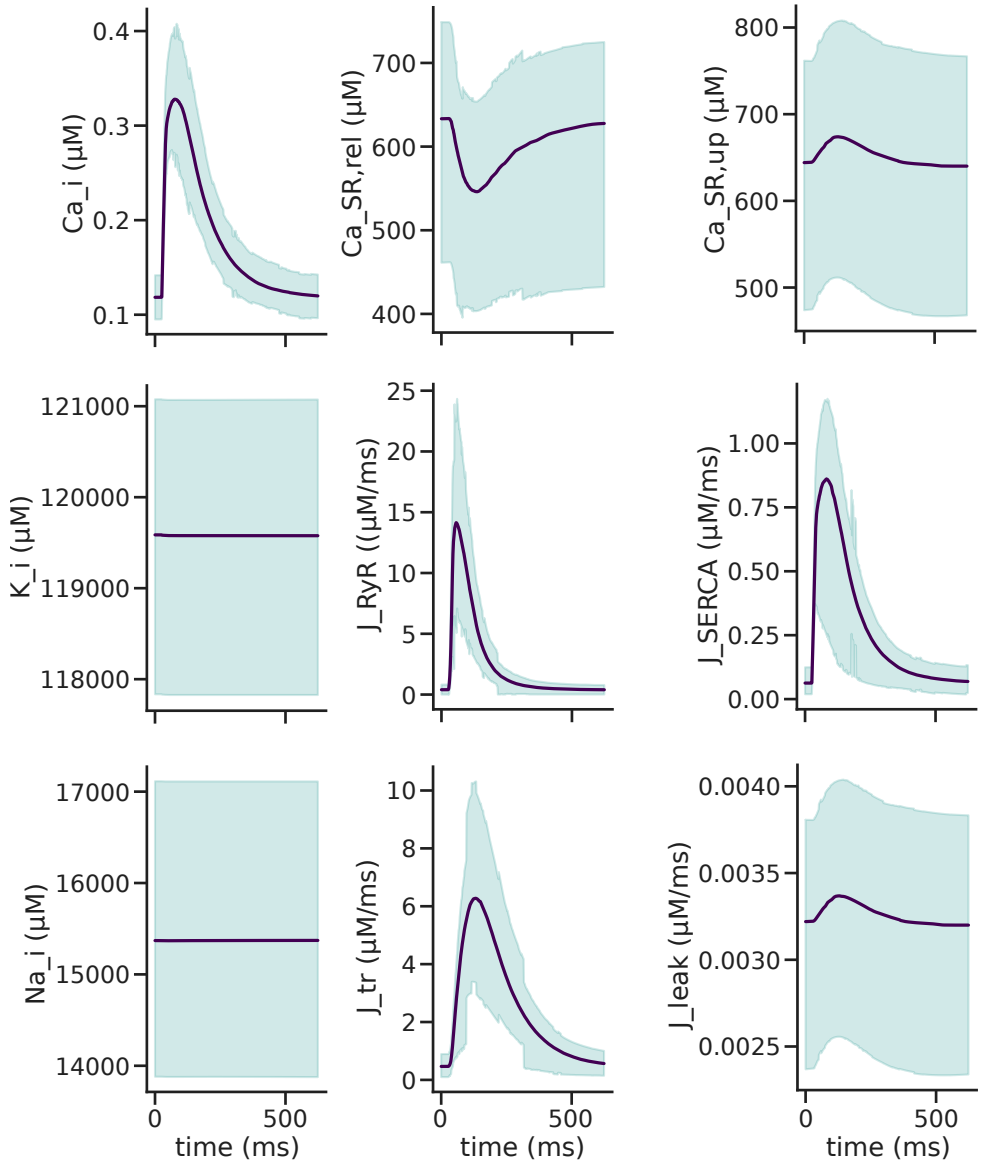


Figure 4.13: Traces of Ca^{2+} transient and Ca^{2+} fluxes generated during the final Ca^{2+} transient of the second experiment from whole cell calibration. Results are plotted for 1000 model parameterisations as median lines with 89% HPDI represented by shading.

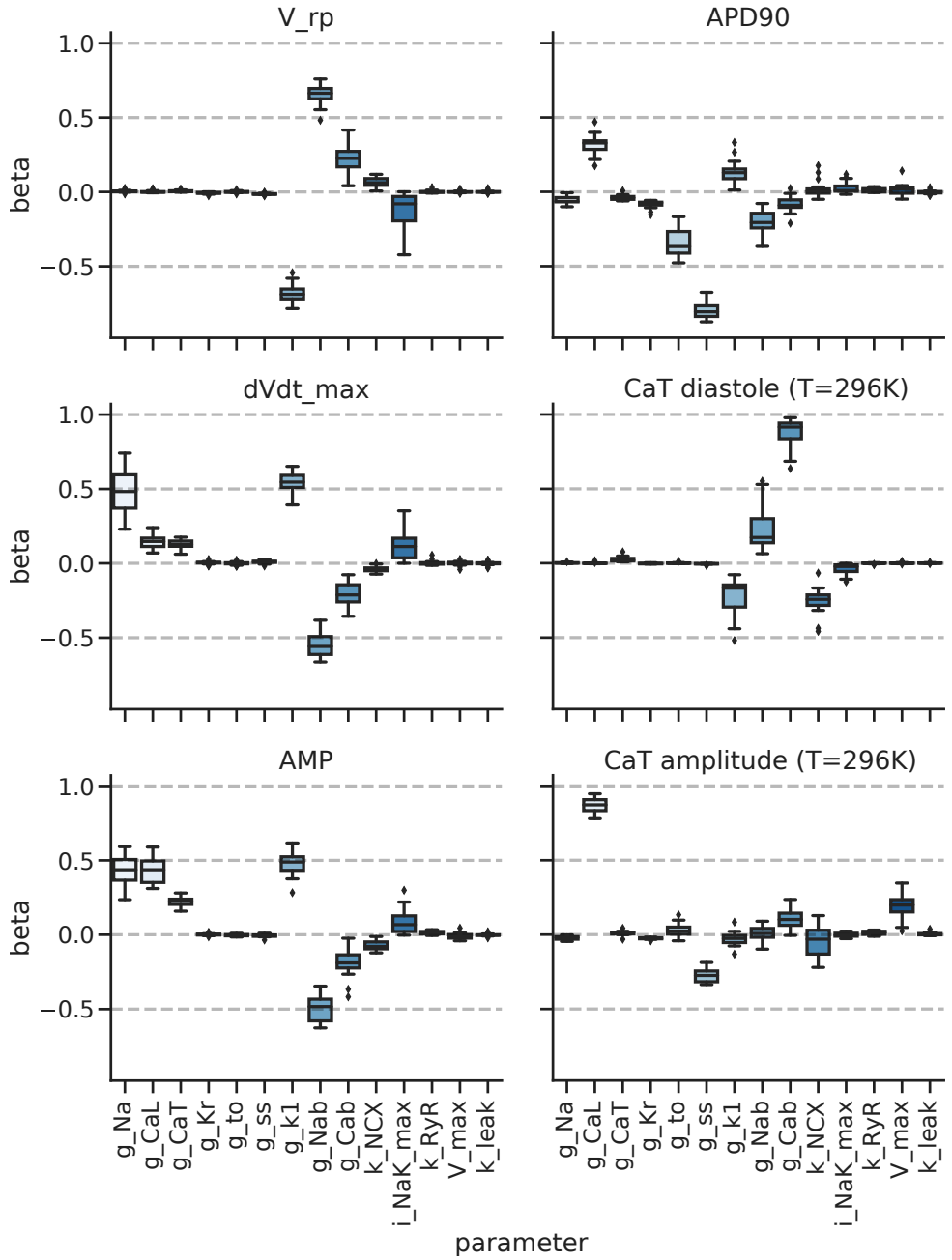


Figure 4.14: Sensitivity coefficients of conductance (or similar) parameters for measurements in first whole cell calibration experiment.

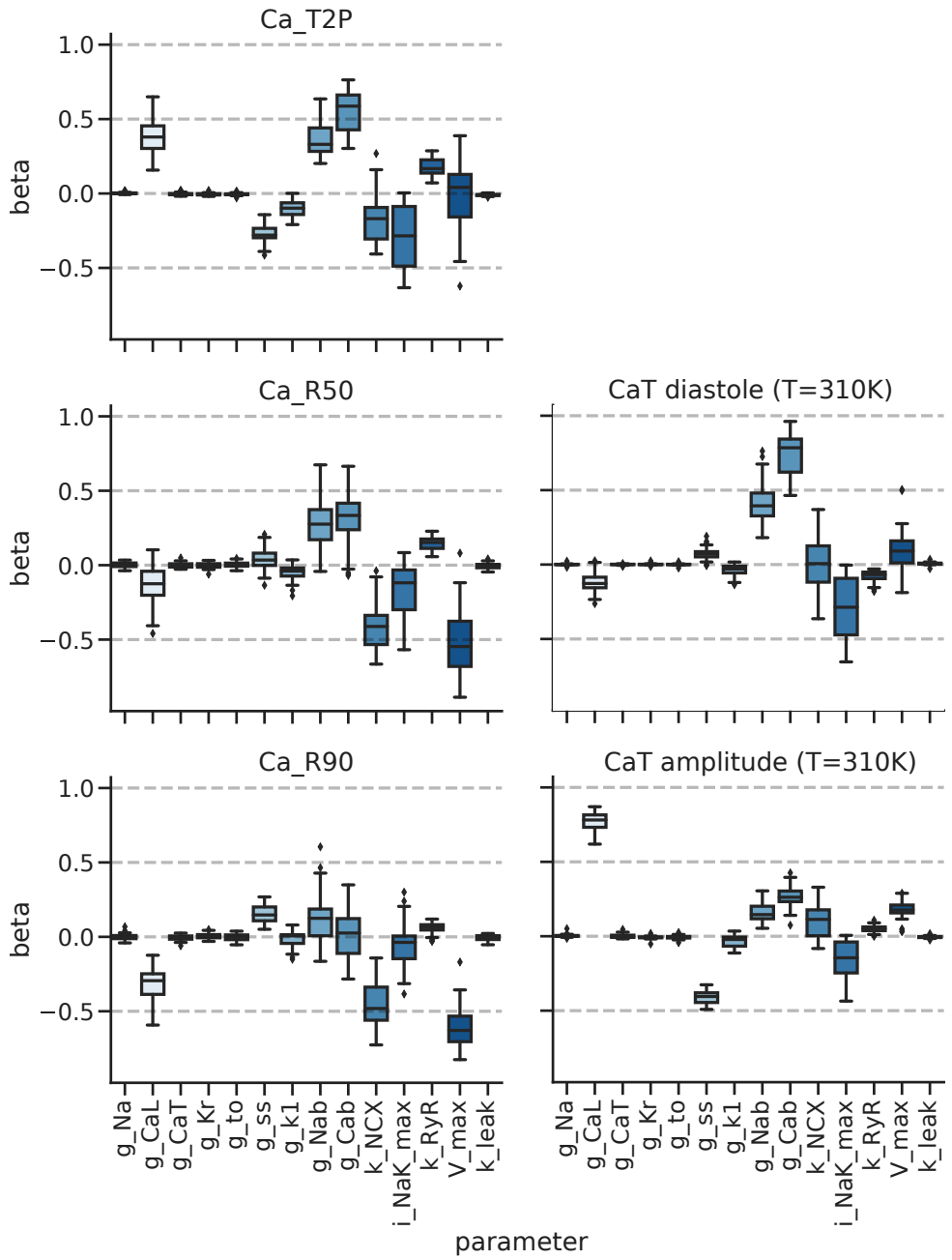


Figure 4.15: Sensitivity coefficients of conductance (or similar) parameters for measurements in second whole cell calibration experiment.

which activate early in the upstroke of the action potential (I_{Na} and I_{CaT}) and shortly after (I_{CaL}). I_{K1} also has a reinforcing effect on this measure, as increasing the conductance of this channel tends to lower the resting potential (see first plot in Figure 4.14), this moves the resting potential further from the Nernst potential for depolarising Na^+ and Ca^{2+} channels thus increasing their current through an increase in the forcing for these channels.

Action potential duration (APD90) is predominantly controlled by a balance between the conductance of I_{CaL} and the repolarising K^+ currents (I_{to}, I_{ss}). I_{Kr}, which was previously stated to be the dominant K^+ current in the original HL-1 cell line [199], has a much smaller effect on the action potential duration (or any other measures).

Diastolic Ca^{2+} and Ca^{2+} transient amplitude are generally influenced by similar parameters at either temperature: I_{Cab} for the former and I_{CaL} for the latter. The lower regression coefficient for the magnitude of Ca^{2+} flux through ryanodine receptors (k_{RyR}) suggests a reduced role of Ca^{2+} release from the sarcoplasmic reticulum in this model.

Measurements of Ca^{2+} transient parameters in the second whole cell experiment (Figure 4.15) appear to be influenced by a wider combination of parameters than in measurements of the action potential. There also appears to be a wider range of behaviours between different samples from parameter posteriors (indicated by the increased height of the box plots). For example, in measuring Ca^{2+} time to peak ($\mathrm{Ca}_{\mathrm{T2P}}$), the magnitude of the SERCA pump flux (V_{max}) appears to have variants in which increases in this parameter will both increase and decrease the measure.

4.3.14 Spontaneous automaticity

All model parameterisations analysed above remained quiescent if not stimulated. Next, the I_{f} current was switched back on in each of these model parameterisations and run using the protocol described in Section 4.2.6 to assess whether including this current would induce spontaneous automaticity.

Using the exclusion criteria to eliminate non-physiological cells (see Section 4.2.6), 40.3% of parameterisations with I_{f} were accepted ($n = 403$), 54.6% were rejected due to

high intracellular Ca^{2+} concentration ($n = 546$) 3.7% failed to repolarise ($n = 37$) and 1.4% failed due to numerical error ($n = 14$). Of the accepted parameterisations, 28.3% exhibited automaticity ($n = 114/403$), and the remainder remained quiescent. Figure 4.16 shows 10 s traces of 5 random parameterisations that exhibited automaticity. The median frequency of automaticity in the single cells was 2.7 Hz, with 89% HPDI of $(1.4, 4.2)$ Hz.

A final population of cell model parameterisations was generated to export for solving in simulations of HL1-6 cell monolayers in Chapters 5 and 6. This final population was created by taking 700 random samples from the quiescent (no I_f) cell population, and 300 random samples from the 'possibly beating' (includes I_f) cell population. This proportion is based on the approximate frequency of I_f expression in the original HL-1 cell line (30%) [62], and assuming that HL1-6 myocytes exhibit similar proportion of the channel.

4.3.15 Effect of blocking ion channel currents

To validate the cell model, we next compared the effect of blocking individual ion currents to experimental measurements in the original HL-1 cell line. It was unfortunately not possible to obtain direct measurements in HL1-6 monolayers due to experimental restrictions at the time of this research.

The effect of each ion channel blocker (except for Ryanodine and Thapsigargin) was estimated from dose-response curves generated in HL-1 cells [142, 200]. For Lidocaine, values were estimated from [223]. For each curve, the data points from experiments were digitised and fit to the Hill equation using `scipy.optimize.curve_fit`. During curve fitting only the Hill coefficient was varied, and the IC50 value was assumed to be the mean value reported from experiments.

To generate a distribution of possible results, 1000 samples were taken from a normal distribution for the mean and standard deviation for the experimentally reported IC50 value, and used to generate a family of dose-response curves with the previously fitted Hill coefficient. To test the effect of the drug in each simulation a randomly selected dose-response curve was sampled to determine the proportion of blocking applied to the corresponding ion channel. For Ryanodine and Thapsigargin, complete block of the corre-

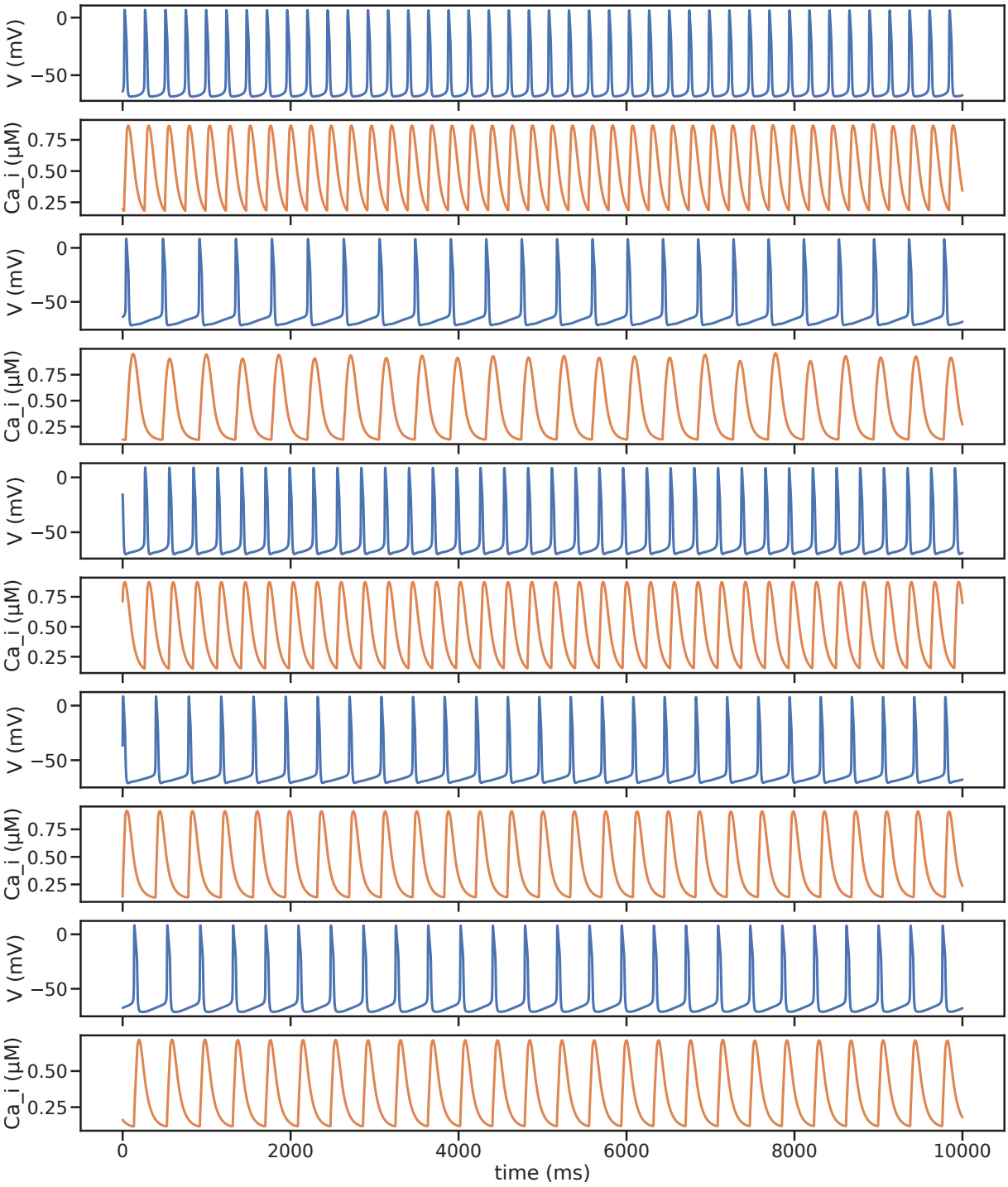


Figure 4.16: Five examples of automaticity in model parameterisations with the hyperpolarisation-activated 'funny' current.

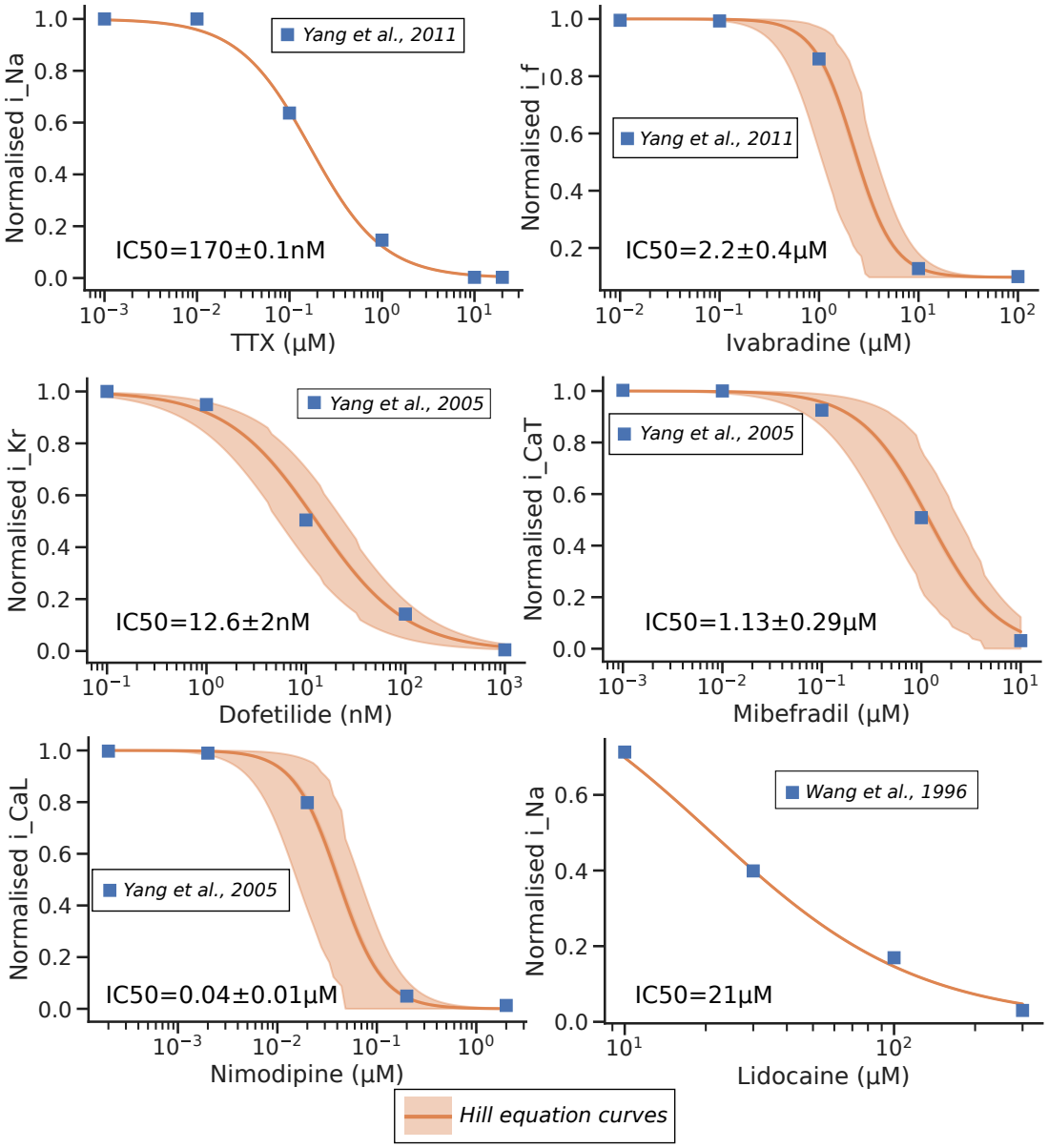


Figure 4.17: Dose response curves generated to determine blocking of specific ion channel currents with shading indicating 89% HPDI. Data points are plotted from the source indicated.

sponding intracellular Ca^{2+} flux (J_{RyR} and J_{SERCA} respectively) was assumed. Figure 4.17 shows the IC50 curves generated for each drug. Table 4.7 summarises the action of the drug.

Each of the 1000 parameterisations generated were tested by blocking specific ion currents and recording features of either a spontaneously generated action potential, or a stimulated action potential. The features recorded were maximum diastolic potential (MDP), action potential amplitude (AMP) and action potential duration to 50% repolarisation (APD50). The results were compared to experimental measurements recorded

Drug	Dose (μM)	Channel	Current block median (%)	Current block HPDI (%)
Tetrodotoxin (TTX)	20	I_{Na}	100.0	(100.0,100.0)
Ivabradine	10	I_{f}	86.8	(81.9,90.3)
Dofetilide	1	I_{Kr}	98.4	(97.4,99.4)
Mibefradil	10	I_{CaT}	93.4	(87.7,100.0)
Nimodipine	2	I_{CaL}	99.9	(99.9,100.0)
Ryanodine	30	J_{RyR}	100.0*	
Thapsigargin	5	J_{SERCA}	100.0*	
Lidocaine	50	I_{Na}	72.7	

Table 4.7: Inferred current blocked from action of each drug. $*$ indicates complete block was assumed. For Lidocaine, only the mean value of current block was provided so a distribution could not be generated.

using current patch clamp of HL-1 cells in a cellular synctium [142]. Figure 4.18 shows the action potential feature changes for 100 random samples from the 1000 parameterisations in response to each drug. The experimental change is plotted as mean value with error bars indicating one standard deviation.

The width of experimental error bars in Figure 4.18 indicates a wide range of experiment responses, and highlights the heterogeneity of the original HL-1 cell line. The simulation results are generally within one standard deviation of the experimental results, with some exceptions. The effect of the I_{CaL} blocker Nimodipine appears to be well reflected by the model.

There are also some clear disparities from experimental results. Blocking I_{Na}, using either TTX or Lidocaine, is expected to reduce the action potential amplitude by approximately 16% and 9% respectively (admittedly with wide experimental variability), but no noticeable effect is reflected in the simulation. In addition, the experimental prolongation of action potential duration by inhibiting I_{Kr} is not reproduced in the model. This is consistent with the conductance of I_{Kr} having a lesser impact on the action potential duration in the parameter sensitivity study compared to other repolarising currents (namely I_{to} and I_{ss} for which comparable validation data could not be obtained).

In the simulation results for blocking the hyperpolarisation-activating 'funny' current using Ivabradine, two populations of cell model parameterisations group at different effects. These groups represent model parameterisations with and without the channel.

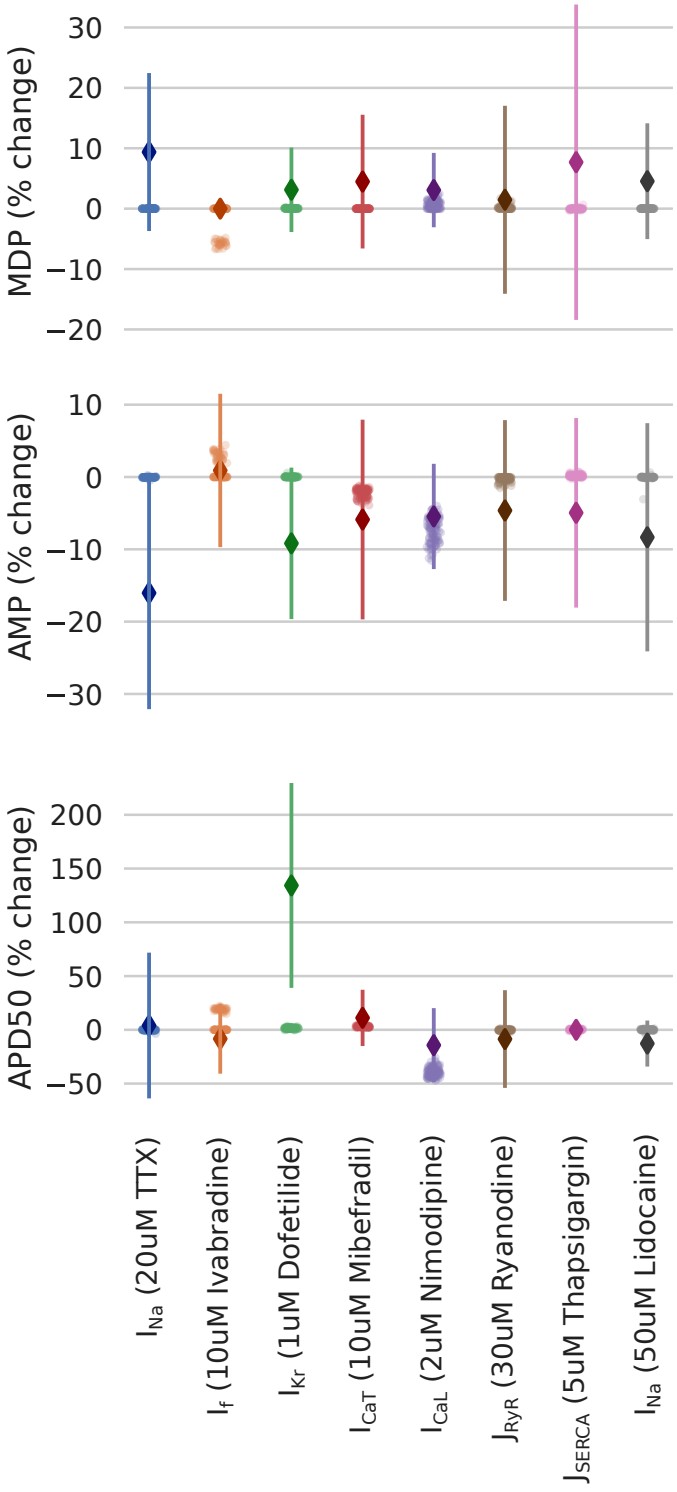


Figure 4.18: Effect of blocking specific ion channel currents in the HL1-6 cell model variants compared to experimental results in the original HL-1 cell line. Circles show 100 random samples from the 1000 variants tested. Diamonds show the mean experimental result with error bars indicating one standard deviation. Results are shown for maximum diastolic potential (MDP), action potential amplitude (AMP) and action potential duration to 50% repolarisation (APD50).

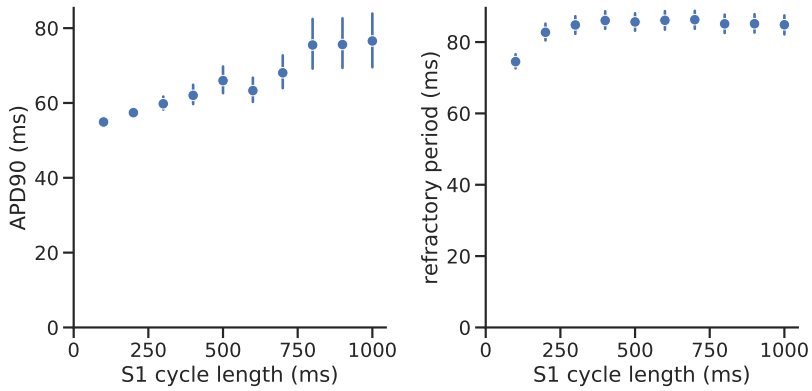


Figure 4.19: **a** Action potential duration at 90% repolarisation of penultimate S1 action potential at different S1 cycle lengths. **b** Minimum S2 delay to initiate action potential response (to nearest 10ms) at different S1 cycle lengths. Results are plotted as mean with one standard deviation of the responses from each model variant.

4.3.16 Restitution properties

We studied the restitution properties of our model by measuring the action potential duration and refractory period at different pacing rates. An S1-S2 protocol was applied to all 1000 cell model parameterisations. The model was left at rest for 10 s before an S1 stimulus was then applied at 40 pA/pF with duration 0.5 ms and a constant cycle length (which differed between experiments). The S1 stimulus train was applied for 10 s. After the final S1 pulse, an identical S2 stimulus was applied out of phase with the S1 train. The full S1-S2 protocol was repeated with reducing delays to the S2 stimulus until an S2 stimulus did not elicit an action potential. Once the S2 stimulus did not elicit an action potential response, the previous pulse train response (i.e. with slightly longer delay to S2 stimulus) was recorded for analysis.

Action potential duration at 90% repolarisation was measured in the penultimate action potential from the S1 stimulus. The refractory period was determined by the smallest S1-S2 delay that still resulted in an action potential response (defined as a peak above -20 mV).

Figure 4.19a shows that as the S1 cycle length decreased (increasing S1 pacing rate), the action potential duration reduces from approximately 75 ms to 55 ms. The spread of results from different model variants is also reduced as the cycle length decreases. The refractory period of the cell model was always greater than the action potential duration.

The refractory period remained constant around 85 ms as cycle length decreased until 10 Hz pacing, where it reduced to approximately 75 ms.

4.4 Discussion

The goal of this chapter was to develop an action potential model of an HL1-6 myocyte for use in future simulations of action potential propagation in monolayers of the cells. We sought to use the methodology developed in Chapter 3 to build the cell model in a way that accounts for the uncertainty and variability in parameter estimates by calibrating distributions for each parameter rather than single point estimates. The resulting whole cell model is composed of a population of 1000 different parameter variants which show good agreement to experimental measurements. A subset of these variants exhibit spontaneous automaticity at a comparable rate to biological experiments.

4.4.1 Standardised ion channel gating models calibrated well to experimental data

In Chapter 3, the use of a standardised gating formulation [168, 191] instead of more complex equations typically used in cell models (e.g. [165, 166, 213, 224]) resulted in parameters which were better identified when calibrated to the available experimental data. Consequently, when developing the model of an HL1-6 myocyte, we sought to use this standardised formulation as the basis for key ion channel currents, and only modified it as necessary for the idiosyncrasies of individual currents (e.g. by adding a simple Ca^{2+}-dependent inactivation gate to I_{CaL}).

The 8 ion channel models formulated using this approach calibrated closely to experimental data, with most parameter posterior distributions also exhibiting low relative standard deviations (RSDs) characteristic of well identified parameters (Figure 4.8). A conventional optimisation algorithm (e.g least-squares) may be able to recover similarly good approximations. The particular advantage of a Bayesian approach like ABC is that it does not consider single point estimates for each parameter and instead gives a discrete

approximation to its posterior distribution. This distribution can provide additional information about how 'certain' we are of individual parameters in the model, and accounts for variability present in the complete cell model due to underlying experimental and modelling uncertainties. A drawback of this approach is that it does not explicitly separate each of these sources of uncertainty and separately quantify their effect, which would be desirable to be able to produce a model which is truly reflective of the underlying biological variability. An approach to quantify the additional uncertainty due to deficiencies in model structure (model discrepancy) was previously investigated in Chapter 3, but was not feasible to implement in this work.

Across individual channel calibrations, the variability observed in model output was low when processed into summary statistics which could be compared to corresponding experimental data. Taking a closer look at the underlying gating functions (Figure 4.7) for these calibrated channels showed that there is hidden variability which is masked by processing through the summary statistic function. In most instances, this variability was apparent in voltage ranges for which experimental data was not readily available (e.g. activation time constant data for I_{CaL}), or outside the range of experimental measurements (e.g. lower voltage range of I_{Na}).

Particularly large variability was noted in the steady-state gate of I_{to} as well as the conductance parameter of this channel. This variability is likely to be a consequence of multiple combinations of parameters being able to produce very similar current traces, and the limited data for this channel (i.e. practical unidentifiability). This variability could potentially be reduced by including data relating to deactivation of the channel in the lower voltage ranges to constrain the corresponding gate.

For I_{K1}, the steady-state function had little variability, despite the high RSD values of all but the conductance parameter (Figure 4.8). In this case, the parameters may suffer from structural identifiability as they can co-vary to produce similar steady-state curves. As this channel model only has a single steady-state gate, a simpler formulation could potentially alleviate the issue.

4.4.2 The complete cell model closely matches experimental data and accounts for variability

When calibrating the complete cell model, we retained the posterior parameter distributions from individual ion channels while calibrating new distributions for remaining key parameters in the cell. The calibrated model output showed good agreement with experimental measurements of action potentials and Ca^{2+} transients measured in the HL1-6 cell line [69].

For most measurements, the model had less variability than implied from experimentally reported standard deviations (Figures 4.9 and 4.10). This could be a consequence of the relatively sparse sampling of the parameter hyperspace in this step (using 1000 particles for 14 parameters), a necessary concession due to the increased computational load of forward evaluations of the complete model. Sparse sampling would tend to cause the parameter posterior distributions to collapse onto single minima, rather than spreading across possible parameterisations [161]. For some rise and recovery measurements of the Ca^{2+} transient however, the model produces very similar variability to the experimental data. Use of the general form of ABC [190] (as investigated in Chapter 3), or more appropriate representations of the experimental data that provide more detail of the distribution of results (rather than assuming a normal distribution), may make it possible to better represent the experimental variability.

Kernik et al. previously applied a similar bottom-up approach to develop a cell model for induced pluripotent stem cells to account for their heterogeneous phenotype [87]. To incorporate variability into their model, the authors fit (using a conventional minimisation algorithm) ion channels to data sets obtained from three different labs, to develop three distinct parameter sets for selected ion channels. They then averaged the parameters to develop a 'baseline' model, and used the standard deviation of parameters across the three lab models to infer normal distributions for estimating experimental variability. In this chapter, a similar bottom-up approach was used but the variability within experiments (i.e. intra-experiment as opposed to inter-experiment), in combination with a Bayesian calibration approach, was the source of variability in the final model. Moreover, we did

not impose a specific distribution on our parameter posterior distributions but rather used populations of discrete particles to represent the continuous distribution.

Recently, a cell model of the original HL-1 cell line was developed by Takeuchi et al. [202]. As we used several of the same data sets, due to the paucity of available data for the specific sub-clone HL1-6, it would be expected that our two models produce similar output. The authors based their model on a model of a human atrial cell [204] while the model developed in this chapter emphasises the use of standardised gating functions, and adopts models from either mouse ventricular [79] or neonatal rat cells [84] when the standardised form is not operable. Similarities between the two models include peak I_{CaT} higher than peak I_{CaL} during the action potential, larger peak I_{to} and I_{ss} compared to I_{Kr} and similar resting potentials (see Electronic Supplementary Information to [202]). The spontaneous beat rate of their model (3.5 Hz) also falls within the range observed in the 'beating' variants of our model. A notable difference is that the action potential duration of their model is longer lasting than our model, though this is explained by the difference in experimentally measured action potential duration between the original cell line and sub-clone. In addition, as iterated above, the model developed in this chapter incorporates experimental variability and uncertainty to give a population of model variants, of which only a subset spontaneously beat.

4.4.3 Incorporating the 'funny' current results in spontaneous automaticity in a subset of model variants

When originally calibrating the complete cell model, the hyperpolarisation-activated 'funny' current (I_{f}) was 'switched off' (i.e. completely blocked). This was for two reasons. Firstly, in initial test calibrations, it was found that including this channel would cause it to be the dominant factor in regulation of the resting potential rather than mediating any automatic activity. This is potentially a result of the simulations used to calibrate the complete cell measuring action potential and Ca^{2+} transient responses to a stimulus current. Any automatic activity could interfere with this protocol and lower the likelihood for parameter samples which use I_{f} to regulate automaticity. The second reason was that experimental

measurements of this channel in the original HL-1 cell line [62] show that approximately 30% of cells exhibit this current. Not including the current in the initial complete cell calibration therefore serves to represent the more dominant quiescent phenotype (assuming it is similar in HL-1 and the sub-clone HL1-6).

Subsequently re-adding I_{f} into the model resulted in spontaneous automaticity in 11.4% ($n = 114$) of the 1000 variants. The beat rate differed between variants with a median value of 2.7 Hz and HPDI (1.4, 4.2) Hz. This compares well to the experimentally observed mean beating rate of the original HL-1 cell line (3.5 Hz) [142].

The final population of model variants exported to the solver for simulations of action potential propagation in cellular monolayers in following chapters was generated by randomly selecting 700 variants from the population without I_{f} and 300 variants from the population with I_{f}. Despite accounting for the heterogeneous expression of I_{f}, this is still a simplification of the cell population, as other channels in the original HL-1 cell line and sub-clone are also heterogeneously expressed. The proportion of HL-1 cells expressing both I_{CaL} and I_{CaT}, or exclusively one or the other, has been described in a number of studies [64, 65, 200, 215]. I_{CaL} is generally expressed exclusively in ∼15-20% of cells, I_{CaT} exclusively in ∼35-45% and both in ∼30-45% [200, 215]. The proportion of cells expressing I_{CaL} is comparable in HL1-6 myocytes [69], suggesting this feature of heterogeneity was retained in the more homogeneous sub-clone. Limited experiments were conducted where the complete cell was calibrated by including a random Bernoulli variable to control whether a specific model variant expressed these heterogeneous ion channels, however the ABC calibration always converged upon a single subset expressing both. A possible future path for this work would be to develop separate distinct populations of model variants with different combinations of the heterogeneous channels, though this would also benefit from experimental measurements from corresponding cells which were not available.

4.4.4 Blocking ion channels has a similar qualitative effect to experimental measurements in the original cell line

The model variants were validated against measurements in the original HL-1 cell line of the effects on action potential morphology of pharmacological inhibition of specific ion channels. Unfortunately it was not possible to obtain comparable results in HL1-6 myocytes due to experimental restrictions at the time of the research. Regardless, the sub-clone is derived from the HL-1 cell line and would be expected to exhibit at least broadly similar behaviour.

When comparing simulation output to this 'unseen' data set, the model showed generally good agreement with changes to maximum diastolic potential, action potential amplitude and action potential duration, with some notable disparities. The results of blocking most channels fell within one (admittedly large) standard deviation of the mean result from experimental data. In particular, blocking I_{CaL} and I_{CaT} showed similar trends to experimental measurements. The variability in the output of different model variants was lower than the standard deviation in most experimental measurements. This could be a result of the more homogeneous sub-clone model compared to the heterogeneous original cell line, or the sparse sampling of the parameter hyper space in ABC calibration (as mentioned in this discussion above).

Blocking I_{Na} had little effect on measurements in the model output compared to the experimental mean measurements. The peak I_{Na} current density in HL1-6 myocytes is approximately -80 pA/pF [69] compared to approximately -160 pA/pF [63] in the original cell line. This reduced current density could potentially explain the apparent lack of sensitivity of blocking this channel to changes in action potential measurements compared to the original cell line. In addition, the response in single cell experiments may be different from the response in a cellular synctium from which the validation data was obtained [142].

The effect of blocking I_{Kr} was not reflected in the model output. Our model has a lower peak current density of I_{Kr} compared to I_{to} and I_{ss} when considering the repolarising K^+ currents. This is similar to the previous model developed for HL-1 myocytes [202]. HL1-6

myocytes also have a much shorter action potential duration than the HL-1 myocytes used in the experimental study of ion channel blocking (action potential duration to 90% repolarisation is ∼41 ms in HL1-6 [69] compared to ∼144 ms in HL-1 [200]). It is possible that there is therefore a different dominant mechanism of repolarisation in the sub-clone compared to the original cell line.

Explaining the disparity between the HL1-6 cell model and experimental measurements in HL-1 cells by differences between the two cell types may be admissible, but could also be misleading. It is possible that the model in its current form is simply wrong. Further experiments in HL1-6 myocytes could serve to further investigate the validity of this approach, and identify which areas of the cell model need further attention.

4.4.5 Limitations

One of the most significant limitations of this work is the experimental data used to calibrate the model. Only two data sets for I_{Na} and I_{CaL} were specifically obtained from the HL1-6 cell line. The remaining data sets were predominantly in the original HL-1 cell line with a few from murine primary ventricular cells. Data was also gathered from across different laboratories which may use different experimental setups and conditions when taking measurements. While all simulations matched the experimental conditions and replicated the published protocols as closely as possible, this model still relies on the validity of these data.

Although the key ion channel models are formed from standardised equations, we incorporate published models with single point estimates for parameters of the Na^+-Ca^{2+} exchanger, Na^+-K^+ pump and internal Ca^{2+} handling dynamics from [84]. The overall conductance of the majority of these currents was included in the complete cell calibration. However, there is likely additional variability in other parameters in these models that were not included in ABC. Given the limited effect that the variability in conductance parameters had on the overall action potential output of the model, this additional variability would not be expected to have a significant effect on 'macro' measurements of the model.

In our model, it appears that I_{f} at least partially modulates automaticity. We have not explicitly considered other candidates to regulate automaticity in these cells. I_{f} only mildly slows automaticity in HL-1 cells [142] and the HL1-6 sub-clone (personal correspondence, Dr Dupont, unpublished). Future work could investigate the more exact mechanisms underlying automaticity in HL1-6 cells which could then be more faithfully represented in a computer model. ■

Chapter 5

A multi-domain discrete-cell model of action potential propagation

5.1 Introduction

In Chapter 2, we examined a simplified biological model of self-sustaining circuits characteristic of propagation patterns observed during arrhythmias *in vivo*, and sought to further understand the conditions and substrate properties governing its initiation and perpetuation. To this end, we began developing a computer model that would make it possible to generate and further probe hypotheses surrounding this activity. Through Chapters 3 and 4, a model of the action potential of HL1-6 myocytes was constructed which provides quantification of uncertainty and variability in parameter estimates, as it was recognised that these factors may play a key role at the microscopic scale. In this chapter, the methodology used to simulate the propagation of action potentials between connected cells is now developed.

Action potential propagation has been simulated through discretely-coupled cardiac cells using finite difference [121], finite volume [120, 225] and finite element [107, 110] approaches, and in this work, we focus on the latter. The classical approach of the finite element method is to split a computational domain into multiple non-overlapping segments (i.e. elements) and to approximate the unknown solution to a partial differential

equation by weighted linear functions with local support in each element [226]. However, the use of low-order basis functions often means the method fails to capture detailed features of the solution without resorting to excessive mesh refinement. An alternative is to use spectral methods, which use high-order basis functions to improve accuracy, but are limited to relatively simple computational domains.

High-order finite element methods, such as the spectral/hp element method [227], alleviate these issues by incorporating features of both classical finite elements and spectral methods. They retain the desirable numerical properties of spectral methods and allow the modelling of complex domains as in classical finite elements. Two forms of refinement are used to improve the accuracy of the approximation to the unknown solution: h-type and p-type refinement. H-type refinement refers to splitting a computational domain into an increasingly larger number of elements, and reduces the error in the numerical solution algebraically. P-type refinement keeps the number of elements fixed and increases the order of the basis functions to reduce the error in the numerical solution, resulting in exponential error decay.

The propagation of action potentials through cardiac tissue is characterised by a sharp spatial gradient at the leading edge of the wave caused by the rapid upstroke at the beginning of an action potential. The spectral/hp element method is an appropriate numerical approach to simulate this sharp gradient in a computationally efficient way through high-order discretisation [90]. In this chapter, we construct a formulation for the action potential propagation through discretely-coupled cardiac cells, a *multi-domain* model, using the spectral/hp element method. At the discrete-cell level, the sharp spatial gradient is spread over multiple cells and the advantage of using spectral/hp element methods is primarily in the accuracy of capturing complex geometry.

The remainder of this chapter proceeds as follows. In Section 5.1.1, theoretical results for passive electrical flow in a one-dimensional cable of discretely-coupled cells are derived for use in validation of the solver. Next, in Section 5.2, a brief outline of the spectral/hp element method is provided before the application to problems of action potential propagation is detailed. In Section 5.3, the analytical solutions are compared to numerical

results in an idealised cable in one and three dimensions, propagation of an action potential through a cable is demonstrated and the parallel scaling properties of the solver are investigated. Finally, Section 5.4 concludes the chapter by summarising and discussing the results.

5.1.1 The cable equation

Before describing the spectral/hp element formulation, we first derive some theoretical results for the passive electrical flow in a one-dimensional cable of discretely-coupled cardiac cells. These solutions will be used to validate the computational implementation.

The problem of how electricity flows in a continuum cable of cells is described by the *cable equation* [2]. This describes a cardiac fibre as composed of two spaces: an intracellular space built of the cytoplasmic space of connected cardiac myocytes, and the extracellular space surrounding the cells. The two spaces can be visualised as a core cable (the myocytes) surrounded by an outer layer (extracellular space) aligned longitudinally in the fibre direction (Figure 5.1a). Discretising the cable into sections length of dx, and assuming a continuous space between individual cells for now (i.e. no gap junctions), we can formulate this into an equivalent circuit diagram, shown in Figure 5.1b. Here, r_i and r_e represent the resistance per unit length of the cable in the intracellular and extracellular spaces respectively, C_m is the capacitance per unit area of membrane, p is the perimeter of the cylindrical cells and I_{ion} represents the ionic current. This is equivalent to a bidomain model, where there are two distinct one-dimensional spaces connected at all points through membrane dynamics.

Assuming a one-dimensional problem and balancing currents flowing along the cable and across the membrane between the two spaces, one can derive the standard form of the cable equation (see Appendix A.4 for a full derivation):

$$p\left(C_m\frac{\partial V_m}{\partial t}+I_{\text{ion}}\right)=\frac{\partial}{\partial x}\left(\frac{1}{r_i+r_e}\frac{\partial V_m}{\partial x}\right), \tag{5.1}$$

where V_m is the transmembrane potential, t is time and other parameters are as above.

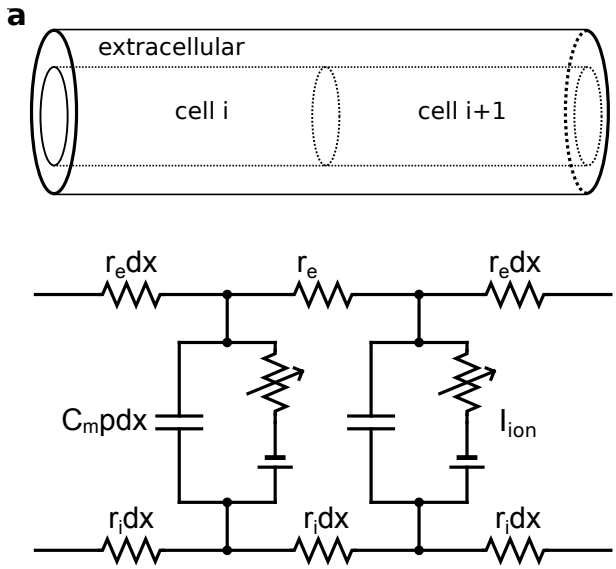


Figure 5.1: **a** A diagram representing the assumed geometry of the cable equation showing a cable with an inner core of coupled cells surrounded by extracellular space. The cable can continue infinitely in either direction. **b** Equivalent circuit diagram for the continuous cable equation assuming discretisation in the axial direction of elements size dx. The meaning of symbols is given in the text.

The transmembrane potential is defined at every point along the one-dimensional cable as $V_m = V_i - V_e$, where V_i is the potential in the intracellular space and V_e is the potential in the extracellular space. r_i and r_e are related to the intracellular and extracellular resistivities by $r_x = {}^{\rho_x}/_{A_x}$ for $x = i, e$ where ρ_x is the resistivity and A_x is the cross-sectional area of each space.

The cable equation broadly states that any change in transmembrane potential along the cable is due to capacitive and ionic currents flowing across the membrane between the two spaces. In the continuous form above, it does not account for discrete jumps in intracellular resistivity at abutting cell ends (though their effect could be broadly represented by *blending* the additional resistance into the intracellular r_i term). From a similar approach, one can derive the commonly used bidomain and monodomain continuum models of cardiac propagation in higher-dimensional spaces.

The discrete jump in intracellular resistivity caused by high resistance (relative to cytoplasmic space) gap junctions between abutting cells can be incorporated into the cable equation. Considering the cable as a series of cells connected axially by zero-length high-resistance interfaces (gap junctions) and assuming that the gap junctions behave like ohmic resistors, there will be a jump in intracellular potential between each cell

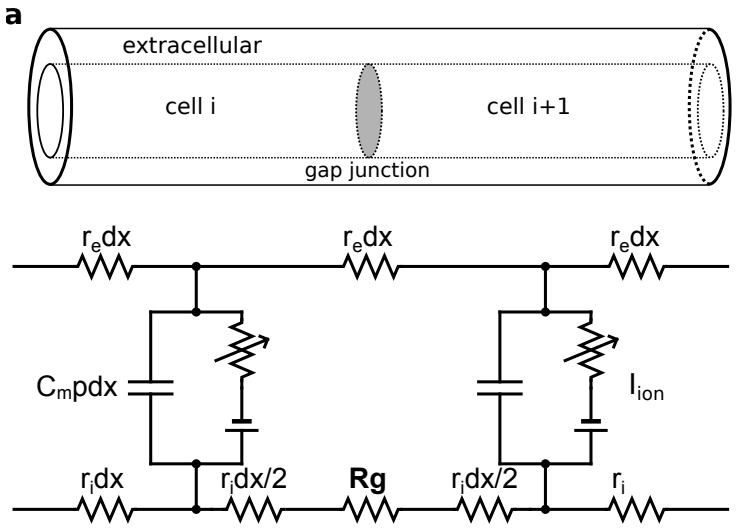


Figure 5.2: **a** A diagram representing the assumed geometry of the cable equation showing a cable with an inner core of cells coupled through high resistance gap junctions, and surrounded by extracellular space. The cable can continue infinitely in either direction. **b** Equivalent circuit diagram for the discontinuous cable equation assuming discretisation in the axial direction of elements size dx. The meaning of symbols is given in the text.

proportional to the current through the junction such that

$$\frac{V_i^+ - V_i^-}{R_g} = \frac{1}{r_i}\frac{\partial V_i}{\partial x}\bigg|_- = -\frac{1}{r_i}\frac{\partial V_i}{\partial x}\bigg|_+, \tag{5.2}$$

where V_i^+ and V_i^- are the intracellular potentials immediately up- and downstream of the junction and R_g is the gap junction resistance [2]. The extracellular space is continuous and thus unaffected by gap junctions. Figure 5.2 shows how this changes the cable diagram and equivalent circuit diagram. The only change is the addition of a high resistance gap junction in the intracellular domain (here assumed to be positioned at the midpoint of an element).

If the ionic current across the membrane is assumed to be a linear ohmic passive current (i.e. $I_{\text{ion}} = {}^{V_m}/_{R_m}$ where R_m is the resistance of a unit area of membrane) then two analytical solutions can be derived taking account of the discrete jumps in potential across gap junctions [2]. The first considers a cable with Dirichlet (fixed) boundary conditions applied at either end of a finite length cable, and the second considers an injected current into the extracellular space flowing from one finite length cable end and out of the other (Neumann conditions applied at both cable ends, where a Dirichlet condition must also be applied at an arbitrary location to fix a unique solution). For brevity, the full equations

and derivations are consigned to Appendices A.5 and A.6. However, we expand briefly on the concept of space and time constants to provide context to the solutions.

If the values of r_i and r_e are assumed constant, then Equation 5.1 can be rearranged into the form

$$\tau_m \frac{\partial V_m}{\partial t} + R_m I_{\text{ion}} = \lambda^2 \frac{\partial^2 V_m}{\partial x^2}, \tag{5.3}$$

where R_m is the resistance of a unit area of membrane, τ_m is the membrane time constant:

$$\tau_m = R_m C_m, \tag{5.4}$$

and λ is the cable space constant:

$$\lambda = \sqrt{\frac{R_m}{p(r_i + r_e)}}. \tag{5.5}$$

If the ionic current is considered as a passive ohmic resistor then $I_{\text{ion}} = {}^{V_m}/_{R_m}$ and Equation 5.3 becomes

$$\tau_m \frac{\partial V_m}{\partial t} + V_m = \lambda^2 \frac{\partial^2 V_m}{\partial x^2}, \tag{5.6}$$

and at steady state $\frac{\partial V_m}{\partial t} \to 0$ giving

$$\lambda^2 \frac{\partial^2 V_m}{\partial x^2} - V_m = 0, \tag{5.7}$$

which has the general solution

$$V_m = A e^{-|x|/\lambda}, \tag{5.8}$$

where A is a constant. This equation demonstrates how a passive transmembrane potential decays along a cable from value A at $x = 0$. The space constant λ represents the length over which V_m decays by a factor $1/e$. The greater the space constant, the less decay in a given length (i.e. a large space constant corresponds to a small resistance). The value of τ_m can be understood in a similar fashion by assuming transmembrane potential does not change in space, and defines the time taken for the transmembrane voltage to change under such conditions [225].

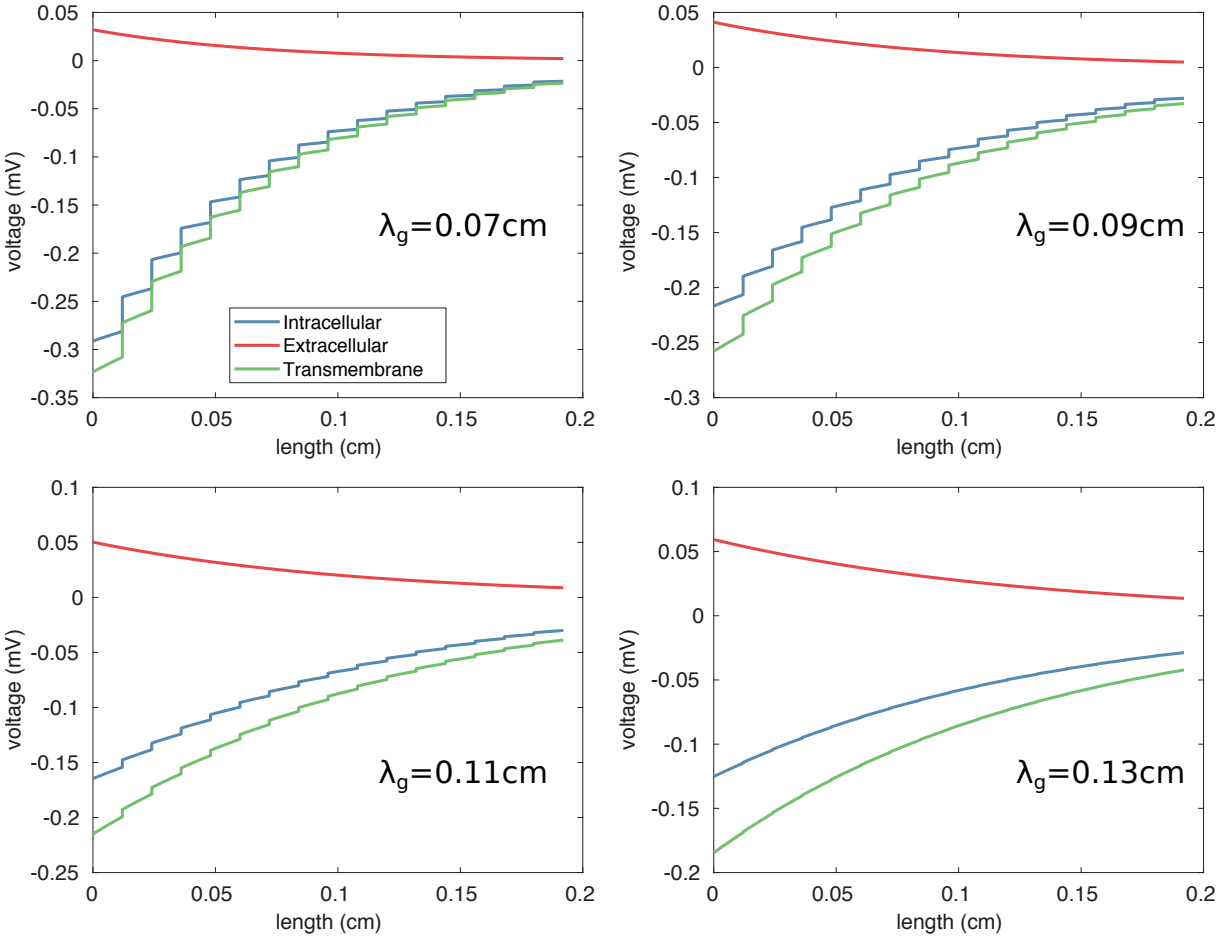


Figure 5.3: Analytical solution for a discretely-coupled cable of cells with constant sub-threshold potential held at either end for increasing values of the space constant. Solutions are shown for the extracellular, intracellular and transmembrane potential along the cable using the parameters in Table 5.1. Solutions are generated following the equations derived in Appendix A.5 and [2].

Figure 5.3 shows the first analytical solution for a cable of 16 discretely-coupled cells of length 0.012 cm with fixed (Dirichlet) boundary conditions at either cable end. The analytical solution is shown for the intracellular, extracellular and transmembrane potential for four increasing values of the gap junction space constant λ_g (representing decreasing gap junction resistance). The parameters used to generate this analytical solution are given in Table 5.1.

At the lowest space constant (highest gap junction resistance), the first graph in Figure 5.3 shows how the intracellular solution takes discrete jumps at each cell end along the length of the cable, while the extracellular solution is unaffected and decays smoothly. As the space constant is increased (gap junction resistance decreased), these discrete jumps reduce in size and more of the decay in the intracellular potential takes

Parameter	Symbol	Value	Units
Resistance of unit area of membrane	R_m	7	kΩ cm^2
Cell length	L	0.012	cm
Intracellular resistivity	ρ_i	0.15	kΩ cm
Extracellular resistivity	ρ_e	0.075	kΩ cm
Cell perimeter	p	0.0071	cm
Space constant	λ_g	indicated in figure	cm

Table 5.1: Parameters to generate analytical cable solutions.

place along the length of the cell rather than across the cell ends. At the extreme case in the final graph, the discrete jumps are barely visible and the intracellular solution appears to decay smoothly in a similar fashion to the extracellular solution.

Figure 5.4 shows the second analytical solution for the transmembrane potential in a cable of 50 cells where a current has been injected into the extracellular space at one end of the cable and flows out of the extracellular space at the other end (two Neumann conditions). To fix a unique solution, the extracellular potential has been set to zero at the left hand end of the cable. The injected current is arbitrarily set to 50 pA. All other parameters are the same as in Table 5.1.

Figure 5.4 demonstrates the characteristic *sawtooth* pattern in the transmembrane potential of this analytical solution. This is caused by the redistribution of the current at cell ends between the intracellular and the extracellular space as it reaches the high resistance gap junction. In the first graph, this pattern is distinct and, as the space constant is increased, the jumps gradually reduce until the solution appears continuous (as in the previous analytical solution).

5.2 Methods

5.2.1 Spectral/hp element method

This section provides a general outline of the spectral/hp element method. The following description is adapted from Karniadakis and Sherwin [227] and Cantwell et al. [228].

The spectral/hp element method can be applied to approximate a numerical solution

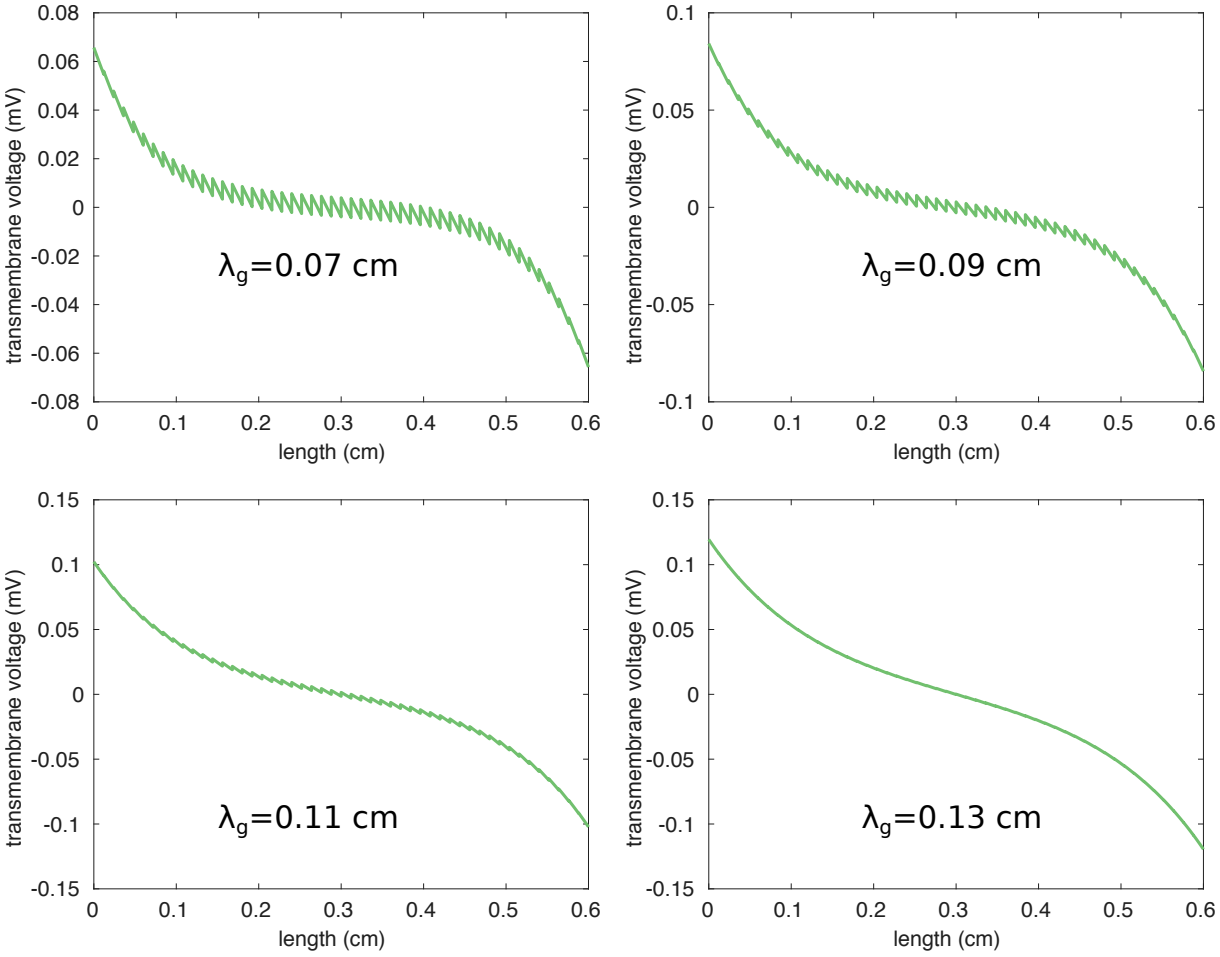


Figure 5.4: Analytical solution for a discretely-coupled cable of cells with injected current into the extracellular space at one end for increasing values of the space constant. Solutions are shown for transmembrane potential along the cable using the parameters in Table 5.1. Solutions are generated following the equations derived in Appendix A.6 and [2].

to some partial differential equation. As a demonstrative example, we use the Helmholtz equation:

$$\nabla^2 u - \lambda u + f = 0 \tag{5.9}$$

in some domain Ω where λ is a real positive constant (unrelated to the space constant term in the previous section) and f is the forcing term. Ω is a d-dimensional mesh split into non-overlapping *elements* Ω_e such that $\Omega = \cup\Omega_e$ and $\Omega_{e_1} \cap \Omega_{e_2} = \partial\Omega_{e_{12}}$ where $\partial\Omega_{e_{12}}$ is either an interface between elements (of lower dimension than Ω) if the elements are adjacent or an empty set otherwise.

The problem is cast into the weak form using the classical Galerkin formulation. This form is obtained by pre-multiplying both sides of the equation by some test function $v(\mathbf{x})$ and integrating over the domain. The problem can then be expressed as: *find* $u \in \mathcal{X}$ *such that*

$$\int_\Omega v \cdot \nabla^2 u \, \mathrm{d}\mathbf{x} - \lambda \int_\Omega vu \, \mathrm{d}\mathbf{x} + \int_\Omega vf \, \mathrm{d}\mathbf{x} = 0, \qquad \forall v \in \mathcal{V} \tag{5.10}$$

where $\mathcal{X}$ and $\mathcal{V}$ are the chosen trial and test space respectively. The effect of casting the equation in the weak form means it no longer has to hold absolutely, and only holds with respect to the test function. This permits the use of linear algebra to numerically solve this form of equations. If $u(\mathbf{x})$ and $v(\mathbf{x})$ are sufficiently smooth, the first term in Equation 5.10 can be integrated by parts to obtain:

$$\int_\Omega \nabla v \cdot \nabla u \, \mathrm{d}\mathbf{x} + \lambda \int_\Omega vu \, \mathrm{d}\mathbf{x} = \int_\Omega vf \, \mathrm{d}\mathbf{x} + \int_{\partial\Omega} v\nabla u \cdot \mathbf{n} \, \mathrm{d}\mathbf{x}. \tag{5.11}$$

This is still an infinite-dimensional problem because the trial and test spaces contain an infinite number of functions. To make the problem computationally tractable, we select subspaces of each $\mathcal{X}^\delta \subset \mathcal{X}$ and $\mathcal{V}^\delta \subset \mathcal{V}$ which contain a finite number of functions. In the hp element method, these subspaces can be thought of as mathematical representations of either h-type or p-type refinement.

We assume that the solution can be approximated by the weighted sum of N trial functions $\Phi_n(\mathbf{x})$ that span the space $\mathcal{X}^\delta$ so that $u^\delta = \sum_n \hat{u}_n \Phi_n(\mathbf{x})$. This reduces the problem to determining the coefficients $\hat{u}_n$. v^δ is similarly approximated with test functions

$\Psi_n(\mathbf{x})$ and in the classical Galerkin approach $\Psi_n = \Phi_n$. Substituting into Equation 5.11, we arrive at the approximate form of the weak solution: *find* $u^\delta \in \mathcal{X}^\delta$ *, such that*

$$\sum_m \sum_n \hat{v}_m \hat{u}_n \int_\Omega \nabla\Phi_m \cdot \nabla\Phi_n + \lambda \sum_m \sum_n \hat{v}_m \hat{u}_n \int_\Omega \Phi_m \cdot \Phi_n = \sum_m \hat{v}_m \int_\Omega f \cdot \Phi_m + \sum_m \sum_n \hat{v}_m \hat{u}_n \int_{\partial\Omega} \Phi_m \nabla\Phi_n \quad (5.12)$$

The global solution u_n^δ is assembled from contributions within each element Ω_e. Each Ω_e is mapped onto a standard reference element Ω_{st} in a reference space $\mathcal{E} \subset [-1,1]^d$. The local coordinate $\xi \in \mathcal{E}$ can be mapped to the global coordinate $\mathbf{x} \in \Omega_e$ through a parametric mapping $\mathbf{x} = \chi^e(\xi)$. In each reference element, a local polynomial basis is constructed to build the local solution, given as $\phi_p(\xi)$ with $0 \leq p \leq P$ where P is the order of the basis function. The basis functions can be modal or nodal, with the choice dictated by the numerical properties. In this thesis, we exclusively use (modal) modified hierarchical Jacobi polynomial basis functions of varying order, given as

$$\phi_p(\xi) = \begin{cases} \frac{1-\xi}{2} & p = 0, \\ \left(\frac{1-\xi}{2}\right)\left(\frac{1+\xi}{2}\right) P_{p-1}^{1,1}(\xi) & 0 < p < P, \\ \frac{1+\xi}{2} & p = P, \end{cases} \quad (5.13)$$

where $P_p^{\alpha,\beta}$ are Jacobi polynomials. The approximate solution within a particular element Ω_e can then be represented in terms of these local expansion modes:

$$u_e^\delta(\mathbf{x}) = \sum_p \hat{u}_p^e \phi_p^e(\xi), \quad (5.14)$$

where $\phi_p^e(\xi) = \phi_p([\chi^e]^{-1}(\mathbf{x}))$.

An assembly matrix $\mathcal{A}$ is used to combine the elemental contributions into a global solution, defined so that $\hat{u}_l = \mathcal{A}\hat{u}_g$ where $\hat{u}_l$ is the concatenated vector of all elemental coefficients. Generally, in continuous Galerkin methods, this operator sums contributions from neighbouring elements to enforce C^0 continuity of the global solution (modifications

to account for multiple sub-domains with non-continuous potential across interfaces will be discussed in our specific implementation below).

To make practical use of the Galerkin formulation above, we require to be able to integrate and differentiate the polynomial bases within the standard elemental regions. To integrate within the standard region, we can approximate the integral using a finite summation known as quadrature:

$$\int_{\Omega_{\text{st}}} u(\xi)d\xi \approx \sum_{q=0}^{Q-1} w_i u(\xi_i), \tag{5.15}$$

where w_i are specified weights and ξ_i represent Q distinct points to evaluate the solution within the standard elemental region. Specifically, in this thesis, we use Gauss-Lobatto-Legendre quadrature. Defining $\xi_{i,P}^{\alpha,\beta}$ as the P zeros of the Pth-order Jacobi polynomial $P_P^{\alpha,\beta}$, the quadrature points and weights are defined as:

$$\xi_i = \begin{cases} -1, & i = 0, \\ \xi_{i-1,Q-2}^{1,1}, & i = 1, \ldots, Q-2, \\ 1, & i = Q-1, \end{cases} \tag{5.16}$$

$$w_i = \frac{2}{Q(Q-1)[L_{Q-1}(\xi_i)]^2}, \qquad i = 0, \ldots, Q-1, \tag{5.17}$$

where $L_Q(\xi)$ is the Legendre polynomial (i.e. $L_Q(\xi) = P_Q^{0,0}(\xi)$) [227]. Using this quadrature rule of order Q we can integrate exactly polynomial bases of order $2Q-3$.

We can differentiate the approximate elemental solution using the chain rule to obtain

$$\frac{du^\delta(\xi)}{dx} = \frac{du^\delta(\xi)}{d\xi}\frac{d\xi}{dx} = \sum_p \hat{u}_p \frac{d\phi_p(\xi)}{d\xi}\frac{d\xi}{dx}. \tag{5.18}$$

Therefore, to evaluate the derivative of the solution we need to be able to evaluate $\frac{d\phi_p(\xi)}{d\xi}$ and $\frac{d\xi}{dx}$. The modal polynomial bases can be represented in terms of Lagrange polynomials, $h_i(\xi)$, to differentiate the solution. The derivative is generally only required at the nodal

points ξ_i of the Lagrange polynomial and is given as

$$\left.\frac{du(\xi)}{d\xi}\right|_{\xi=\xi_i} = \sum_{j\in Q} d_{ij} u(\xi_j), \tag{5.19}$$

where

$$d_{ij} = \left.\frac{dh_j(\xi)}{d\xi}\right|_{\xi=\xi_i}. \tag{5.20}$$

In this thesis the nodal points are, as with integration, given by Gauss-Lobatto-Legendre as in Equation 5.16, with the resulting value of the differentiation matrix d_{ij} at these points given as:

$$d_{ij} = \begin{cases} \frac{-Q(Q-1)}{4}, & i = j = 0, \\ \frac{L_{Q-1}(\xi_i)}{L_{Q-1}(\xi_j)} \frac{1}{\xi_i - \xi_j}, & i \neq j, 0 \leq i, j \leq Q-1, \\ 0, & 1 \leq i = j \leq Q-2, \\ \frac{Q(Q-1)}{4}, & i = j = Q-1, \end{cases} \tag{5.21}$$

where L_Q is the Legendre polynomial as before [227].

In practice, each of these operations is represented by a linear algebra operation on the vector of solution coefficients. Adopting the notation of Cantwell et al. [228]: the basis function is represented by a $P \times Q$ basis matrix on the standard elemental region so that $\phi_p(\xi_q) = \mathbf{B}[p][q]$; the basis derivative is also a $P \times Q$ matrix so that $\nabla\phi_p|_{\xi_q} = \mathbf{DB}[p][q]$; and the quadrature weights are represented by a $Q \times Q$ diagonal matrix $w_i = \mathbf{W}[i][i]$. The mass (or stiffness) matrix $\mathbf{M}$ is a discrete representation of $\int_\Omega \Phi_p \Phi_q \, \mathrm{d}\mathbf{x}$ and can be calculated by $\mathbf{M} = \mathbf{B}^\top \mathbf{W} \mathbf{B}$. The Laplacian matrix $\mathbf{L}$ is a discrete representation of $\int_\Omega \nabla\Phi_p \nabla\Phi_q \, \mathrm{d}\mathbf{x}$ and is analogously calculated by $\mathbf{L} = (\mathbf{DB})^\top \mathbf{W} (\mathbf{DB})$.

Equation 5.12 can now be formulated in linear algebra form:

$$\hat{\mathbf{v}}^\top \mathbf{L} \hat{\mathbf{u}} + \lambda \hat{\mathbf{v}}^\top \mathbf{M} \hat{\mathbf{u}} = \hat{\mathbf{v}}^\top \mathbf{B}^\top \mathbf{W} \mathbf{f}. \tag{5.22}$$

Setting $\mathbf{H} = \mathbf{L} + \lambda \mathbf{M}$ (the Helmholtz matrix) and $\hat{\mathbf{f}} = \mathbf{B}^\top \mathbf{W} \mathbf{f}$, we see the problem is reduced to a simple linear algebra problem $\mathbf{H}\hat{\mathbf{u}} = \hat{\mathbf{f}}$ which can be solved for $\hat{\mathbf{u}}$ using direct or iterative solvers.

5.2.2 Numerical implementation in one dimension

In this section, the spectral/hp element implementation specific to action potential propagation is introduced, for problems in one and three dimensions. The solvers were implemented using the *Nektar++* framework [228, 229] (version 5.0, `https://nektar.info`). Nektar++ gives scope to choose the geometric order and discretisation order of the simulation independently.

In one dimension, we solve the cable equation by treating each cell as an individual sub-domain which is coupled to other cells via current continuity conditions imposed at interfaces. The extracellular space is treated as a single continuous domain.

First, the cable equation is rearranged into a form that can be solved by the spectral/hp element method. If we make the assumption that resistances do not change in the axial direction in either the intracellular or extracellular domains then Equation 5.1 becomes

$$p\left(C_m\frac{\partial V_m}{\partial t}+I_{\text{ion}}\right)=\frac{1}{r_i+r_e}\nabla^2 V_m, \tag{5.23}$$

where parameters are as given previously. Using an implicit backwards Euler scheme for the time derivative gives

$$p\left(C_m\frac{V_m^{n+1}-V_m^n}{\Delta t}+I_{\text{ion}}\right)=\frac{1}{r_i+r_e}\nabla^2 V_m^{n+1}, \tag{5.24}$$

where Δt is the time step and V_m^n denotes the value of V_m at time step n. This equation can then be rearranged into the familiar Helmholtz form (Equation 5.9):

$$\nabla^2 V_m^{n+1}-\lambda V_m^{n+1}+f=0, \tag{5.25}$$

$$f=\lambda\left(V_m^n-\frac{\Delta t}{C_m}I_{\text{ion}}\right), \tag{5.26}$$

where $\lambda=\frac{pC_m(r_i+r_e)}{\Delta t}$. When solving the passive membrane problems of the analytical solutions, the ionic current is assumed to be linear ohmic, i.e. $I_{\text{ion}}={}^{V_m^n}/_{R_m}$, and the forcing becomes

$$f=\lambda\left(1-\frac{\Delta t}{R_m C_m}\right)V_m^n. \tag{5.27}$$

To obtain the extracellular (and, by relation, intracellular) potentials, we consider the conservation of current in each space. The currents flowing through intracellular and extracellular space are given by

$$I_i = -\frac{1}{r_i}\frac{\partial V_i}{\partial x}, \tag{5.28}$$

$$I_e = -\frac{1}{r_e}\frac{\partial V_e}{\partial x}. \tag{5.29}$$

Assuming no external current entering either domain, any changes of intracellular or extracellular current along the cable length must be caused by current flowing across the membrane such that

$$\frac{\partial I_i}{\partial x} + \frac{\partial I_e}{\partial x} = 0. \tag{5.30}$$

This leads to a relationship between the potentials in intracellular and extracellular domains:

$$-\frac{1}{r_i}\nabla^2 V_i - \frac{1}{r_e}\nabla^2 V_e = 0. \tag{5.31}$$

Using the definition of the transmembrane potential ($V_m = V_i - V_e$), Equation 5.31 can be rearranged into Poisson form for V_e:

$$\nabla^2 V_e + f = 0, \tag{5.32}$$

$$f = \frac{r_e}{r_e + r_i}\nabla^2 V_m. \tag{5.33}$$

Lastly, between adjacent intracellular sub-domains, current continuity is enforced across the interfaces. At the Cartesian point which represents the end of one cell and the start of the next, there are two solutions for the intracellular potential (one for each sub-domain, making the assumption that the gap junction is zero length). At a cell end, the current flowing through the gap junction must be conserved and, assuming the gap

junction is a simple resistor,

$$-\frac{1}{r_i}\frac{\partial V_i^-}{\partial x} = I_{\mathrm{GJ}}, \tag{5.34}$$

$$I_{\mathrm{GJ}} = \frac{V_i^+ - V_i^-}{R_g}, \tag{5.35}$$

where + and − indicate the solution at either side of the interface (at the same point in Cartesian space), and R_g is the effective gap junction resistance. Reformulating in terms of V_m and V_e gives

$$-\frac{1}{r_i}\frac{\partial(V_m^- + V_e^-)}{\partial x} = \frac{1}{R_g}\left(V_m^+ - V_m^- + V_e^+ - V_e^-\right). \tag{5.36}$$

The extracellular space is continuous and thus $V_e^+ = V_e^-$ and $\nabla V_e^+ = \nabla V_e^-$. The Neumann condition in terms of V_m then becomes (calculated using values from the previous time step)

$$\left.\frac{\partial V_m^{n+1}}{\partial x}\right|_- = \frac{r_i}{R_g}(V_m^{+,n} - V_m^{-,n}) - \nabla V_e^n. \tag{5.37}$$

To summarise, the computational problem in one dimension can be stated as: *find V_m and V_e in domain Ω such that*

$$\begin{aligned} \nabla^2 V_m^{n+1} - \lambda V_m^{n+1} &= \lambda\left(\frac{\Delta t}{C_m R_m} - 1\right) V_m^n, \\ \nabla^2 V_e^{n+1} &= -\frac{r_e}{r_i + r_e}\nabla^2 V_m^{n+1}, \end{aligned} \tag{5.38}$$

and subject to the boundary conditions described above.

5.2.3 Numerical implementation in three dimensions

The one-dimensional numerical implementation above is analogous to the general bidomain equations in the sense that the extracellular and intracellular spaces exist at the same physical locations and are connected at every point through the membrane equations. In the three-dimensional case, which will be used to generate the results of the following chap-

ter, the intracellular and extracellular spaces now become distinct sub-domains. These multiple sub-domains, $\Omega^{(i)}$, represent individual cells with a separate sub-domain interweaving between cells and representing the extracellular space. The entire computational domain is the union of these sub-domains, $\Omega = \cup_i \Omega^{(i)}$ (each sub-domain is usually also a tessellation of elemental regions as described in Section 5.2.1).

In this model, there are three possible interface surfaces on the boundaries of these sub-domains: (1) a *membrane* where an intracellular sub-domain shares an interface surface with an extracellular sub-domain; (2) a *gap junction* where two intracellular sub-domains share an interface; and (3) on the external boundary of the global domain, where conditions depend on the specific problem. In the first two cases, these interfaces are shared boundaries of each sub-domain (i.e. we do not consider any space to exist in the space between the boundaries, and geometrically they are the same surface): $\partial\Omega_{\text{membrane}} = \Omega^{(i)} \cap \Omega^{(j)}$ when i and j are intracellular/extracellular sub-domains, $\partial\Omega_{\text{GJ}} = \Omega^{(i)} \cap \Omega^{(j)}$ when i and j are both intracellular sub-domains. In contrast to other parts of the computational domain, two global solutions to the potential exist at these interfaces (one in either of the intersecting sub-domains).

Each sub-domain (both cells and extracellular space) is assumed to be a volume conductor that contains no current sources. Using a quasi-static approximation gives Laplace's equation within each sub-domain:

$$\nabla\sigma^{(i)}\nabla V^{(i)} = 0, \tag{5.39}$$

where $\sigma^{(i)}$ is the scalar conductivity of sub-domain $\Omega^{(i)}$ and $V^{(i)}$ is the electrostatic potential. Note that in the three-dimensional implementation the intracellular and extracellular spaces are distinct in space, so there is no requirement to distinguish between the intracellular and extracellular potentials, and the transmembrane potential only exists on membrane interfaces.

The equations are recast into weak form by pre-multiplying by a test function v and

integrating over the sub-domain Ω_i:

$$(v^{(i)}, \nabla\sigma^{(i)}\nabla V^{(i)})_{\Omega^{(i)}} = 0, \tag{5.40}$$

where v is by definition zero on all Dirichlet boundaries and the inner product is defined as $(v, V)_\Omega = \int_\Omega v(\mathbf{x})V(\mathbf{x})\,\mathrm{d}\mathbf{x}$.

The divergence theorem is applied to obtain (dropping the sub-domain indexing for brevity)

$$(\nabla v, \sigma\nabla V_\Omega) - \langle v, \sigma\nabla V \cdot \mathbf{n}\rangle = 0, \tag{5.41}$$

where

$$\langle v, \sigma\nabla V \cdot \mathbf{n}\rangle = \int_{\partial\Omega} v(\mathbf{x})\sigma\nabla V(\mathbf{x}) \cdot \mathbf{n}\,\mathrm{d}\mathbf{x} \tag{5.42}$$

represents the flux term and is non-zero only on Neumann boundaries, since the test function v is defined as zero on all Dirichlet boundaries [227]. The current flux through membranes or gap junctions between sub-domains is enforced through this term.

At an interface between an intracellular domain and the extracellular domain, this current term $\sigma\nabla V \cdot \mathbf{n}$ represents the current flowing across a cellular membrane, defined as

$$-\sigma\nabla V \cdot \mathbf{n} = I_m \qquad \text{for intracellular,} \tag{5.43}$$

$$-\sigma\nabla V \cdot \mathbf{n} = -I_m \qquad \text{for extracellular,} \tag{5.44}$$

$$I_m = C_m\frac{\partial V_m}{\partial t} + I_{\text{ion}}(V_m, t), \tag{5.45}$$

where I_m is the membrane current per unit area, C_m is the capacitance per unit area, V_m is the transmembrane voltage difference ($V_m = V_i - V_e$) and I_{ion} is the current per unit area calculated using a cell model (as described in Chapters 3 and 4).

On an interface between two intracellular domains, the current is assumed to flow through gap junctions which are approximated as linear ohmic resistors with a parallel

capacitor made of the abutting cell membranes:

$$-\sigma \nabla V \cdot \mathbf{n} = I_{12} \qquad \text{for cell 1,} \tag{5.46}$$

$$-\sigma \nabla V \cdot \mathbf{n} = -I_{12} \qquad \text{for cell 2,} \tag{5.47}$$

$$I_{12} = C_{12} \frac{\partial w}{\partial t} + I_{\text{GJ}}, \tag{5.48}$$

$$I_{\text{GJ}} = \frac{w}{R_{\text{GJ}}}, \tag{5.49}$$

where I_{12} is the current per unit area between cell subdomains Ω_1 and Ω_2, C_{12} is the capacitance per unit area of the two abutting membranes (assumed to have no extracellular space in between), w is the potential difference across the gap junction interface $w = V_1 - V_2$, and R_{GJ} is the resistance of a unit area of gap junction interface.

At both of these types of interfaces, values of the potential on either side of the interface are used to determine the boundary condition. Rather than calculate the value of this Neumann condition from the previous time step solution to impose it in the present time step, the boundary condition equations can be discretised and incorporated into the problem matrix and right hand side forcing function. This avoids the situation where individual cell sub-domains are subject only to Neumann boundary conditions causing the problem to become ill-posed.

On a membrane interface, the time derivative can be discretised using finite difference:

$$-\sigma \nabla V \cdot \mathbf{n} = \frac{C_m}{\Delta t} \left[\left(V_i^{n+1} - V_e^{n+1} \right) - \left(V_i^n - V_e^n \right) \right] + I_{\text{ion}}, \tag{5.50}$$

where the transmembrane potential, V_m, has been expanded into the solution at the interface in the intracellular, V_i, and extracellular sub-domains, V_e. The $n+1$ time terms are unknown so their multiplying constants can be incorporated into the global matrix on the left hand side of the problem (recall the computational problem using spectral/hp element methods will reduce to a simple matrix problem of the form $\mathbf{H}\hat{\mathbf{u}} = \hat{\mathbf{f}}$). The n time terms are known so can be added to the forcing term on the right hand side of the problem. As the current flux is enforced via the inner product with the test function, it results in using the elemental mass matrix for the interface multiplied by some constant,

either $\frac{C_m}{\Delta t}$ or $-\frac{C_m}{\Delta t}$. The I_{ion} term is separately added to the forcing term and calculated using the transmembrane potential at the previous time step as input to the cell model.

The time derivative of the gap junction can be discretised in a similar fashion:

$$-\sigma \nabla V \cdot \mathbf{n} = \frac{C_{12}}{\Delta t}\left[\left(V_1^{n+1} - V_2^{n+1}\right) - \left(V_1^n - V_2^n\right)\right] + \frac{1}{R_{\text{GJ}}}(V_1^{n+1} - V_2^{n+1}). \tag{5.51}$$

Again the $n+1$ terms appear on the left hand side of the matrix problem and the n terms appear on the right hand side. The left hand side terms can be multiplied by the elemental mass matrix, and a multiplying constant, $\pm\left(\frac{C_{12}}{\Delta t} + \frac{1}{R_{\text{GJ}}}\right)$. The right hand side terms will be multiplied by the elemental mass matrix and a multiplying constant $\pm\frac{C_{12}}{\Delta t}$.

Considering the above, the discrete form of the equations for the global solution can be stated as

$$\mathbf{L}\hat{\mathbf{V}}_g + \mathbf{\Gamma}_{\text{LHS}}\mathbf{M}\hat{\mathbf{V}}_g = \mathbf{\Gamma}_{\text{RHS}}\mathbf{M}\hat{\mathbf{V}}_{\text{prev,g}} + \hat{\mathbf{f}}, \tag{5.52}$$

where $\mathbf{L}$ is the Laplacian matrix, $\mathbf{M}$ is the mass matrix and we introduce the sparse interface mapping matrices on both sides of the equation, $\mathbf{\Gamma}$, which impose the flux conditions between sub-domains described above.

To break down each of these terms, we first have the Laplacian matrix which has the structure

$$\begin{bmatrix} \sigma^{(i,e)} l_{1,1} & \sigma^{(i,e)} l_{1,2} & \cdots & \sigma^{(i,e)} l_{1,N} \\ \sigma^{(i,e)} l_{2,1} & \sigma^{(i,e)} l_{2,2} & \cdots & \sigma^{(i,e)} l_{2,N} \\ \vdots & \vdots & \ddots & \vdots \\ \sigma^{(i,e)} l_{N,1} & \sigma^{(i,e)} l_{N,2} & \cdots & \sigma^{(i,e)} l_{N,N} \end{bmatrix} \hat{\mathbf{V}}_g, \tag{5.53}$$

where each term $l_{i,j}$ is calculated from the basis functions $\int_\Omega \nabla\Phi_i \nabla\Phi_j \, \mathrm{d}\mathbf{x}$ as described in Section 5.2.1 and multiplied by a conductivity term according to which sub-domain the solution coefficient exists in.

To demonstrate the form of $\mathbf{\Gamma}$ we consider one global solution coefficient on an interface where $\hat{\mathbf{V}}_g^i$ and $\hat{\mathbf{V}}_g^j$ are on either side of the interface. Firstly, if the interface is a membrane,

the submatrix for $\mathbf{\Gamma}_{\text{LHS}}\mathbf{M}\hat{\mathbf{V}}_g$ containing these solution terms will look like

$$\begin{bmatrix} \frac{C_m}{\Delta t}m_{i,i} & -\frac{C_m}{\Delta t}m_{i,j} \\ -\frac{C_m}{\Delta t}m_{j,i} & \frac{C_m}{\Delta t}m_{j,j} \end{bmatrix} \begin{bmatrix} \hat{V}_g^i \\ \hat{V}_g^j \end{bmatrix}, \tag{5.54}$$

where $m_{i,j}$ are mass matrix terms $\int_\Omega \Phi_i \Phi_j \mathrm{d}\mathbf{x}$. The right hand side submatrix of $\mathbf{\Gamma}_{\text{RHS}}\mathbf{M}\hat{\mathbf{V}}_{\text{prev,g}}$ will be identical, though using the global solution vector for the previous time step. The forcing in this case would have the I_{ion} term added, where it is calculated using the previous time step solution, i.e.

$$\hat{\mathbf{f}}_{\text{membrane}} = \hat{\mathbf{f}} + \begin{bmatrix} -I_{\text{ion}} \\ I_{\text{ion}} \end{bmatrix}, \tag{5.55}$$

where we have assumed the ith solution coefficient is on the intracellular side and the jth solution coefficient is on the extracellular side (the signs would be inverted in the other case).

Analogously, for a gap junction interface, on the left hand side we have

$$\begin{bmatrix} (\frac{C_{12}}{\Delta t} + \frac{1}{R_g})m_{i,i} & -(\frac{C_{12}}{\Delta t} + \frac{1}{R_g})m_{i,j} \\ -(\frac{C_{12}}{\Delta t} + \frac{1}{R_g})m_{j,i} & (\frac{C_{12}}{\Delta t} + \frac{1}{R_g})m_{j,j} \end{bmatrix} \begin{bmatrix} \hat{V}_g^i \\ \hat{V}_g^j \end{bmatrix}, \tag{5.56}$$

and on the right hand side

$$\begin{bmatrix} \frac{C_{12}}{\Delta t}m_{i,i} & -\frac{C_{12}}{\Delta t}m_{i,j} \\ -\frac{C_{12}}{\Delta t}m_{j,i} & \frac{C_{12}}{\Delta t}m_{j,j} \end{bmatrix} \begin{bmatrix} \hat{V}^i_{\text{prev,g}} \\ \hat{V}^j_{\text{prev,g}} \end{bmatrix}, \tag{5.57}$$

and no additional current term is added to the forcing vector.

The global solution vector is ordered such that Dirichlet solution coefficients are first, followed by solution coefficients on interfaces. This reduces the bandwidth of the resulting global matrix. Only element boundary coefficients are assembled into the global matrix, the interior coefficients are solved at the elemental level using static condensation [227]. The matrix system is solved using a conjugate gradient algorithm with linear

preconditioner.

5.2.4 Parallelisation

As the linear system is solved using an iterative solver, it can be parallelised to improve performance or satisfy memory requirements of large problems. However, as the interfaces are solved by using the solution on either side, a problem can arise when these sides are split between multiple processes, and thus a solution coefficient required to solve a given interface may not be locally available to a process.

To handle these cases, 'ghost' interfaces are created on either process which the interface is split between. Practically, this involves creating additional faces on the local process which then hold the solution values from the opposing interface on the other process. These solution values are transferred between processes prior to the iterative solve step using MPI.

Figure 5.5a shows a simple two-dimensional example where the left hand element is assigned to the rank 0 process and the right hand element is assigned to the rank 1 process. These elements are connected across one edge through an interface. Thus, to solve the problem in the rank 0 process requires the solution at vertices 5 and 6, and to solve the problem in the rank 1 process requires the solution at vertices 3 and 4.

Figure 5.5b shows how the full problem would be assembled into a global matrix problem if all on one process. The shaded boxes are non-zero values in the array. We can see the matrix has a diagonal structure with off-diagonal elements connecting either side of the interface. The matrix multiplying the previous time step solution only acts on these points as only interfaces require this information. The dashed line through the centre of the matrices and vectors highlights how the solution coefficients would be split between processes if run in parallel. Figure 5.5c now demonstrates how this case is handled in parallel on the rank 0 process (the rank 1 process is analogous). The ghost interface solutions are copied across onto the end of the solution vector, which makes it possible to fill in the off-diagonal component in the problem matrices.

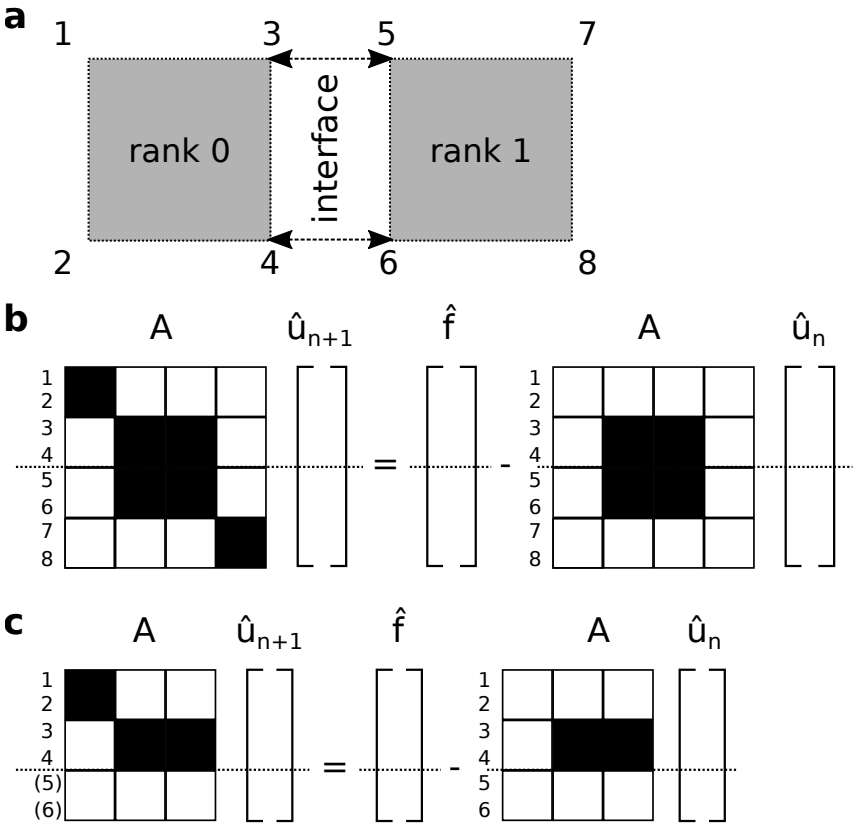


Figure 5.5: **a** An example split-process interface setup in two dimensions. The elements are connected by one edge through an interface, and thus require access to the solution space on the opposing process. **b** The global matrix problem. Filled boxes in the matrix represent non-zero values. The off-diagonal filled boxes highlight how the interface is connected. **c** Matrix problem for the rank 0 process demonstrating the ghost vertices being added to the solution space to expand the matrix allowing the interface to be solved correctly.

Parameter	Value	Units
R_m	7	kΩ cm^2
C_m	1.2	μF/cm^2
p	0.00709	cm
r_i	37.5	MΩ/cm
r_e	$0.5r_i$	MΩ/cm
L	0.012	cm

Table 5.2: One-dimensional cable simulation parameters and values.

5.2.5 Simulation setup

One-dimensional cable validation. A line geometry was created and discretised into elements of length 0.001 cm (units of length are generally given in cm as the resulting simulation parameters will end up at the same order of magnitude). The 'cable' is assumed to be composed of cells of length 0.012 cm (i.e. each cell is split into 12 one-dimensional elements). The number of cells is 16 for the fixed boundaries validation, and 50 for the injected current validation case. Within each element, fourth-order Jacobi polynomials are used as basis functions to approximate the solution to the transmembrane and extracellular potentials. Other parameters are given in Table 5.2.

The analytical solution was calculated for four values of the space constant from 0.07 cm to 0.13 cm in steps of 0.02 cm, chosen to cover a wide range of effective gap junction resistances. These space constants correspond to gap junction resistances of (in order of increasing decay constant): 1750 kΩ, 788 kΩ, 304 kΩ and 26 kΩ. For the simulation of the first analytical case, Dirichlet boundary conditions were set for both V_m and V_e at either cable end equal to the analytical value at those points. For the simulation of the second analytical case, Neumann boundary conditions corresponding to no current into the intracellular space were set at either cable end, and Neumann boundary conditions corresponding to injecting a current of 50 pA were set for V_e at either cable end (in practice, conditions were $\frac{1}{r_e}\frac{\mathrm{d}V_m}{\mathrm{d}x} = I$ and $\frac{1}{r_e}\frac{\mathrm{d}V_e}{\mathrm{d}x} = -I$ at $x = 0$ where I is the injected current, with the signs reversed at the opposite cable end). To fix a unique solution in this second case, a Dirichlet boundary condition for V_e was arbitrarily set to zero at $x = 0$.

The simulations were run on a single CPU (Intel(R) Xeon(R) CPU E5-2697 v2 @ 2.7

GHz) using a time step of 5 μs, with the exception of the lowest gap junction resistance simulations which used a time step of 0.05 μs to maintain numerical stability. Simulations were run to 0.5 ms to ensure a steady-state solution had been reached, from initial conditions for both solutions set to zero throughout the domains.

Three-dimensional cable validation. The three-dimensional cable model for the validation cases was created as a cylindrical cable of cells surrounded by extracellular space. The cells each have length 0.012 cm and radius 0.0011 cm (giving perimeter equivalent to the one-dimensional case above). The extracellular cylindrical sub-domain extended along the length of the cable, with radius 0.01 cm to reduce far-field effects of the outer boundary. The domain was discretised into triangular prisms with length in the axial direction of 0.001 cm and mesh size in the plane of 25 μm within cells, increasing to 250 μm on the outer boundary of the extracellular sub-domain. Linear basis functions were used to approximate the solution within each element.

The intracellular conductivity, σ_i, was set to 0.0067 mS/cm, which is equivalent to the resistivity assumed in the one-dimensional case (which can be calculated from the intracellular resistance per unit length and cable cross-sectional area). The extracellular conductivity, σ_e, was set to 0.00018 mS/cm, which is analogously calculated using the resistivity assumed in the one-dimensional case and the cross-sectional area of the extracellular sub-domain in the model.

As the gap junction occurs over a surface rather than a discrete point in the three-dimensional case, its resistance value is given in terms of unit area as with the membrane resistance value. In the three-dimensional validation, we simulated space constants of 0.07, 0.09 and 0.11 cm which correspond to effective gap junction resistances of: 0.0070 kΩ cm^2, 0.0032 kΩ cm^2 and 0.0012 kΩ cm^2. For the validation cases, the membrane was assumed passive with the same resistance and capacitance values as in the one-dimensional case. For simulations of the first analytical case, Dirichlet boundary conditions were imposed on the outer surfaces representing the cable ends of both intracellular and extracellular space, equal to the analytical value at those points. For simulations of the second analytical case, zero Neumann boundary conditions were imposed on the surfaces representing the

intracellular cable ends, a zero Dirichlet boundary condition was imposed on the surface representing the extracellular cable end at $x = 0$ to fix a unique solution, and a Neumann boundary condition corresponding to the injected current was imposed on the surface representing the other extracellular cable end ($\nabla V \cdot \mathbf{n} = {}^{I}/_{\sigma_e}$ where I is the injected current). In simulations for both analytical cases, the farfield boundary surface was set to a zero Neumann boundary condition.

The simulations were run using a time step of 0.1 ms until 50 ms when steady-state had been reached. Initial conditions of zero potential were imposed everywhere at the start of the simulation. Both validation cases were run in serial on a single CPU (Intel(R) Xeon(R) CPU E5-2697 v2 @ 2.7 GHz) using a cable of 16 cells for both validation cases.

Three-dimensional cable propagation. The validation cases assume a passive membrane model where $I_{\text{ion}} = {}^{V_m}/_{R_m}$. To demonstrate propagation, a human atrial cell model [166] (the Courtemanche model studied in Chapter 3) was solved at the membrane interface using the Rush-Larsen integration scheme for gating variables [230].

The cable for these simulations was composed of 16 cylindrical cells with length 0.01 cm and radius 0.001 cm. The cells were surrounded by an extracellular space with outer radius 0.005 cm. As opposed to the above validation case where the cable touches the edges of the domain (so that specific boundary conditions could be set), in this case a 0.002 cm buffer of extracellular space was created at either end of the cable. The cable ends were thus also assumed to be membrane interfaces.

The geometry was discretised into triangular prisms with height along the length of the cable of 0.001 cm (10 μm) and mesh size in the transverse plane of 5×10^{-4} cm within the cells increasing to 0.002 cm on the outer domain boundary. This resulted in a mesh containing $\sim$50,000 elements. Intracellular and extracellular conductivity values were 4 and 20 mS/cm respectively [121]. C_m was set to 1 μF/cm^2. Each simulation was run for 50 ms, with time step of 0.1 ms and the cell model sub-stepped at 0.025 ms. The iterative solver tolerance was set to 1×10^{-5}. The solution in each element was approximated using third-order modified Jacobi polynomial basis functions.

All cells were initialised at rest by setting the initial solution to -81.19 mV in the

cellular sub-domains (the resting potential of the Courtemanche cell model). The extracellular sub-domain was initialised at 0 mV, and fixed Dirichlet boundary conditions were imposed on the outer far-field boundary to 0 mV. To initiate an action potential response at one cable end, the first cell in the cable was stimulated by applying a stimulus current of 120 μA/cm^2 at $t = 0.5$ ms for 1 ms across all of its membrane interfaces.

The propagation simulations were run on a computing cluster across 16 CPUs (Intel(R) Xeon(R) CPU E5-2697 v2 @ 2.7 GHz). The simulations were run with values for gap junction resistance of 0.016, 0.032, 0.064 and 0.128 kΩ cm^2 to demonstrate the effect of increasing gap junction resistance on propagation.

Parallel scaling performance. Strong and weak parallel scaling were assessed using regular grids of idealised three-dimensional cells surrounded by extracellular space, to represent an idealised monolayer. Each cell was constructed as a cuboid of length and width 20 μm and height 5 μm. The edges of the monolayer are surrounded by a 50 μm buffer of extracellular space off either side, and 10 μm above the cells. The lower surface of the cell monolayer touched the bottom domain boundary (i.e. the microscopy dish) and was assigned a no-flux Neumann boundary condition. The outer far-field boundary was set to a zero Dirichlet condition as above. The monolayer was discretised into triangular prisms of height 5 μm and mesh size 5 μm within cells increasing to 10 μm on the outer edges of the domain.

Intracellular and extracellular conductivity were set to 4 and 20 mS/cm respectively. The membrane capacitance was set to 1 μF/cm^2. The gap junction resistance was not varied in these experiments and held at 0.018 kΩ cm^2. The elemental solutions were approximated using linear basis functions. Simulations were run with a time step of 0.01 ms for 50 ms. A variant of the HL1-6 cell model developed in Chapter 4 was assigned to each cell and solved on its membrane interfaces. The random distribution of variants was kept the same between experiments. The cell model was sub-stepped at 0.025 ms and solved using the Rush-Larsen scheme as previously [230].

For strong scaling, which tests the simulation time of a constant problem size as the number of processors is increased, the size of the monolayer was 80×10 cells. Cells

were stimulated by injecting a current through a circular region of the lower 'dish' surface, representing an electrode. The electrode was positioned on the centre line of the monolayer strip and 100 μm in from one edge. It had diameter 30 μm and injected a stimulus current of 500 μA/cm^2 for 10 ms at the beginning of the simulation.

Weak scaling tests how the simulation time changes as the number of processors is increased and the problem size increases proportionally (to maintain a constant problem size on each processor). In this case, a monolayer of $10n \times 10$ cells was generated where n represents the number of processors. All cell sub-domains were assigned the same HL1-6 cell model variant. In this case, the monolayer was stimulated by applying a current across membrane boundaries on the edge along the length of the monolayer strip, to ensure each processor is approximately solving the same problem. A current of 100 μA/cm^2 was injected through these interfaces for the first 2 ms of the simulation.

Parallel scaling tests were run on the Imperial College CX1 computing cluster on nodes containing 32 CPUs (AMD EPYC 64-core processor @ 2.25 GHz) and across up to 4 nodes (i.e. 128 CPUs).

5.3 Results

5.3.1 Validating the numerical implementation in one dimension

Firstly the one-dimensional numerical implementation was validated against the two analytical solutions described previously. Figure 5.6 plots the intracellular, extracellular and transmembrane potentials from simulation against the analytical solutions for four different values of gap junction resistance (given as decay constants in annotations), for the case where either end of the cable has fixed potentials on the intracellular and extracellular solutions.

The simulation results show the same features as described previously for the theoretical results. Across the range of gap junction resistances and along the cable length, the analytical solution (plotted as dashed lines) and simulation results (solid lines) clearly match closely.

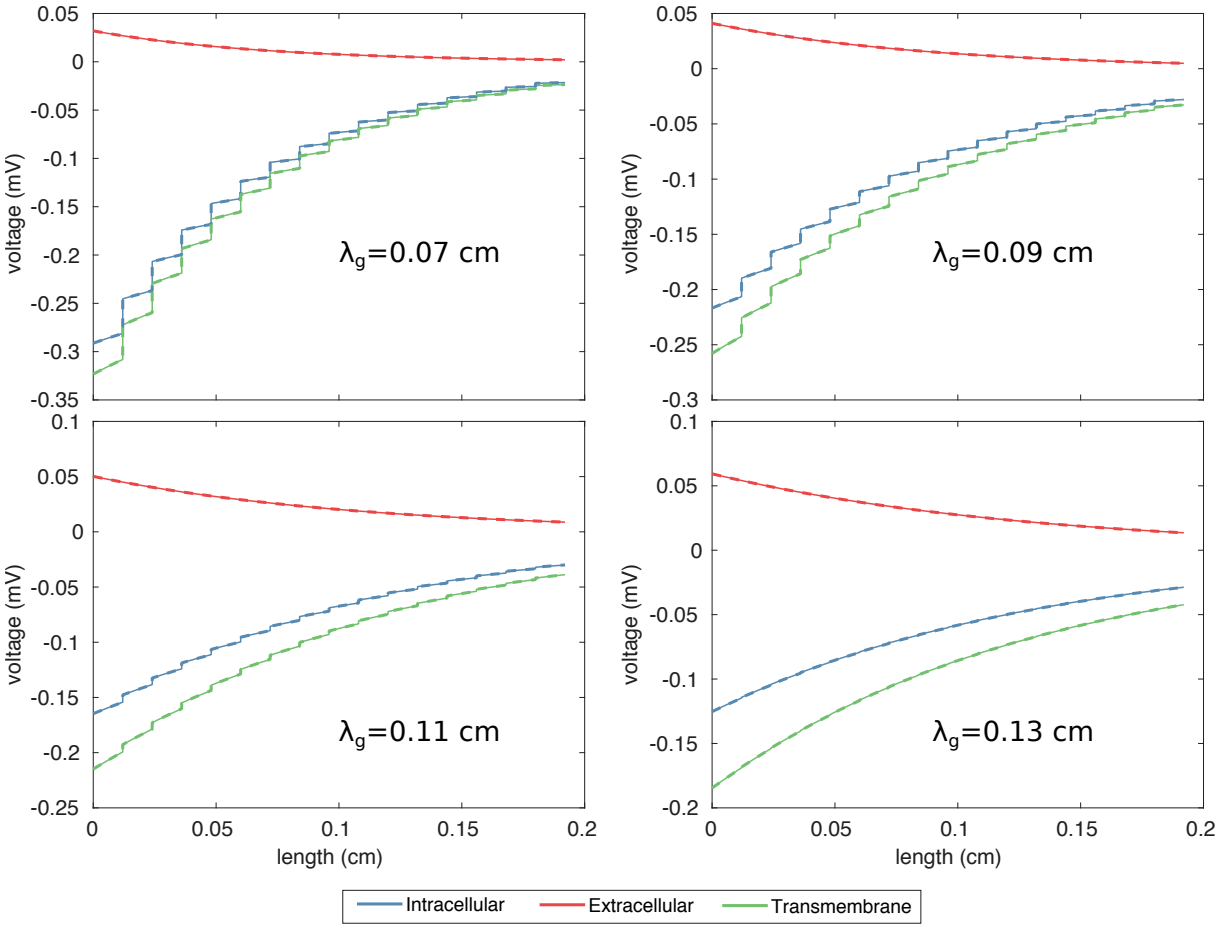


Figure 5.6: One-dimensional simulation results for fixed end potentials for four values of gap junction resistance (indicated by different decay constants given in figures). Simulation results are plotted as solid lines and analytical solutions as dashed lines.

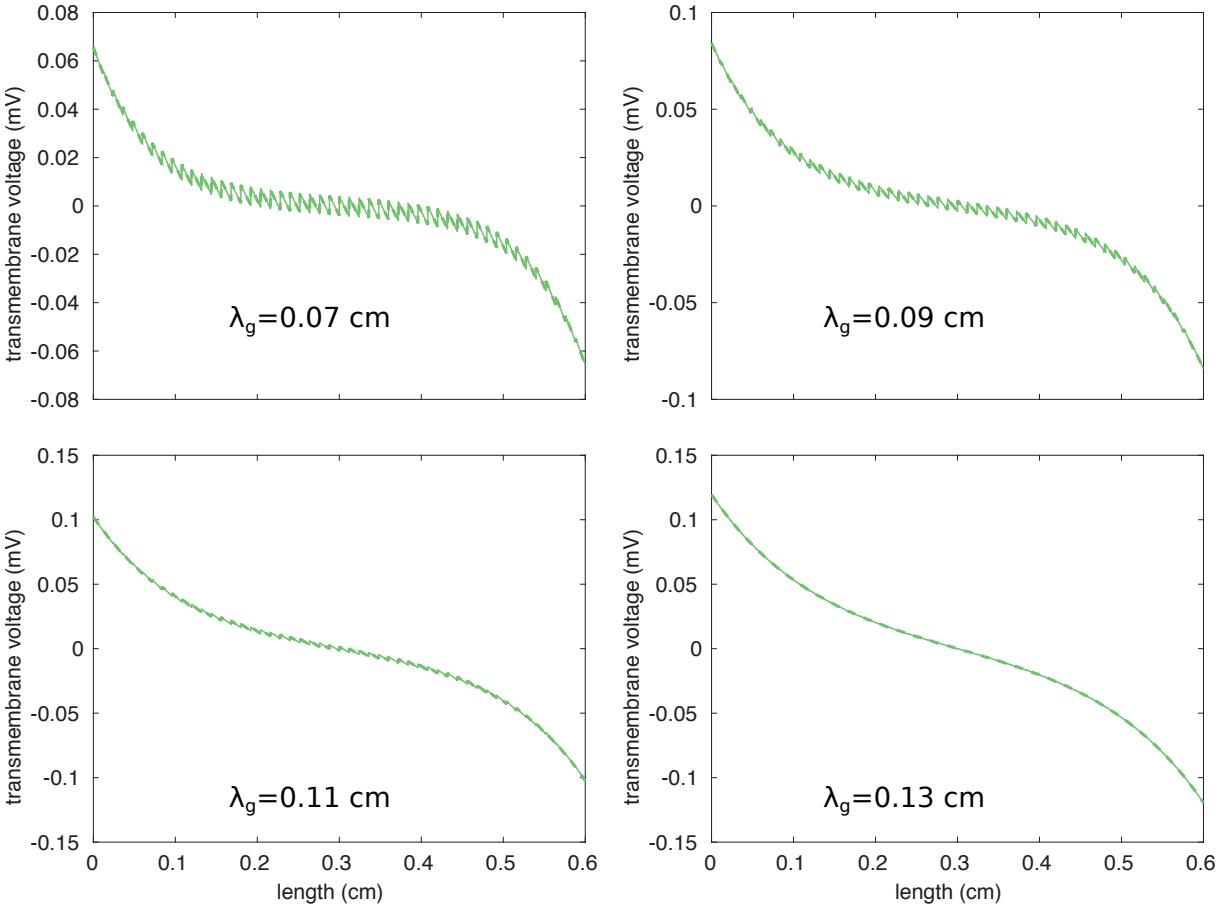


Figure 5.7: One-dimensional simulation results for current injected into one end of the cable for four values of gap junction resistance (indicated by different decay constants given in figures). Simulation results are plotted as solid lines and analytical solutions as dashed lines.

Figure 5.7 shows the one-dimensional cable simulation for the second analytical case of injecting a current into the cable end. Again, the simulation matches the analytical solution at all gap junction resistance values and along the cable length, displaying the characteristic sawtooth pattern which gradually reduces to being barely distinguishable at the lowest level of gap junction resistance.

5.3.2 Model validation in three dimensions

Having shown that a one-dimensional implementation closely matches the analytical solutions, we next sought to validate an equivalent three-dimensional model. In the following cases, the intracellular solution and extracellular solution values were extracted from an axial line immediately on either side of the membrane interface along the length of the cable, and the transmembrane potential was calculated as the difference between these

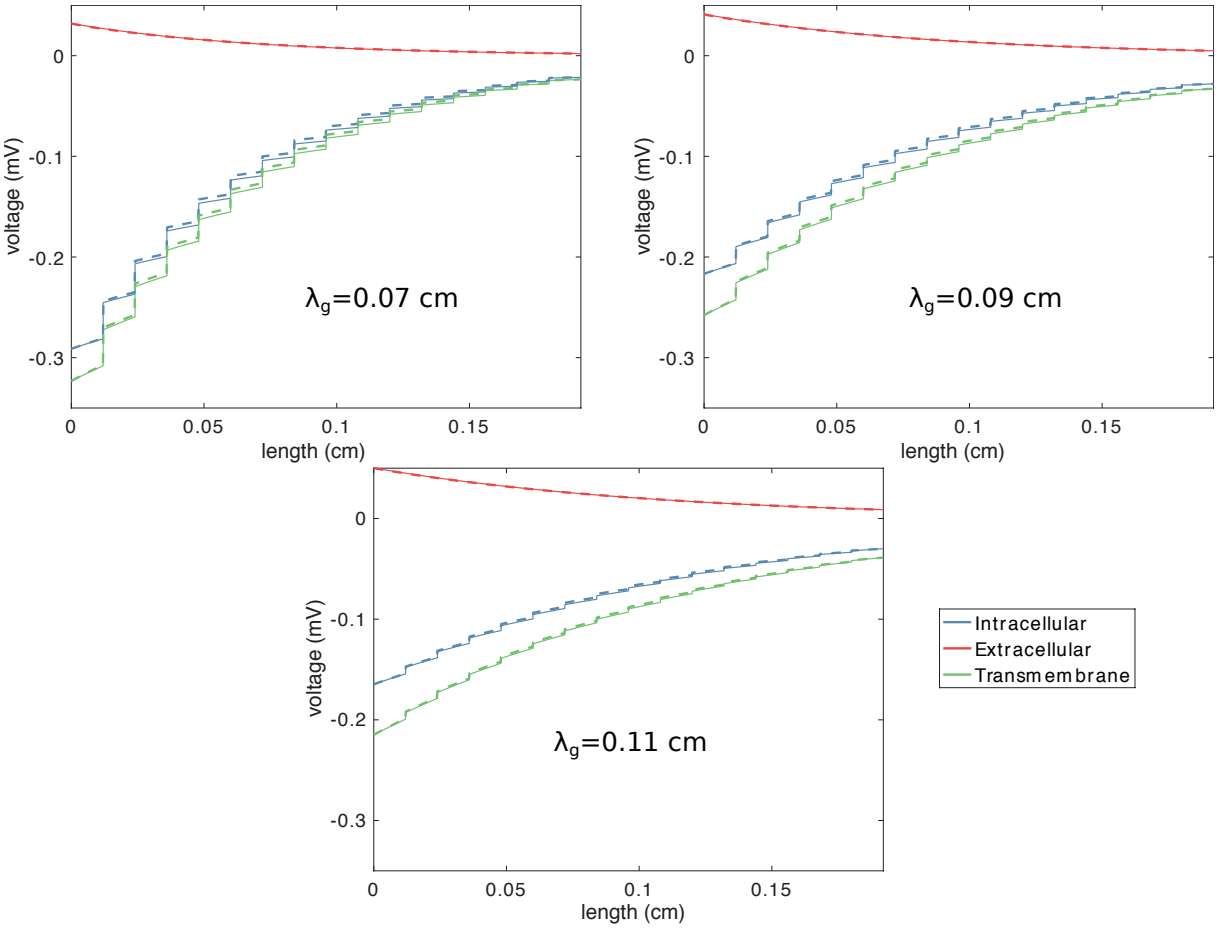


Figure 5.8: Three-dimensional cable simulation results compared to analytical solution for fixed potential at either cable end for different values of gap junction resistance (indicated by decay constants in annotations). Solid line is plotted from an axial line through the three-dimensional cable (refer to text) and the analytical solution is plotted as a dashed line.

two lines.

Figure 5.8 shows the three-dimensional simulation results compared to the analytical solution for fixed potentials at either end of a cable of 16 coupled cells. As in the one-dimensional case, the extracellular solution decays smoothly and is close to the analytical values. The intracellular solution shows the expected jumps across gap junction surfaces at cell ends. However, as opposed to the one-dimensional case, the solution does not match the analytical values as closely, with discrepancy at higher gap junction resistance values in the central portion of the cable.

Figure 5.9 plots the transmembrane potential for a simulation of injecting current into a cable of 16 coupled cells compared to the analytical solution. As in the one-dimensional case, the solution exhibits the expected sawtooth pattern, which is more prominent at higher values of gap junction resistance (though less noticeable in these plots as the cable

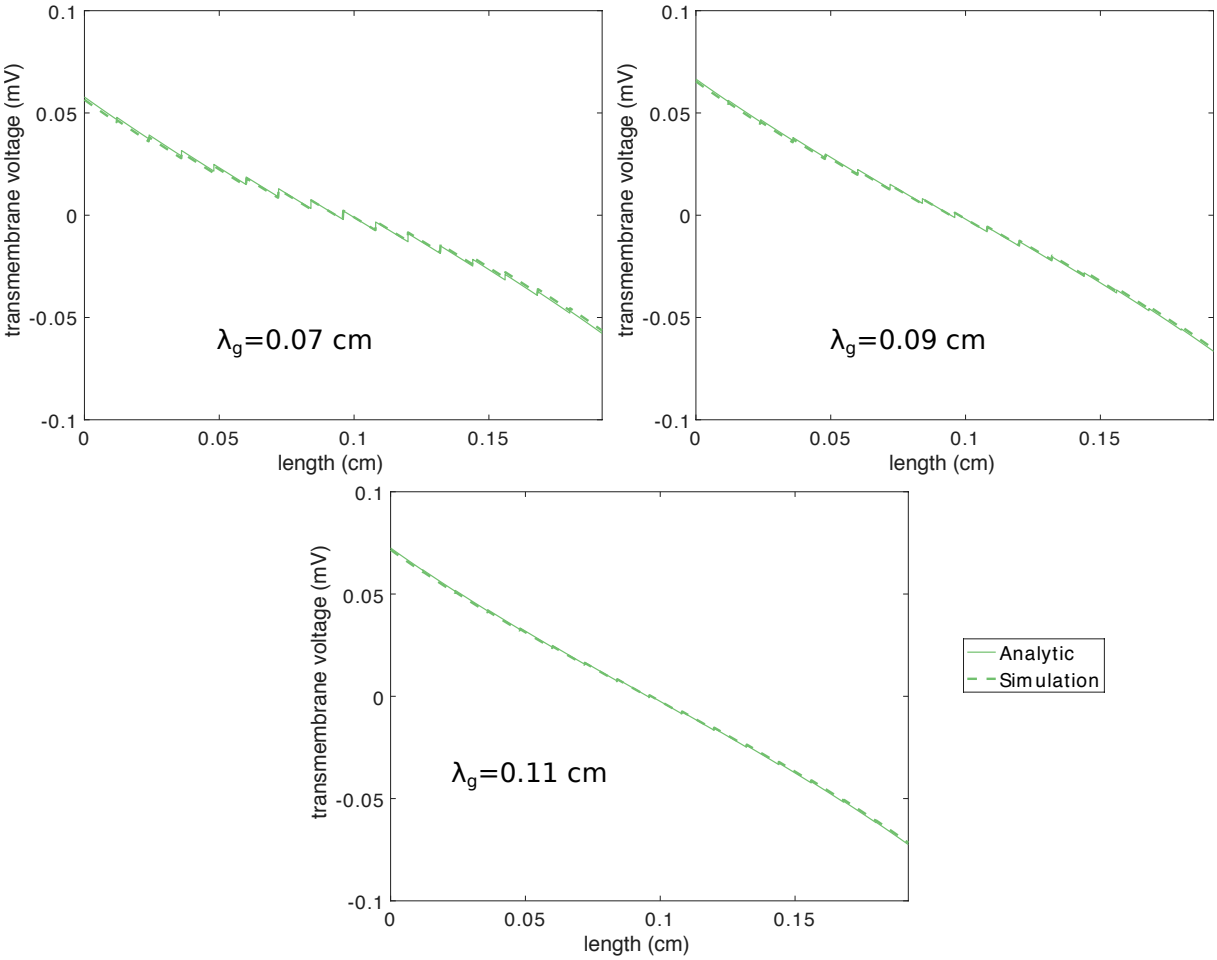


Figure 5.9: Three-dimensional cable simulation results compared to analytical solution for an injected current for different values of gap junction resistance (indicated by decay constants in annotations). The simulation results are calculated from the difference between the potential along two axial lines (one in intracellular and the other in extracellular space, refer to text), and the analytical solution is plotted as dashed line.

is shorter). The simulation results are close, but not identical to, the analytical solution across the gap junction resistances tested. The discrepancy is minimal in the central portion of the cable and increases towards the cable ends.

5.3.3 Propagation along a cable of cells

The previous simulations used a passive membrane model where $I_{\text{ion}} = {}^{V_m}/_{R_m}$ to compare with theoretical solutions which can be derived under these conditions. Next, an active membrane is demonstrated where the ionic current is the solution to some cell model which can fire an action potential. The action potential initiated at one end of the cable would be expected to propagate along the cable as current flows between coupled cells.

Figure 5.10 shows snapshots of the potential plotted along the centre line of the cable at different time points for each of four gap junction resistance values. At $t = 0$ ms, the cells in the cable start at rest with an intracellular potential of approximately -80 mV. At $t = 1$ ms, the stimulus current causes the intracellular potential to rise in the rightmost cell (where it is injected at $t = 0.5$ ms). This rise in intracellular potential is largest for the simulation with highest gap junction resistance, as less current flows into adjacent cells (note how the second-from-right cell has the lowest potential of the different resistance plots at this time point). At $t = 2$ ms, the stimulus current has initiated an action potential response in the first cell. In the following sub-figures, the current flowing from this initial cell raises neighbouring cells above their threshold potential causing them to similarly fire and propagate the action potential signal along the cable.

Discrete steps in potential are clearly visible across the gap junction interfaces at cell ends, as we saw in the validation plots above. As expected, increasing gap junction resistance increases the time taken for the activation wave front to reach the opposing end of the cable. Increasing gap junction resistance reduces the amount of charge which flows into adjacent cells, which can be seen by the higher peak potential reached by cells in the slowest propagating cable compared to other values (e.g. $t = 2$ ms in Figure 5.10).

5.3.4 Parallel scaling performance

The previous simulations were all conducted in idealised cables of 50 or fewer cells. The overall goal of this thesis is to simulate a monolayer which may contain thousands of cells. Therefore, it was necessary to develop a scalable implementation that could be run across many CPUs. This section presents results for strong and weak scaling properties of the three-dimensional implementation.

Strong scaling was assessed by running the same size of problem (i.e. the same geometry) across an increasing number of compute processes. Ideal scaling would be expected to produce an inverse linear relationship between the number of compute processes and time taken for the simulation to run. Simulations were run across an increasing number of processors as described in the methods. For each simulation the total time taken was

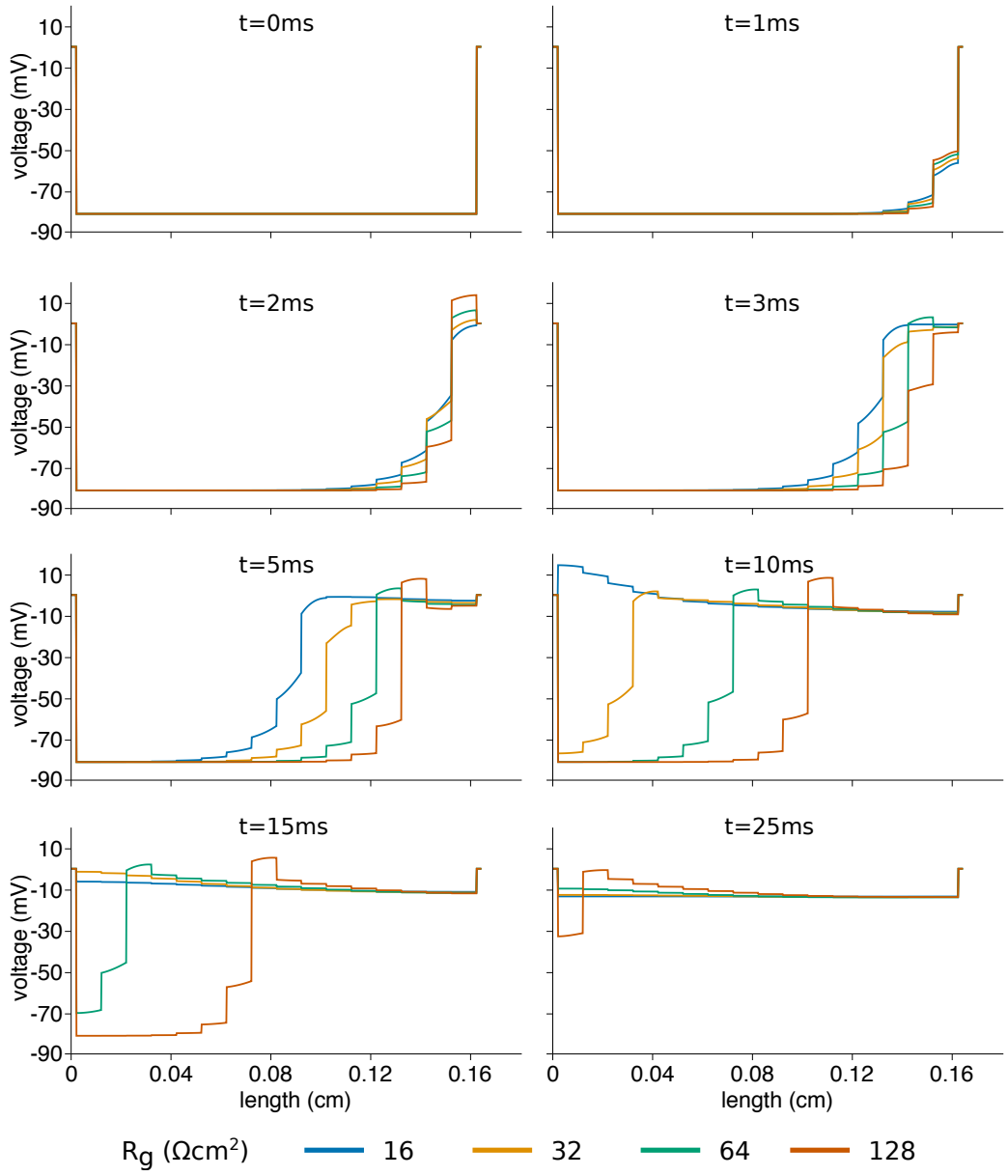


Figure 5.10: Simulated propagation along an idealised cable for four different values of gap junction resistance (R_g): 16, 32, 64 and 128 Ωcm^2. Snapshots are shown at different time steps for the potential plotted along the centre line of the cable.

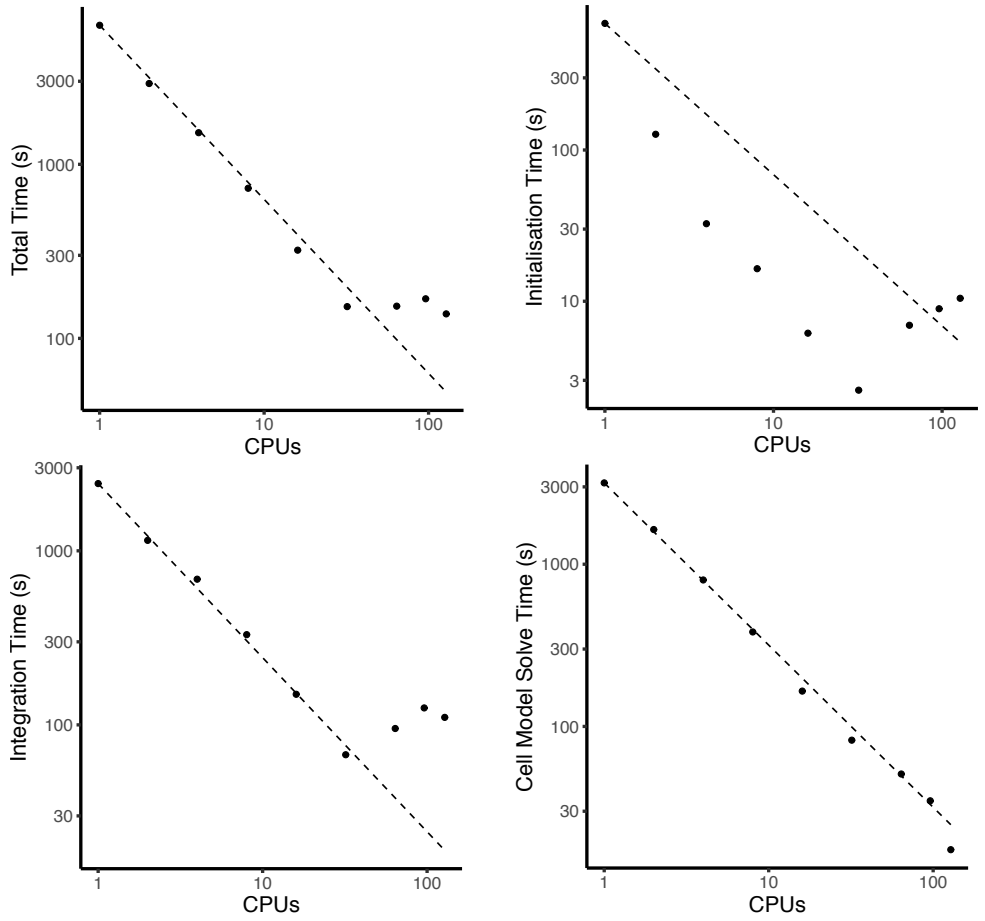


Figure 5.11: Total and split timings for strong scaling. Dashed line indicates optimal linear scaling in each case.

recorded, along with the split between different stages of the simulation (time to initialise the problem by generating the matrix system to be solved, time to integrate the cell model and time to integrate the resulting matrix system).

Figure 5.11 shows the results of the strong scaling experiments. The total time follows the optimal line up to 32 CPUs (one node), before levelling off as the simulation begins to split across multiple nodes. The increased time as the simulation is split across more than one node is primarily seen to be from the initialisation and integration steps, shown by a similar jump in these split timings. Up to this point, the initialisation time reduces at a faster rate than ideal scaling while the integration time follows the ideal scaling closely. In contrast, the cell model solve time scales linearly along the ideal scaling line across the full range of processor numbers tested.

Weak scaling, which primarily demonstrates the impact of inter-process communication, was assessed by increasing the size of the computational problem so that each

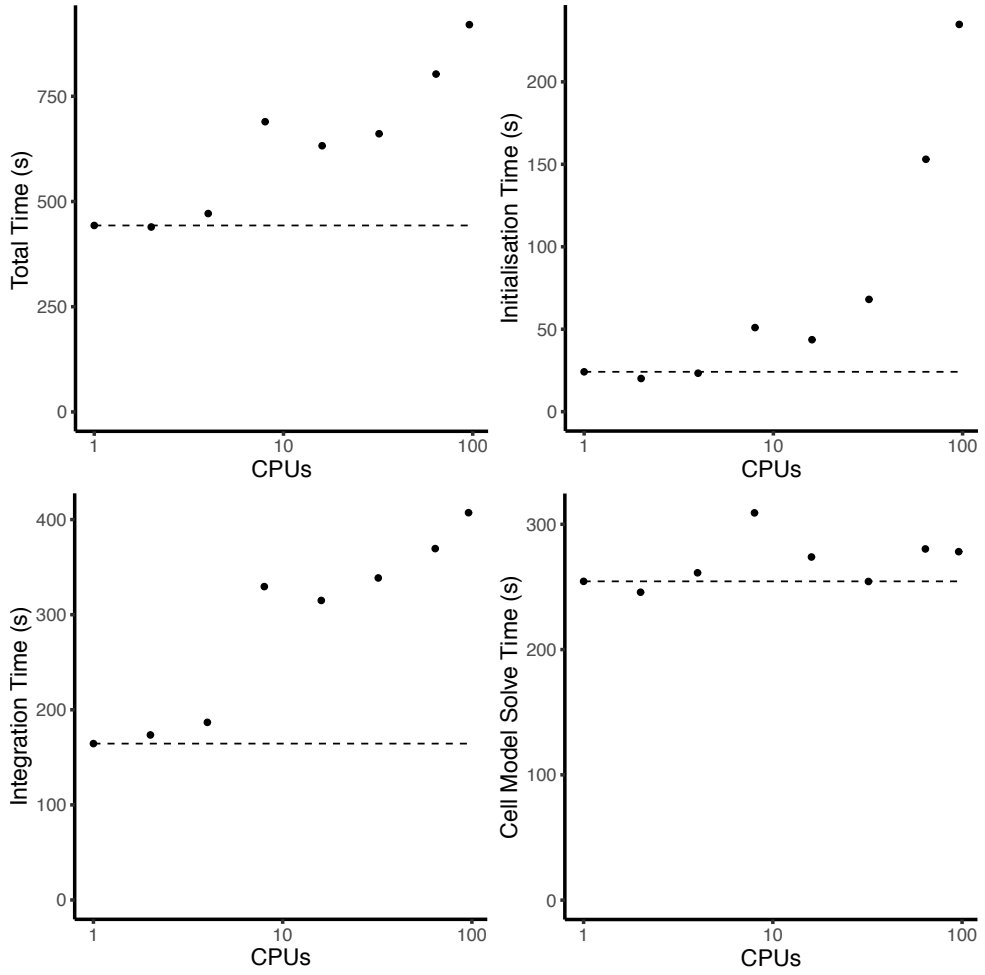


Figure 5.12: Timings for weak scaling. Dashed line indicates optimal scaling in each case.

compute process maintains an approximately constant problem size as the number of compute processes is increased. In this case, ideal scaling would be represented by constant simulation time regardless of the number of compute processes used. Simulations were run across up to 96 processors as described in the methods.

Figure 5.12 shows the timing results from weak scaling simulations. The total time remains approximately constant up to 4 processors, beyond which it begins to rise above the dashed line representing the ideal case. The timing breakdown indicates this is caused by the initialisation and integration timing which follow a similar trend. Once again, the cell model solve time approximately follows the ideal line as the processor number is increased.

5.4 Discussion

The purpose of this chapter was to develop a numerical model to simulate action potential propagation through discretely-coupled cardiac cells. This model can then be combined with the cell model developed in Chapter 4 to simulate action potential propagation in virtual monolayers of HL1-6 myocytes, and compare to the features observed in the biological investigations of Chapter 2.

First, we outlined the equations underpinning the numerical implementation in the one-dimensional and three-dimensional cases. The one-dimensional case is restricted to simulating a cable of cells, and is analogous to the commonly used bidomain continuum approach where the intracellular and extracellular spaces exist at all points in the domain and are coupled through membrane equations. In contrast, the three-dimensional implementation is different in the sense that the intracellular and extracellular spaces are distinct and interact through their intersecting boundaries (interfaces). Rather than imposing Neumann conditions at these interfaces (which would need to be determined from previous time step solutions), the interface conditions are incorporated into the global matrix problem. The solution vectors are ordered to take advantage of static condensation, where interior coefficients may be solved elementally and only the boundary coefficients need to be assembled into the global problem.

A potential disadvantage of incorporating the interface conditions into the matrix problem is that it may increase the bandwidth of the global matrix making it more difficult to solve using an iterative approach. This disadvantage has been somewhat alleviated by ordering the solution vector so that solution coefficients at an interface are ordered immediately after Dirichlet coefficients. As these interface coefficients lead to off-diagonal terms in the matrix, ordering them early and adjacent in the solution vector minimises any bandwidth increase.

The model in its current form assumes there is no space between abutting cell membranes at a gap junction interface. In reality, this assumption is inaccurate as there will be a thin extracellular space between the two membranes, with the gap junctions bridging this short gap to connect the two cytoplasmic spaces. While this small extracellular

gap may be important for investigations of ephaptic coupling [122], computer models have found this mode of conduction to require both a very small gap between the cells and highly localised sodium channels at cell ends [118, 119, 121, 231]. In particular, the second of these conditions is unlikely to be satisfied in HL1-6 myocytes which possess a neonatal morphology with no clear definition of a 'cell end'. However, the model could be extended to account for this potential role of conduction by (1) explicitly modelling a physical extracellular space between gap junction interfaces and connecting the interfaces mathematically but not physically; or (2) solving a mathematical approximation of the membrane interactions across the thin extracellular space as part of the gap junction interface, akin to the approach of Lin and Keener [119]. The second approach is the more promising option, as the first would likely lead to either greatly increased mesh size due to the fine mesh size requirements and/or a mesh of poor quality affecting the numerical solution in these regions.

Having outlined the numerical implementations, they were next validated against theoretical results. The one-dimensional model matched the theoretical solution within numerical error, whereas there was a small discrepancy between the simulation results and theoretical solution in the three-dimensional case. In the one-dimensional case, the equations being solved are a rearranged version of the equations used to derive the theoretical results, and so we would expect them to match. In three dimensions, there is a difference in how the problem is constructed that may lead to the discrepancy emerging. As there are distinct separate sub-domains, the membrane current no longer exists at every point in the domain and is instead an interface condition akin to the gap junctions. As a result, a small gradient in the potential will exist in the planar direction caused by the current flux across the membrane. As opposed to the one-dimensional case, there is not a single extracellular or intracellular potential at each axial point and so the axial solution depends on the location of axial lines along which the solution was plotted. In addition, in three dimensions we also need to account for the far-field conditions along the outer boundary (which were set to no-flux Neumann conditions). The outer boundary had approximately $10\times$ the radius of the cell cable, but this condition may still have had a minor impact on

the solution. Despite the small discrepancy, general features of the potential along the three-dimensional cable match the features of the theoretical results, such as the discrete jumps at cable ends gradually reducing with reducing gap junction resistance and the sawtooth current pattern.

Having compared the multi-domain model to theoretical solutions using a passive membrane, simulations using an active membrane model which could propagate an action potential were next demonstrated. In these simulations, a cell at one end of a cable was stimulated by injecting a current across membrane interfaces, and the resulting action potential propagates through each connected cell. The simulations were carried out for four different resistance values. As expected, lower gap junction resistances led to faster propagation as greater current flows into adjacent cells. Increasing the gap junction resistance was found to increase the peak potential reached within an individual cell (as less of the 'source' current flows into the neighbouring 'sink' cell). This is related to the concept of safety of propagation, where increasing gap junction resistance in biological substrates will slow propagation velocity but also make it less likely to fail [29, 31].

Lastly, the parallel scaling properties of the developed multi-domain model were investigated using an idealised monolayer of cuboidal 'cells'. Using multiple processors to solve the model is essential to be able to simulate a sufficient size of monolayer in the subsequent chapter. We first demonstrated the strong scaling properties of the model across up to 128 processors on a cluster of nodes (each composed of 32 processors). The results indicated that the performance (simulation time) approximates the ideal case up to 32 processors. Beyond this point, the performance begins to plateau. The timing breakdown indicated that the plateau was due to the increased time taken for the initialisation and integration steps (though the integration steps represent the majority of the increased time). The plateauing performance is caused by slower MPI communication in inter-node compared to intra-node MPI communication. Both the initialisation and integration steps require communication in their routines (in the initialisation case to construct the appropriate matrix problem including potential 'ghost' interfaces on each process, and in the integration case during the conjugate gradient algorithm). In contrast, the cell model

step followed ideal scaling as it can be solved independently on each process.

Weak scaling characterises the performance of the simulation across processors when each processor maintains an approximately constant problem size. In this case, the model followed ideal scaling up to 4 CPUs, before the performance reduced from the ideal case beyond this point. The increase in time was once again caused by the initialisation and integration steps, with the cell model steps following approximately the ideal scaling. In the current implementation, as the problem size is increased the initialisation step becomes more complex due to the number of interfaces that must be set up across the domain. Similarly, an increasing number of interfaces requires a greater amount of MPI communication when interfaces become split between processes, causing the integration time to increase. The higher total time at 8 CPUs compared to 16 CPUs could be a consequence of the solution mesh being partitioned in a sub-optimal way which generates a higher number of ghost interfaces, increasing the amount of MPI communication that takes place.

In both cases, the scaling performance could potentially be improved through optimising the implementation, and the results highlight which stages should be targeted in this task. The scaling properties satisfy the requirements for the current work, and performance was not the limiting factor in simulations which will follow in the next chapter. ■

Chapter 6

Investigating the genesis of self-sustaining rotational activity

6.1 Introduction

In Chapter 2, we studied propagation in a simplified 'two-dimensional' biological model of cardiac tissue which exhibited self-sustaining circuits similar to those observed in clinical cases of arrhythmia. Recordings at the core of this self-sustaining activity revealed distinct lines of apparent conduction block around which the activity remained stable. The overarching goal of this thesis is to investigate the genesis of this activity through the development of a multi-domain computational model that explicitly takes into account the discrete nature of action potential propagation between cardiac cells.

The previous chapter discussed the development of the multi-domain model and demonstrated the computational implementation including parallel scaling properties using idealised geometries. This chapter now applies the model to address the overarching goal of the thesis. In particular, a complex cell-like geometry is used to represent the morphology of HL1-6 monolayers. A frequent challenge encountered with electrophysiology models that explicitly account for individual cells is how to best represent the cell geometry. Among the common approaches are to use idealised geometries specific to the research question being studied (e.g. [118–121]), to use artificial geometries with morphol-

ogy visually similar to generic cardiac cells (e.g. [105, 106, 112]) or to base the geometry on biological measurements such as histology (e.g. [110]).

Kudryashova et al. [232] developed a novel solution to this problem and reproduced realistic two-dimensional shapes of myocytes and coupled fibroblast cells based on a mathematical description of how these cells grow *in vitro*. The authors simulated action potential propagation in their virtual monolayers with and without anisotropy and showed the results compared well with experimental measurements. The work was further developed [233] to investigate how branching networks of viable cells surrounded by non-conducting tissue form complex patterns of conduction leading to wave break. This approach provides a balance between basing the geometry on direct biological measurements, which can be challenging particularly for monolayers with very large numbers of cells, and idealised geometries, which may not be as representative of reality.

This chapter starts with an overview of the methods used to generate the geometry model of an HL1-6 monolayer, how this geometry is combined with the HL1-6 cell model developed in Chapter 4 and the specific setup for each set of simulation experiments. To calibrate an appropriate value of the gap junction resistance in the monolayer, a parameter sweep is performed while measuring the conduction velocity of a propagating wave. The observed change in conduction velocity due to ion current block is next compared to experimental results to validate the model. We then determine the necessary substrate size for self-sustaining activity to be initiated in an HL1-6 monolayer. In the final results section, we test two hypotheses for why the self-sustaining activity *in vitro* remains stable in a fixed location: high variability in gap junction resistance throughout the monolayer, and a concentrated increase of gap junction resistance along a line of interfaces connecting cells. We conclude by discussing the results and highlighting specific limitations of the study.

6.2 Methods

6.2.1 Creating a representative monolayer geometry

In the previous chapter, simulations of action potential propagation were conducted in idealised monolayers of 'cells'. The goal of this chapter is to reproduce features observed *in vitro*, and so a more representative model of a monolayer of HL1-6 myocytes was desirable. Initially, image segmentation approaches were investigated to generate morphology directly from HL1-6 monolayers. Attempts were made to capture and segment an entire drop colony (created as in Chapter 2) so that *in silico* geometry could match one-to-one with an *in vitro* experiment. This approach ultimately did not succeed due to (1) the long time to capture images imposing a limit to both the image quality and the combination of dyes that could be used, (2) limitations to the segmentation methods requiring significant time to manually adjust very large volumetric images, (3) photobleaching of cells due to the prior fluorescence mapping experiment, and (4) time limitations on equipment required for the process (both widefield and confocal microscopes). As a result of these limitations, a representative geometry was instead generated based on measurements from a set of smaller high-resolution volumetric images from confocal microscopy.

Small drop colonies were seeded on ibidi μ-dishes (following the same protocol described in Section 2.2.3 in Chapter 2). The dishes were stained with a dye solution containing 1 mg/ml Wheat Germ Agglutinin (Sigma-Aldrich, USA) diluted 1/40 in HBSS containing 1% bovine serum albumin, combined with nuclear dye 5 μg/ml Hoescht 33342 (Fisher Scientific, USA) for 20 minutes. Three-dimensional z-stack images were captured at various locations in the drop colonies using a Zeiss LSM-780 inverted confocal laser scanning microscope (Zeiss, Germany). Each image was captured in 16-bit format using a 40$\times$ oil lens with no spatial binning (0.42 μm/px) and 0.85 μm spacing between slices in the z-axis. To reduce noise, 4 images were captured at each location and averaged. The nuclear dye (Hoescht) was excited at a wavelength of 405 nm and captured at 450 nm; the membrane dye (Wheat Germ Agglutinin) was excited at 488 nm and captured at 535 nm.

These higher quality images, with both a membrane and nuclear stain, were semi-automatically segmented using Cellpose open source software [234]. This software provides a framework for general segmentation of microscopy images of cells built on a deep learning model trained from a community-generated data set. The addition of a nuclear dye improves the segmentation outcome requiring less manual adjustment.

Measurements from analysis of the segmented cells were used to 'grow' a virtual two-dimensional monolayer. The cell growth algorithm was developed previously by the Panfilov group [232, 233] and used in studies of propagation in two-dimensional computer models of neonatal rat ventricular cardiomyocytes mixed with fibroblasts. Their algorithm is based on the Glazier-Graner-Hogeweg tissue growth model. In this model, cells, and the surrounding medium, are represented as groups of sub-cells in a grid (akin to pixels in an image). These sub-cells of different types (i.e. cardiomyocyte or medium) interact with each other via mathematically-defined forces and fields, expressed in terms of a Hamiltonian, through discrete time steps of the algorithm. At each time step, a randomly selected sub-cell attempts to copy itself into a neighbouring sub-cell, which either succeeds or fails based on whether the action would result in a reduction in total energy of the system [232].

In the Panfilov group's implementation, an iterative Markov chain Monte Carlo algorithm is used to accept changes to cell shapes with probability linked to the Hamiltonian. In addition to the minimal Glazer-Graner-Hogeweg energy terms for adhesive and elastic energy, Kudryashova et al. also developed three important additions to the Hamiltonian to account for the shape of cardiac cells: a term to describe protrusion dynamics, a term accounting for the higher rigidity of cell nuclei, and a term to account for alignment of cytoskeletons in neighbouring cells [233]. For further detail of the virtual monolayer growth model see [232, 233].

HL1-6 cells have similar morphology to neonatal cells [69], but are smaller as they are a murine atrial cell line. Due to this similarity, two-dimensional virtual monolayers of HL1-6 cells were generated using the same parameters as reported by Kudryashova et al. [232] for a pure monolayer of 100% cardiomyocytes, with a scale factor applied to

the final image to reduce the size of the cells. This scale factor was determined from analysis of segmented slices from the confocal images (and is detailed in the results of this chapter).

The output of the monolayer growth model is a two-dimensional image representing the connected layer of cells. To create the three-dimensional models used in this work, the two-dimensional image was extruded in the z-axis and surrounded by a buffer of extracellular space on all sides other than the bottom cell surface (which represents the microscopy dish of *in vitro* experiments). Cell height in the extruded monolayer was estimated from the same confocal microscopy image stacks using the mean z intensity profile of each slice (again, further detailed in the results of this chapter).

In all cases, a mesh was generated from the final geometry using Gmsh (`http://gmsh.info/`, version 4.6.0). Cell sub-domains were discretised into triangular prisms with height 4 μm and a target size in the plane also of 4 μm. The extracellular space was discretised into an unstructured mesh of pyramids and tetrahedrons with a target size increasing in a sigmoidal fashion from 4 μm at the cell surfaces to 40 μm on the outer boundary.

6.2.2 Monolayer geometries

Three different sizes of monolayer geometries were generated. The first was created for experiments to calibrate the gap junction resistance parameter to conduction velocity measurements in the HL1-6 cell line conducted by Dias et al. [69]. This monolayer model was grown from an irregular 117×13 grid of sub-cell seed points for 50,000 steps of the cell growth algorithm [232]. The seed points were spaced such that the resulting monolayer had dimensions 1600×200 μm to represent one row of electrodes on the micro-electrode array dish used to measure the conduction velocity [69]. A buffer of extracellular space of 100 μm was added in each direction other than beneath the cells. Five different monolayers were grown in this fashion. This geometry had 1521 cellular sub-domains which were discretised into meshes with $\sim$700,000 elements.

Two square monolayer geometries were also generated with different areas, 1 mm^2 and 4 mm^2, for investigations of self-sustaining activity. The 1 mm^2 geometry was grown from

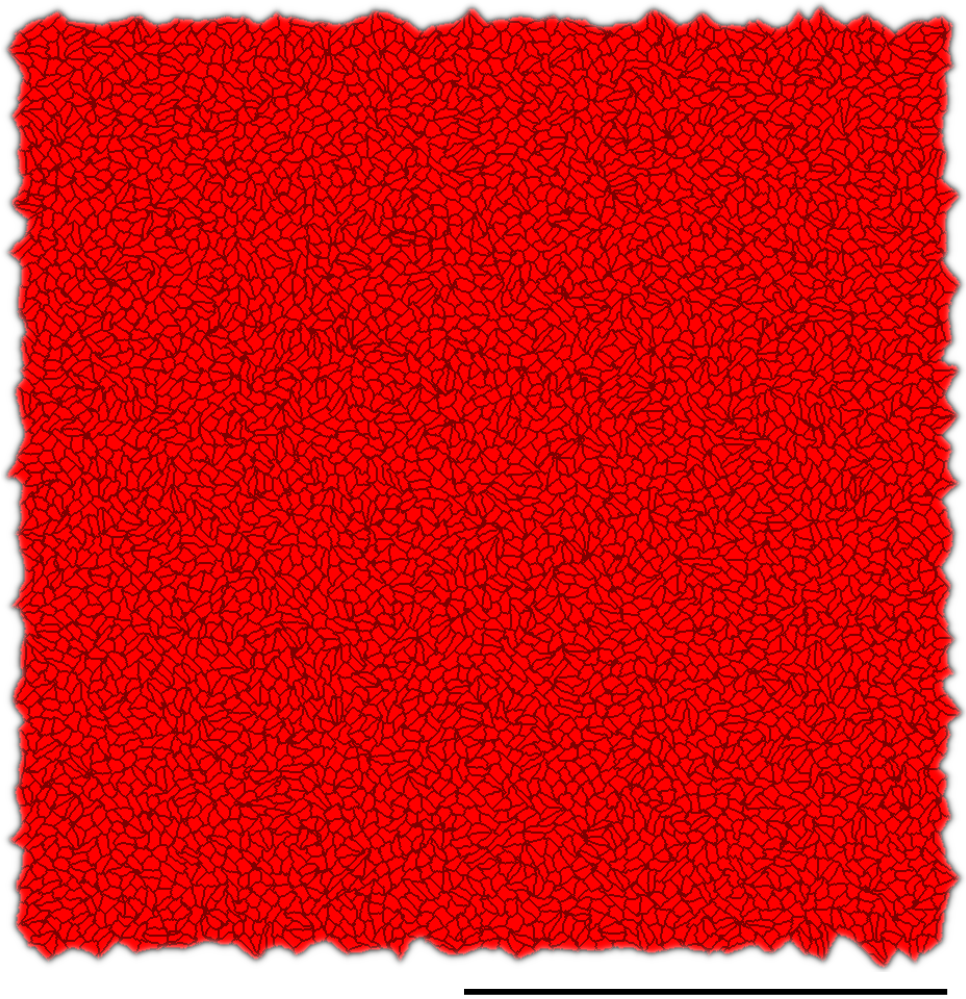


Figure 6.1: Virtual monolayer generated using the cell growth algorithm from starting seed of 72×72 cells. Scale bar: 0.5 mm.

an irregular grid of 72×72 seed points for 50,000 steps of the cell growth algorithm. The resulting monolayer contained 5184 cell sub-domains and is shown in Figure 6.1. The 4 mm^2 geometry was grown from a grid of 145×145 seed points in the same manner and contained 21,025 cell sub-domains. The resulting number of elements for the 1 mm^2 and 4 mm^2 geometries once meshed were approximately 1 and 10 million respectively. Figure 6.2 shows a zoomed image at the corner of the mesh for the 4 mm^2 virtual monolayer domain.

6.2.3 Incorporating the HL1-6 cell model

HL1-6 myocytes exhibit more homogeneous phenotype than the original HL-1 cell line [69]. Regardless, as discussed in previous chapters, there is still variability between individual cells in ion current density and the resulting action potential morphology. The cell model

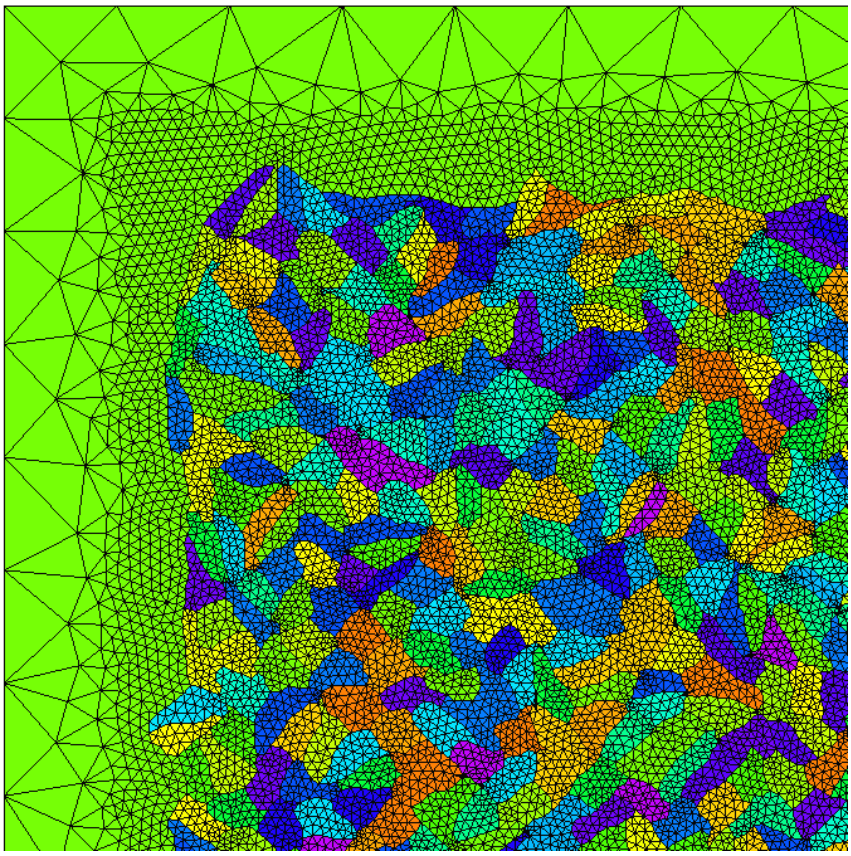


Figure 6.2: Lower surface of mesh at corner of 4 mm^2 virtual monolayer.

developed in Chapter 4 incorporates biological variability as well as uncertainty from experimental measurements. When including this cell model in the multi-domain model, we make the assumption that this variability is largely between cells as opposed to variability in a single cell from beat to beat.

The cell model variability is incorporated into the simulations in this chapter by assigning a different variant from the HL1-6 cell model (including both those that are quiescent, and those exhibiting automaticity) to each intracellular sub-domain. This is handled practically by using a random number generator at initialisation of the simulation to randomly set cell model variants. The random number generator seed ensures that simulation results are reproducible. By assigning a specific variant of the cell model to each cell sub-domain, any membrane interfaces that belong to this domain solve the assigned cell model variant.

To increase the propensity for re-entry in the simulations investigating self-sustaining activity, the cell model variants were pre-paced at 10 Hz to reduce the cell refractory

Parameter	Value	Source
C_m	1 μF/cm^2	[235]
C_g	0.5 μF/cm^2	[121]
σ_i	4 mS/cm	[121]
σ_e	20 mS/cm	[105]
Δt	0.01 ms	
$\Delta t_{\text{cell model}}$	0.0025 ms	

Table 6.1: Default simulation parameters and values.

period (see Figure 4.19 in Chapter 4).

6.2.4 Simulation set-up

All simulations of action potential propagation through HL1-6 monolayers were conducted using the spectral/hp element implementation in Nektar++ discussed in Chapter 5.

In the three-dimensional model, intersection surfaces between cellular sub-domains are assigned gap junction interface conditions, and intersection surfaces between a cellular sub-domain and the extracellular sub-domain are assigned a membrane interface condition. When a cellular sub-domain has a boundary at the edge of the solution space (i.e. $\partial \cup \Omega_{(i,e)}$), this represents a cell touching the microscopy dish and a no-flux condition is assumed at these boundaries. When the extracellular domain has a boundary at the edge of the solution space, this is classified as a farfield boundary and is set to a fixed zero Dirichlet condition to pin a unique global solution.

Gap junction resistance is calibrated in the first set of simulation experiments. Other default simulation parameters are given in Table 6.1 using general values from the literature. The tolerance of the preconditioned conjugate gradient solver was set to 1×10^{-5} in all simulations.

When calibrating the gap junction resistance parameter or validating the effect of ion channel blockers, virtual electrograms were generated to calculate the conduction velocity in an analogous fashion to the biological experiments. In these cases, the virtual

electrogram $\Phi(t)$ was generated by

$$\Phi(t) = \int_{\Omega} \nabla V_m(t) \left(\frac{1}{\nabla r} \right) \mathrm{d}\Omega, \tag{6.1}$$

where V_m is the transmembrane potential on membrane interfaces, and r is the Euclidean distance from the electrode location to the corresponding vertex on the membrane interface (each virtual electrode only exists at a single point). When electrograms were recorded, their value was written out every time step.

Simulations were run across up to 256 CPUs (AMD EPYC 64-core processor @ 2.25 GHz) on the Imperial College CX1 computing cluster. Snapshots of the entire solution domain were generally written every 10 ms of simulation time, corresponding to the same rate as *in vitro* fluorescence microscopy recordings in Chapter 2.

6.2.5 Stimulation protocols

Dias et al. [69] measured conduction velocity in monolayers of HL1-6 myocytes seeded on a micro electrode array (MEA) plate. The MEA plate has a grid of 8×8 30 μm diameter electrodes and inter-electrode spacing (centre-to-centre) of 200 μm. An action potential wave was initiated by stimulation along one row of electrodes at the edge of the grid, and the remaining electrodes measured the path of the wave as it crossed the array. Using this experimental set-up, Dias et al. [69] measured the conduction velocity in confluent HL1-6 monolayers as 41±1 mm/s (n=12).

To measure conduction velocity in the model, a stimulus 'electrode' was placed 200 μm in from one end of the domain boundary (i.e. 100 μm from the edge of the cell strip), and 7 recording electrodes were equally spaced 200 μm along the remainder of the strip (all electrodes were located on the centreline along the length of the strip). The stimulus was modelled as a cylindrical current source with radius 15 μm applied through the lower surface of the cells within the radius. In each simulation, the electrode injected a stimulus current of 500 pA for 10 ms to replicate the experimental conditions [69].

For simulations investigating self-sustaining activity in the 1 mm^2 and 4 mm^2 geome-

tries, the initial aim was for action potential propagation to be initiated 'naturally' as in biological experiments. The HL1-6 cell model includes variants which exhibit automaticity, so we first simulated the 1 mm^2 geometry without stimulation in an attempt to allow action potential propagation to be initiated by these pacemaker cells. At the default simulation settings, no pacemaker activity was observed in multiple simulation runs with randomised cell model variants. Attempts to increase the likelihood of a pacemaker cell being able to initiate action potential propagation were investigated, including increasing the conductance of the 'funny' current in pacemaker cells and increasing the safety of propagation for these cells (by increasing their gap junction resistance). However, in the former case, the increased current flowed into adjacent cells raising the resting potential of the entire monolayer and, in the latter case, the increase in gap junction resistance required to initiate an action potential in a pacemaker cell was too high to allow it to also successfully propagate.

As a consequence, a traditional S1-S2 stimulus approach was applied to attempt to initialise self-sustaining activity in the square geometries [236]. The S1 stimulus was initiated by applying a 100 pA stimulus current through membrane interfaces on one edge of the square geometry for 2 ms at the beginning of the simulation. This causes an initial planar wave to cross the domain. The S2 stimulus was applied after a delay of 70 ms for the 1 mm^2 geometry and 80 ms for the 4 mm^2 geometry. A stimulus current of 50 pA lasting 2 ms was applied through the dish boundary of cells in the lower quarter strip perpendicular to the initial S1 wave.

6.3 Results

6.3.1 Creating HL1-6 cell monolayer geometries

Figure 6.3 shows slices from three confocal image slices of an HL1-6 cell monolayer with the membrane fluorescence channel overlaid on the nuclear fluorescence channel. The slices were selected to be at the assumed mid-height of the majority of cells in the image (see following height estimation results). Each slice was semi-automatically segmented

using Cellpose [234], and the resulting segmentation masks are shown next to each image slice. The images show a confluent monolayer with a few small gaps between some cells. Checking the volumetric image confirmed that these gaps only existed in the two-dimensional plane, and cells in the monolayer in these locations made contact with other cells either above or below the slice. It is also apparent from the microscopy images and segmentation masks that the cell size is not uniform, in particular with a small number of larger cells in the field of view.

The area of each segmented cell was calculated from the number of pixels in each segmentation mask and is plotted in Figure 6.4. The measurements show that most cells in this slice have a cross-sectional area less than 500 μm^2. The data points for the larger cells can be clearly seen separate from, and higher than, the main bulk of data points. The median area across all image slices is 168 μm^2 with 89% highest posterior density interval of (36.9, 329) μm^2, and mean of 202 μm^2 with standard deviation 160 μm^2.

Kudryashova et al. [232] stated that the cells in their virtually-grown isotropic monolayer models had a mean area of 1100 μm^2 with little variation between cells. To generate appropriate cell areas for HL1-6 myocytes, an area scale factor of $^1/_5$ was applied after 'growing' virtual monolayers.

Next, an effective height of the monolayer was determined to extrude the two-dimensional cell cross-sections. To this end, the mean fluorescence intensity of the confocal microscopy image slices was analysed through the complete z-stack. Figure 6.5 shows an example for one image slice. The z-profile for the membrane fluorescence channel shows two peaks in all slices. The first peak corresponds approximately to the base of the dish. The trough before the second peak is the point at the mid-height inside most cells, or when the membranes are 'most parallel' to the z-axis. The second peak occurs as the full height of most cells is reached as the top membrane surface produces fluorescence in a greater area, and then this gradually reduces to the background intensity as the plane moves above the height of the cells. The height varies throughout the monolayer as clear from Figure 6.5.

An effective height of the virtual monolayers was calculated as the distance in the z-axis from the first peak in the intensity z-profile (i.e. the base of the dish) to the median

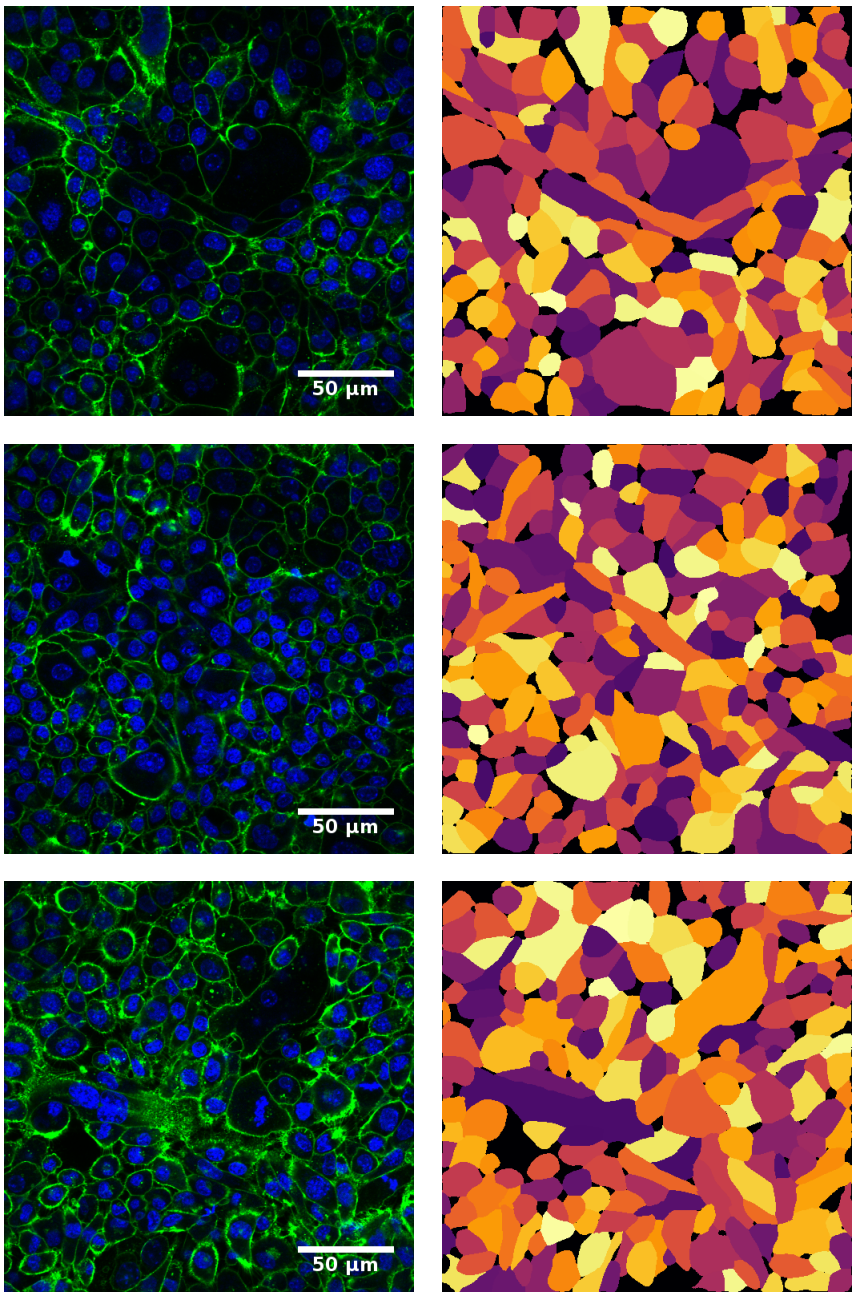


Figure 6.3: Cellpose segmentation of confocal microscopy image slices of confluent HL1-6 monolayers. The left column shows three different image slices from different locations in cell colonies. Membranes are highlighted from a Wheat Germ Agglutinin stain and nuclei from a Hoescht dye. The right column shows the resulting semi-automatic segmentation cell masks. The area of view of each image is 213×213 μm. Mask colour has no meaning other than to differentiate cells.

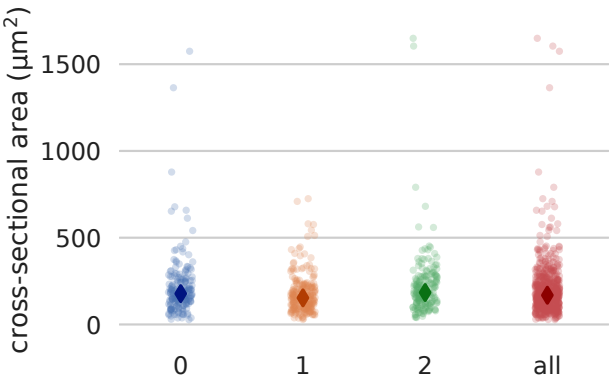


Figure 6.4: HL1-6 cell cross-sectional areas measured from segmentation of confocal microscopy image slices. The first three columns are each of the image slices, and the final column combines all measurements. Each dot is one measurement and the diamond shows the median result.

value of the region spanning the intensity trough upwards. This median value was an estimate to the median height of the upper surface of cells in the confocal microscopy images. Across each of the three confocal microscopy image slices, this height estimation was approximately 8 μm, and is the height of the extruded monolayer geometries in all following results.

6.3.2 Calibrating gap junction resistance

Each of the five monolayer strip geometries were simulated for total time of 50 ms with gap junction resistance values from 2^{-9} to 2^{-1} kΩ cm^2. Figure 6.6 shows representative activation maps and corresponding virtual electrograms generated by one of the monolayer strip geometries. In these simulations, activation time is defined as the time when the potential reaches -20 mV. These monolayer strips were stimulated as described in methods from an electrode at the left, and the resulting wave is measured by recording electrodes as it travels along the remainder of the strip. As would be expected, simulations with lower gap junction resistance show the propagating wave reaching the other end faster and, in the extreme case of the highest gap junction resistance, the wave does not reach the other end within the total simulation time (Figure 6.6, bottom row).

Conduction velocity was calculated by measuring the time difference between the earliest and latest peak from the virtual electrograms recorded along the strip, and dividing the distance between those electrodes by the time difference. Figure 6.7 plots the measured conduction velocity against different values of gap junction resistance, along with

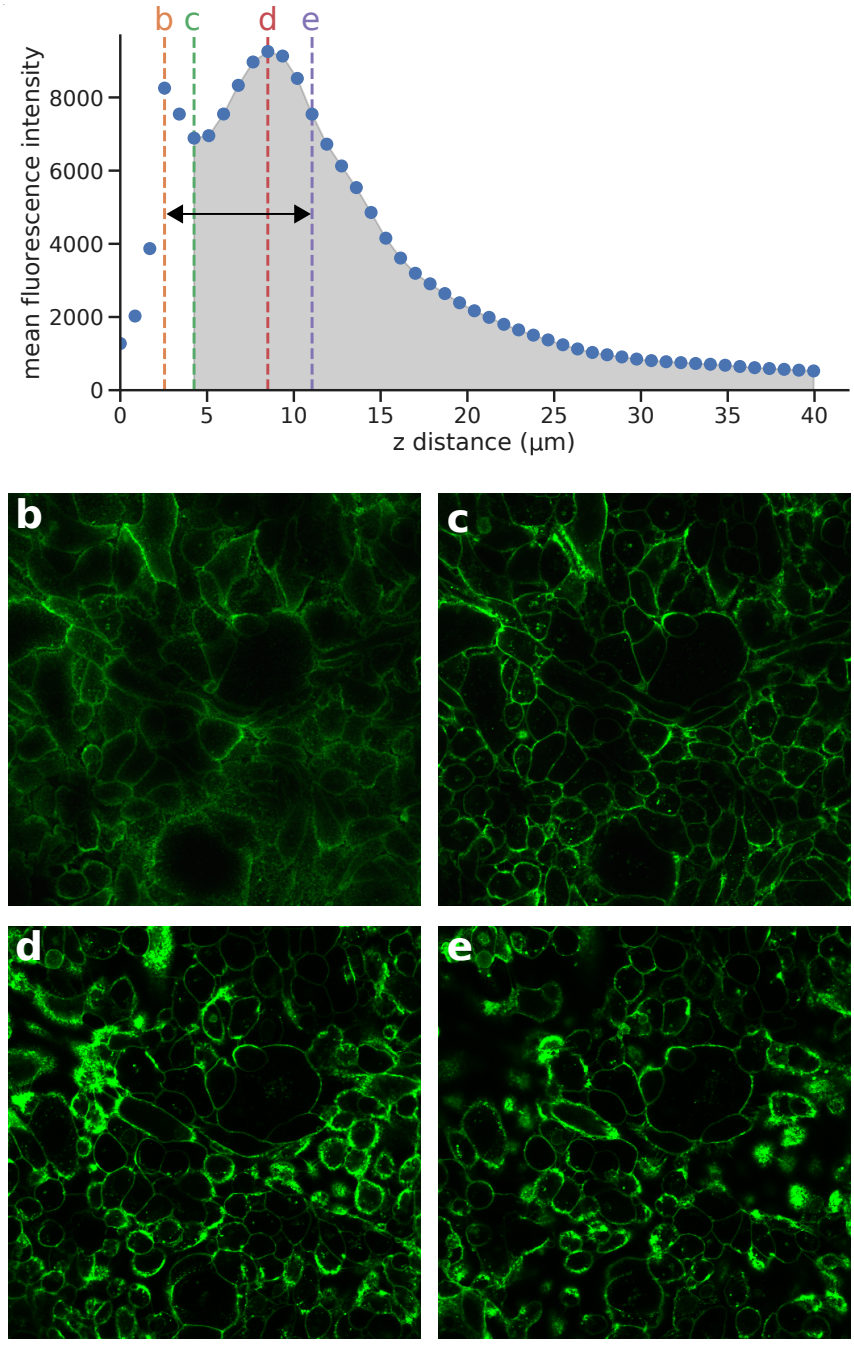


Figure 6.5: Example of monolayer height estimation. **a** Mean fluorescence intensity z-profile from a confocal microscopy volumetric image of membrane stained monolayer. The dots are the mean fluorescence intensity of each slice. Each line corresponds to an image in **b**-**e**. The first peak (b) in the profile is the base of the microscopy dish, as the bottom of cells are coming into focus. The trough (c) is the point at which we are in the middle of most of the cells, as there is a lot of non-stained cytoplasmic space in view. The rise to the second peak (d) is caused by the top surface of shorter cells coming into view. This gradually drops off as their heights are surpassed, leaving only unstained extracellular space at their location. The height (black arrow) was estimated by using the median level (e) from the shaded region as the median upper height of cells, and subtracting the base level.

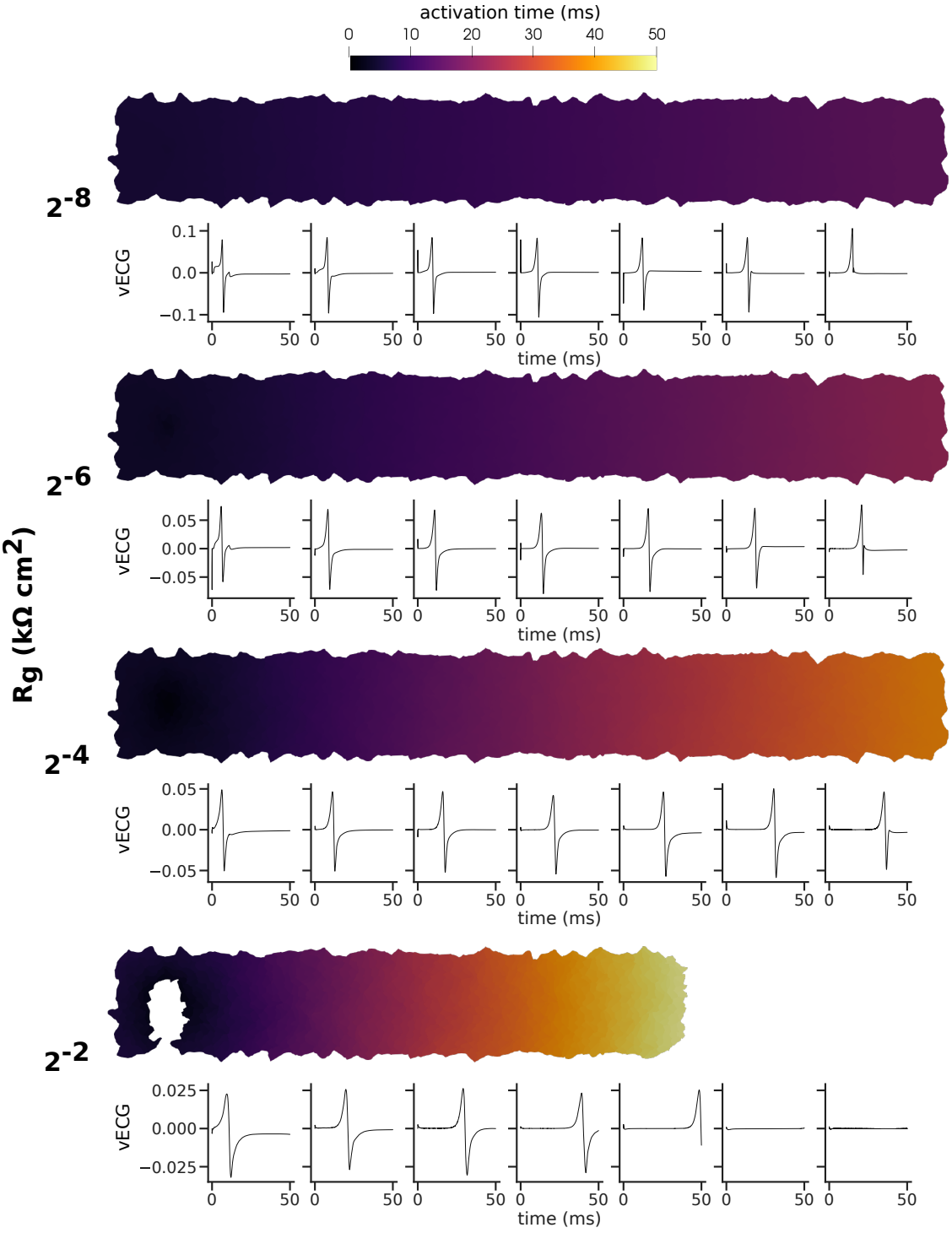


Figure 6.6: Example activation maps in one of five monolayer geometries for different values of gap junction resistance. Virtual electrograms measured from recording electrodes along the length of the monolayer are shown below each activation map. The bottom activation map is shorter as the propagating wave did not reach the other end of the monolayer within simulation time.

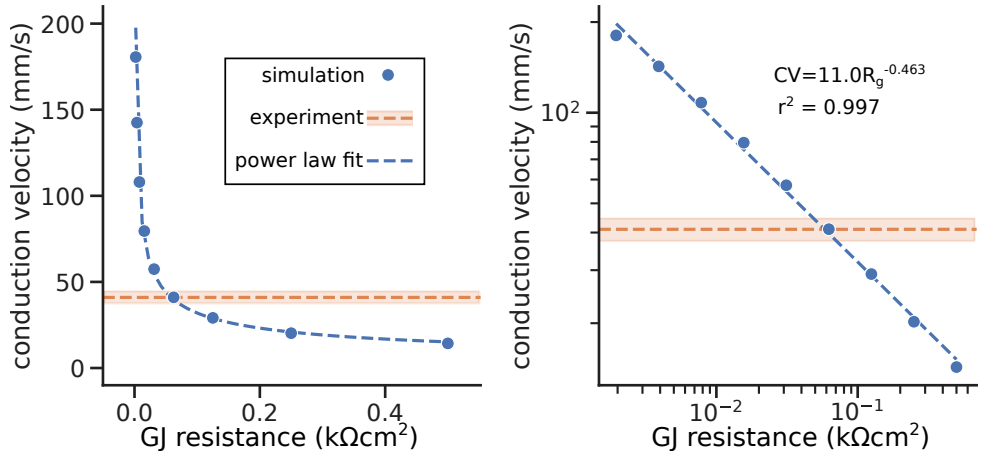


Figure 6.7: Conduction velocity plotted against gap junction resistance. The right-hand plot is the same data plotted on log axes. Five simulations were completed using different monolayer geometries at each value, and the median value and 95% confidence intervals are shown (error bars not visible due small size). The experimental mean value is shown as a dashed line with shading representing one standard deviation.

the experimental measurement. Median values with 95% confidence intervals are plotted for the five different monolayer strips on these graphs (though error bars are not visible due to their small size).

The results of conduction velocity and gap junction resistance approximately followed a power-law relationship. When the simulation conduction velocities were fit (in log space) to a power-law equation, $y = ax^{-k}$, the fit gave an exponent $k = 0.463$ and constant $a = 11.0$, with $r^2 = 0.997$. The horizontal dashed line and shading in Figure 6.7 shows the experimental mean conduction velocity measurement and one standard deviation [69]. The mean value of 41 mm/s from experiments corresponds to a gap junction resistance of almost exactly 2^{-4} kΩ cm^2 (0.0625 kΩ cm^2). This value was used as the control value for all following simulations.

6.3.3 Validation through pharmacological block of ion currents

Validation simulations were conducted for the effect of pharmacological drugs on conduction velocity in HL1-6 monolayers. Dias et al. [69] applied Lidocaine to HL1-6 monolayers in increasing doses which progressively blocks the fast Na^+ current [223]. Their experiment was replicated in this computational model using the dose-response curve from Figure 4.17 in Chapter 4 and assuming scaling of the fast Na^+ current conductance as

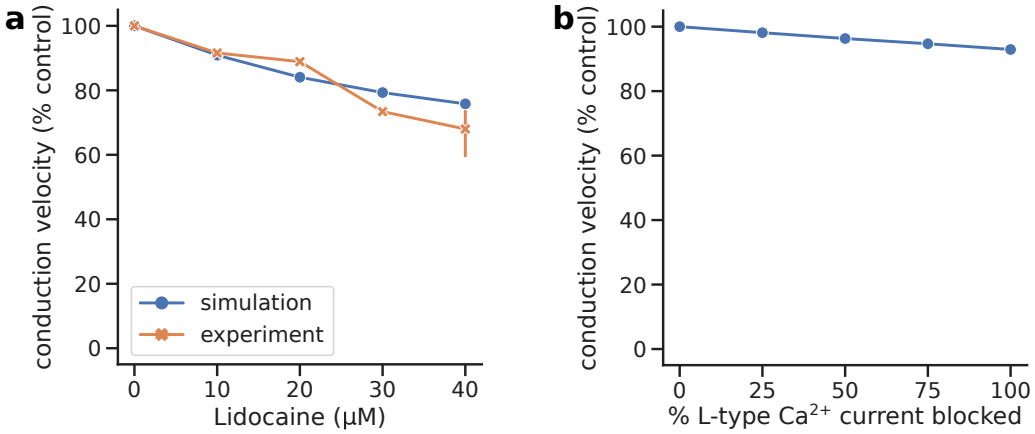


Figure 6.8: **a** Effect on conduction velocity of blocking fast Na^+ current with Lidocaine in simulations and experiments. Current conductance was scaled using the dose-response curve for Lidocaine from Figure 4.17. Five simulations using random monolayer geometries were carried out at each value, and the median value with 95% confidence intervals is shown (error bars not visible due to small size). Experimental data is shown as mean value with error bars indicating one standard deviation for only the last data point. **b** Effect of blocking L-type Ca^{2+} current on conduction velocity. Simulations were executed and plotted as in a.

the only action of the drug. Figure 6.8a compares the simulation output for the five monolayer strip geometries with experimental results (experimental error measurements were only given for the final data point [69]). The simulations show a moderate reduction in conduction velocity in line with experimental measurements. The conduction velocity measured at the largest dose falls within one standard deviation of the mean experimental value.

Conduction velocity in HL1-6 monolayers was also measured experimentally under the effect of Nifedipine [69]. Although the data was not explicitly provided, the authors stated that "treatment with nifedipine [...] did not result in any change in [conduction velocity]" [69]. The effect of Nifedipine was reproduced in simulations by linearly reducing the conductance of the L-type Ca^{2+} current [237]. Figure 6.8b shows the effect of increasing levels of L-type Ca^{2+} current block on the measured conduction velocity. The conduction velocity reduces linearly to approximately 93% of its control value at full L-type Ca^{2+} current block.

6.3.4 Conduction velocity restitution

Monolayers were paced at increasing rates to investigate restitution properties. As the conduction velocity in preceding experiments appeared invariant to the geometry used,

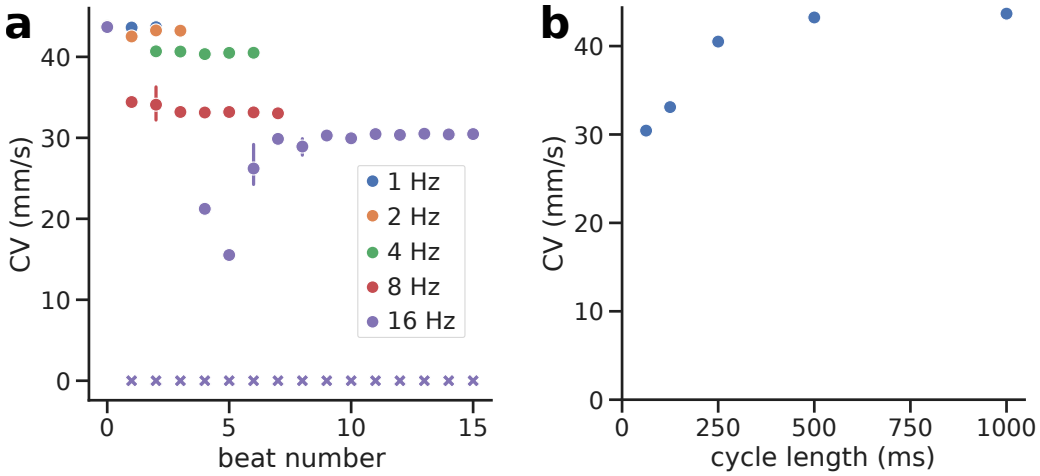


Figure 6.9: **a** Conduction velocity (CV) plotted for each beat at different stimulation rates. Crosses indicate a stimulus did not propagate along the monolayer. Results are plotted as median values with 95% confidence intervals. **b** Conduction velocity restitution curve generated by using the final conduction velocity at each rate from a.

simulations were run in one of the strip monolayer geometries with five repeats at each pacing rate using randomised HL1-6 cell model variants at each membrane interface. The monolayers were paced at rates from 1 to 16 Hz until the conduction velocity stabilised.

In Figure 6.9a, conduction velocity measured along the monolayer for each stimulated beat is plotted across the five repeats. At all rates, the first beat propagates at approximately the same base conduction velocity. At 1 Hz, there is very little change in conduction velocity with each beat, indicating cells are able to recover between each stimulation. Figure 6.9b shows that as the rate is increased (i.e. cycle length reduced), the conduction velocity settles at a lower stable level.

At the highest stimulation rate of 16 Hz, the monolayer was unable to propagate each beat. At the stable conduction velocity of approximately 30 mm/s, every other beat was propagated (indicated by the purple crosses at the base of Figure 6.9a). This property was affected by the randomised cell model variants between the five repeats, where either the odd- or even-numbered beat was propagated.

There was little variation in conduction velocity measurements between repeats with different cell model variants at stimulation rates between 1-4 Hz. At the higher 8 and 16 Hz rates, some variation was observed in beats before the conduction velocity levels stabilised. As all other variables were held constant, this variation is likely due to the randomised cell model variants.

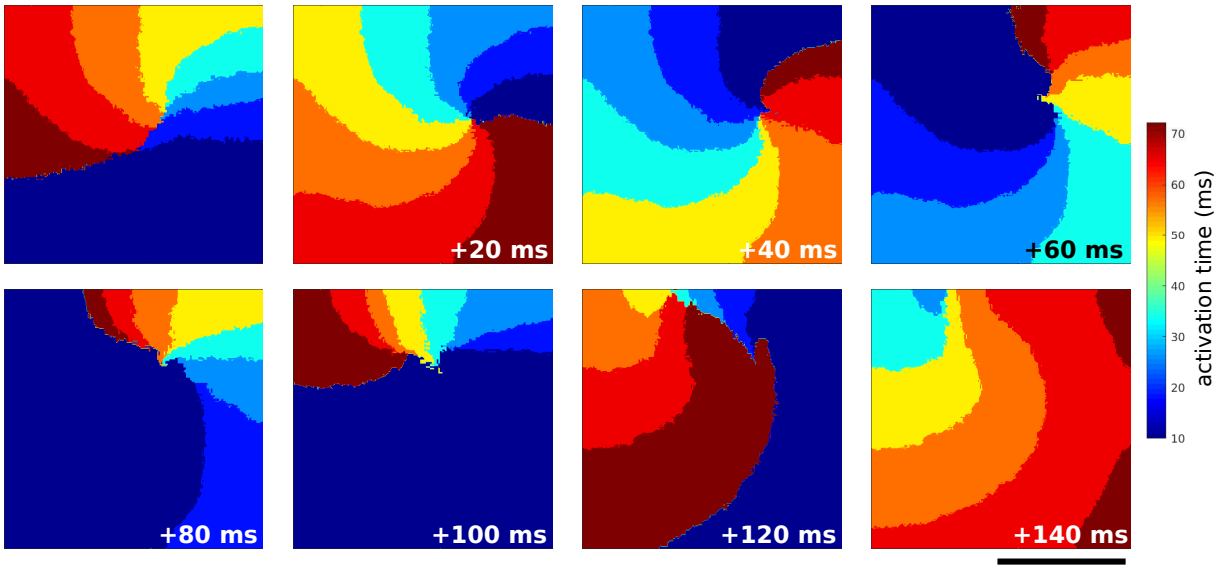


Figure 6.10: Attempt to initiate self-sustaining activity in the 1 mm^2 monolayer geometry. The first activation map was generated at the time of the S2 stimulus (70 ms). Labels indicate the offset to subsequent activation maps. Scale bar: 0.5 mm.

6.3.5 Monolayer size requirement for self-sustaining activity

It was possible to initiate self-sustaining activity in both the 1 mm^2 and 4 mm^2 geometries using the S1-S2 stimulus protocol described in methods (the S2 delay for each geometry was determined using a parameter sweep). Figure 6.10 shows activation maps generated at a series of time points in the 1 mm^2 simulation. Only a single simulation was carried out due to invariance to both geometry and cell model variants observed in previous results.

The first frame in Figure 6.10 shows an activation map generated at the start time of the S2 stimulus (i.e. 70 ms into the simulation). The S2 wave is only able to propagate upwards on the right hand side of this geometry, as the cells on the left hand side have not yet recovered from the S1 stimulus. By the time the S2 wave has travelled part way up the geometry the cells on the left hand side have recovered sufficiently to allow the wave to re-enter, which can be observed in the second frame generated 20 ms later. This second frame shows an activation map characteristic of a spiral wave.

The remaining activation maps show that the activity is not stable around a single fixed location. There is not enough space within the 1 mm^2 geometry to allow the core of the spiral wave to meander and, consequently, it eventually terminates on the right hand side boundary (final frame).

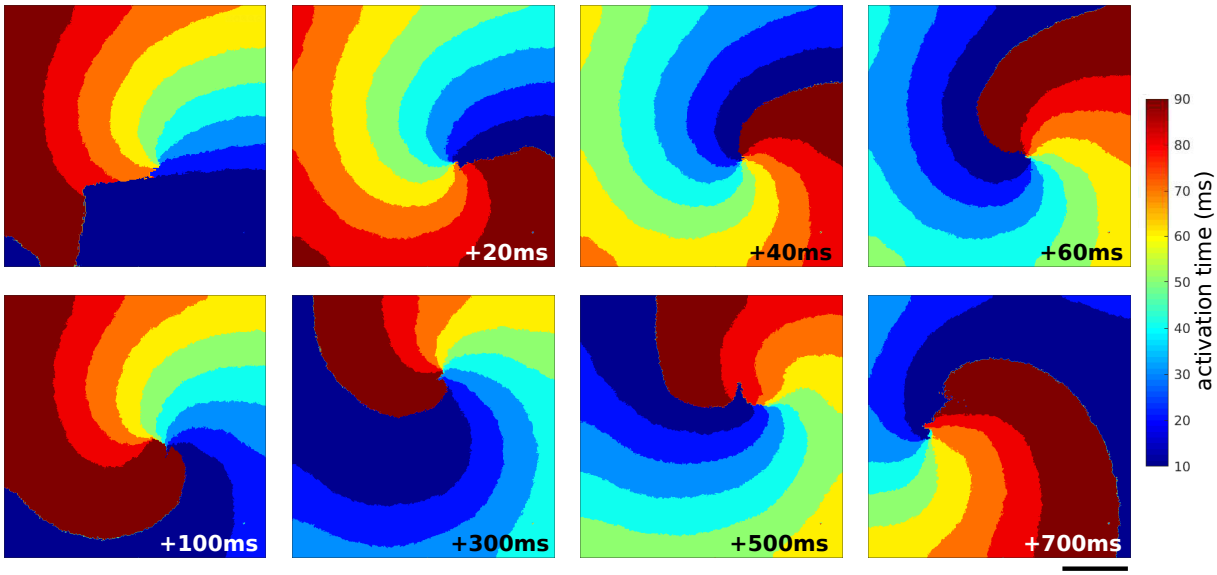


Figure 6.11: Initiation of meandering self-sustaining activity in the 4 mm^2 monolayer geometry. The first activation map was generated at the time of the S2 stimulus (80 ms). Labels indicate the offset to subsequent activation maps. Scale bar: 0.5 mm.

Figure 6.11 shows activation maps generated from the corresponding simulation in the 4 mm^2 geometry. As before, the first frame shows an activation map generated at the start time of the S2 stimulus. The propagating wave again shows characteristics of a spiral wave, with a curved wave front emanating outwards from a central location. In this case, there is sufficient room for the spiral wave to meander and it remained self-sustaining for the duration of the 1000 ms simulation. The dominant frequency of the self-sustaining activity was approximately 12 Hz.

6.3.6 Increasing variability of gap junction resistance

The self-sustaining activity observed in the control experiment above did not remain anchored around a single fixed point. In Chapter 2, experimental recordings of this activity *in vitro* always showed anchored activity. Therefore, we next sought to investigate conditions necessary to anchor the activity in this geometry by testing two hypotheses relating to the gap junction resistance. The first hypothesis is that increased variation of the gap junction resistance throughout cells in the monolayer would cause stable self-sustaining activity. This is based on the heterogeneity of gap junction distribution observed in immunohistochemistry of HL1-6 cells [69]. To test this hypothesis, the gap junction resis-

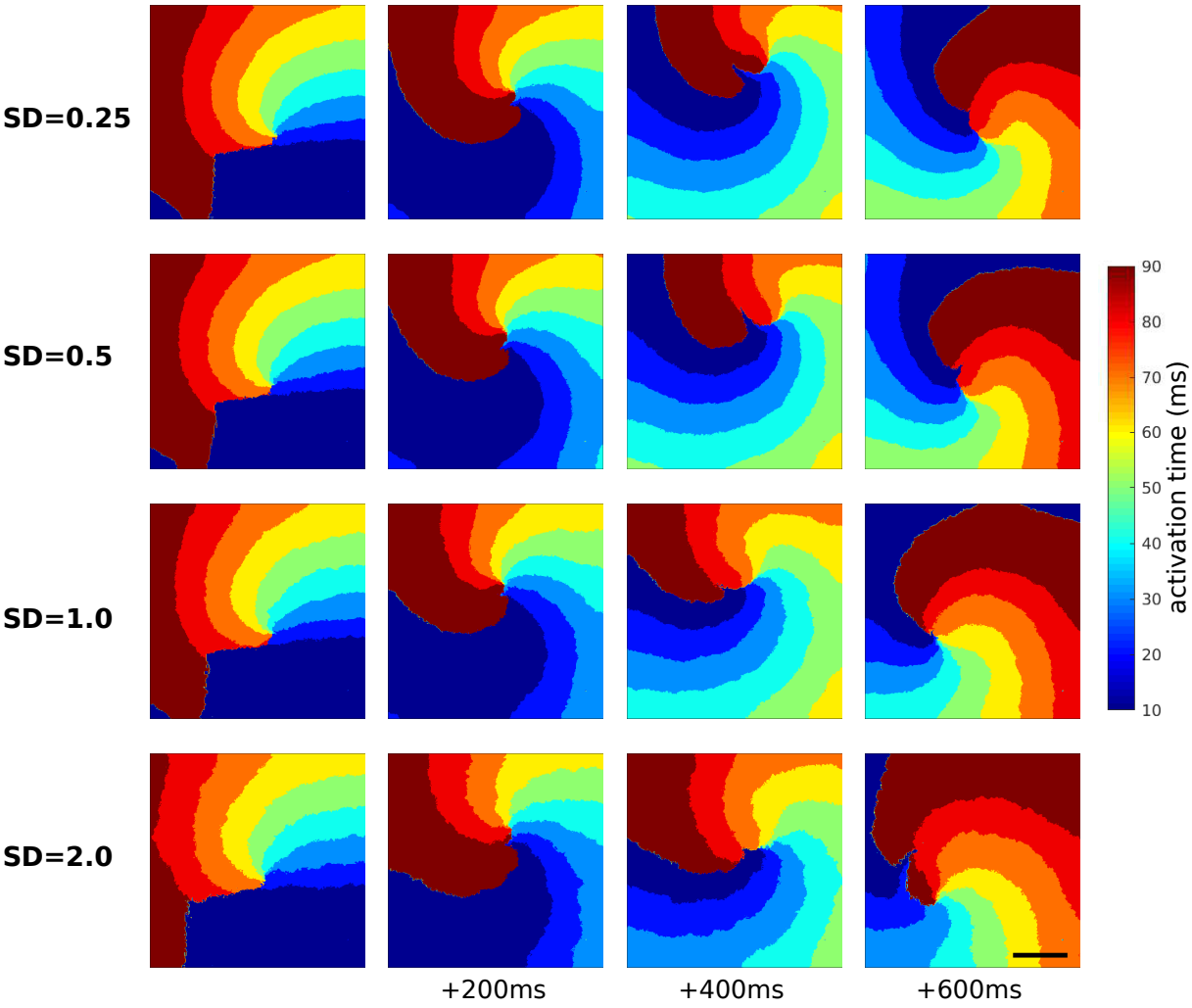


Figure 6.12: Activation maps for simulations run using the same initiation protocol in 4 mm^2 monolayer geometry. Labels indicate the increase in the standard deviation of a lognormal distribution with median 1 used to draw a multiple for each gap junction interface. The first activation map is generated at the time of the S2 stimulation. Scale bar: 0.5 mm.

tance parameter for each interface in the geometry was scaled from the calibrated value by a random draw from a lognormal distribution with median 1 (mean 0) and standard deviation increasing from 0.25 to 2.

Figure 6.12 shows activation maps generated at four time points from simulations with increasing amounts of gap junction resistance variation. The action potential wave from the simulation with the lowest variability in gap junction resistance propagates in a similar fashion to the control simulation shown in Figure 6.11. As the variability in gap junction resistance increases, the wave front becomes more irregular. This is most apparent in the lower row of activation maps which have the greatest degree of variation in gap junction resistance throughout the monolayer.

The dominant frequency of the self-sustaining activity increased from 12 Hz in the two simulations with smallest variability, to 13 Hz in the simulation with standard deviation of 1, and to 14 Hz in the simulation with standard deviation of 2. Increasing the variability in gap junction resistance did not stabilise the self-sustaining activity.

6.3.7 Concentrated increase in gap junction resistance

Next, we tested the hypothesis that the self-sustaining activity would be stabilised by anchoring to a region with a concentrated increase in gap junction resistance. In Chapter 2, stable self-sustaining activity was seen to rotate around a constant line of apparent conduction block. In light of this observation, the resistance of gap junction interfaces along a 0.75 mm line in the centre of the monolayer was progressively increased, to reproduce a similar size as lines observed *in vitro*.

Figure 6.13 displays activation maps and conduction block/slowing heat maps (as developed in Chapter 2) for simulations with increasing multiples of resistance along the line. The activation maps are generated from the same time point 500 ms after the start of the simulation (i.e. 420 ms after the S2 stimulus). Conduction block/slowing heat maps are generated as described in Chapter 2 using all recorded time frames.

Increasing the gap junction resistance by multiples of 4× or 8× had minimal effect on the characteristics of the self-sustaining activity (top two rows in Figure 6.13). The lower two rows show that as the gap junction resistance along this line was increased by a multiple greater than 16×, the self-sustaining activity stabilised around the line. The conduction block heat maps for these simulations reveal the constant feature of the underlying substrate that is being circulated, akin to the experimental maps generated in Chapter 2. Increasing the gap junction resistance in this manner had no effect on the dominant frequency of the resultant activity.

Figure 6.14 compares the conduction block heat map generated from the simulation with 32× increased gap junction resistance along the line to a map generated from an experimental recording from Chapter 2. Both maps are qualitatively similar in appearance, though there are a few differences. Firstly, the cluster of cells at the right end of the

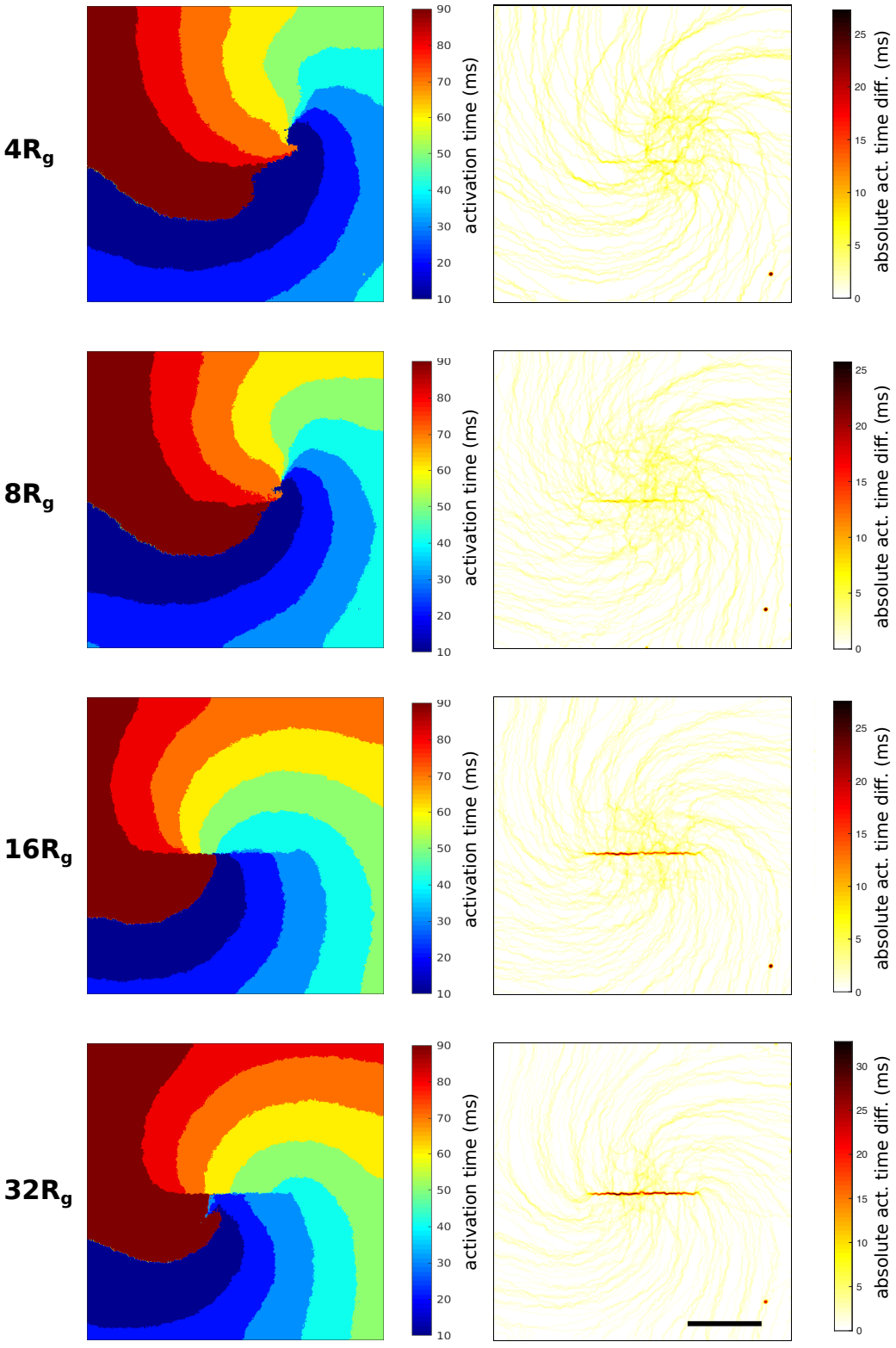


Figure 6.13: Activation maps and conduction block/slowing heat maps for simulations run using the same initiation protocol in 4 mm^2 monolayer geometry. Labels indicate the increase from the base gap junction resistance along a line length 0.75 mm and width 2 μm at the centre of the monolayer. The activation maps are generated 500 ms after the simulation started. Conduction block/slowing heat maps are generated from the entire 1 s simulated recording. Scale bar: 0.5 mm.

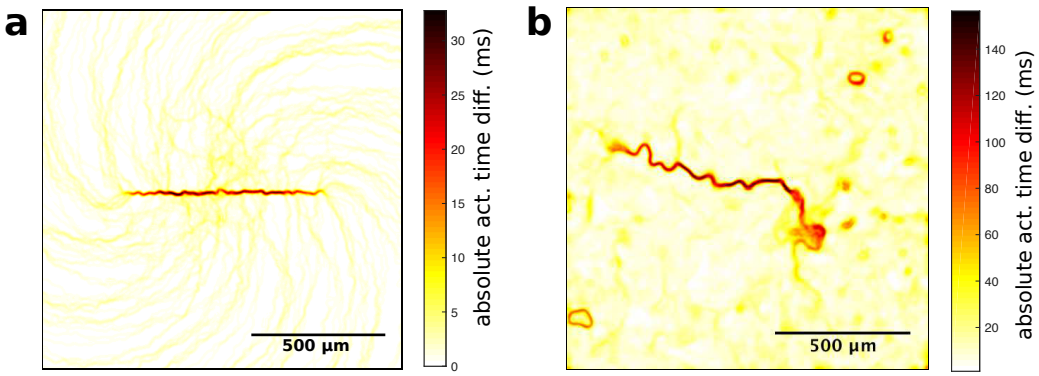


Figure 6.14: **a** Conduction block heat map from simulation with 32× increase of gap junction resistance along 0.75 mm line at centre of monolayer. The heat map has been cropped to the same field of view as the experiment. **b** Conduction block heatmap showing a line of apparent conduction block generated from results in Chapter 2.

experimental map is not present in the simulation. Secondly, the absolute time difference across the line is approximately 32 ms for the simulation and 155 ms for the experiment. Finally, the simulated map does not have any isolated regions of apparent conduction block visible in the experimental map (top right and bottom left corners of this map).

6.4 Discussion

The goal of this chapter was to develop a computer model of action potential propagation through monolayers of HL1-6 cardiomyocytes and to apply it to investigate potential mechanisms underlying the stability of self-sustaining activity in this substrate. The gap junction resistance parameter of the model was first calibrated and the model validated against the effects of ion channel blockers on conduction velocity. We then attempted to initiate self-sustaining activity in the monolayer and found that this activity would only perpetuate in a 4 mm^2 geometry, terminating at a boundary in the 1 mm^2 geometry due to spiral wave meander. Lastly, two possible mechanisms relating to gap junction inhomogeneities were investigated to explain the stability of self-sustaining activity *in vitro*. Increased variability of gap junction resistance throughout the monolayer resulted in the wave front becoming more irregular and increased the dominant frequency of activity, but did not stabilise it. A concentrated increase of gap junction resistance along a line at the centre of the monolayer, akin to biological observations in Chapter 2, caused the

self-sustaining activity to anchor to this location and remain stable for the duration of the simulation. Conduction block heat maps generated from the simulation and experimental results were qualitatively similar, though differed in the magnitude of absolute activation time difference across the line.

6.4.1 Conduction velocity calibration and validation

Calibration of the gap junction resistance parameter to conduction velocity measurements from micro-electrode array recordings [69] resulted in a control value of 0.0625 kΩ cm^2. Dias et al. [69] also conducted dual voltage clamp recordings to estimate cell-to-cell junctional coupling between pairs of HL1-6 cells, and measured a conductance of 11.2$\pm$3.1 nS. Using a rough approximation assuming an idealised square cross-sectional cell area of 220 μm^2 (1100 μm^2 multiplied by the $^1/_5$ scale factor) and height 8 μm, and assuming cells are connected along one side, would result in an equivalent gap junction resistance parameter of 0.0106 kΩ cm^2, which is encouragingly on the same order of magnitude as the estimation from calibration.

The effects of Lidocaine and Nifedipine were simulated by progressive blocking of the fast Na^+ and L-type Ca^{2+} currents respectively. The drop, or lack thereof, in conduction velocity was in line with observations from experimental measurements [69]. In the case of the Nifedipine simulation, at full L-type Ca^{2+} current block, the conduction velocity reduced to 93% of the control value, while in experiments no effect was observed [69]. No quantitative data was provided for Nifedipine experiments however, given the size of the error bars in the final data point of the Lidocaine experiment, it is conceivable that this experimental uncertainty would mask a small effect on conduction velocity measured *in vitro*. It is important to also note that the effect of Nifedipine was assumed to act solely to block the L-type Ca^{2+} current. This is likely a gross over-simplification of the real mechanism of action of the drug [237, 238], though it also reduced the Ca^{2+} transient of the cell model which was similarly observed *in vitro* by Dias et al. [69].

6.4.2 Restitution

In restitution experiments, conduction velocity was stable until pacing at 4 Hz, after which it began to reduce until only every second beat could be captured at 16 Hz. This is similar to experimental observations [69], where conduction velocity reduced beyond 4 Hz pacing rate as a result of the pacing infringing on the partial refractory period of the HL1-6 cells.

There was little variation of conduction velocity or restitution properties either between different geometry models, or different draws of cell model variants. The similar results between geometry models is likely a consequence of the large number of cells being simulated reducing variation in macroscopic measurements using the virtual electrogram. In the case where gap junction resistance does not vary across the monolayer, one would expect similar results from a continuum model with an appropriately calibrated diffusivity constant. The lack of variation between different randomised cell model variants could be attributed to the effect of connecting cells in a functional synctium, where passive current will flow across gap junction interfaces between cells to homogenise differences in the electrostatic potential.

6.4.3 Lack of automaticity in the monolayer

In the biological experiments of Chapter 2, drop colonies generally exhibited automatic activity originating from 'pacemaker' cells located near to the colony edges. This pacemaker phenotype was present in a subset of cell model variants developed in Chapter 4. However, when introduced into the monolayer multi-domain model, all cells remained quiescent without external stimulation.

It is likely that a critical mass of pacemaker cells at a location between poorly coupled and well coupled cells is required to overcome the source-sink mismatch present in the connected monolayer and propagate an action potential spontaneously. The edges of *in vitro* colonies are more sparse than the central region and more likely to have the required dynamics between poorly-coupled and well-coupled regions [29,117]. While this effect was not introduced into the simulations of this chapter, it could be incorporated into future

work, for example by imposing a gradient of increasing gap junction resistance moving from the centre to the edge of the virtual monolayer.

Duverger et al. used a simple 2D computer model of coupled neonatal rat ventricular myocytes to demonstrate how cells with natural automaticity could lead to wave propagation in a monolayer [239]. In their model, localised density of pacemaker cells was a critical factor for initiation of wave activity, with completely diffuse location of pacemaker cells resulting in no spontaneous activity. In reality, our assumption that pacemaking cells are randomly distributed around the monolayer is inherently flawed, as the HL1-6 myocytes used in the biological experiments continuously divide in culture. Thus a pacemaker cell originally seeded in one location will divide, and it would be expected that at least some of its daughter cells would possess a pacemaking phenotype, creating a small region of pacemaking cells, some of which would be expected to reach critical mass.

6.4.4 Simulated self-sustaining activity

In the biological experiments conducted in Chapter 2, there was low occurrence of self-sustaining activity in the smallest colony size (3.5 mm^2) compared to the larger colony sizes (6.4 mm^2 and 9.8 mm^2). Similarly, in simulations using the smallest monolayer size (1 mm^2) activity terminated on a boundary after approximately 140 ms (from the time of the S2 stimulus), whereas in the larger monolayer (4 mm^2) it remained self-sustaining for the duration of the 1000 ms simulation.

This is by no means an ideal comparison, as the drop colonies were circular in shape while the simulated monolayers were square. If one makes the rough approximation that the simulated square monolayer represents the confluent central portion of a drop colony (and outside of this area is the sparser region at the boundaries), then the square monolayer of 4 mm^2 would relate to a drop colony area of 6.3 mm^2 (assuming the square fits exactly in the corresponding circle), close to the area from experiments which saw more regular occurrence of self-sustaining activity. In contrast, the 1 mm^2 square monolayer would relate to a drop colony area of 1.6 mm^2, which is smaller than the smallest drop colony from biological experiments. Therefore it appears unsurprising that activity was

unable to sustain in this geometry.

Self-sustaining activity in the 4 mm^2 monolayer control simulation had a dominant frequency of 12 Hz. In contrast, recordings of activity *in vitro* revealed that the mean dominant frequency was 2.7±1.0 Hz. One explanation for this discrepancy could be that the gap junction resistance value calibrated in the first set of simulations is not appropriate for the small drop colonies in which self-sustaining activity was visualised. The experimental measurements of conduction velocity on a micro-electrode array used larger colonies in which cells may be better coupled. However, from Figure 6.7 it can be inferred that a very large increase in gap junction resistance up to 0.5 $k\Omega\ cm^2$ would be required to achieve a roughly 50% reduction in conduction velocity from the control value, so further factors are likely to play a role.

A more realistic monolayer geometry may bring results closer to biological experiments. *In vitro* cell monolayers are often purported to be simplified two dimensional models. However, as seen in Figures 6.3 and 6.5, this is not necessarily the reality as there is an uneven distribution of heights and cells can rest on top of their neighbours leaving gaps of extracellular space in the monolayer. This non-ideal arrangement of cells, which contrasts the extrusion approach adopted for the simulation geometry, would be expected to increase the effective gap junction resistance between cells, and thus could bring the dominant frequency in the simulation closer to experimental values.

Control simulations using the calibrated value of gap junction resistance revealed that the self-sustaining activity meandered around the monolayer. In contrast, in Chapter 2, all self-sustaining activity that was observed remained stable around an apparent line of conduction block for up to 10 s of recording time. Two hypotheses were tested as possible mechanisms to underlie this behaviour. Increasing the variability in gap junction resistance at interfaces across the monolayer did not stabilise the activity, though it caused the leading wave front to become more irregular and, in doing so, more similar to the wave fronts observed *in vitro*. Immunofluorescent labelling of connexins in the HL1-6 cell line revealed a heterogeneous distribution of gap junctions around the membrane of cells [69]. The variation in gap junction resistance is likely more representative of reality but does

not explain the stability of self-sustaining activity.

Creating a line of increased gap junction resistance at the centre of the monolayer simulation caused the self-sustaining activity to anchor to this region of heterogeneity and remain stable for the duration of the recording. A multiple of 16× the control gap junction value was required before this behaviour was observed. Generating conduction block heat maps akin to those from Chapter 2 produced similar core morphology to that observed in biological experiments. The difference in the absolute activation time difference in these maps can be attributed to the difference in conduction velocity in the monolayers as discussed above. The biological map was generated from Ca^{2+} transient recordings whereas the simulation map was generated from results of the electrostatic potential. They are therefore not directly comparable, though experiments conducted in Chapter 2 suggest they should be approximately similar.

These results suggest that a possible mechanism for the stable self-sustaining activity in HL1-6 monolayers are lines and/or regions of poor coupling between cells. However, *correlation is not causation* and it is also possible that a different mechanism underlies the stability. We only tested hypotheses relating to gap junction resistance to anchor the self-sustaining activity. Geometrical factors such as variation in height or cell size, that were not investigated in this work, could cause a similar effect by leading to source-sink mismatch resulting in conduction slowing/block.

A number of previous computational studies have focused on the role of microfibrosis in the genesis of cardiac arrhythmias using idealised monolayer models [117, 232, 233, 240]. Regions of microfibrosis, or their border zone, are generally found to be arrhythmogenic due to the propensity for this tissue to result in complex propagation paths within the region and heterogeneity in coupling causing wave breakthrough to occur. The simulations in this work demonstrate that a single microscopic line of reduced cellular coupling, which would be difficult or impossible to represent faithfully in conventional continuum models of cardiac electrophysiology, can result in stable self-sustaining activity in an otherwise homogeneous substrate.

6.4.5 Limitations

One limitation of the work in this chapter is that the virtual monolayers were approximations to *in vitro* monolayers based on extruding the output from a two-dimensional cell growth model. This was necessary as a result of the challenges encountered when trying to virtually replicate a drop colony by segmenting confocal microscopy images as outlined in the methods. However, the spectral/hp element implementation developed is not restricted by the geometry model and, should the direct segmentation approach become feasible, simulation using a more representative geometry would be possible.

The computational cost of running the multi-domain model imposes limits on the geometry size that can be simulated. This is a result of the sub-cellular resolution required for mesh discretisation. In this work, the largest simulated monolayer was 4 mm^2 and contained approximately 20,000 HL1-6 myocytes. By comparison, bidomain simulations can be used to simulate the entire heart organ (billions of cells), though without representing the micro-structure of cardiac tissue. Recent approaches have been suggested that could work towards bridging this gap [241–243]. For example, Bruce et al. [241] suggest that the micro-structure could be explicitly represented in a multi-domain formulation at the locations of the wave front in a macro-scale model, with the simulation reverting to a bidomain formulation elsewhere to maintain computational feasibility without losing the effects of the discrete structure on the action potential upstroke.

Finally, the conclusion that the stable self-sustaining activity is caused by poor cellular coupling along a line in the monolayer does not necessarily translate to other *in vitro* models of fibrillation. It is possible that this behaviour is unique to HL1-6 cell monolayers and simulations based on other biological models are needed to generalise the conclusion.

■

Chapter 7

Conclusions and future work

The goal of this thesis was to develop a biophysically and geometrically accurate computational model of action potential propagation through HL1-6 myocytes cultured in a monolayer and to use this model to investigate the role of microscopic heterogeneities in activity characteristic of that observed in re-entrant arrhythmias and fibrillation *in vivo*. In this chapter, an outline of the main outcomes of this thesis is provided in relation to the specific aims outlined in the Introduction, along with potential future research paths to build upon the work.

Improve understanding of the self-sustaining activity observed in HL1-6 monolayers. Self-sustaining activity could be reliably initiated in colonies provided they had a sufficient area (between 3.5 mm^2 and 6.4 mm^2) which was attributed to a combination of the increased likelihood of a suitable underlying substrate existing as area increases, and more spontaneous triggers on the edges of colonies increasing the likelihood of wave interactions initiating the activity. These automatic triggers were found to be a constant feature of the underlying substrate, i.e. particular cells in the monolayer could fire spontaneously and they did not depend on the 'initial conditions'. In contrast, the self-sustaining activity was not observed to return to the same location but did return elsewhere in the colony, suggesting that there are multiple sites at which it can occur.

Self-sustaining activity in HL1-6 monolayers was always observed to remain stable (though it is also possible that meandering activity exists but was simply never observed). The conduction block/slowing detection algorithm developed in Chapter 2 revealed that

the core of this stable activity consisted of distinct lines connecting small groups of cells around which wave fronts would rotate. At a lower resolution than used in these experiments, it is possible that this feature could be mistaken for a larger group of cells held in a depolarised or inactivated state akin to the leading circle or spiral wave theories. Experiments conducted in artificially anisotropic monolayers revealed that the core lines preferentially align in the fibre direction.

Construct an action potential model of an HL1-6 myocyte, with consideration of uncertainty and variability. Retrospective studies using approximate Bayesian computation with two human atrial cell models demonstrated that sufficient data combined with an appropriate model structure is needed to constrain the parameters in these models with confidence. A full data set will not necessarily reduce the uncertainty present in parameter estimates if the model is complex, as multiple combinations of parameters can produce the same observed output. A simpler model with fewer parameters can reduce the parameter uncertainty (in this case in particular for the fast Na^+ current) but a more tailored model may be required for other channels (in this case the L-type Ca^{2+} current and ultra-rapidly activating delayed rectifier K^+ current).

The retrospective analysis informed the development of the HL1-6 action potential model. A standardised gating formulation, based on transition rate theory, calibrated well to experimental data sets for ion currents present in the cell line. A final calibration step combined the separate channel models with intracellular ion handling dynamics to action potential and Ca^{2+} transient measurements. The result was a cell model represented by 1000 different variants of parameter combinations producing a range of output representing uncertainty and biological variability. A subset of these cells exhibit spontaneous automaticity at a rate comparable to *in vitro* observations. The resulting cell model population was validated by comparing the effect of blocking individual ion currents to experimental results. Blocking sarcolemmal Ca^{2+} currents showed good agreement with experiment, however the effects of blocking the fast Na^+ current and delayed rectifier K^+ current did not agree.

Build a multicellular model of HL1-6 monolayers, validated against biolog-

ical experiments. A multi-domain solver for action potential propagation through cell monolayers was derived and implemented using the spectral/hp element method, enabling high solution accuracy and geometric flexibility. The solver was validated against analytical solutions to the discrete form of the cable equation in one and three dimensions. The simulations were demonstrated to scale well as the number of processors was increased which made it feasible to run large simulations of monolayers with many cells necessary to capture self-sustaining activity observed in biology.

Finally, the cell model and multi-domain solver were brought together to investigate the underlying mechanism of the stable self-sustaining activity observed *in vitro*. Virtual monolayers were grown with dimensions derived from area and height measurements in confocal microscopy images. The gap junction resistance was calibrated to conduction velocity measurements from biological experiments, and the model was validated against the effect of two ion channel blockers on conduction velocity. When coupled in a monolayer, cells did not exhibit automaticity despite a subset of the cell model variants possessing this property, which was attributed to an improper representation of the more poorly coupled boundary region of the monolayers and/or the likely localised nature of groups of pacemaker cells.

Using the control value for gap junction resistance, the self-sustaining activity was not stable and meandered around the monolayer. As a result, it was possible to initiate self-sustaining activity in a square monolayer with area 4 mm^2, but not in a smaller monolayer with area 1 mm^2 due to the spiral wave terminating on a boundary. Increasing variation in gap junction coupling throughout the monolayer produced an irregular wave front more similar to those observed *in vitro*, but did not stabilise the activity. A concentrated increase of 16$\times$ the control value of gap junction resistance on interfaces along a line at the centre of the monolayer was sufficient to anchor the self-sustaining activity around the line. Core heat maps generated from the simulations were qualitatively similar to those generated from biological recordings, with the key differences being the higher dominant frequency in the simulation and the absence of any small groups of cells that also constituted the core. The implication of this result is that an order of magnitude

increase in gap junction resistance along a very small line (<1 mm) is sufficient to anchor self-sustaining activity in an otherwise homogeneous cellular synctium.

It is important to highlight that this final aim has only been partially achieved. While the multi-domain implementation was validated in a very limited sense against measurements in conduction velocity under different ion channel blockers, it is difficult to confer validation to other behaviours such as the simulations demonstrating self-sustaining activity. Further work, outlined below, would be necessary to complete the process of validation. Despite shortcomings, both the approximate Bayesian calibration approach and multi-domain spectral/hp element solver are general and could be extended to complement experiments in any *in vitro* multi-cellular model.

Future work. There are a number of paths for future research which could build on the work in this thesis. As identified above, further validation and more accurate geometrical representation of the cellular monolayer would be a key next step relating directly to this work with HL1-6 monolayers.

More complex features could be added to the geometry of the virtual monolayer model to investigate hypotheses relating to the formation of stable self-sustaining activity outwith changes in gap junction resistance. These could include changes in the cell height based on biological measurements, explicitly representing the few large cells which may cause conduction abnormalities due to source-sink mismatch or studying the effects of anisotropy.

The connexin expression level at the core region could be investigated using immunohistochemistry to determine whether the increase in gap junction resistance applied in the simulation is representative of the biological reality. This experiment would involve first capturing stable activity using the methods in this thesis, and also recording its location so it could be re-located after being fixed and labelled for cardiac connexins.

The morphology imaging approach could be optimised to be able to capture an entire drop colony which is capable of harbouring self-sustaining activity at sufficient detail to allow segmentation. The Cellpose segmentation software [234] was recently extended to segment in three dimensions in a limited capacity; further improvements to this software

may make this approach feasible in the future. Once the protocol was refined, direct validation between biological and simulated results could be achieved. First, activity would be captured using the methods developed in this thesis, before the entire cell colony in which the activity occurred was imaged and segmented as described above. Ideally, a one-to-one *in silico* geometry model would be generated to match the *in vitro* experiment. This would enable direct validation of the simulation solver against full colonies of cells, and enable further development and refining of parameters in an iterative approach with biological experiments.

The spectral/hp element solver itself could be further developed to more closely represent other features of action potential propagation in cardiac monolayers. The majority of the biological results in this work were derived from recordings of Ca^{2+} transients rather than the electrostatic potential. Currently, the cell model is solved on the membrane interfaces and each model includes its own memory of the intracellular/extracellular ion concentrations. These ion concentrations could be explicitly represented within the multi-domain model by building in a diffusion solver and allowing the cell model to use the ion concentration on either side of the interface directly. This would then allow simulations of Ca^{2+} transient propagation as well as action potential propagation.

The performance of the solver could be improved further, in particular with regards to scaling beyond a single node when run in parallel. This work could focus on identifying specific performance bottlenecks, code optimisation and/or the use of different preconditioners or iterative methods. Improvements to performance may enable larger colonies of cells to be simulated, aiding the pursuit of direct biological validation.

The gap junction interface conditions in the multi-domain model could be developed to more accurately represent the biological reality. In particular, approaches to model the interactions between abutting membranes and the thin extracellular space between them could be included using an explicit physical representation or a mathematical approximation akin to Lin and Keener [119]. This would extend the multi-domain model to be able to generate and test hypotheses relating to the role of ephaptic coupling in cardiac conduction.

Finally, the work and validation efforts could be transferred to a different cell type. Induced pluripotent stem cells are increasingly used in cardiac research and cell models have been developed that additionally account for their variability in phenotype [87]. As it becomes possible to achieve a higher purity of stem cell cultures, the multi-domain model could be validated against measurements within that *in vitro* model rather than the HL1-6 cell line. Stem cell *in vitro* models, being derived from human cells, may be more representative of human disease. ■

Bibliography

[1] J. Malmivuo and R. Plonsey, *Bioelectromagnetism: principles and applications of bioelectric and biomagnetic fields*. New York, NY: Oxford University Press, 1995.

[2] J. Keener, J. Sneyd, S. S. Antman, J. E. Marsden, and L. Sirovich, eds., *Mathematical Physiology*, vol. 8/2 of *Interdisciplinary Applied Mathematics*. New York, NY: Springer New York, 2009.

[3] A. G. Kléber and Y. Rudy, "Basic Mechanisms of Cardiac Impulse Propagation and Associated Arrhythmias," *Physiological Reviews*, vol. 84, pp. 431–488, Apr. 2004.

[4] B. Heath, K. Gingrich, and R. S. Kass, "Ion Channels in the Heart: Cellular and Molecular Properties of Cardiac Na, Ca, and K Channels," in *Comprehensive Physiology* (R. Terjung, ed.), p. cp020114, Hoboken, NJ, USA: John Wiley & Sons, Inc., Jan. 2011.

[5] D. M. Bers, "Cardiac excitation–contraction coupling," *Nature*, vol. 415, pp. 198–205, Jan. 2002.

[6] M. S. Spach, "Transition From a Continuous to Discontinuous Understanding of Cardiac Conduction," *Circulation Research*, vol. 92, pp. 125–126, Feb. 2003.

[7] R. Veeraraghavan, R. G. Gourdie, and S. Poelzing, "Mechanisms of cardiac conduction: a history of revisions," *American Journal of Physiology-Heart and Circulatory Physiology*, vol. 306, pp. H619–H627, Mar. 2014.

[8] G. Sohl, "Gap junctions and the connexin protein family," *Cardiovascular Research*, vol. 62, pp. 228–232, May 2004.

[9] J. A. Jansen, T. A. van Veen, J. M. de Bakker, and H. V. van Rijen, "Cardiac connexins and impulse propagation," *Journal of Molecular and Cellular Cardiology*, vol. 48, pp. 76–82, Jan. 2010.

[10] H. L. Kanter, J. E. Saffitz, and E. C. Beyer, "Cardiac myocytes express multiple gap junction proteins.," *Circulation Research*, vol. 70, pp. 438–444, Feb. 1992.

[11] C. Vozzi, E. Dupont, S. R. Coppen, H.-I. Yeh, and N. J. Severs, "Chamber-related Differences in Connexin Expression in the Human Heart," *Journal of Molecular and Cellular Cardiology*, vol. 31, pp. 991–1003, May 1999.

[12] A. Moreno, "Biophysical properties of homomeric and heteromultimeric channels formed by cardiac connexins," *Cardiovascular Research*, vol. 62, pp. 276–286, May 2004.

[13] R. G. Gourdie, C. R. Green, and N. J. Severs, "Gap junction distribution in adult mammalian myocardium revealed by an anti-peptide antibody and laser scanning confocal microscopy," *Journal of Cell Science*, vol. 99 (Pt 1), pp. 41–55, May 1991.

[14] R. H. Hoyt, M. L. Cohen, and J. E. Saffitz, "Distribution and three-dimensional structure of intercellular junctions in canine myocardium.," *Circulation Research*, vol. 64, pp. 563–574, Mar. 1989.

[15] A. G. Kléber and J. E. Saffitz, "Role of the intercalated disc in cardiac propagation and arrhythmogenesis," *Frontiers in Physiology*, vol. 5, Oct. 2014.

[16] J. E. Saffitz, H. L. Kanter, K. G. Green, T. K. Tolley, and E. C. Beyer, "Tissue-specific determinants of anisotropic conduction velocity in canine atrial and ventricular myocardium.," *Circulation Research*, vol. 74, pp. 1065–1070, June 1994.

[17] S. Rohr, "Role of gap junctions in the propagation of the cardiac action potential," *Cardiovascular Research*, vol. 62, pp. 309–322, May 2004.

[18] J. P. Kucera, A. G. Kléber, and S. Rohr, "Slow conduction in cardiac tissue: Insights from optical mapping at the cellular level," *Journal of Electrocardiology*, vol. 34, pp. 57–64, Oct. 2001.

[19] S. Rohr and B. M. Salzberg, "Discontinuities in Action Potential Propagation Along Chains of Single Ventricular Myocytes in Culture: Multiple Site Optical Recording of Transmembrane Voltage (MSORTV) Suggests Propagation Delays at the Junctional Sites Between Cells," *The Biological Bulletin*, vol. 183, pp. 342–343, Oct. 1992.

[20] S. Rohr, J. P. Kucera, and A. G. Kléber, "Slow Conduction in Cardiac Tissue, I: Effects of a Reduction of Excitability Versus a Reduction of Electrical Coupling on Microconduction," *Circulation Research*, vol. 83, pp. 781–794, Oct. 1998.

[21] P. Kojodjojo, P. Kanagaratnam, O. R. Segal, W. Hussain, and N. S. Peters, "The Effects of Carbenoxolone on Human Myocardial Conduction," *Journal of the American College of Cardiology*, vol. 48, pp. 1242–1249, Sept. 2006.

[22] P. A. Guerrero, R. B. Schuessler, L. M. Davis, E. C. Beyer, C. M. Johnson, K. A. Yamada, and J. E. Saffitz, "Slow ventricular conduction in mice heterozygous for a connexin43 null mutation.," *Journal of Clinical Investigation*, vol. 99, pp. 1991–1998, Apr. 1997.

[23] B. Eloff, "High resolution optical mapping reveals conduction slowing in connexin43 deficient mice," *Cardiovascular Research*, vol. 51, pp. 681–690, Sept. 2001.

[24] S. P. Thomas, J. P. Kucera, L. Bircher-Lehmann, Y. Rudy, J. E. Saffitz, and A. G. Kléber, "Impulse Propagation in Synthetic Strands of Neonatal Cardiac Myocytes With Genetically Reduced Levels of Connexin43," *Circulation Research*, vol. 92, pp. 1209–1216, June 2003.

[25] H. V. van Rijen, D. Eckardt, J. Degen, M. Theis, T. Ott, K. Willecke, H. J. Jongsma, T. Opthof, and J. M. de Bakker, "Slow Conduction and Enhanced Anisotropy Increase the Propensity for Ventricular Tachyarrhythmias in Adult Mice With Induced Deletion of Connexin43," *Circulation*, vol. 109, pp. 1048–1055, Mar. 2004.

[26] N. S. Peters, "New Insights into Myocardial Arrhythmogenesis: Distribution of Gap-Junctional Coupling in Normal, Ischaemic and Hypertrophied Human Hearts," *Clinical Science*, vol. 90, pp. 447–452, June 1996.

[27] R. R. Kaprielian, M. Gunning, E. Dupont, M. N. Sheppard, S. M. Rothery, R. Underwood, D. J. Pennell, K. Fox, J. Pepper, P. A. Poole-Wilson, and N. J. Severs, "Downregulation of Immunodetectable Connexin43 and Decreased Gap Junction Size in the Pathogenesis of Chronic Hibernation in the Human Left Ventricle," *Circulation*, vol. 97, pp. 651–660, Feb. 1998.

[28] J. M. de Bakker and H. M. van Rijen, "Continuous and Discontinuous Propagation in Heart Muscle," *Journal of Cardiovascular Electrophysiology*, vol. 17, pp. 567–573, May 2006.

[29] Y. Xie, D. Sato, A. Garfinkel, Z. Qu, and J. N. Weiss, "So Little Source, So Much Sink: Requirements for Afterdepolarizations to Propagate in Tissue," *Biophysical Journal*, vol. 99, pp. 1408–1415, Sept. 2010.

[30] R. M. Shaw and Y. Rudy, "Ionic Mechanisms of Propagation in Cardiac Tissue: Roles of the Sodium and L-type Calcium Currents During Reduced Excitability and Decreased Gap Junction Coupling," *Circulation Research*, vol. 81, pp. 727–741, Nov. 1997.

[31] S. Rohr, "Paradoxical Improvement of Impulse Conduction in Cardiac Tissue by Partial Cellular Uncoupling," *Science*, vol. 275, pp. 841–844, Feb. 1997.

[32] J. W. Waks and M. E. Josephson, "Mechanisms of Atrial Fibrillation – Reentry, Rotors and Reality," *Arrhythmia & Electrophysiology Review*, vol. 3, no. 2, p. 90, 2014.

[33] G. Mines, "On circulating excitations in heart muscle and their possible relation to tachycardia and fibrillation," *Trans R Soc Can*, vol. 8, pp. 43–52, 1914.

[34] L. H. Frame, R. L. Page, P. A. Boyden, J. J. Fenoglio, and B. F. Hoffman, "Circus movement in the canine atrium around the tricuspid ring during experimental atrial flutter and during reentry in vitro.," *Circulation*, vol. 76, pp. 1155–1175, Nov. 1987.

[35] M. A. Allessie, F. I. M. Bonke, and F. J. G. Schopman, "Circus Movement in Rabbit Atrial Muscle as a Mechanism of Tachycardia," *Circulation Research*, vol. 33, pp. 54–62, July 1973.

[36] M. A. Allessie, F. I. Bonke, and F. J. Schopman, "Circus movement in rabbit atrial muscle as a mechanism of tachycardia. II. The role of nonuniform recovery of excitability in the occurrence of unidirectional block, as studied with multiple microelectrodes.," *Circulation Research*, vol. 39, pp. 168–177, Aug. 1976.

[37] M. A. Allessie, F. I. Bonke, and F. J. Schopman, "Circus movement in rabbit atrial muscle as a mechanism of tachycardia. III. The "leading circle" concept: a new model of circus movement in cardiac tissue without the involvement of an anatomical obstacle.," *Circulation Research*, vol. 41, pp. 9–18, July 1977.

[38] J. Brugada, L. Boersma, C. J. Kirchhof, V. V. Heynen, and M. A. Allessie, "Reentrant excitation around a fixed obstacle in uniform anisotropic ventricular myocardium.," *Circulation*, vol. 84, pp. 1296–1306, Sept. 1991.

[39] J. M. Davidenko, A. V. Pertsov, R. Salomonsz, W. Baxter, and J. Jalife, "Stationary and drifting spiral waves of excitation in isolated cardiac muscle," *Nature*, vol. 355, pp. 349–351, Jan. 1992.

[40] R. A. Gray, A. M. Pertsov, and J. Jalife, "Spatial and temporal organization during cardiac fibrillation," *Nature*, vol. 392, pp. 75–78, Mar. 1998.

[41] A. M. Pertsov, J. M. Davidenko, R. Salomonsz, W. T. Baxter, and J. Jalife, "Spiral waves of excitation underlie reentrant activity in isolated cardiac muscle.," *Circulation Research*, vol. 72, pp. 631–650, Mar. 1993.

[42] C. Cabo, A. Pertsov, J. Davidenko, W. Baxter, R. Gray, and J. Jalife, "Vortex shedding as a precursor of turbulent electrical activity in cardiac muscle," *Biophysical Journal*, vol. 70, pp. 1105–1111, Mar. 1996.

[43] S. V. Pandit and J. Jalife, "Rotors and the Dynamics of Cardiac Fibrillation," *Circulation Research*, vol. 112, pp. 849–862, Mar. 2013.

[44] M. S. Guillem, A. M. Climent, M. Rodrigo, F. Fernández-Avilés, F. Atienza, and O. Berenfeld, "Presence and stability of rotors in atrial fibrillation: evidence and therapeutic implications," *Cardiovascular Research*, vol. 109, pp. 480–492, Apr. 2016.

[45] J. Heijman, V. Algalarrondo, N. Voigt, J. Melka, X. H. Wehrens, D. Dobrev, and S. Nattel, "The value of basic research insights into atrial fibrillation mechanisms as a guide to therapeutic innovation: a critical analysis," *Cardiovascular Research*, vol. 109, pp. 467–479, Apr. 2016.

[46] P. R. R. van Gorp, S. A. Trines, D. A. Pijnappels, and A. A. F. de Vries, "Multicellular In vitro Models of Cardiac Arrhythmias: Focus on Atrial Fibrillation," *Frontiers in Cardiovascular Medicine*, vol. 7, p. 43, Mar. 2020.

[47] M. T. Burrows, "Rhythmical activity of isolated heart muscle cells in vitro," *Science (New York, N.Y.)*, vol. 36, pp. 90–92, July 1912.

[48] E. Entcheva and H. Bien, "Macroscopic optical mapping of excitation in cardiac cell networks with ultra-high spatiotemporal resolution," *Progress in Biophysics and Molecular Biology*, vol. 92, pp. 232–257, Oct. 2006.

[49] L. Tung and Y. Zhang, "Optical imaging of arrhythmias in tissue culture," *Journal of Electrocardiology*, vol. 39, pp. S2–S6, Oct. 2006.

[50] B. J. Boukens and I. R. Efimov, "A Century of Optocardiography," *IEEE Reviews in Biomedical Engineering*, vol. 7, pp. 115–125, 2014.

[51] N. Bursac, K. Parker, S. Iravanian, and L. Tung, "Cardiomyocyte Cultures With Controlled Macroscopic Anisotropy: A Model for Functional Electrophysiological Studies of Cardiac Muscle," *Circulation Research*, vol. 91, Dec. 2002.

[52] V. G. Fast and A. G. Kléber, "Microscopic conduction in cultured strands of neonatal rat heart cells measured with voltage-sensitive dyes.," *Circulation Research*, vol. 73, pp. 914–925, Nov. 1993.

[53] V. G. Fast and A. G. Kléber, "Cardiac tissue geometry as a determinant of unidirectional conduction block: assessment of microscopic excitation spread by optical mapping in patterned cell cultures and in a computer model," *Cardiovascular Research*, vol. 29, pp. 697–707, May 1995.

[54] V. G. Fast and A. G. Kléber, "Role of wavefront curvature in propagation of cardiac impulse," *Cardiovascular Research*, vol. 33, pp. 258–271, Feb. 1997.

[55] W. Bian and L. Tung, "Structure-Related Initiation of Reentry by Rapid Pacing in Monolayers of Cardiac Cells," *Circulation Research*, vol. 98, Mar. 2006.

[56] E. Entcheva, S. N. Lu, R. H. Troppman, V. Sharma, and L. Tung, "Contact Fluorescence Imaging of Reentry in Monolayers of Cultured Neonatal Rat Ventricular Myocytes," *Journal of Cardiovascular Electrophysiology*, vol. 11, pp. 665–676, June 2000.

[57] L. Hou, M. Deo, P. Furspan, S. V. Pandit, S. Mironov, D. S. Auerbach, Q. Gong, Z. Zhou, O. Berenfeld, and J. Jalife, "A Major Role for hERG in Determining Frequency of Reentry in Neonatal Rat Ventricular Myocyte Monolayer," *Circulation Research*, vol. 107, pp. 1503–1511, Dec. 2010.

[58] N. Badie, J. A. Scull, R. Y. Klinger, A. Krol, and N. Bursac, "Conduction block in micropatterned cardiomyocyte cultures replicating the structure of ventricular cross-sections," *Cardiovascular Research*, vol. 93, pp. 263–271, Feb. 2012.

[59] C. Kane and C. M. N. Terracciano, "Concise Review: Criteria for Chamber-Specific Categorization of Human Cardiac Myocytes Derived from Pluripotent Stem Cells: Criteria for Chamber-Specific Categorization of Myocytes," *STEM CELLS*, vol. 35, pp. 1881–1897, Aug. 2017.

[60] W. C. Claycomb, N. A. Lanson, B. S. Stallworth, D. B. Egeland, J. B. Delcarpio, A. Bahinski, and N. J. Izzo, "HL-1 cells: A cardiac muscle cell line that contracts and retains phenotypic characteristics of the adult cardiomyocyte," *Proceedings of the National Academy of Sciences*, vol. 95, pp. 2979–2984, Mar. 1998.

[61] S. M. White, P. E. Constantin, and W. C. Claycomb, "Cardiac physiology at the cellular level: use of cultured HL-1 cardiomyocytes for studies of cardiac muscle cell structure and function," *American Journal of Physiology-Heart and Circulatory Physiology*, vol. 286, pp. H823–H829, Mar. 2004.

[62] L. Sartiani, P. Bochet, E. Cerbai, A. Mugelli, and R. Fischmeister, "Functional expression of the hyperpolarization-activated, non-selective cation current $I_{\,\mathrm{f}}$ in immortalized HL-1 cardiomyocytes," *The Journal of Physiology*, vol. 545, pp. 81–92, Nov. 2002.

[63] T. Nakajima, S. Davies, E. Matafonova, F. Potet, V. Amarnath, K. Tallman, R. Serwa, N. Porter, J. Balser, S. Kupershmidt, and L. Roberts, "Selective γ-ketoaldehyde scavengers protect NaV1.5 from oxidant-induced inactivation," *Journal of Molecular and Cellular Cardiology*, vol. 48, pp. 352–359, Feb. 2010.

[64] F. Rao, C.-Y. Deng, S.-L. Wu, D.-Z. Xiao, X.-Y. Yu, S.-J. Kuang, Q.-X. Lin, and Z.-X. Shan, "Involvement of Src in L-type Ca2+ channel depression induced by macrophage migration inhibitory factor in atrial myocytes," *Journal of Molecular and Cellular Cardiology*, vol. 47, pp. 586–594, Nov. 2009.

[65] N. Nguyen, M. Biet, E. Simard, E. Béliveau, N. Francoeur, G. Guillemette, R. Dumaine, M. Grandbois, and G. Boulay, "STIM1 participates in the contractile rhythmicity of HL-1 cells by moderating T-type Ca2+ channel activity," *Biochimica et Biophysica Acta (BBA) - Molecular Cell Research*, vol. 1833, pp. 1294–1303, June 2013.

[66] J. H. Hong, J. H. Choi, T. Y. Kim, and K. J. Lee, "Spiral reentry waves in confluent layer of HL-1 cardiomyocyte cell lines," *Biochemical and Biophysical Research Communications*, vol. 377, pp. 1269–1273, Dec. 2008.

[67] K. Umapathy, S. Masse, K. Kolodziejska, G. D. Veenhuyzen, V. S. Chauhan, M. Husain, T. Farid, E. Downar, E. Sevaptsidis, and K. Nanthakumar, "Electrogram fractionation in murine HL-1 atrial monolayer model," *Heart Rhythm*, vol. 5, pp. 1029–1035, July 2008.

[68] A. M. Climent, M. S. Guillem, L. Fuentes, P. Lee, C. Bollensdorff, M. E. Fernández-Santos, S. Suárez-Sancho, R. Sanz-Ruiz, P. L. Sánchez, F. Atienza, and F. Fernández-Avilés, "Role of atrial tissue remodeling on rotor dynamics: an in vitro study," *American Journal of Physiology-Heart and Circulatory Physiology*, vol. 309, pp. H1964–H1973, Dec. 2015.

[69] P. Dias, T. Desplantez, M. A. El-Harasis, R. A. Chowdhury, N. D. Ullrich, A. Cabestrero de Diego, N. S. Peters, N. J. Severs, K. T. MacLeod, and E. Dupont, "Characterisation of connexin expression and electrophysiological properties in stable clones of the HL-1 myocyte cell line," *PloS One*, vol. 9, no. 2, p. e90266, 2014.

[70] P. Beauchamp, K. A. Yamada, A. J. Baertschi, K. Green, E. M. Kanter, J. E. Saffitz, and A. G. Kléber, "Relative Contributions of Connexins 40 and 43 to Atrial Impulse Propagation in Synthetic Strands of Neonatal and Fetal Murine Cardiomyocytes," *Circulation Research*, vol. 99, pp. 1216–1224, Nov. 2006.

[71] C. Houston, K. N. Tzortzis, C. Roney, A. Saglietto, D. S. Pitcher, C. D. Cantwell, R. A. Chowdhury, F. S. Ng, N. S. Peters, and E. Dupont, "Characterisation of reentrant circuit (or rotational activity) in vitro using the HL1-6 myocyte cell line," *Journal of Molecular and Cellular Cardiology*, vol. 119, pp. 155–164, 2018.

[72] A. L. Hodgkin and A. F. Huxley, "A quantitative description of membrane current and its application to conduction and excitation in nerve," *The Journal of Physiology*, vol. 117, pp. 500–544, Aug. 1952.

[73] S. A. Niederer, M. Fink, D. Noble, and N. P. Smith, "A meta-analysis of cardiac electrophysiology computational models," *Experimental Physiology*, vol. 94, pp. 486–495, May 2009.

[74] E. M. Cherry, H. M. Hastings, and S. J. Evans, "Dynamics of human atrial cell models: Restitution, memory, and intracellular calcium dynamics in single cells," *Progress in Biophysics and Molecular Biology*, vol. 98, pp. 24–37, Sept. 2008.

[75] O. Dössel, M. W. Krueger, F. M. Weber, M. Wilhelms, and G. Seemann, "Computational modeling of the human atrial anatomy and electrophysiology," *Medical & Biological Engineering & Computing*, vol. 50, pp. 773–799, Aug. 2012.

[76] D. Noble and Y. Rudy, "Models of cardiac ventricular action potentials: iterative interaction between experiment and simulation," *Philosophical Transactions of the Royal Society of London. Series A: Mathematical, Physical and Engineering Sciences*, vol. 359, pp. 1127–1142, June 2001.

[77] R. Wilders, "Computer Modelling of the Sinoatrial Node," in *Biopacemaking* (J. H. Nagel, J. A. E. Spaan, R. Coronel, J. M. T. de Bakker, and A. Zaza, eds.), pp. 121–148, Berlin, Heidelberg: Springer Berlin Heidelberg, 2007. Series Title: Series in Biomedical Engineering.

[78] P. Stewart, O. V. Aslanidi, D. Noble, P. J. Noble, M. R. Boyett, and H. Zhang, "Mathematical models of the electrical action potential of Purkinje fibre cells," *Philosophical Transactions of the Royal Society A: Mathematical, Physical and Engineering Sciences*, vol. 367, pp. 2225–2255, June 2009.

[79] V. E. Bondarenko, G. P. Szigeti, G. C. L. Bett, S.-J. Kim, and R. L. Rasmusson, "Computer model of action potential of mouse ventricular myocytes," *American Journal of Physiology-Heart and Circulatory Physiology*, vol. 287, pp. H1378–H1403, Sept. 2004.

[80] L. J. Wang and E. A. Sobie, "Mathematical model of the neonatal mouse ventricular action potential," *American Journal of Physiology-Heart and Circulatory Physiology*, vol. 294, pp. H2565–H2575, June 2008.

[81] A. Mayer, P. Bittihn, and S. Luther, "Complex restitution behavior and reentry in a cardiac tissue model for neonatal mice," *Physiological Reports*, vol. 5, p. e13449, Oct. 2017.

[82] D. S. Lindblad, C. R. Murphey, J. W. Clark, and W. R. Giles, "A model of the action potential and underlying membrane currents in a rabbit atrial cell," *American Journal of Physiology-Heart and Circulatory Physiology*, vol. 271, pp. H1666–H1696, Oct. 1996.

[83] Y. Kurata, I. Hisatome, S. Imanishi, and T. Shibamoto, "Dynamical description of sinoatrial node pacemaking: improved mathematical model for primary pacemaker cell," *American Journal of Physiology-Heart and Circulatory Physiology*, vol. 283, pp. H2074–H2101, Nov. 2002.

[84] T. Korhonen, S. L. Hänninen, and P. Tavi, "Model of Excitation-Contraction Coupling of Rat Neonatal Ventricular Myocytes," *Biophysical Journal*, vol. 96, pp. 1189–1209, Feb. 2009.

[85] C. H. Luo and Y. Rudy, "A model of the ventricular cardiac action potential. Depolarization, repolarization, and their interaction.," *Circulation Research*, vol. 68, pp. 1501–1526, June 1991.

[86] C. H. Luo and Y. Rudy, "A dynamic model of the cardiac ventricular action potential. I. Simulations of ionic currents and concentration changes.," *Circulation Research*, vol. 74, pp. 1071–1096, June 1994.

[87] D. C. Kernik, S. Morotti, H. Wu, P. Garg, H. J. Duff, J. Kurokawa, J. Jalife, J. C. Wu, E. Grandi, and C. E. Clancy, "A computational model of induced pluripotent stem-cell derived cardiomyocytes incorporating experimental variability from multiple data sources," *The Journal of Physiology*, vol. 597, pp. 4533–4564, Sept. 2019.

[88] N. A. Trayanova, "Whole-Heart Modeling: Applications to Cardiac Electrophysiology and Electromechanics," *Circulation Research*, vol. 108, pp. 113–128, Jan. 2011.

[89] E. Vigmond, R. Weber dos Santos, A. Prassl, M. Deo, and G. Plank, "Solvers for the cardiac bidomain equations," *Progress in Biophysics and Molecular Biology*, vol. 96, pp. 3–18, Jan. 2008.

[90] C. D. Cantwell, S. Yakovlev, R. M. Kirby, N. S. Peters, and S. J. Sherwin, "High-order spectral/hp element discretisation for reaction–diffusion problems on surfaces: Application to cardiac electrophysiology," *Journal of Computational Physics*, vol. 257, pp. 813–829, Jan. 2014.

[91] S. A. Niederer, J. Lumens, and N. A. Trayanova, "Computational models in cardiology," *Nature Reviews. Cardiology*, vol. 16, pp. 100–111, Feb. 2019.

[92] M. S. Spach, W. T. Miller, D. B. Geselowitz, R. C. Barr, J. M. Kootsey, and E. A. Johnson, "The discontinuous nature of propagation in normal canine cardiac muscle. Evidence for recurrent discontinuities of intracellular resistance that affect the membrane currents.," *Circulation Research*, vol. 48, pp. 39–54, Jan. 1981.

[93] R. W. Joyner, "Effects of the discrete pattern of electrical coupling on propagation through an electrical syncytium.," *Circulation Research*, vol. 50, pp. 192–200, Feb. 1982.

[94] P. J. Diaz, Y. Rudy, and R. Plonsey, "Intercalated discs as a cause for discontinuous propagation in cardiac muscle: A theoretical simulation," *Annals of Biomedical Engineering*, vol. 11, pp. 177–189, May 1983.

[95] R. Joyner, R. Veenstra, D. Rawling, and A. Chorro, "Propagation through electrically coupled cells. Effects of a resistive barrier," *Biophysical Journal*, vol. 45, pp. 1017–1025, May 1984.

[96] Y. Rudy and W. L. Quan, "A model study of the effects of the discrete cellular structure on electrical propagation in cardiac tissue.," *Circulation Research*, vol. 61, pp. 815–823, Dec. 1987.

[97] W. Cole, J. Picone, and N. Sperelakis, "Gap junction uncoupling and discontinuous propagation in the heart. A comparison of experimental data with computer simulations," *Biophysical Journal*, vol. 53, pp. 809–818, May 1988.

[98] J. P. Keener, "The Effects of Gap Junctions on Propagation in Myocardium: A Modified Cable Theory," *Annals of the New York Academy of Sciences*, vol. 591, pp. 257–277, June 1990.

[99] M. S. Spach and J. F. Heidlage, "A multidimensional model of cellular effects on the spread of electrotonic currents and on propagating action potentials," *Critical Reviews in Biomedical Engineering*, vol. 20, no. 3-4, pp. 141–169, 1992.

[100] M. S. Spach and J. F. Heidlage, "The Stochastic Nature of Cardiac Propagation at a Microscopic Level: Electrical Description of Myocardial Architecture and Its Application to Conduction," *Circulation Research*, vol. 76, pp. 366–380, Mar. 1995.

[101] M. S. Spach and J. P. Boineau, "Microfibrosis Produces Electrical Load Variations Due to Loss of Side-to-Side Cell Connections; A Major Mechanism of Structural Heart Disease Arrhythmias," *Pacing and Clinical Electrophysiology*, vol. 20, pp. 397–413, Feb. 1997.

[102] M. S. Spach, J. F. Heidlage, P. C. Dolber, and R. C. Barr, "Extracellular Discontinuities in Cardiac Muscle: Evidence for Capillary Effects on the Action Potential Foot," *Circulation Research*, vol. 83, pp. 1144–1164, Nov. 1998.

[103] M. S. Spach, J. F. Heidlage, P. C. Dolber, and R. C. Barr, "Electrophysiological Effects of Remodeling Cardiac Gap Junctions and Cell Size: Experimental and Model Studies of Normal Cardiac Growth," *Circulation Research*, vol. 86, pp. 302–311, Feb. 2000.

[104] M. S. Spach, J. Heidlage, R. C. Barr, and P. C. Dolber, "Cell size and communication: Role in structural and electrical development and remodeling of the heart," *Heart Rhythm*, vol. 1, pp. 500–515, Oct. 2004.

[105] J. G. Stinstra, B. Hopenfeld, and R. S. MacLeod, "On the Passive Cardiac Conductivity," *Annals of Biomedical Engineering*, vol. 33, pp. 1743–1751, Dec. 2005.

[106] J. G. Stinstra, S. Shome, B. Hopenfeld, and R. S. MacLeod, "Modelling passive cardiac conductivity during ischaemia," *Medical & Biological Engineering & Computing*, vol. 43, pp. 776–782, Nov. 2005.

[107] J. Stinstra, S. Roberts, J. Pormann, R. Macleod, and C. Henriquez, "A Model of 3D Propagation in Discrete Cardiac Tissue," *Computers in Cardiology*, vol. 33, pp. 41–44, 2006.

[108] S. F. Roberts, J. G. Stinstra, and C. S. Henriquez, "Effect of Nonuniform Interstitial Space Properties on Impulse Propagation: A Discrete Multidomain Model," *Biophysical Journal*, vol. 95, pp. 3724–3737, Oct. 2008.

[109] J. Stinstra, C. Henriquez, and R. MacLeod, "Comparison of microscopic and bidomain models of anisotropic conduction," in *2009 36th Annual Computers in Cardiology Conference (CinC)*, pp. 657–660, Sept. 2009. ISSN: 2325-8853.

[110] J. Stinstra, R. MacLeod, and C. Henriquez, "Incorporating Histology into a 3D Microscopic Computer Model of Myocardium to Study Propagation at a Cellular Level," *Annals of Biomedical Engineering*, vol. 38, pp. 1399–1414, Apr. 2010.

[111] M. L. Hubbard, W. Ying, and C. S. Henriquez, "Effect of gap junction distribution on impulse propagation in a monolayer of myocytes: a model study," *Europace*, vol. 9, pp. vi20–vi28, Nov. 2007.

[112] J. M. Kim, N. Bursac, and C. S. Henriquez, "A Computer Model of Engineered Cardiac Monolayers," *Biophysical Journal*, vol. 98, pp. 1762–1771, May 2010.

[113] V. Jacquemet and C. S. Henriquez, "Loading effect of fibroblast-myocyte coupling on resting potential, impulse propagation, and repolarization: insights from a microstructure model," *American Journal of Physiology-Heart and Circulatory Physiology*, vol. 294, pp. H2040–H2052, May 2008.

[114] Y. Xie, A. Garfinkel, P. Camelliti, P. Kohl, J. N. Weiss, and Z. Qu, "Effects of fibroblast-myocyte coupling on cardiac conduction and vulnerability to reentry: A computational study," *Heart Rhythm*, vol. 6, pp. 1641–1649, Nov. 2009.

[115] V. Jacquemet and C. S. Henriquez, "Genesis of complex fractionated atrial electrograms in zones of slow conduction: A computer model of microfibrosis," *Heart Rhythm*, vol. 6, pp. 803–810, June 2009.

[116] M. L. Hubbard and C. S. Henriquez, "Microscopic variations in interstitial and intracellular structure modulate the distribution of conduction delays and block in cardiac tissue with source-load mismatch," *Europace*, vol. 14, pp. v3–v9, Nov. 2012.

[117] M. L. Hubbard and C. S. Henriquez, "A microstructural model of reentry arising from focal breakthrough at sites of source-load mismatch in a central region of slow conduction," *American Journal of Physiology-Heart and Circulatory Physiology*, vol. 306, pp. H1341–H1352, May 2014.

[118] J. Lin and J. P. Keener, "Ephaptic Coupling in Cardiac Myocytes," *IEEE Transactions on Biomedical Engineering*, vol. 60, pp. 576–582, Feb. 2013.

[119] J. Lin and J. Keener, "Microdomain Effects on Transverse Cardiac Propagation," *Biophysical Journal*, vol. 106, pp. 925–931, Feb. 2014.

[120] A. Tveito, K. H. Jæger, M. Kuchta, K.-A. Mardal, and M. E. Rognes, "A Cell-Based Framework for Numerical Modeling of Electrical Conduction in Cardiac Tissue," *Frontiers in Physics*, vol. 5, p. 48, Oct. 2017.

[121] K. H. Jæger, A. G. Edwards, A. McCulloch, and A. Tveito, "Properties of cardiac conduction in a cell-based computational model," *PLoS computational biology*, vol. 15, p. e1007042, May 2019.

[122] N. Sperelakis and K. McConnell, "Electric field interactions between closely abutting excitable cells," *IEEE Engineering in Medicine and Biology Magazine*, vol. 21, pp. 77–89, Feb. 2002.

[123] K. H. Jæger, S. Wall, and A. Tveito, "Detecting undetectables: Can conductances of action potential models be changed without appreciable change in the transmembrane potential?," *Chaos: An Interdisciplinary Journal of Nonlinear Science*, vol. 29, p. 073102, July 2019.

[124] G. R. Mirams, P. Pathmanathan, R. A. Gray, P. Challenor, and R. H. Clayton, "Uncertainty and variability in computational and mathematical models of cardiac physiology," *The Journal of Physiology*, vol. 594, no. 23, pp. 6833–6847, 2016.

[125] R. H. Clayton, Y. Aboelkassem, C. D. Cantwell, C. Corrado, T. Delhaas, W. Huberts, C. L. Lei, H. Ni, A. V. Panfilov, C. Roney, and R. W. dos Santos, "An audit of uncertainty in multi-scale cardiac electrophysiology models," *Philosophical Transactions of the Royal Society A: Mathematical, Physical and Engineering Sciences*, vol. 378, p. 20190335, June 2020.

[126] R. H. Johnstone, E. T. Y. Chang, R. Bardenet, T. P. de Boer, D. J. Gavaghan, P. Pathmanathan, R. H. Clayton, and G. R. Mirams, "Uncertainty and variability in models of the cardiac action potential: Can we build trustworthy models?," *Journal of Molecular and Cellular Cardiology*, vol. 96, pp. 49–62, 2016.

[127] M. Fink and D. Noble, "Markov models for ion channels: versatility versus identifiability and speed," *Philosophical Transactions. Series A, Mathematical, Physical, and Engineering Sciences*, vol. 367, pp. 2161–2179, June 2009.

[128] E. T. Y. Chang, M. Strong, and R. H. Clayton, "Bayesian Sensitivity Analysis of a Cardiac Cell Model Using a Gaussian Process Emulator," *PLOS ONE*, vol. 10, p. e0130252, June 2015.

[129] M. Zaniboni, I. Riva, F. Cacciani, and M. Groppi, "How different two almost identical action potentials can be: a model study on cardiac repolarization," *Mathematical Biosciences*, vol. 228, pp. 56–70, Nov. 2010.

[130] A. C. Daly, D. J. Gavaghan, C. Holmes, and J. Cooper, "Hodgkin-Huxley revisited: reparametrization and identifiability analysis of the classic action potential model with approximate Bayesian methods," *Royal Society Open Science*, vol. 2, p. 150499, Dec. 2015.

[131] P. Pathmanathan, J. M. Cordeiro, and R. A. Gray, "Comprehensive Uncertainty Quantification and Sensitivity Analysis for Cardiac Action Potential Models," *Frontiers in Physiology*, vol. 10, p. 721, June 2019.

[132] B. S. Handa, C. H. Roney, C. Houston, N. A. Qureshi, X. Li, D. S. Pitcher, R. A. Chowdhury, P. B. Lim, E. Dupont, S. A. Niederer, C. D. Cantwell, N. S. Peters, and F. S. Ng, "Analytical approaches for myocardial fibrillation signals," *Computers in Biology and Medicine*, vol. 102, pp. 315–326, 2018.

[133] C.-T. Tsai, F.-T. Chiang, W.-P. Chen, J.-J. Hwang, C.-D. Tseng, C.-K. Wu, C.-C. Yu, Y.-C. Wang, L.-P. Lai, and J.-L. Lin, "Angiotensin II induces complex fractionated electrogram in a cultured atrial myocyte monolayer mediated by calcium and sodium-calcium exchanger," *Cell Calcium*, vol. 49, pp. 1–11, Jan. 2011.

[134] A. M. Climent, M. S. Guillem, P. Lee, C. Bollensdorff, F. Atienza, M. E. Fernández-Santos, R. Sanz-Ruiz, P. L. Sánchez, and F. Fernández-Avilés, "An In-Vitro Model of Cardiac Fibrillation with Different Degrees of Complexity," in *XIII Mediterranean Conference on Medical and Biological Engineering and Computing 2013* (L. M. Roa Romero, ed.), vol. 41, pp. 340–343, Cham: Springer International Publishing, 2014. Series Title: IFMBE Proceedings.

[135] Y.-L. Huang, A. S. Walker, and E. W. Miller, "A Photostable Silicon Rhodamine Platform for Optical Voltage Sensing," *Journal of the American Chemical Society*, vol. 137, pp. 10767–10776, Aug. 2015.

[136] Z. Püspöki, M. Storath, D. Sage, and M. Unser, "Transforms and Operators for Directional Bioimage Analysis: A Survey," in *Focus on Bio-Image Informatics* (W. H. De Vos, S. Munck, and J.-P. Timmermans, eds.), vol. 219, pp. 69–93, Cham: Springer International Publishing, 2016. Series Title: Advances in Anatomy, Embryology and Cell Biology.

[137] C. H. Roney, *Mathematical techniques for assessing cardiac wavefront dynamics*. PhD thesis, June 2015. Publisher: Imperial College London.

[138] J. I. Laughner, F. S. Ng, M. S. Sulkin, R. M. Arthur, and I. R. Efimov, "Processing and analysis of cardiac optical mapping data obtained with potentiometric dyes," *American Journal of Physiology-Heart and Circulatory Physiology*, vol. 303, pp. H753–H765, Oct. 2012.

[139] P. Bayly, B. KenKnight, J. Rogers, R. Hillsley, R. Ideker, and W. Smith, "Estimation of conduction velocity vector fields from epicardial mapping data," *IEEE Transactions on Biomedical Engineering*, vol. 45, pp. 563–571, May 1998.

[140] S. Iravanian, Y. Nabutovsky, C.-R. Kong, S. Saha, N. Bursac, and L. Tung, "Functional reentry in cultured monolayers of neonatal rat cardiac cells," *American Journal of Physiology-Heart and Circulatory Physiology*, vol. 285, pp. H449–H456, July 2003.

[141] C. de Diego, F. Chen, Y. Xie, R. K. Pai, L. Slavin, J. Parker, S. T. Lamp, Z. Qu, J. N. Weiss, and M. Valderrábano, "Anisotropic conduction block and reentry in neonatal rat ventricular myocyte monolayers," *American Journal of Physiology-Heart and Circulatory Physiology*, vol. 300, pp. H271–H278, Jan. 2011.

[142] Z. Yang and K. T. Murray, "Ionic Mechanisms of Pacemaker Activity in Spontaneously Contracting Atrial HL-1 Cells:," *Journal of Cardiovascular Pharmacology*, vol. 57, pp. 28–36, Jan. 2011.

[143] M. E. Josephson, "Electrophysiology at a crossroads: A revisit," *Heart Rhythm*, vol. 13, pp. 2317–2322, Dec. 2016.

[144] G. R. Juszczak and A. H. Swiergiel, "Properties of gap junction blockers and their behavioural, cognitive and electrophysiological effects: Animal and human studies," *Progress in Neuro-Psychopharmacology and Biological Psychiatry*, vol. 33, pp. 181–198, Mar. 2009.

[145] E. M. L. Bastiaanse, H. J. Jongsma, A. van der Laarse, and B. R. Takens-Kwak, "Heptanol-induced decrease in cardiac gap junctional conductance is mediated by a decrease in the fluidity of membranous cholesterol-rich domains," *The Journal of Membrane Biology*, vol. 136, pp. 135–145, Nov. 1993.

[146] E. W. Miller, "Small molecule fluorescent voltage indicators for studying membrane potential," *Current Opinion in Chemical Biology*, vol. 33, pp. 74–80, Aug. 2016.

[147] M. J. Schalij, L. Boersma, M. Huijberts, and M. A. Allessie, "Anisotropic Reentry in a Perfused 2-Dimensional Layer of Rabbit Ventricular Myocardium," *Circulation*, vol. 102, pp. 2650–2658, Nov. 2000.

[148] P. Comtois, J. Kneller, and S. Nattel, "Of circles and spirals: Bridging the gap between the leading circle and spiral wave concepts of cardiac reentry," *EP Europace*, vol. 7, pp. S10–S20, Jan. 2005.

[149] K. Agladze, M. W. Kay, V. Krinsky, and N. Sarvazyan, "Interaction between spiral and paced waves in cardiac tissue," *American Journal of Physiology-Heart and Circulatory Physiology*, vol. 293, pp. H503–H513, July 2007.

[150] S. M. Narayan, D. E. Krummen, P. Clopton, K. Shivkumar, and J. M. Miller, "Direct or Coincidental Elimination of Stable Rotors or Focal Sources May Explain Successful Atrial Fibrillation Ablation," *Journal of the American College of Cardiology*, vol. 62, pp. 138–147, July 2013.

[151] K. Shivkumar, K. A. Ellenbogen, J. D. Hummel, J. M. Miller, and J. S. Steinberg, "Acute Termination of Human Atrial Fibrillation by Identification and Catheter Ablation of Localized Rotors and Sources: First Multicenter Experience of Focal Impulse and Rotor Modulation (FIRM) Ablation," *Journal of Cardiovascular Electrophysiology*, vol. 23, pp. 1277–1285, Dec. 2012.

[152] M. Haissaguerre, M. Hocini, A. Denis, A. J. Shah, Y. Komatsu, S. Yamashita, M. Daly, S. Amraoui, S. Zellerhoff, M.-Q. Picat, A. Quotb, L. Jesel, H. Lim, S. Ploux, P. Bordachar, G. Attuel, V. Meillet, P. Ritter, N. Derval, F. Sacher, O. Bernus, H. Cochet, P. Jais, and R. Dubois, "Driver Domains in Persistent Atrial Fibrillation," *Circulation*, vol. 130, pp. 530–538, Aug. 2014.

[153] N. Bursac and L. Tung, "Acceleration of functional reentry by rapid pacing in anisotropic cardiac monolayers: Formation of multi-wave functional reentries," *Cardiovascular Research*, vol. 69, pp. 381–390, Feb. 2006.

[154] J. Yan, J. K. Thomson, W. Zhao, V. G. Fast, T. Ye, and X. Ai, "Voltage and Calcium Dual Channel Optical Mapping of Cultured HL-1 Atrial Myocyte Monolayer," *Journal of Visualized Experiments*, p. 52542, Mar. 2015.

[155] P. Beauchamp, T. Desplantez, M. L. McCain, W. Li, A. Asimaki, G. Rigoli, K. K. Parker, J. E. Saffitz, and A. G. Kleber, "Electrical Coupling and Propagation in Engineered Ventricular Myocardium With Heterogeneous Expression of Connexin43," *Circulation Research*, vol. 110, pp. 1445–1453, May 2012.

[156] T. Desplantez, M. L. McCain, P. Beauchamp, G. Rigoli, B. Rothen-Rutishauser, K. K. Parker, and A. G. Kleber, "Connexin43 ablation in foetal atrial myocytes decreases electrical coupling, partner connexins, and sodium current," *Cardiovascular Research*, vol. 94, pp. 58–65, Apr. 2012.

[157] C. Houston, B. Marchand, L. Engelbert, and C. D. Cantwell, "Reducing complexity and unidentifiability when modelling human atrial cells," *Philosophical Transactions of the Royal Society A: Mathematical, Physical and Engineering Sciences*, vol. 378, p. 20190339, June 2020.

[158] M. Fink, S. A. Niederer, E. M. Cherry, F. H. Fenton, J. T. Koivumäki, G. Seemann, R. Thul, H. Zhang, F. B. Sachse, D. Beard, E. J. Crampin, and N. P. Smith, "Cardiac cell modelling: observations from the heart of the cardiac physiome project," *Progress in Biophysics and Molecular Biology*, vol. 104, pp. 2–21, Jan. 2011.

[159] C. L. Lei, S. Ghosh, D. G. Whittaker, Y. Aboelkassem, K. A. Beattie, C. D. Cantwell, T. Delhaas, C. Houston, G. M. Novaes, A. V. Panfilov, P. Pathmanathan, M. Riabiz, R. W. dos Santos, J. Walmsley, K. Worden, G. R. Mirams, and R. D. Wilkinson, "Considering discrepancy when calibrating a mechanistic electrophysiology model," *Philosophical Transactions of the Royal Society A: Mathematical, Physical and Engineering Sciences*, vol. 378, p. 20190349, June 2020.

[160] A. C. Daly, J. Cooper, D. J. Gavaghan, and C. Holmes, "Comparing two sequential Monte Carlo samplers for exact and approximate Bayesian inference on biological models," *Journal of the Royal Society, Interface*, vol. 14, no. 134, 2017.

[161] M. Sunnåker, A. G. Busetto, E. Numminen, J. Corander, M. Foll, and C. Dessimoz, "Approximate Bayesian computation," *PLoS computational biology*, vol. 9, no. 1, p. e1002803, 2013.

[162] D. Csercsik, K. M. Hangos, and G. Szederkényi, "Identifiability analysis and parameter estimation of a single Hodgkin–Huxley type voltage dependent ion channel under voltage step measurement conditions," *Neurocomputing*, vol. 77, pp. 178–188, Feb. 2012.

[163] A. A. Sher, K. Wang, A. Wathen, P. J. Maybank, G. R. Mirams, D. Abramson, D. Noble, and D. J. Gavaghan, "A local sensitivity analysis method for developing biological models with identifiable parameters: Application to cardiac ionic channel modelling," *Future Generation Computer Systems*, vol. 29, pp. 591–598, Feb. 2013.

[164] O. J. Walch and M. C. Eisenberg, "Parameter identifiability and identifiable combinations in generalized Hodgkin–Huxley models," *Neurocomputing*, vol. 199, pp. 137–143, July 2016.

[165] A. Nygren, C. Fiset, L. Firek, J. W. Clark, D. S. Lindblad, R. B. Clark, and W. R. Giles, "Mathematical model of an adult human atrial cell: the role of K+ currents in repolarization," *Circulation Research*, vol. 82, pp. 63–81, Jan. 1998.

[166] M. Courtemanche, R. J. Ramirez, and S. Nattel, "Ionic mechanisms underlying human atrial action potential properties: insights from a mathematical model," *The American Journal of Physiology*, vol. 275, no. 1, pp. H301–321, 1998.

[167] D. M. Lombardo and W.-J. Rappel, "Systematic reduction of a detailed atrial myocyte model," *Chaos: An Interdisciplinary Journal of Nonlinear Science*, vol. 27, p. 093914, Sept. 2017.

[168] K. A. Beattie, A. P. Hill, R. Bardenet, Y. Cui, J. I. Vandenberg, D. J. Gavaghan, T. P. de Boer, and G. R. Mirams, "Sinusoidal voltage protocols for rapid characterisation of ion channel kinetics," *The Journal of Physiology*, vol. 596, no. 10, pp. 1813–1828, 2018.

[169] R. W. Tsien and D. Noble, "A transition state theory approach to the kinetics of conductance changes in excitable membranes," *The Journal of Membrane Biology*, vol. 1, pp. 248–273, Dec. 1969.

[170] Y. Sakakibara, J. A. Wasserstrom, T. Furukawa, H. Jia, C. E. Arentzen, R. S. Hartz, and D. H. Singer, "Characterization of the sodium current in single human atrial myocytes," *Circulation Research*, vol. 71, pp. 535–546, Sept. 1992.

[171] M. Schneider, T. Proebstle, V. Hombach, A. Hannekum, and R. Rüdel, "Characterization of the sodium currents in isolated human cardiocytes," *Pflugers Archiv: European Journal of Physiology*, vol. 428, pp. 84–90, Aug. 1994.

[172] T. Mewes and U. Ravens, "L-type Calcium Currents of Human Myocytes from Ventricle of Non-failing and Failing Hearts and from Atrium," *Journal of Molecular and Cellular Cardiology*, vol. 26, pp. 1307–1320, Oct. 1994.

[173] G. R. Li and S. Nattel, "Properties of human atrial ICa at physiological temperatures and relevance to action potential," *The American Journal of Physiology*, vol. 272, pp. H227–235, Jan. 1997.

[174] H. Sun, N. Leblanc, and S. Nattel, "Mechanisms of inactivation of L-type calcium channels in human atrial myocytes," *The American Journal of Physiology*, vol. 272, pp. H1625–1635, Apr. 1997.

[175] E. F. Shibata, T. Drury, H. Refsum, V. Aldrete, and W. Giles, "Contributions of a transient outward current to repolarization in human atrium," *American Journal of Physiology-Heart and Circulatory Physiology*, vol. 257, pp. H1773–H1781, Dec. 1989.

[176] Z. Wang, B. Fermini, and S. Nattel, "Sustained depolarization-induced outward current in human atrial myocytes. Evidence for a novel delayed rectifier K+ current similar to Kv1.5 cloned channel currents," *Circulation Research*, vol. 73, pp. 1061–1076, Dec. 1993.

[177] L. Firek and W. R. Giles, "Outward currents underlying repolarization in human atrial myocytes," *Cardiovascular Research*, vol. 30, pp. 31–38, July 1995.

[178] G. Bertorelle, A. Benazzo, and S. Mona, "ABC as a flexible framework to estimate demography over space and time: some cons, many pros: THE ABC REVOLUTION IN NINE STEPS," *Molecular Ecology*, vol. 19, pp. 2609–2625, June 2010.

[179] K. Csilléry, M. G. Blum, O. E. Gaggiotti, and O. François, "Approximate Bayesian Computation (ABC) in practice," *Trends in Ecology & Evolution*, vol. 25, pp. 410–418, July 2010.

[180] M. A. Beaumont, "Approximate Bayesian Computation in Evolution and Ecology," *Annual Review of Ecology, Evolution, and Systematics*, vol. 41, pp. 379–406, Dec. 2010.

[181] J.-M. Marin, P. Pudlo, C. P. Robert, and R. J. Ryder, "Approximate Bayesian computational methods," *Statistics and Computing*, vol. 22, pp. 1167–1180, Nov. 2012.

[182] D. J. Wilkinson, "Bayesian methods in bioinformatics and computational systems biology," *Briefings in Bioinformatics*, vol. 8, pp. 109–116, Mar. 2007.

[183] K. Cranmer, J. Brehmer, and G. Louppe, "The frontier of simulation-based inference," *Proceedings of the National Academy of Sciences*, p. 201912789, May 2020.

[184] M. A. Beaumont, W. Zhang, and D. J. Balding, "Approximate Bayesian computation in population genetics," *Genetics*, vol. 162, pp. 2025–2035, Dec. 2002.

[185] T. Toni, D. Welch, N. Strelkowa, A. Ipsen, and M. P. H. Stumpf, "Approximate Bayesian computation scheme for parameter inference and model selection in dynamical systems," *Journal of the Royal Society, Interface*, vol. 6, pp. 187–202, Feb. 2009.

[186] C. C. Drovandi and A. N. Pettitt, "Estimation of parameters for macroparasite population evolution using approximate bayesian computation," *Biometrics*, vol. 67, pp. 225–233, Mar. 2011.

[187] M. A. Beaumont, J.-M. Cornuet, J.-M. Marin, and C. P. Robert, "Adaptive approximate Bayesian computation," *Biometrika*, vol. 96, pp. 983–990, Dec. 2009.

[188] E. Klinger, D. Rickert, and J. Hasenauer, "pyABC: distributed, likelihood-free inference," *Bioinformatics*, vol. 34, pp. 3591–3593, Oct. 2018.

[189] B. W. Silverman, *Density Estimation for Statistics and Data Analysis*. Boston, MA: Springer US, 1986.

[190] R. D. Wilkinson, "Approximate Bayesian computation (ABC) gives exact results under the assumption of model error," *Statistical Applications in Genetics and Molecular Biology*, vol. 12, Jan. 2013.

[191] M. Clerx, K. A. Beattie, D. J. Gavaghan, and G. R. Mirams, "Four Ways to Fit an Ion Channel Model," *Biophysical Journal*, p. S0006349519306666, Aug. 2019.

[192] M. Clerx, P. Collins, E. de Lange, and P. G. A. Volders, "Myokit: A simple interface to cardiac cellular electrophysiology," *Progress in Biophysics and Molecular Biology*, vol. 120, pp. 100–114, Jan. 2016.

[193] R. McElreath, *Statistical rethinking: A Bayesian course with examples in R and Stan*. Chapman and Hall/CRC, 2018.

[194] J. Carro, J. F. Rodríguez-Matas, V. Monasterio, and E. Pueyo, "Limitations in electrophysiological model development and validation caused by differences between simulations and experimental protocols," *Progress in Biophysics and Molecular Biology*, vol. 129, pp. 53–64, 2017.

[195] D. M. Lombardo, F. H. Fenton, S. M. Narayan, and W.-J. Rappel, "Comparison of Detailed and Simplified Models of Human Atrial Myocytes to Recapitulate Patient Specific Properties," *PLOS Computational Biology*, vol. 12, p. e1005060, Aug. 2016.

[196] R. Kula, M. Bébarová, P. Matejovič, J. Šimurda, and M. Pásek, "Distribution of data in cellular electrophysiology: Is it always normal?," *Progress in Biophysics and Molecular Biology*, p. S0079610720300419, July 2020.

[197] Q. Zhang, C. Deng, F. Rao, R. M. Modi, J. Zhu, X. Liu, L. Mai, H. Tan, X. Yu, Q. Lin, D. Xiao, S. Kuang, and S. Wu, "Silencing of desmoplakin decreases connexin43/Nav1.5 expression and sodium current in HL-1 cardiomyocytes," *Molecular Medicine Reports*, vol. 8, pp. 780–786, Sept. 2013.

[198] C. Deng, F. Rao, S. Wu, S. Kuang, X. Liu, Z. Zhou, Z. Shan, Q. Lin, W. Qian, M. Yang, Q. Geng, Y. Zhang, X. Yu, and S. Lin, "Pharmacological effects of carvedilol on T-type calcium current in murine HL-1 cells," *European Journal of Pharmacology*, vol. 621, pp. 19–25, Oct. 2009.

[199] F. Toyoda, W.-G. Ding, D. P. Zankov, M. Omatsu-Kanbe, T. Isono, M. Horie, and H. Matsuura, "Characterization of the Rapidly Activating Delayed Rectifier Potassium Current, I Kr, in HL-1 Mouse Atrial Myocytes," *Journal of Membrane Biology*, vol. 235, pp. 73–87, June 2010.

[200] Z. Yang, W. Shen, J. Rottman, J. Wikswo, and K. Murray, "Rapid stimulation causes electrical remodeling in cultured atrial myocytes," *Journal of Molecular and Cellular Cardiology*, vol. 38, pp. 299–308, Feb. 2005.

[201] D. Goldoni, Y. Zhao, B. D. Green, B. J. McDermott, and A. Collins, "Inward rectifier potassium channels in the HL-1 cardiomyocyte-derived cell line," *Journal of Cellular Physiology*, vol. 225, pp. 751–756, Dec. 2010.

[202] A. Takeuchi, B. Kim, and S. Matsuoka, "The mitochondrial Na+-Ca2+ exchanger, NCLX, regulates automaticity of HL-1 cardiomyocytes," *Scientific Reports*, vol. 3, p. 2766, Dec. 2013.

[203] Y. Hu, Y. Duan, A. Takeuchi, L. Hai-Kurahara, J. Ichikawa, K. Hiraishi, T. Numata, H. Ohara, G. Iribe, M. Nakaya, M. X. Mori, S. Matsuoka, G. Ma, and R. Inoue, "Uncovering the arrhythmogenic potential of TRPM4 activation in atrial-derived HL-1 cells using novel recording and numerical approaches," *Cardiovascular Research*, vol. 113, pp. 1243–1255, Aug. 2017.

[204] E. Grandi, S. V. Pandit, N. Voigt, A. J. Workman, D. Dobrev, J. Jalife, and D. M. Bers, "Human atrial action potential and Ca2+ model: sinus rhythm and chronic atrial fibrillation," *Circulation Research*, vol. 109, pp. 1055–1066, Oct. 2011.

[205] H. Xu, W. Guo, and J. M. Nerbonne, "Four Kinetically Distinct Depolarization-activated K $^+$ Currents in Adult Mouse Ventricular Myocytes," *The Journal of General Physiology*, vol. 113, pp. 661–678, May 1999.

[206] A. M. Correa, R. Latorre, and F. Bezanilla, "Ion permeation in normal and batrachotoxin-modified Na+ channels in the squid giant axon.," *The Journal of General Physiology*, vol. 97, pp. 605–625, Mar. 1991.

[207] K. H. W. J. ten Tusscher, D. Noble, P. J. Noble, and A. V. Panfilov, "A model for human ventricular tissue," *American Journal of Physiology. Heart and Circulatory Physiology*, vol. 286, pp. H1573–1589, Apr. 2004.

[208] T. Kiyosue, M. Arita, H. Muramatsu, A. J. Spindler, and D. Noble, "Ionic mechanisms of action potential prolongation at low temperature in guinea-pig ventricular myocytes.," *The Journal of Physiology*, vol. 468, pp. 85–106, Aug. 1993.

[209] P. Dias, *Influence of Connexin Expression/Co-Expression Levels on Electrical Impulse Propagation Investigated in the HL-1 Cell Model*. PhD thesis, Apr. 2011. Publisher: Imperial College London.

[210] E. A. Sobie, "Parameter Sensitivity Analysis in Electrophysiological Models Using Multivariable Regression," *Biophysical Journal*, vol. 96, pp. 1264–1274, Feb. 2009.

[211] G. W. Beeler and H. Reuter, "Reconstruction of the action potential of ventricular myocardial fibres," *The Journal of Physiology*, vol. 268, pp. 177–210, June 1977.

[212] T. R. Shannon, F. Wang, J. Puglisi, C. Weber, and D. M. Bers, "A Mathematical Treatment of Integrated Ca Dynamics within the Ventricular Myocyte," *Biophysical Journal*, vol. 87, pp. 3351–3371, Nov. 2004.

[213] T. O'Hara, L. Virág, A. Varró, and Y. Rudy, "Simulation of the Undiseased Human Cardiac Ventricular Action Potential: Model Formulation and Experimental Validation," *PLoS Computational Biology*, vol. 7, p. e1002061, May 2011.

[214] R. Majumder, W. Jangsangthong, I. Feola, D. L. Ypey, D. A. Pijnappels, and A. V. Panfilov, "A Mathematical Model of Neonatal Rat Atrial Monolayers with Constitutively Active Acetylcholine-Mediated K+ Current," *PLOS Computational Biology*, vol. 12, p. e1004946, June 2016.

[215] M. Xia, "Functional expression of L- and T-type Ca2+ channels in murine HL-1 cells," *Journal of Molecular and Cellular Cardiology*, vol. 36, pp. 111–119, Jan. 2004.

[216] S. Kupershmidt, I. C.-H. Yang, K. Hayashi, J. Wei, S. Chanthaphaychith, C. I. Petersen, D. C. Johns, A. L. George, D. M. Roden, and J. R. Balser, "I_{kr} drug response is modulated by *KCR1* in transfected cardiac and noncardiac cell lines," *The FASEB Journal*, vol. 17, pp. 2263–2265, Dec. 2003.

[217] Y.-Y. Lu, Y.-C. Chen, Y.-H. Kao, T.-J. Wu, S.-A. Chen, and Y.-J. Chen, "Extracellular Matrix of Collagen Modulates Intracellular Calcium Handling and Electrophysiological Characteristics of HL-1 Cardiomyocytes With Activation of Angiotensin II Type 1 Receptor," *Journal of Cardiac Failure*, vol. 17, pp. 82–90, Jan. 2011.

[218] Y.-Y. Lu, Y.-C. Chen, Y.-H. Kao, Y.-K. Lin, Y.-H. Yeh, S.-A. Chen, and Y.-J. Chen, "Colchicine modulates calcium homeostasis and electrical property of HL-1 cells," *Journal of Cellular and Molecular Medicine*, vol. 20, pp. 1182–1190, June 2016.

[219] Y.-H. Kao, J.-C. Hsu, Y.-C. Chen, Y.-K. Lin, B. Lkhagva, S.-A. Chen, and Y.-J. Chen, "ZFHX3 knockdown increases arrhythmogenesis and dysregulates calcium homeostasis in HL-1 atrial myocytes," *International Journal of Cardiology*, vol. 210, pp. 85–92, May 2016.

[220] H. Xu, H. Li, and J. M. Nerbonne, "Elimination of the transient outward current and action potential prolongation in mouse atrial myocytes expressing a dominant negative Kv4 α subunit," *The Journal of Physiology*, vol. 519, pp. 11–21, Aug. 1999.

[221] J. M. Nerbonne, "Molecular basis of functional voltage-gated K^+ channel diversity in the mammalian myocardium," *The Journal of Physiology*, vol. 525, pp. 285–298, June 2000.

[222] J. M. Nerbonne and R. S. Kass, "Molecular Physiology of Cardiac Repolarization," *Physiological Reviews*, vol. 85, pp. 1205–1253, Oct. 2005.

[223] D. Wang, L. Nie, A. George, and P. Bennett, "Distinct local anesthetic affinities in Na+ channel subtypes," *Biophysical Journal*, vol. 70, pp. 1700–1708, Apr. 1996.

[224] K. H. Ten Tusscher and A. V. Panfilov, "Influence of diffuse fibrosis on wave propagation in human ventricular tissue," *EP Europace*, vol. 9, pp. vi38–vi45, Nov. 2007.

[225] S. F. Roberts, *Non-uniform interstitial loading in cardiac microstructure during impulse propagation*. PhD Thesis, Duke University, 2009.

[226] O. C. Zienkiewicz, R. L. Taylor, and D. Fox, *The finite element method for solid and structural mechanics*. Amsterdam ; Boston: Elsevier/Butterworth-Heinemann, 7th ed ed., 2014. OCLC: ocn858011693.

[227] G. Karniadakis and S. J. Sherwin, *Spectral/hp element methods for computational fluid dynamics*. Numerical mathematics and scientific computation, Oxford: Oxford University Press, second edition ed., 2013.

[228] C. D. Cantwell, D. Moxey, A. Comerford, A. Bolis, G. Rocco, G. Mengaldo, D. De Grazia, S. Yakovlev, J.-E. Lombard, D. Ekelschot, and others, "Nektar++: An open-source spectral/hp element framework," *Computer physics communications*, vol. 192, pp. 205–219, 2015. Publisher: Elsevier.

[229] D. Moxey, C. D. Cantwell, Y. Bao, A. Cassinelli, G. Castiglioni, S. Chun, E. Juda, E. Kazemi, K. Lackhove, J. Marcon, and others, "Nektar++: Enhancing the capability and application of high-fidelity spectral/hp element methods," *Computer Physics Communications*, vol. 249, p. 107110, 2020. Publisher: Elsevier.

[230] S. Rush and H. Larsen, "A Practical Algorithm for Solving Dynamic Membrane Equations," *IEEE Transactions on Biomedical Engineering*, vol. BME-25, pp. 389–392, July 1978.

[231] R. Veeraraghavan, J. Lin, G. S. Hoeker, J. P. Keener, R. G. Gourdie, and S. Poelzing, "Sodium channels in the Cx43 gap junction perinexus may constitute a cardiac ephapse: an experimental and modeling study," *Pflügers Archiv - European Journal of Physiology*, vol. 467, pp. 2093–2105, Oct. 2015.

[232] N. Kudryashova, V. Tsvelaya, K. Agladze, and A. Panfilov, "Virtual cardiac monolayers for electrical wave propagation," *Scientific Reports*, vol. 7, no. 1, p. 7887, 2017.

[233] N. Kudryashova, A. Nizamieva, V. Tsvelaya, A. V. Panfilov, and K. I. Agladze, "Self-organization of conducting pathways explains electrical wave propagation in cardiac tissues with high fraction of non-conducting cells," *PLoS computational biology*, vol. 15, no. 3, p. e1006597, 2019.

[234] C. Stringer, M. Michaelos, and M. Pachitariu, "Cellpose: a generalist algorithm for cellular segmentation," preprint, Bioinformatics, Feb. 2020.

[235] S. Weidmann, "Electrical constants of trabecular muscle from mammalian heart," *The Journal of Physiology*, vol. 210, pp. 1041–1054, Nov. 1970.

[236] J. Wall, N. Trayanova, K. Skouibine, and W. Krassowska, "Modeling induction of reentry with a realistic S2 stimulus," in *Proceedings of the First Joint BMES/EMBS Conference. 1999 IEEE Engineering in Medicine and Biology 21st Annual Conference and the 1999 Annual Fall Meeting of the Biomedical Engineering Society (Cat. No.99CH37015)*, vol. 1, (Atlanta, GA, USA), p. 154, IEEE, 1999.

[237] T. F. McDonald, S. Pelzer, W. Trautwein, and D. J. Pelzer, "Regulation and modulation of calcium channels in cardiac, skeletal, and smooth muscle cells," *Physiological Reviews*, vol. 74, pp. 365–507, Apr. 1994.

[238] T. M. Curtis and C. N. Scholfield, "Nifedipine blocks Ca $^{2+}$ store refilling through a pathway not involving L-type Ca $^{2+}$ channels in rabbit arteriolar smooth muscle," *The Journal of Physiology*, vol. 532, pp. 609–623, May 2001.

[239] J. E. Duverger, J. Boudreau-Béland, M. D. Le, and P. Comtois, "Multicellular automaticity of cardiac cell monolayers: effects of density and spatial distribution of pacemaker cells," *New Journal of Physics*, vol. 16, p. 113046, Nov. 2014.

[240] T. A. Gokhale, H. Asfour, S. Verma, N. Bursac, and C. S. Henriquez, "Microheterogeneity-induced conduction slowing and wavefront collisions govern macroscopic conduction behavior: A computational and experimental study," *PLOS Computational Biology*, vol. 14, p. e1006276, July 2018.

[241] D. Bruce, P. Pathmanathan, and J. P. Whiteley, "Modelling the effect of gap junctions on tissue-level cardiac electrophysiology," *Electronic Proceedings in Theoretical Computer Science*, vol. 92, pp. 1–15, Aug. 2012.

[242] C. Mendonca Costa, P. Arroyo Silva, and R. Weber dos Santos, "Mind the gap: A semi-continuum model for discrete electrical propagation in cardiac tissue," *IEEE Transactions on Biomedical Engineering*, pp. 1–1, 2015.

[243] D. E. Hurtado, J. Jilberto, and G. Panasenko, "Non-ohmic tissue conduction in cardiac electrophysiology: Upscaling the non-linear voltage-dependent conductance of gap junctions," *PLOS Computational Biology*, vol. 16, p. e1007232, Feb. 2020.

Appendix A

Appendices

A.1 Human atrial model equations and numerical results from calibration

This section is adapted from the Supplementary Material to [157] (CC BY).

A.1.1 Fast Na^+ channel, I_{Na}

$$I_{\mathrm{Na}} = P_{\mathrm{Na}} m^3 \left(\mathbf{s_1} h_1 + (1-\mathbf{s_1}) h_2\right) \left[\mathrm{Na}^+\right]_{\mathrm{c}} \mathrm{V} \frac{\mathrm{F}^2}{\mathrm{RT}} \frac{e^{(\mathrm{V}-\mathrm{E_{Na}})\mathrm{F/RT}} - 1.0}{e^{\mathrm{VF/RT}} - 1.0}$$

$$\frac{\mathrm{d}m}{\mathrm{dt}} = \frac{\overline{m} - m}{\tau_m}, \qquad \frac{\mathrm{d}h_1}{\mathrm{dt}} = \frac{\overline{h} - h_1}{\tau_{h_1}}, \qquad \frac{\mathrm{d}h_2}{\mathrm{dt}} = \frac{\overline{h} - h_2}{\tau_{h_2}}$$

$$\overline{m} = \frac{1.0}{1.0 + e^{-(\mathrm{V}+\mathbf{r_1})/\mathbf{r_2}}}, \qquad \tau_m = 1000(\mathbf{r_3} e^{-((\mathrm{V}+\mathbf{r_4})/\mathbf{r_5})^2} + \mathbf{r_6})$$

$$\overline{h} = \frac{1.0}{1.0 + e^{(\mathrm{V}+\mathbf{q_1})/\mathbf{q_2}}}$$

$$\tau_{h_1} = 1000 \left(\frac{\mathbf{q_3}}{1.0 + e^{(\mathrm{V}+\mathbf{q_4})/\mathbf{q_5}}} + \mathbf{q_6} \right), \qquad \tau_{h_2} = 1000 \left(\frac{\mathbf{q_7}}{1.0 + e^{(\mathrm{V}+\mathbf{q_4})/\mathbf{q_5}}} + \mathbf{q_8} \right)$$

Table A.1: Gating kinetics in Nygren model of I_{Na} channel current (see Table 6 in [165]). Time constants are multiplied by 1000 to convert from s to ms.

		Original				Unified		
Name	Published	Prior	Median	89% HPDI	$\log_{10}$RSD	Median	89% HPDI	$\log_{10}$RSD
r1	27.12	$\mathcal{U}$(0, 100)	52.25	(50.93, 53.52)	-1.795	42.83	(33.91, 55.13)	-0.7966
r2	8.21	$\mathcal{U}$(0, 20)	10.69	(9.769, 11.64)	-1.256	13.19	(7.761, 19.94)	-0.5127
r3*	4.2e-05	$\mathcal{U}$(-6, -3)	2.097e-05	(1.009e-06, 0.000325)	-0.749	1.371e-05	(1.002e-06, 0.0002247)	-0.7856
r4	25.57	$\mathcal{U}$(0, 100)	57.99	(22.82, 99.97)	-0.3404	56.79	(16.97, 99.79)	-0.293
r5	28.8	$\mathcal{U}$(0, 20)	9.979	(0.2856, 17.75)	-0.2282	8.932	(0.03437, 17.49)	-0.1981
r6*	2.4e-05	$\mathcal{U}$(-6, -3)	2.191e-05	(1.001e-06, 0.0005717)	-0.7021	9.662e-05	(5.195e-05, 0.0001536)	-1.43
q1	63.6	$\mathcal{U}$(0, 200)	95.57	(95.11, 96.11)	-2.465	93.94	(88.3, 99.55)	-1.4
q2	5.3	$\mathcal{U}$(0, 20)	6.5	(6.085, 6.841)	-1.432	8.182	(1.222, 13.13)	-0.3487
q3*	0.03	$\mathcal{U}$(-3, 0)	0.09214	(0.001002, 0.4502)	-0.1696	0.004096	(0.002543, 0.02547)	-0.7312
q4	35.1	$\mathcal{U}$(0, 100)	34.98	(0.1474, 147.7)	-0.02249	53.57	(48.79, 57.53)	-1.263
q5	3.2	$\mathcal{U}$(0, 20)	12.76	(4.548, 19.99)	-0.361	10.61	(7.184, 13.18)	-0.7463
q6*	0.0003	$\mathcal{U}$(-5, -2)	0.0002548	(1.002e-05, 0.004472)	-0.6137	0.0002403	(1.006e-05, 0.001556)	-0.7811
q7*	0.12	$\mathcal{U}$(-3, 0)	0.07443	(0.001005, 0.3999)	-0.1983	0.02022	(0.002551, 0.02706)	-0.6835
q8*	0.003	$\mathcal{U}$(-4, -1)	0.002224	(0.0001001, 0.04665)	-0.4589	0.0005268	(0.0001001, 0.00171)	-0.9219
s1	0.9	$\mathcal{U}$(0, 1)	0.5015	(0.08985, 0.9754)	-0.2317	0.4717	(0.1367, 0.8259)	-0.334

Table A.2: Summary of results for parameters of Nygren I_{Na} model using original and unified dataset. *Parameters were searched in $\log_{10}$ space based on the scale of their published values and are presented in linear space. The prior for these parameters is still in the original $\log_{10}$ space.

$$
\begin{aligned}
I_{\mathrm{Na}} &= g_{\mathrm{Na}} m^3 h j (\mathrm{V} - \mathrm{E}_{\mathrm{Na}}) \\
\frac{\mathrm{d}\phi}{\mathrm{dt}} &= \frac{\phi_\infty - \phi}{\tau_\phi}, \qquad \text{for } \phi = m, h, j \\
\tau_\phi &= (\alpha_\phi + \beta_\phi)^{-1}, \qquad \phi_\infty = \alpha_\phi \tau_\phi, \qquad \text{for } \phi = m, h, j \\
\alpha_m &= \begin{cases} \mathbf{a_{m,2}} \frac{\mathrm{V} - \mathbf{a_{m,1}}}{1 - e^{-\mathbf{a_{m,3}}(\mathrm{V} - \mathbf{a_{m,1}})}} \\ \mathbf{a_{m,4}}, \text{ if } \mathrm{V} = \mathbf{a_{m,1}} \end{cases}, \qquad \beta_m = \mathbf{b_{m,1}} e^{-\mathrm{V}/\mathbf{b_{m,2}}} \\
\alpha_h &= \begin{cases} \mathbf{a_{h,1}} e^{(\mathrm{V} + \mathbf{a_{h,3}})/-\mathbf{a_{h,2}}} \\ a_{h,5}, \qquad \text{if } \mathrm{V} \geq \mathbf{c_{h,1}} \end{cases}, \qquad a_{h,5} = \mathbf{a_{h,1}} e^{(\mathbf{c_{h,1}} + \mathbf{a_{h,3}})/-\mathbf{a_{h,2}}} \\
\beta_h &= \begin{cases} \mathbf{b_{h,4}} e^{\mathbf{b_{h,5}}\mathrm{V}} + \mathbf{b_{h,6}} e^{\mathbf{b_{h,7}}\mathrm{V}} \\ \left(b_{h,1}\left[1.0 + e^{(V + \mathbf{b_{h,2}})/-\mathbf{b_{h,3}}}\right]\right)^{-1}, \quad \text{if } V \geq \mathbf{c_{h,1}} \end{cases} \\
b_{h,1} &= \left(\mathbf{b_{h,4}} e^{\mathbf{b_{h,5}}\mathbf{c_{h,1}}} + \mathbf{b_{h,6}} e^{\mathbf{b_{h,7}}\mathbf{c_{h,1}}}\right)^{-1} \left(1.0 + e^{(\mathbf{c_{h,1}} + \mathbf{b_{h,2}})/-\mathbf{b_{h,3}}}\right)^{-1} \\
\alpha_j &= \begin{cases} \left[-\mathbf{a_{j,1}} e^{\mathbf{a_{j,2}}\mathrm{V}} - \mathbf{a_{j,3}} e^{-\mathbf{a_{j,4}}\mathrm{V}}\right] \frac{\mathrm{V} + a_{j,5}}{1.0 + e^{\mathbf{a_{j,6}}(\mathrm{V} + \mathbf{a_{j,7}})}} \\ 0, \quad \text{if } V \geq \mathbf{c_{j,1}} \end{cases}, \qquad a_{j,5} = -\mathbf{c_{j,1}} \\
\beta_j &= \begin{cases} \mathbf{b_{j,5}} \frac{e^{-\mathbf{b_{j,6}}\mathrm{V}}}{1 + e^{-\mathbf{b_{j,7}}(\mathrm{V} + \mathbf{b_{j,8}})}} \\ b_{j,1} \frac{e^{-b_{j,2}\mathrm{V}}}{1 + e^{-\mathbf{b_{j,3}}(\mathrm{V} + \mathbf{b_{j,4}})}}, \quad \text{if } V \geq \mathbf{c_{j,1}} \end{cases}, \\
b_{j,1} &= \mathbf{b_{j,5}} \frac{e^{-\mathbf{b_{j,6}}\mathbf{c_{j,1}}}}{1 + e^{-\mathbf{b_{j,7}}(\mathbf{c_{j,1}} + \mathbf{b_{j,8}})}} \left[\frac{e^{-b2_j \mathbf{c_{j,1}}}}{(1 + e^{-\mathbf{b_{j,3}}(\mathbf{c_{j,1}} + \mathbf{b_{j,4}})}}\right]^{-1}, \qquad b_{j,2} = 0.0
\end{aligned}
$$

Table A.3: Gating kinetics in Courtemanche model of I_{Na} channel current (see Appendix in [166]). Values of $a_{h,5}$, $b_{h,1}$, $a_{j,5}$ and $b_{j,1}$ are set to enforce continuity in piecewise functions. $b_{j,2}$ is set to zero to reduce dimensionality of the calibration problem as the published parameter was effectively zero (2.535×10^{-7}).

Original/Unified					
Name	Published	Prior	Median	89% HPDI	$\log_{10}$RSD
$a1_m$	-47.13	$\mathcal{U}(-100, 0)$	-75.97	(-79.77, -73.65)	-1.586
$a2_m$	0.32	$\mathcal{U}(0, 1)$	0.2639	(0.2476, 0.2741)	-1.476
$a3_m$	0.1	$\mathcal{U}(0, 1)$	0.3355	(0.1947, 0.7643)	-0.2765
$a4_m$	3.2	$\mathcal{U}(0, 10)$	4.895	(1.699, 9.998)	-0.2421
$b1_m$	0.08	$\mathcal{U}(0, 10)$	1.263	(1.225, 1.322)	-1.64
$b2_m$	11.0	$\mathcal{U}(0, 100)$	23.21	(22.48, 23.74)	-1.774
$a1_h^*$	0.135	$\mathcal{U}(-2, 1)$	0.3845	(0.01157, 3.35)	0.269
$a2_h$	6.8	$\mathcal{U}(0, 50)$	15.48	(14.49, 15.99)	-1.465
$a3_h$	80.0	$\mathcal{U}(0, 200)$	122.2	(67.51, 155.4)	-0.6085
$b2_h$	10.66	$\mathcal{U}(0, 100)$	18.35	(5.525, 31.86)	-0.3218
$b3_h$	11.1	$\mathcal{U}(0, 50)$	16.73	(12.42, 21.47)	-0.7582
$b4_h^*$	3.56	$\mathcal{U}(-1, 2)$	15.11	(14.51, 15.79)	-1.999
$b5_h^*$	0.079	$\mathcal{U}(-3, 0)$	0.05808	(0.05716, 0.05887)	-2.492
$b6_h^*$	310000.0	$\mathcal{U}(3, 6)$	21500.0	(1002.0, 321300.0)	-0.6777
$b7_h^*$	0.35	$\mathcal{U}(-2, 1)$	1.327	(0.2776, 6.324)	0.4741
$c1_h$	-40.0	$\mathcal{U}(-100, 0)$	-37.27	(-45.94, -32.91)	-0.8902
$a1_j^*$	127100.0	$\mathcal{U}(3, 7)$	123700.0	(1180.0, 4778000.0)	-0.6361
$a2_j^*$	0.2444	$\mathcal{U}(-2, 2)$	5.144	(0.1528, 50.75)	0.02476
$a3_j^*$	3.474e-05	$\mathcal{U}(-5, -1)$	0.0003798	(1.015e-05, 0.001191)	-0.7783
$a4_j^*$	0.04391	$\mathcal{U}(-4, 0)$	0.003784	(0.0001, 0.02896)	-0.5131
$a6_j$	0.311	$\mathcal{U}(0, 1)$	0.4461	(0.01244, 0.8846)	-0.2087
$a7_j$	79.23	$\mathcal{U}(0, 100)$	41.53	(4.671, 91.36)	-0.1966
$b3_j$	0.1	$\mathcal{U}(0, 1)$	0.4481	(0.001746, 0.8611)	-0.1977
$b4_j$	32.0	$\mathcal{U}(0, 100)$	67.64	(21.51, 99.97)	-0.3641
$b5_j$	0.1212	$\mathcal{U}(0, 1)$	0.3552	(0.04405, 0.7968)	-0.1691
$b6_j^*$	0.01052	$\mathcal{U}(-4, 0)$	0.001531	(0.0001004, 0.01829)	-0.5618
$b7_j$	0.1378	$\mathcal{U}(0, 1)$	0.2679	(0.0008117, 0.7773)	-0.09422
$b8_j$	40.14	$\mathcal{U}(0, 100)$	72.38	(31.39, 99.94)	-0.4359
$c1_j$	-40.0	$\mathcal{U}(-100, 0)$	-33.07	(-74.3, -0.5147)	-0.179

Table A.4: Summary of results for parameters of Courtemanche I_{Na} model using original/unified (equivalent) dataset. *Parameters were searched in $\log_{10}$ space based on the scale of their published values and are presented in linear space. The prior for these parameters is still in the original $\log_{10}$ space.

Unified				
Name	Prior	Median	89% HPDI	$\log_{10}$RSD
p_1^*	$\mathcal{U}$(1, 5)	5134.0	(1620.0, 9786.0)	-1.241
p_2	$\mathcal{U}$(1e-7, 0.2)	0.126	(0.1048, 0.1524)	-0.9488
p_3^*	$\mathcal{U}$(-3, 1)	3.374	(0.5586, 6.144)	-0.2008
p_4	$\mathcal{U}$(1e-7, 0.4)	0.0234	(0.002225, 0.04426)	-0.2237
p_5^*	$\mathcal{U}$(-1, 3)	6.091	(5.572, 6.662)	-1.495
p_6	$\mathcal{U}$(1e-7, 0.2)	0.0441	(0.04209, 0.04601)	-1.523
p_7^*	$\mathcal{U}$(-4, 0)	0.005353	(0.004147, 0.006667)	-1.496
p_8	$\mathcal{U}$(1e-7, 0.2)	0.04053	(0.03871, 0.04302)	-1.44
A^*	$\mathcal{U}$(0, 1)	4.195	(4.049, 4.314)	-1.869

Table A.5: Summary of results for parameters of standardised I_{Na} model using unified dataset. *Parameters were searched in $\log_{10}$ space and are presented in linear space. The prior for these parameters is still in the original $\log_{10}$ space.

A.1.2 L-type Ca^{2+} channel, I_{CaL}

$$
\begin{aligned}
I_{\mathrm{CaL}} &= \bar{g}_{\mathrm{Ca,L}} d_{\mathrm{L}} \left[f_{\mathrm{Ca}} f_{\mathrm{L_1}} + (1 - f_{\mathrm{Ca}}) f_{\mathrm{L_2}} \right] (\mathrm{V} - \mathrm{E_{Ca,app}}) \\
\frac{\mathrm{d}d_{\mathrm{L}}}{\mathrm{dt}} &= \frac{\overline{d_{\mathrm{L}}} - d_{\mathrm{L}}}{\tau_{d_{\mathrm{L}}}}, \qquad \frac{\mathrm{d}f_{\mathrm{L_1}}}{\mathrm{dt}} = \frac{\overline{f_{\mathrm{L}}} - f_{\mathrm{L_1}}}{\tau_{f_{\mathrm{L_1}}}}, \qquad \frac{\mathrm{d}f_{\mathrm{L_2}}}{\mathrm{dt}} = \frac{\overline{f_{\mathrm{L}}} - f_{\mathrm{L_2}}}{\tau_{f_{\mathrm{L_2}}}} \\
\overline{d_{\mathrm{L}}} &= \frac{1.0}{1.0 + e^{(\mathrm{V}+\mathbf{p_1})/-\mathbf{p_2}}}, \qquad \tau_{d_{\mathrm{L}}} = 1000 \left(\mathbf{p_3} e^{-((\mathrm{V}+\mathbf{p_4})/\mathbf{p_5})^2} + \mathbf{p_6} \right) \\
\overline{f_{\mathrm{L}}} &= \frac{1.0}{1.0 + e^{(\mathrm{V}+\mathbf{q_1})/\mathbf{q_2}}} \\
\tau_{f_{\mathrm{L_1}}} &= 1000 \left(\mathbf{q_3} e^{-((\mathrm{V}+\mathbf{q_4})/\mathbf{q_5})^2} + \mathbf{q_6} \right), \qquad \tau_{f_{\mathrm{L_2}}} = 1000 \left(\mathbf{r_1} e^{-((\mathrm{V}+\mathbf{r_2})/\mathbf{r_3})^2} + \mathbf{r_4} \right)
\end{aligned}
$$

Table A.6: Gating kinetics in Nygren model of I_{CaL} channel current (see Table 7 in [165]). Time constants are multiplied by 1000 to convert from s to ms.

		Original				Unified		
Name	Published	Prior	Median	89% HPDI	$\log_{10}$RSD	Median	89% HPDI	$\log_{10}$RSD
p1	9.0	$\mathcal{U}$(-100, 100)	2.684	(2.529, 2.906)	-1.29	9.317	(5.103, 10.51)	-0.5683
p2	5.8	$\mathcal{U}$(0, 50)	5.055	(5.022, 5.083)	-2.416	7.378	(6.679, 8.916)	-0.9407
p3*	0.0027	$\mathcal{U}$(-7, 3)	0.1048	(0.096, 0.1063)	-1.869	0.001129	(1e-07, 0.02533)	-0.2353
p4	35.0	$\mathcal{U}$(-100, 100)	-11.51	(-11.6, -11.36)	-2.151	-39.18	(-99.98, 74.02)	0.4508
p5	30.0	$\mathcal{U}$(0, 50)	18.58	(18.39, 18.86)	-2.078	28.21	(6.568, 49.05)	-0.2817
p6*	0.002	$\mathcal{U}$(-7, 3)	0.00996	(0.009237, 0.0108)	-1.919	0.0009303	(1.027e-07, 0.0009643)	-0.5757
q1	27.4	$\mathcal{U}$(0, 100)	32.02	(21.21, 47.51)	-0.5415	32.02	(21.21, 47.51)	-0.5415
q2	7.1	$\mathcal{U}$(0, 50)	8.06	(1.553, 18.14)	-0.2068	8.06	(1.553, 18.14)	-0.2068
q3*	0.161	$\mathcal{U}$(-7, 3)	0.04208	(1.103e-07, 0.7733)	-0.002009	0.04208	(1.103e-07, 0.7733)	-0.002009
q4	40.0	$\mathcal{U}$(0, 100)	59.81	(29.52, 99.4)	-0.3934	59.81	(29.52, 99.4)	-0.3934
q5	14.4	$\mathcal{U}$(0, 50)	25.73	(2.594, 43.97)	-0.2737	25.73	(2.594, 43.97)	-0.2737
q6*	0.01	$\mathcal{U}$(-7, 3)	0.007372	(0.002444, 0.05932)	-0.5916	0.007372	(0.002444, 0.05932)	-0.5916
r1*	1.332	$\mathcal{U}$(-7, 3)	0.05255	(1.14e-07, 2.713)	0.05333	0.05255	(1.14e-07, 2.713)	0.05333
r2	40.0	$\mathcal{U}$(0, 100)	45.95	(13.92, 96.56)	-0.2224	45.95	(13.92, 96.56)	-0.2224
r3	14.2	$\mathcal{U}$(0, 100)	46.89	(0.5929, 88.34)	-0.1519	46.89	(0.5929, 88.34)	-0.1519
r4*	0.0626	$\mathcal{U}$(-7, 3)	0.01455	(1.051e-07, 0.05889)	-0.2101	0.01455	(1.051e-07, 0.05889)	-0.2101

Table A.7: Summary of results for parameters of Nygren I_{CaL} model. Only activation parameters (p) recalibrated to unified dataset. *Parameters were searched in $\log_{10}$ space based on the scale of their published values and are presented in linear space. The prior for these parameters is still in the original $\log_{10}$ space.

$$
\begin{aligned}
I_{\mathrm{CaL}} &= g_{\mathrm{Ca,L}} df f_{\mathrm{Ca}} (\mathrm{V} - \mathrm{E}_{\mathrm{Ca,app}}) \\
\frac{\mathrm{d}d}{\mathrm{dt}} &= \frac{\overline{d} - d}{\tau_d}, \qquad \frac{\mathrm{d}f}{\mathrm{dt}} = \frac{\overline{f} - f}{\tau_f} \\
\overline{d} &= \frac{1.0}{1.0 + e^{(\mathrm{V}+\mathbf{p_4})/-\mathbf{p_5}}}, \qquad \tau_d = \frac{1 - e^{(\mathrm{V}+\mathbf{p_1})/-\mathbf{p_2}}}{\mathbf{p_3}(\mathrm{V} + \mathbf{p_1})\left[1 + e^{(\mathrm{V}+\mathbf{p_1})/-\mathbf{p_2}}\right]} \\
\overline{f} &= \frac{1.0}{1.0 + e^{(\mathrm{V}+\mathbf{q_6})/\mathbf{q_7}}}, \qquad \tau_f = \mathbf{q_1}\left[\mathbf{q_2} e^{-\mathbf{q_3}^2 (\mathrm{V}+\mathbf{q_4})^2} + \mathbf{q_5}\right]^{-1}
\end{aligned}
$$

Table A.8: Gating kinetics in Courtemanche model of I_{CaL} channel current (see Appendix in [166]).

		Original				Unified		
Name	Published	Prior	Median	89% HPDI	$\log_{10}$RSD	Median	89% HPDI	$\log_{10}$RSD
p1	10.0	$\mathcal{U}$(-100, 100)	-63.91	(-90.59, -30.08)	-0.5153	-38.24	(-99.15, 54.23)	0.2831
p2	6.24	$\mathcal{U}$(0, 50)	9.655	(1.853, 18.57)	-0.2793	19.17	(0.1832, 43.09)	-0.1334
p3*	0.035	$\mathcal{U}$(-7, 3)	2.072e-07	(1.559e-07, 0.0001709)	-0.6749	0.02479	(0.01392, 0.0721)	-0.7863
p4	10.0	$\mathcal{U}$(-100, 100)	19.07	(6.624, 20.71)	-0.5022	10.44	(10.05, 10.71)	-1.66
p5	8.0	$\mathcal{U}$(0, 50)	6.078	(5.647, 7.053)	-1.029	7.447	(7.267, 7.638)	-1.754
q1*	9.0	$\mathcal{U}$(0, 3)	57.97	(1.072, 435.5)	-0.372	5.315	(1.004, 19.81)	-0.2447
q2*	0.0197	$\mathcal{U}$(-2, 3)	0.2487	(0.01006, 3.008)	0.2592	1.825	(0.1754, 6.422)	0.3113
q3*	0.0337	$\mathcal{U}$(-4, 0)	0.01259	(0.0001002, 0.1925)	-0.3061	0.1147	(0.08051, 0.1534)	-1.006
q4	10.0	$\mathcal{U}$(-100, 100)	-11.13	(-71.3, 88.69)	0.8784	1.305	(-1.347, 4.125)	0.07887
q5*	0.02	$\mathcal{U}$(-4, 0)	0.02488	(0.0001023, 0.4122)	-0.1906	0.1955	(0.03626, 0.6931)	-0.2331
q6	28.0	$\mathcal{U}$(-100, 100)	27.82	(25.28, 30.52)	-1.177	33.32	(25.89, 40.27)	-0.8614
q7	6.9	$\mathcal{U}$(0, 50)	6.879	(5.583, 8.993)	-0.8052	10.95	(7.257, 13.98)	-0.704

Table A.9: Summary of results of parameters of Courtemanche I_{CaL} model. *Parameters were searched in $\log_{10}$ space based on the scale of their published values and are presented in linear space. The prior for these parameters is still in the original $\log_{10}$ space.

Unified				
Name	Prior	Median	89% HPDI	$\log_{10}$RSD
p_1^*	$\mathcal{U}$(-7, 3)	0.5513	(1.02e-07, 1.073)	0.1053
p_2	$\mathcal{U}$(1e-7, 0.4)	0.01878	(1.245e-05, 0.05856)	-0.07143
p_3^*	$\mathcal{U}$(-7, 3)	0.375	(0.0056, 1.575)	0.07778
p_4	$\mathcal{U}$(1e-7, 0.4)	0.09998	(0.02278, 0.2473)	-0.1811
p_5^*	$\mathcal{U}$(-7, 3)	0.06489	(0.04241, 0.2347)	-0.6597
p_6	$\mathcal{U}$(1e-7, 0.4)	0.04437	(0.03053, 0.06118)	-0.6387
p_7^*	$\mathcal{U}$(-7, 3)	0.02056	(0.01379, 0.02842)	-1.205
p_8	$\mathcal{U}$(1e-7, 0.4)	0.02449	(0.01303, 0.03353)	-0.5575
A^*	$\mathcal{U}$(0, 3)	4.497	(3.235, 13.56)	-0.5354

Table A.10: Summary of results of parameters of standardised I_{CaL} model using unified dataset. *Parameters were searched in $\log_{10}$ space and are presented in linear space. The prior for these parameters is still in the original $\log_{10}$ space.

A.1.3 Transient outward K^+ channel, I_{to}

$$
\begin{aligned}
I_{\text{to}} &= \bar{g}_{\text{t}} r s \left(\text{V} - \text{E}_{\text{K}}\right) \\
\frac{\text{d}r}{\text{dt}} &= \frac{\overline{r} - r}{\tau_r}, \qquad \frac{\text{d}s}{\text{dt}} = \frac{\overline{s} - s}{\tau_s} \\
\overline{r} &= \frac{1.0}{1.0 + e^{(\text{V} - \mathbf{p_1})/-\mathbf{p_2}}}, \qquad \tau_r = 1000 \left(\mathbf{p_3} e^{-(\text{V}/\mathbf{p_4})^2} + \mathbf{p_5}\right) \\
\overline{s} &= \frac{1.0}{1.0 + e^{(\text{V} + \mathbf{q_1})/\mathbf{q_2}}}, \qquad \tau_s = 1000 \left(\mathbf{q_3} e^{-((\text{V} + \mathbf{q_4})/\mathbf{q_5})^2} + \mathbf{q_6}\right)
\end{aligned}
$$

Table A.11: Gating kinetics in Nygren model of I_{to} channel current (see Table 8 in [165]). Time constants are multiplied by 1000 to convert from s to ms.

			Original			Unified		
Name	Published	Prior	Median	89% HPDI	$\log_{10}$RSD	Median	89% HPDI	$\log_{10}$RSD
p1	1.0	$\mathcal{U}$(-100, 100)	3.25	(0.3302, 6.375)	-0.234	-0.577	(-7.205, 2.269)	0.4008
p2	11.0	$\mathcal{U}$(1e-7, 50)	10.32	(7.678, 12.61)	-0.8453	2.197	(1.381, 2.753)	-0.6039
p3*	0.0035	$\mathcal{U}$(-7, 0)	4.613e-06	(1.013e-07, 0.0001495)	-0.6929	0.008113	(0.007376, 0.008801)	-1.931
p4	30.0	$\mathcal{U}$(1e-7, 50)	22.81	(0.2115, 43.89)	-0.2055	43.54	(40.81, 46.05)	-1.426
p5*	0.0015	$\mathcal{U}$(-7, 0)	0.002083	(1.005e-07, 0.004469)	-0.4898	0.001244	(0.00109, 0.00137)	-1.973
q1	40.5	$\mathcal{U}$(-100, 100)	54.85	(21.94, 90.84)	-0.4189	28.97	(27.85, 30.79)	-1.473
q2	11.5	$\mathcal{U}$(1e-7, 50)	15.86	(5.989, 22.65)	-0.4416	1.161	(0.3452, 1.969)	-0.3639
q3*	0.4812	$\mathcal{U}$(-5, 1)	0.3981	(0.3359, 0.5484)	-0.6558	0.09093	(0.08613, 0.09628)	-1.829
q4	52.45	$\mathcal{U}$(-100, 100)	57.94	(49.6, 63.12)	-1.104	38.16	(37.65, 38.63)	-2.083
q5	14.97	$\mathcal{U}$(1e-7, 50)	12.1	(9.079, 16.57)	-0.7154	16.87	(16.17, 17.58)	-1.577
q6*	0.01414	$\mathcal{U}$(-7, 0)	0.01171	(0.009782, 0.01371)	-1.577	0.008563	(0.008114, 0.008981)	-2.178

Table A.12: Summary of results for parameters of Nygren I_{to} model. *Parameters were searched in $\log_{10}$ space based on the scale of their published values and are presented in linear space. The prior for these parameters is still in the original $\log_{10}$ space.

$$I_{\text{to}} = g_{\text{to}} o_{\text{a}}^3 o_{\text{i}} \left(\text{V} - \text{E}_{\text{K}}\right)$$

$$\frac{\text{d}\phi}{\text{dt}} = \frac{\phi_\infty - \phi}{\tau_\phi}, \qquad \text{for } \phi = o_{\text{a}}, o_{\text{i}}$$

$$\tau_\phi = \left(\alpha_\phi + \beta_\phi\right)^{-1}, \qquad \text{for } \phi = o_{\text{a}}, o_{\text{i}}$$

$$o_{\text{a}(\infty)} = \frac{1.0}{1.0 + e^{(\text{V}+\mathbf{p_1})/-\mathbf{p_2}}}, \qquad \alpha_{o(\text{a})} = \frac{\mathbf{p_3}}{e^{(\text{V}+\mathbf{p_4})/-\mathbf{p_5}} + e^{(\text{V}+\mathbf{p_6})/-\mathbf{p_7}}}, \qquad \beta_{o(\text{a})} = \frac{\mathbf{p_3}}{\mathbf{p_8} + e^{(\text{V}+\mathbf{p_9})/\mathbf{p_10}}}$$

$$o_{\text{i}(\infty)} = \frac{1.0}{1.0 + e^{(\text{V}+\mathbf{q_1})/\mathbf{q_2}}}, \qquad \alpha_{o(\text{i})} = \frac{1.0}{\mathbf{q_3} + e^{(\text{V}+\mathbf{q_4})/\mathbf{q_5}}}, \qquad \beta_{o(\text{i})} = \frac{1.0}{\mathbf{q_6} + e^{(\text{V}+\mathbf{q_7})/-\mathbf{q_8}}}$$

Table A.13: Gating kinetics in Courtemanche model of I_{to} channel current (see Appendix in [166]).

		Original/Unified			
Name	Published	Prior	Median	89% HPDI	$\log_{10}$RSD
p1	20.47	$\mathcal{U}$(-100, 100)	16.34	(7.558, 24.01)	-0.5041
p2	17.54	$\mathcal{U}$(1e-7, 50)	19.03	(14.78, 23.36)	-0.8263
p3*	0.65	$\mathcal{U}$(-3, 2)	0.06738	(0.002023, 0.259)	-0.3748
p4	10.0	$\mathcal{U}$(-100, 100)	28.32	(-0.545, 81.34)	-0.1259
p5	8.5	$\mathcal{U}$(1e-7, 50)	12.98	(0.01876, 41.94)	-0.09246
p6	-30.0	$\mathcal{U}$(-100, 100)	23.19	(4.345, 94.19)	-0.07312
p7	59.0	$\mathcal{U}$(1e-7, 100)	10.41	(0.008675, 37.07)	-0.05074
p8*	2.5	$\mathcal{U}$(-3, 2)	0.1598	(0.001051, 2.304)	0.04982
p9	82.0	$\mathcal{U}$(-100, 100)	62.09	(-8.713, 99.55)	-0.08063
p10	17.0	$\mathcal{U}$(1e-7, 50)	41.35	(21.91, 49.99)	-0.5362
q1	43.1	$\mathcal{U}$(-100, 100)	33.51	(30.65, 35.14)	-1.353
q2	5.3	$\mathcal{U}$(1e-7, 50)	6.981	(5.946, 8.025)	-0.8174
q3*	18.53	$\mathcal{U}$(-1, 4)	3.668	(0.1006, 14.48)	0.1733
q4	113.7	$\mathcal{U}$(0, 200)	125.8	(114.5, 135.2)	-1.178
q5	10.95	$\mathcal{U}$(1e-7, 50)	15.42	(13.43, 17.26)	-0.9771
q6*	35.56	$\mathcal{U}$(-1, 4)	37.67	(36.17, 41.82)	-1.898
q7	1.26	$\mathcal{U}$(-100, 100)	31.78	(27.76, 36.86)	-0.7325
q8	7.44	$\mathcal{U}$(1e-7, 50)	0.6272	(0.003919, 1.28)	0.1188

Table A.14: Summary of results for parameters of Courtemanche I_{to} model. Original and unified datasets are equivalent. *Parameters were searched in $\log_{10}$ space based on the scale of their published values and are presented in linear space. The prior for these parameters is still in the original $\log_{10}$ space.

Unified				
Name	Prior	Median	89% HPDI	$\log_{10}$RSD
p_1^*	$\mathcal{U}$(-7, 3)	0.00556	(0.005179, 0.006032)	-1.904
p_2	$\mathcal{U}$(1e-7, 0.4)	0.07096	(0.06763, 0.07326)	-1.586
p_3^*	$\mathcal{U}$(-7, 3)	0.1906	(0.1817, 0.1991)	-1.774
p_4	$\mathcal{U}$(1e-7, 0.4)	0.02528	(0.02459, 0.0261)	-1.724
p_5^*	$\mathcal{U}$(-7, 3)	0.1066	(0.1019, 0.1129)	-1.83
p_6	$\mathcal{U}$(1e-7, 0.4)	0.05923	(0.05696, 0.06139)	-1.57
p_7^*	$\mathcal{U}$(-7, 3)	0.0002949	(0.0002315, 0.000421)	-1.665
p_8	$\mathcal{U}$(1e-7, 0.4)	0.08746	(0.08027, 0.08944)	-1.478

Table A.15: Summary of results for parameters of standardised I_{to} model using unified dataset. *Parameters were searched in $\log_{10}$ space and are presented in linear space. The prior for these parameters is still in the original $\log_{10}$ space.

A.1.4 Ultra-rapidly activating delayed rectifier K^+ channel, I_{Kur}

$$
\begin{aligned}
I_{\mathrm{sus}} &= \bar{g}_{\mathrm{sus}} r_{\mathrm{sus}} s_{\mathrm{sus}} \left(\mathrm{V} - \mathrm{E_K}\right) \\
\frac{\mathrm{d}r_{\mathrm{sus}}}{\mathrm{dt}} &= \frac{\overline{r_{\mathrm{sus}}} - r_{\mathrm{sus}}}{\tau_{r_{\mathrm{sus}}}}, \qquad \frac{\mathrm{d}s_{\mathrm{sus}}}{\mathrm{dt}} = \frac{\overline{s_{\mathrm{sus}}} - s_{\mathrm{sus}}}{\tau_{s_{\mathrm{sus}}}} \\
\overline{r_{\mathrm{sus}}} &= \frac{1.0}{1.0 + e^{(\mathrm{V}+\mathbf{p_1})/-\mathbf{p_2}}}, \qquad \tau_{r_{\mathrm{sus}}} = 1000 \left(\frac{\mathbf{p_3}}{1.0 + e^{(\mathrm{V}+\mathbf{p_4})/\mathbf{p_5}}} + \mathbf{p_6} \right) \\
\overline{s_{\mathrm{sus}}} &= \frac{1.0 - \mathbf{q_3}}{1.0 + e^{(\mathrm{V}+\mathbf{q_1})/\mathbf{q_2}}} + \mathbf{q_3}, \qquad \tau_{s_{\mathrm{sus}}} = 1000 \left(\frac{\mathbf{q_4}}{1.0 + e^{(\mathrm{V}+\mathbf{q_5})/\mathbf{q_6}}} + \mathbf{q_7} \right)
\end{aligned}
$$

Table A.16: Gating kinetics in Nygren model of I_{sus} (I_{Kur}) channel current (see Table 8 in [165]). Time constants are multiplied by 1000 to convert from s to ms.

		Original				Unified		
Name	Published	Prior	Median	89% HPDI	$\log_{10}$RSD	Median	89% HPDI	$\log_{10}$RSD
p1	4.3	$\mathcal{U}$(-100, 100)	1.895	(1.821, 1.946)	-1.68	2.031	(1.996, 2.056)	-2.028
p2	8.0	$\mathcal{U}$(1e-7, 50)	4.54	(4.487, 4.564)	-2.226	4.305	(4.295, 4.325)	-2.61
p3*	0.009	$\mathcal{U}$(-5, 0)	0.004119	(0.004024, 0.004169)	-2.667	0.002799	(0.002775, 0.002824)	-3.017
p4	5.0	$\mathcal{U}$(-100, 100)	-13.6	(-14.2, -13.1)	-1.582	-19.02	(-19.31, -18.77)	-2.056
p5	12.0	$\mathcal{U}$(1e-7, 50)	7.566	(7.169, 7.953)	-1.496	5.109	(4.959, 5.271)	-1.709
p6*	0.0005	$\mathcal{U}$(-6, -1)	0.0007858	(0.0007327, 0.0008531)	-2.147	0.0008455	(0.0008235, 0.0008719)	-2.58
q1	20.0	$\mathcal{U}$(-100, 100)	21.14	(8.065, 51.78)	-0.1842	21.14	(8.065, 51.78)	-0.1842
q2	10.0	$\mathcal{U}$(1e-7, 50)	12.96	(0.8947, 27.71)	-0.2282	12.96	(0.8947, 27.71)	-0.2282
q3	0.6	$\mathcal{U}$(0, 1)	0.121	(0.0001271, 0.268)	-0.1557	0.121	(0.0001271, 0.268)	-0.1557
q4*	0.047	$\mathcal{U}$(-4, 1)	0.06416	(0.01542, 0.133)	-0.6109	0.06416	(0.01542, 0.133)	-0.6109
q5	60.0	$\mathcal{U}$(-100, 100)	43.27	(-52.21, 99.65)	0.2045	43.27	(-52.21, 99.65)	0.2045
q6	10.0	$\mathcal{U}$(1e-7, 50)	27.02	(1.936, 45.79)	-0.238	27.02	(1.936, 45.79)	-0.238
q7*	0.3	$\mathcal{U}$(-3, 2)	0.286	(0.2161, 0.3196)	-0.221	0.286	(0.2161, 0.3196)	-0.221

Table A.17: Summary of results for parameters of Nygren I_{Kur} model. Only activation parameters (p) were recalibrated to unified dataset. *Parameters were searched in $\log_{10}$ space based on the scale of their published values and are presented in linear space. The prior for these parameters is still in the original $\log_{10}$ space.

$$I_{\mathrm{Kur}} = g_{\mathrm{Kur}} \left(1.0 + \frac{\mathbf{r_1}}{1.0 + e^{(V+\mathbf{r_2})/-\mathbf{r_3}}} \right) u_{\mathrm{a}}^3 u_{\mathrm{i}} \left(\mathrm{V} - \mathrm{E_K} \right)$$

$$\frac{\mathrm{d}u_{\mathrm{a}}}{\mathrm{dt}} = \frac{u_{\mathrm{a}(\infty)} - u_{\mathrm{a}}}{\tau_{u(\mathrm{a})}}, \qquad \frac{\mathrm{d}u_{\mathrm{i}}}{\mathrm{dt}} = \frac{u_{\mathrm{i}(\infty)} - u_{\mathrm{i}}}{\tau_{u(\mathrm{i})}}$$

$$u_{\mathrm{a}(\infty)} = \frac{1.0}{1.0 + e^{(\mathrm{V}+\mathbf{p_1})/-\mathbf{p_2}}}, \qquad \alpha_{u(\mathrm{a})} = \frac{\mathbf{p_3}}{e^{(\mathrm{V}+\mathbf{p_4})/-\mathbf{p_5}} + e^{(\mathrm{V}+\mathbf{p_6})/-\mathbf{p_7}}}, \qquad \beta_{u(\mathrm{a})} = \frac{\mathbf{p_3}}{\mathbf{p_8} + e^{(\mathrm{V}+\mathbf{p_9})/\mathbf{p_{10}}}}$$

$$u_{\mathrm{i}(\infty)} = \frac{1.0}{1.0 + e^{(\mathrm{V}+\mathbf{q_1})/\mathbf{q_2}}}, \qquad \alpha_{u(\mathrm{i})} = \frac{1.0}{\mathbf{q_3} + e^{(\mathrm{V}+\mathbf{q_4})/-\mathbf{q_5}}}, \qquad \beta_{u(\mathrm{i})} = e^{(\mathrm{V}+\mathbf{q_6})/\mathbf{q_7}}$$

$$\tau_\phi = \left(\alpha_\phi + \beta_\phi \right)^{-1}, \qquad \text{for } \phi = u_{\mathrm{a}}, u_{\mathrm{i}}$$

Table A.18: Gating kinetics in Courtemanche model of I_{Kur} channel current (see Appendix in [166]).

		Original				Unified		
Name	Published	Prior	Median	89% HPDI	$\log_{10}$RSD	Median	89% HPDI	$\log_{10}$RSD
p1	30.3	$\mathcal{U}$(-100, 100)	22.15	(20.09, 24.22)	-1.213	22.15	(20.09, 24.22)	-1.213
p2	9.6	$\mathcal{U}$(1e-7, 50)	17.41	(13.63, 21.67)	-0.8446	17.41	(13.63, 21.67)	-0.8446
p3*	0.65	$\mathcal{U}$(-3, 2)	0.04404	(0.00102, 0.1094)	-0.4886	0.04404	(0.00102, 0.1094)	-0.4886
p4	10.0	$\mathcal{U}$(-100, 100)	32.29	(-4.553, 88.19)	-0.1005	32.29	(-4.553, 88.19)	-0.1005
p5	8.5	$\mathcal{U}$(1e-7, 50)	16.13	(3.228, 37.54)	-0.2495	16.13	(3.228, 37.54)	-0.2495
p6	-30.0	$\mathcal{U}$(-100, 100)	32.82	(-2.739, 87.54)	-0.1255	32.82	(-2.739, 87.54)	-0.1255
p7	59.0	$\mathcal{U}$(1e-7, 50)	16.26	(1.388, 32.48)	-0.2607	16.26	(1.388, 32.48)	-0.2607
p8*	2.5	$\mathcal{U}$(-3, 2)	0.06393	(0.001001, 0.5319)	-0.1877	0.06393	(0.001001, 0.5319)	-0.1877
p9	82.0	$\mathcal{U}$(-100, 100)	47.77	(-22.92, 99.54)	0.04513	47.77	(-22.92, 99.54)	0.04513
p10	17.0	$\mathcal{U}$(1e-7, 50)	41.82	(29.25, 49.78)	-0.6841	41.82	(29.25, 49.78)	-0.6841
r1*	10.0	$\mathcal{U}$(0, 2)	8.721	(1.004, 61.18)	-0.2278	8.721	(1.004, 61.18)	-0.2278
r2	-15.0	$\mathcal{U}$(-100, 100)	-6.353	(-84.56, 87.51)	1.22	-6.353	(-84.56, 87.51)	1.22
r3	13.0	$\mathcal{U}$(1e-7, 50)	25.3	(0.04052, 44.01)	-0.231	25.3	(0.04052, 44.01)	-0.231
q1	-99.45	$\mathcal{U}$(-200, 200)	-69.32	(-144.5, -0.2399)	-0.1766	54.84	(54.83, 54.85)	-3.809
q2	27.48	$\mathcal{U}$(1e-7, 50)	34.61	(15.72, 49.44)	-0.4477	39.95	(39.94, 39.96)	-3.968
q3*	21.0	$\mathcal{U}$(-1, 4)	1941.0	(0.1185, 5866.0)	-0.319	674.0	(674.0, 674.0)	-5.458
q4	-185.0	$\mathcal{U}$(-200, 200)	-118.8	(-199.4, -34.61)	-0.2815	74.15	(72.39, 81.09)	-1.373
q5	28.0	$\mathcal{U}$(1e-7, 50)	26.47	(0.6525, 43.54)	-0.2649	3.708	(2.084, 4.118)	-0.6464
q6	-158.0	$\mathcal{U}$(-200, 0)	-172.1	(-199.5, -133.3)	-0.8272	-151.0	(-199.9, -95.79)	-0.6078
q7	16.0	$\mathcal{U}$(1e-7, 50)	23.66	(14.8, 28.97)	-0.5748	1.984	(0.03531, 4.561)	-0.1569

Table A.19: Summary of results for parameters of Courtemanche I_{Kur}. Only inactivation parameters (q) were recalibrated to unified dataset. *Parameters were searched in $\log_{10}$ space based on the scale of their published values and are presented in linear space. The prior for these parameters is still in the original $\log_{10}$ space.

Unified				
Name	Prior	Median	89% HPDI	$\log_{10}$RSD
p_1^*	$\mathcal{U}$(-7, 3)	0.0558	(0.0433, 0.06443)	-1.367
p_2	$\mathcal{U}$(1e-7, 0.4)	0.1464	(0.1281, 0.1683)	-1.043
p_3^*	$\mathcal{U}$(-7, 3)	0.1188	(0.1096, 0.1279)	-1.634
p_4	$\mathcal{U}$(1e-7, 0.4)	0.02021	(0.01904, 0.02213)	-1.306
p_5^*	$\mathcal{U}$(-7, 3)	0.004436	(0.004311, 0.004566)	-2.485
p_6	$\mathcal{U}$(1e-7, 0.4)	0.001568	(0.001221, 0.001863)	-0.8671
p_7^*	$\mathcal{U}$(-7, 3)	1.424e-07	(1.005e-07, 3.607e-07)	-1.417
p_8	$\mathcal{U}$(1e-7, 0.4)	0.02784	(0.02351, 0.03098)	-1.079

Table A.20: Summary of results for parameters of standardised I_{Kur} model using unified dataset. *Parameters were searched in $\log_{10}$ space and are presented in linear space. The prior for these parameters is still in the original $\log_{10}$ space.

A.2 Voltage-clamp protocols and summary statistic functions for human atrial experiments

Throughout this section, the lettering in the headers refers to the figure describing voltage protocols for the channel. All curve fitting for finding time constants was carried out using the *scipy.optimize* Python library. This section is adapted from the Supplementary Material to [157] (CC BY).

A.2.1 Fast Na^+ channel, I_{Na}

All experiments by Sakakibara et al. [170] used equal extracellular and pipette solution sodium concentration of 5mM at a temperature of 290K ($17°C$). The time constant of activation experiment from Schneider et al. [171] used sodium concentration of 120mM in the extracellular solution and 70mM in the pipette solution, and the experiment was conducted at 297K ($24°C$).

a: Steady-state activation (p.538 [170]). The standard protocol to measure steady-state activation of the channel holds the membrane at a sub-threshold potential of −140mV and then steps the channel to a series of voltage steps between −100mV and 20mV, with intervals of 10mV. The steps last for 1s and there are 10s between each step.

The degree of steady-state activation is measured by recording the peak current during the voltage step (normalised to cell capacitance). The conductance is calculated by dividing the peak current by the forcing term, usually assumed to be the potential difference to the Nernst potential of the primary ion carrier, $g = \frac{I}{V - E_X}$. In the computational protocols, we directly measure the conductance of the channel to bypass this calculation. To plot the activation curve, the conductance is plotted against the voltage step normalised to its maximum value in any voltage step.

b: Time constant of activation (p.85 [171]). The time constant constant of inactivation is measured by fitting an equation to the current trace from a standard steady-state activation protocol as described in the previous protocol. In this case, the holding potential is −135mV and the steps are from −65mV and 15mV in steps of 10mV. The time at

holding potential between each step was not given and so assumed to be 10s (more than enough for the I_{Na} channel to return to steady-state) and each test pulse lasted for 12ms.

The activation time constant was measured by fitting the entire current trace at a pulse to the equation $I_{\mathrm{Na}} = I_{\mathrm{Na,max}}\left[1 - e^{-t/\tau_{\mathrm{m}}}\right]^3 e^{-t/\tau_{\mathrm{h}}} + \text{constant}$ (p.87 [171]). In this equation, t is the time in ms, $I_{\mathrm{Na,max}}$ is the peak of the current trace, τ_{m} is the activation time constant and τ_{h} is the inactivation time constant.

c: Steady-state inactivation (p.541 [170]). The protocol used to measure steady-state inactivation is often also referred to as an availability protocol. The membrane is held at a holding potential of −140mV for 10s, then stepped to a conditioning potential for 1s to activate and inactivate the channel. The membrane potential is returned to the holding potential for 2ms before stepping to a test pulse at −20mV for 30ms. A series of different conditioning pulses between −140mV and −40mV in steps of 10mV is used to test the amount of inactivation of the channel at different voltages.

The steady-state inactivation is measured by recording the peak current during the test pulse, normalised to the current in a test pulse when no conditioning step is applied (usually the maximum current amplitude). In the virtual voltage clamp experiment, we measure conductance directly in this step (which is equivalent as the forcing is the same during each test pulse and eliminated during the normalisation).

d: Fast/slow inactivation time constant (p.539 [170]). The protocol to determine inactivation time constants is a simple steptrain of test pulses from a holding potential of −140mV for 10s to a series of 100ms test pulses to voltages from −50mV to −20mV in steps of 10mV.

The fast and slow inactivation constants are determined by fitting the *decay* part of the current trace (after the peak current) to the equation $I_{\mathrm{Na}} = A_1 e^{-t/\tau_{\mathrm{f}}} + A_2 e^{-t/\tau_{\mathrm{s}}} + A_0$ (p.538 [170]) where A are amplitude variables, t is the time and τ_{f} and τ_{s} are the fast and slow time constants of inactivation respectively.

e: Fast/slow recovery time constant (p.538 [170]). The time constants of recovery from inactivation were determined using a double pulse protocol. The first pulse is a conditioning pulse for 1000ms to −20mV followed by a recovery period to a holding

potential between -140mV and -90mV in steps of 10mV, of varying length between $2-1000$ms (this was not specified and we assumed a series of $t_{\mathrm{r}} = 2^i$ where $i = 1, 2...10$). The recovery period is followed by a test pulse identical to the conditioning pulse. We assumed 10s at holding potential between each pair of pulses.

The recovery time constant is measured through a series of processing steps. Firstly, the peak current in the test pulse is normalised to the peak current in the preceding conditioning pulse to give a measurement of proportion of the channel recovery for each recovery time period. This recovery measure is plotted against the recovery time period and the resulting curve is fit to a double exponential equation $r = A_0 - A_1 e^{-t_{\mathrm{r}}/\tau_{\mathrm{r(f)}}} - A_2 e^{-t_{\mathrm{r}}/\tau_{\mathrm{r(s)}}}$ where r is the proportion of recovery, A are amplitude parameters, t is the recovery time period and $\tau_{\mathrm{r(f)}}$ and $\tau_{\mathrm{r(s)}}$ are the fast and slow recovery time constants respectively. These values are calculated for each holding potential.

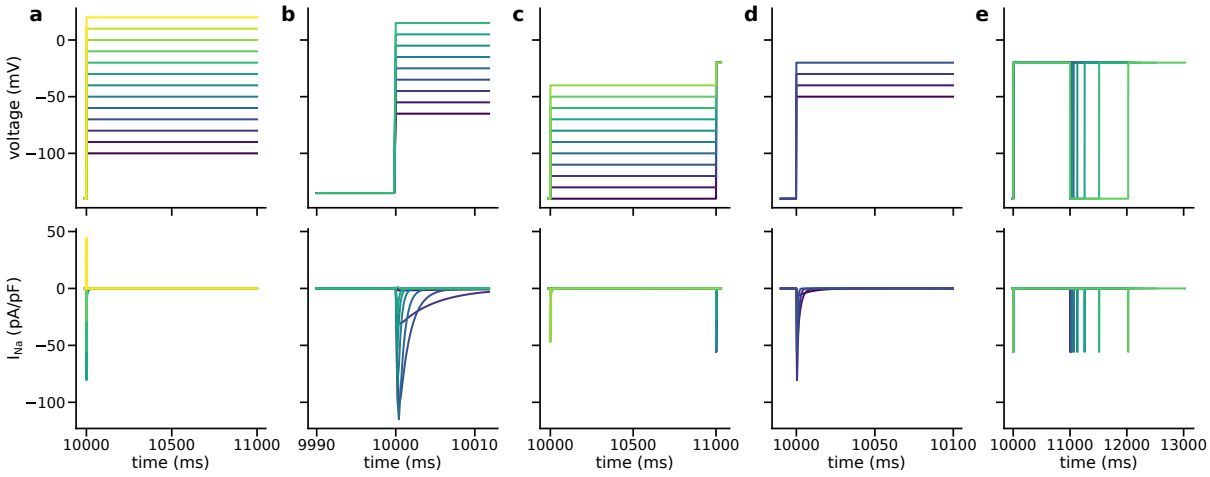


Figure A.1: Voltage steps and current response (from C model) of I_{Na} protocols. **a** steady-state activation, **b** time constant of activation, **c** steady-state inactivation, **d** fast and slow time constants of inactivation, **e** fast and slow time constants of recovery from inactivation. The recovery protocol is repeated at multiple holding potentials (only one shown). See text for details of how the current traces are processed into summary statistics.

A.2.2 L-type Ca^{2+} channel, I_{CaL}

Experiments by Mewes and Ravens [172] were carried out at room temperature (assumed by authors to be 295K) and external solution with calcium concentration of 1.8mM. Those by Li and Nattel [173] were conducted at 309K with 2.0mM external calcium concentration. Experiments by Sun et al. [174] were completed at room temperature (assumed

by authors to be 296K) and external calcium concentration of 1mM. It is difficult to estimate the level of intracellular calcium concentration during these experiments due to the mechanisms of the intracellular calcium stores and buffering. In our virtual voltage clamp experiments, the level of the intracellular calcium was kept constant at the resting value from the published N and C models (72.5nM and 101.3nM respectively) and, for the S model, set to the same value as the C model (101.3nM).

a, b: Steady-state activation (p.1309 [172], p.H228 [173]). In Mewes and Ravens [172], steady-state activation was assessed using a conventional steptrain protocol from a holding potential of −40mV to 450ms steps between −35mV to 15mV in intervals of 5mV, with 10s between each pulse. In Li and Nattel [173], the activation curve was generated from the IV curve dataset which used a similar step train protocol. This time the holding potential was −80mV and the 300ms test pulses ranged from −80mV to 20mV in steps of 10mV. Both activation curves were generated as described in I_{Na} steady-state activation.

b: Activation time constant (p.H233 [173]). The single activation time constant value was determined from the current trace evoked during the 10mV test pulse in the activation protocol from [173]. The activation time constant was estimated by fitting the upstroke of the normalised current trace to $I_{\mathrm{CaL}} = 1 - Ae^{-t/\tau_{\mathrm{a}}}$ where A is an amplitude parameter, t is the time and τ_{a} is the activation time constant.

c: Steady-state voltage-dependent inactivation (p.H229 [173]). The voltage-dependent steady-state inactivation was assessed using a standard availability protocol. Conditioning pulses to a series of voltages between −80mV and 50mV in steps of 10mV were followed immediately by a test pulse to 10mV for 300ms. In [173], there are three datasets using different length of conditioning pulses of either 150ms, 300ms or 1000ms. We use the 1000ms prepulse dataset as this was used for calibration in both modelling papers. The inactivation curve was calculated as in I_{Na} steady-state inactivation.

d, e: Fast/slow voltage-dependent inactivation time constant (p.H229-H230 [173], p.H1628 [174]). Fast and slow inactivation time constants were calculated by fitting a bi-exponential equation to the decay portion of the current trace during test pulses from a holding potential. In [173], three different holding potentials were used and we use

the same as the modelling papers: −80mV. Test pulses lasted 300ms to steps between −10mV and 30mV in intervals of 10mV (we assume 10s between pulses). In [174], the holding potential was −80mV, test pulses had duration 1000ms with the same levels as above, and were preceded by a 500ms pulse to −40mV. In both cases, time constants of inactivation were calculated by fitting the decay portion of the current trace during the test pulses to $I_{\mathrm{CaL}} = A_0 + A_f e^{-t/\tau_{\mathrm{f}}} + A_s e^{-t/\tau_{\mathrm{s}}}$ were A are amplitude parameters, t is the time and τ_{f} and τ_{s} are the fast and slow time constants respectively.

f: Fast/slow voltage-dependent recovery time constant (p.H229-H230 [173]). Recovery time constants were assessed with a two-pulse protocol as in I_{Na} recovery experiments. In this case, the holding potentials were −80mV, −60mV and −40mV with conditioning and test pulses both to 10mV for 300ms. Recovery periods were generated from $t_{\mathrm{r}} = 2^i$ where $i = 1, 2, ..., 11$ based on the range of data points in Fig 4B [173]. The data was processed as in I_{Na} recovery experiments with the exception that a single exponential function was used to fit the −80mV recovery curve to give a single (slow) recovery time constant.

A.2.3 Transient outward K^+ channel, I_{to}

Experiments by Shibata et al. [175] and Wang et al. [176] were conducted at room temperature (assumed to be 295K). Firek and Giles [177] used temperature of 306K ($33°C$). Shibata et al. used an extracellular and pipette potassium concentration of 4.5mM and 150mM respectively, Wang et al. used 5.4mM and 130mM and Firek et al. used 5.4mM and 140mM.

Some data for I_{to} was extracted directly from the N and C modelling papers [165, 166] as the source of the comparison experimental data plotted was not clear from the text. In these cases, conditions were assumed to be the same as the lab which produced the model. Thus, conditions for the assumed experimental data from Nygren et al. [165] was set to the same conditions as Firek and Giles [177] above, and data from Courtemanche et al. [166] was assumed to have been collected at the conditions in Wang et al. [176].

a, b: Steady-state activation (p. H1776 [175], p.1065 [176]). In Shibata et al. [175],

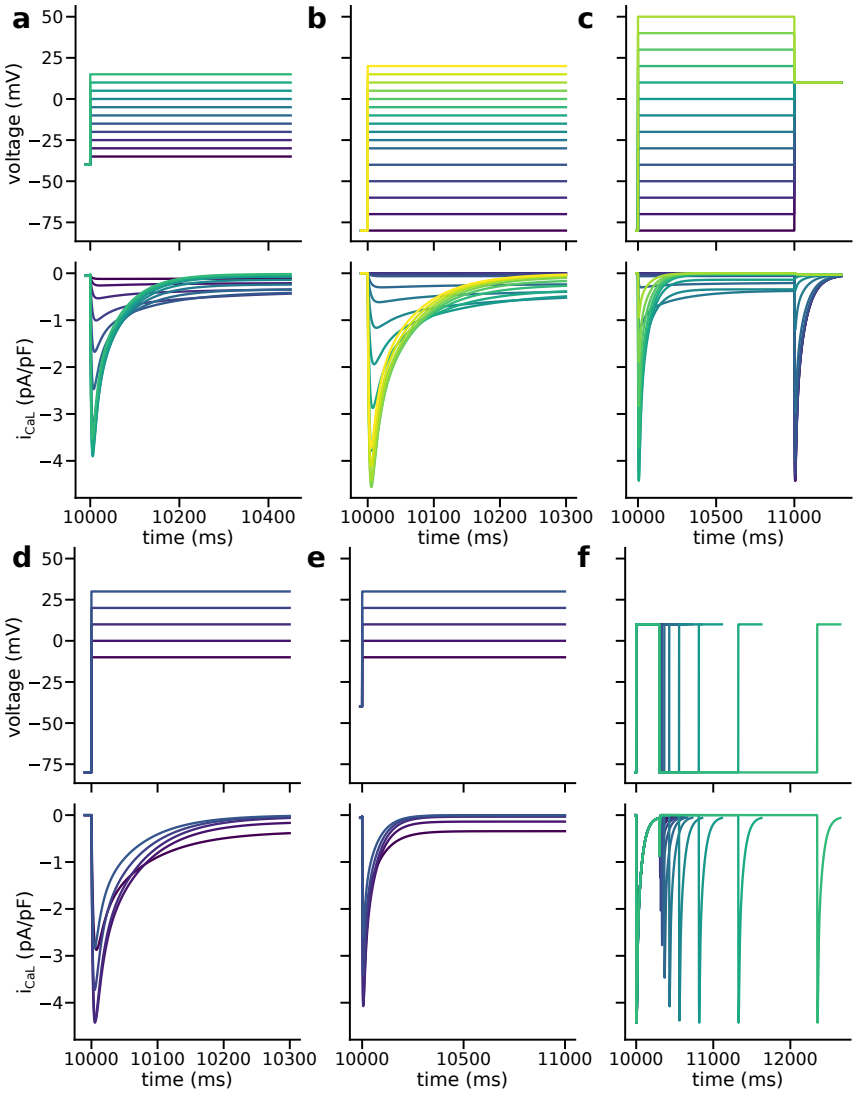


Figure A.2: Voltage steps and current response (from N model) of I_{CaL} protocols. **a** steady-state activation [172], **b** steady-state and time constant of activation [173], **c** steady-state inactivation [173], **d** fast and slow time constants of inactivation [173], **e** fast and slow time constants of inactivation [174], **f** fast and slow time constants of recovery from inactivation [173]. The recovery protocol is repeated at multiple holding potentials (only one shown). See text for details of how the current traces are processed into summary statistics.

steady-state activation was determined by holding at a potential of −60mV for 20s, then depolarising for 15ms to a step between −30mV to 80mV, and finally stepping to −40mV for 100ms. The activation curve was generated by recording the peak current amplitude in the final step (the 'tail' current). Wang et al. [176] used a standard steady-state activation protocol with a holding potential of −80mV to a series of test potentials between −40mV and 50mV and measured the peak current during the 1000ms depolarising step (before processing as above for I_{Na}).

c: Activation time constant (p.H305 [166]). Activation time constant data corre-

sponding to that plotted in the modelling paper could not be found in the cited experimental source [176]. A simple steptrain protocol as described in [176] was assumed with a holding potential of −50mV and 100ms test pulses. The activaton time course of I_{to} was fitted to a single exponential equation: $I_{\text{to}} = A_0 - Ae^{-t/\tau_{\text{a}}}$ where A parameters are amplitudes, t is the time course and τ_{a} is the activation time constant.

d: Deactivation time constant (p.H305 [166]). The deactivation time constant data source is also uncertain and it is assumed to use a similar protocol as in Fig. 9A in Wang et al. [176]. This protocol holds the membrane potential at −50mV for 20s before applying a 10ms conditioning pulse to 50mV. This is followed by a test pulse to elicit a tail current, which is fit to a single exponential (same as the activation time constant above) to determine the deactivation time constant.

e, f: Steady-state inactivation (p.34 [177], p.1065 [176]). In Firek and Giles, a standard steady-state availability protocol was applied as described in more detail in I_{Na} steady-state inactivation. The holding potential is −80mV, followed by a 400ms conditioning pulse to levels between −80mV and 16mV, and finally a 400ms test pulse to 0mV to activate the outward current. Wang et al. [176] similarly uses a standard availability protocol with the same holding potential followed by 1000ms conditioning pulse to a range of voltages between −90mV and 30mV followed by a 1000ms test pulse to 60mV. Output was processed into summary statistics as described in I_{Na} steady-state inactivation.

g, h: Inactivation time constant (p.66 [165], p.H305 [166]). It was not clear in either N or C model where experimental comparison data of time constants of inactivation for I_{to} were obtained from. Consequently, simple protocols were assumed based on single-pulse protocols in experimental papers originating from the same labs. For [165], a single pulse protocol from a holding potential of −80mV to 400ms test pulses between 0mV and 40mV was applied and the decay phase of the current trace fit to a single exponential equation as above for activation time constants. For [166], a similar protocol was assumed based on [176] with a holding potential of −50mV and 100ms test pulses to between −40mV and 50mV.

i, j: Recovery time constant (p.66 [165], p.H305 [166]). Similarly to the inactivation time constant data, it was unclear where the recovery data was obtained from for both N and C models. For the N model, we assume the recovery protocol in [175] was used. This is a standard two-pulse recovery protocol with holding potentials of −100mV, −80mV and −60mv and 100ms test pulses to 20mV. For the C model, we assume the protocol in [176] was used with holding potential between −60mV and 40mV and 200ms test pulses to 50mV.

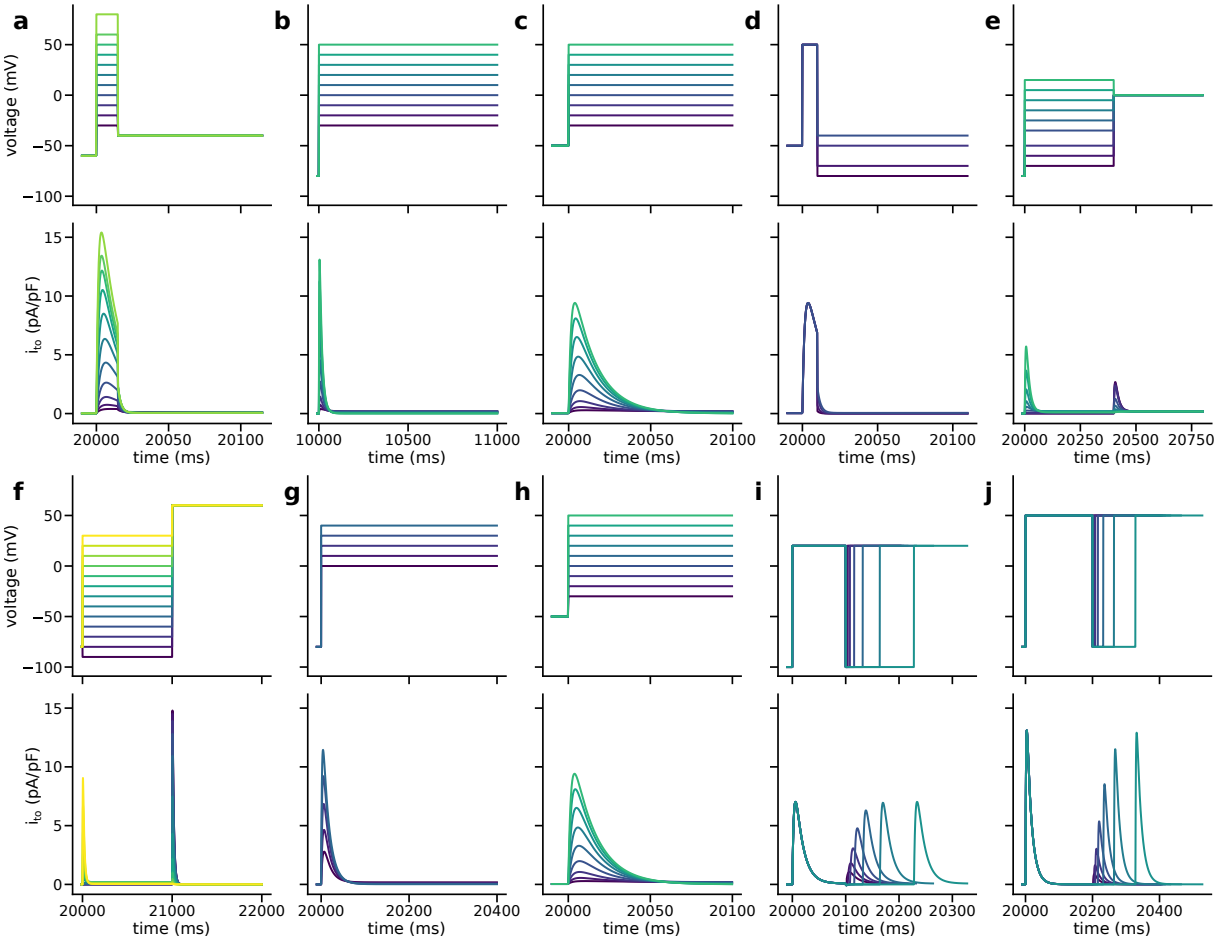


Figure A.3: Voltage steps and current response (from N model) of all I_{to} protocols. From left to right: **a** steady-state activation [175], **b** steady-state activation [176], **c** activation time constants [166], **d** deactivation time constants [166], **e** steady-state inactivation [177], **f** steady-state inactivation [176], **g** time constant of inactivation [165], **h** time constant of inactivation [166], **i** time constant of recovery from inactivation [165], **j** time constant of recovery from inactivation [166]. The recovery protocols are repeated at multiple holding potentials (only one shown for each). See text for details of how the current traces are processed into summary statistics.

A.2.4 Ultra-rapidly activating delayed rectifier K^+ channel, I_{Kur}

Experiments by Wang et al. [176] and Firek and Giles [177] use the same conditions stated above for I_{to}. As before, in some cases it was unclear where the comparison data in the modelling papers was obtained from. Details are given in the following sections.

a: Steady-state activation, activation time constant (p.1069 [176]). I_{Kur} was measured from a holding potential of -50mV followed by a 1s prepulse to 50mV (experimentally used to inactivate the I_{to} current which would otherwise interfere with isolating I_{Kur}). The potential is returned to -50mV for 20ms before being stepped to a range of 100ms test pulses between -40mV to 50mV each followed by a repolarising pulse to -10mV. I_{Kur} was measured as the peak current in the final repolarising pulse and the activation curve determined as previously described for I_{Na} steady-state activation. The activation time constants were determined by fitting the time course of I_{Kur} trace during the test pulses to a single exponential function as described above.

b: Deactivation time constant (p.305 [166]). As it was not clear where the data points were obtained from, the protocol from Fig. 9 in [176] was assumed to have been used. This is the same protocol as described in deactivation time constant for I_{to}.

c, d: Steady-state inactivation (p.34 [177], p.1068 [176]). For Firek and Giles [177], the protocol was the same as the steady-state inactivation protocol described for steady-state inactivation of I_{to} with an increase of the length of the conditioning pulse from 400ms to 2500ms. I_{Kur} was measured as the steady-state current at the end of the test pulse. In Wang et al. [176], steady-state inactivation is measured from the steady-state current at the end of a 2000ms test pulse to 40mV after a 1000ms conditioning pulse from a range of voltages. The holding potential was -60mV.

e, f: Inactivation time constant (p.66 [165], p.H305 [166]). It was unclear where the experimental data points from the N model paper came from. We assume they are generated from the protocol used in [177] from the same lab. This protocol is a simple 400ms step to a range of potentials from a holding potential of -80mV. In [177], the current decay is fit to a double exponential equation in order to separate I_{to} and I_{Kur} decay rates. As in the virtual voltage clamp there is only I_{Kur}, we fit the current decay

to a single exponential.

Similary for the C model, we assume a similar protocol as in [176] was used. This is a simple 2000ms step to a range of test potentials from a holding potential of −50mV. The decay portion of the current trace is fit to a single exponential function as above.

g: Recovery time constant (p.66 [165]). As previously for I_{to}, we assume that the recovery protocol from [175] was used to determine a recovery time constant for I_{Kur}. The protocol is as described for I_{to} recovery time constant.

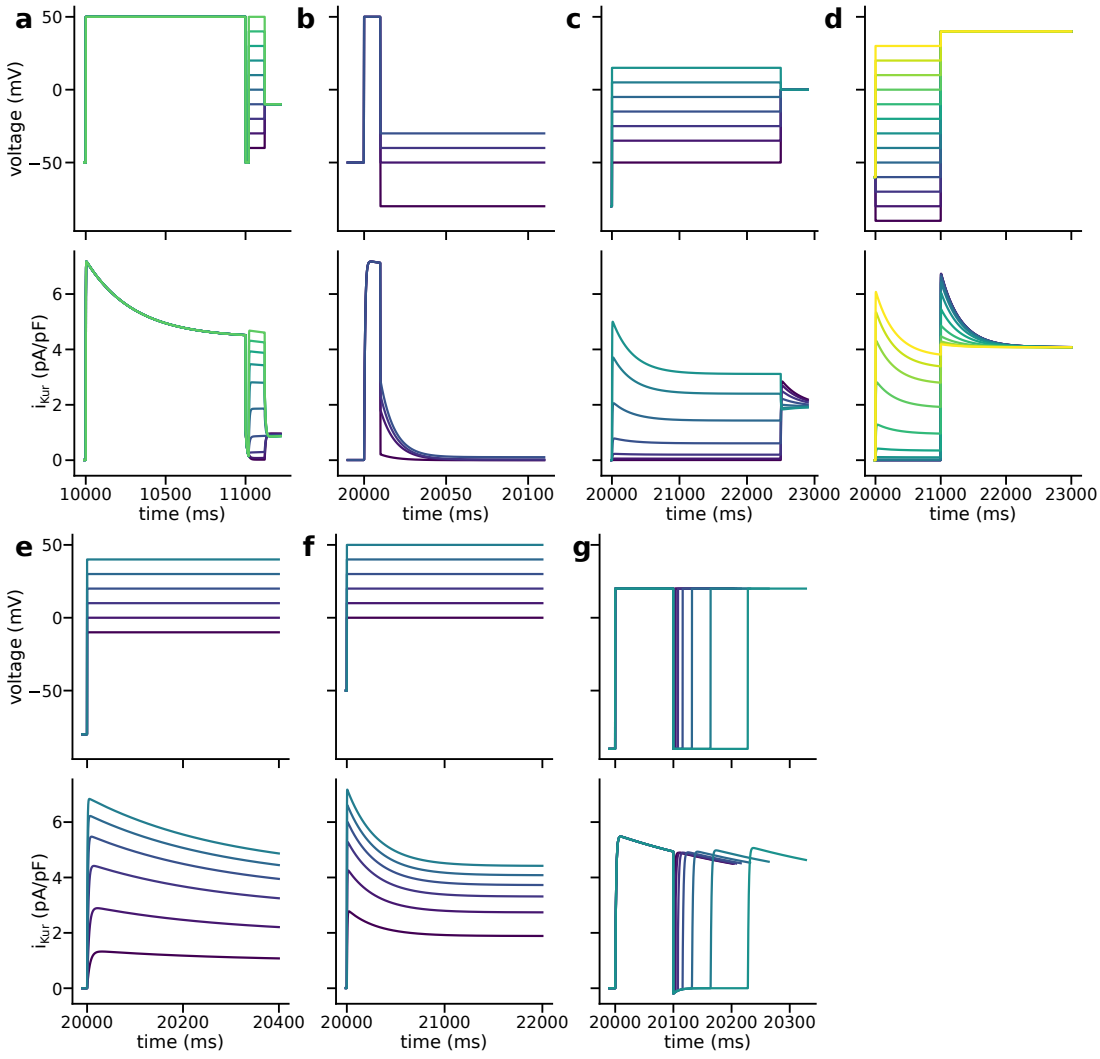


Figure A.4: Voltage steps and current response (from N model) of all I_{Kur} protocols. **a** steady-state activation and activation time constant [176], **b** deactivation time constants [166], **c** steady-state inactivation [177], **d** steady-state inactivation [176], **e** time constant of inactivation [165], **f** time constant of inactivation [166], **g** time constant of recovery from inactivation [165]. See text for details of how the current traces are processed into summary statistics.

A.3 HL1-6 cell model calibration results

Name	Prior	Median	89% HPDI	$\log_{10}$RSD
g^*_{Na}	$\mathcal{U}$(0, 2)	0.6803	(0.6636, 0.6939)	-1.847
A^*	$\mathcal{U}$(0, 2)	2.279	(2.032, 2.547)	-1.062
P_K	$\mathcal{U}$(0, 1)	0.6803	(0.6636, 0.6939)	-1.847
p^*_1	$\mathcal{U}$(-7, 3)	166.9	(134.0, 224.7)	-1.49
p_2	$\mathcal{U}$(1e-7, 0.4)	0.1108	(0.1056, 0.1173)	-1.464
p^*_3	$\mathcal{U}$(-7, 3)	0.0019	(7.287e-5, 0.006022)	-0.7894
p_4	$\mathcal{U}$(1e-7, 0.4)	0.0928	(0.06439, 0.1177)	-0.7399
p^*_5	$\mathcal{U}$(-7, 3)	12.36	(11.02, 13.61)	-1.564
p_6	$\mathcal{U}$(1e-7, 0.4)	0.09255	(0.08976, 0.09525)	-1.715
p^*_7	$\mathcal{U}$(-7, 3)	0.001196	(0.0009144, 0.001528)	-1.619
p_8	$\mathcal{U}$(1e-7, 0.4)	0.04513	(0.04268, 0.04705)	-1.503

Table A.21: Summary of results for parameters of HL1-6 I_{Na}. *Parameters were searched in $\log_{10}$ space and are presented in linear space. The prior for these parameters is still in the original $\log_{10}$ space.

Name	Prior	Median	89% HPDI	$\log_{10}$RSD
g_{CaL}	$\mathcal{U}$(0, 5)	0.7398	(0.7026, 0.7887)	-1.429
E_{CaL}	$\mathcal{U}$(0, 50)	29.11	(28.27, 29.9)	-1.762
p^*_1	$\mathcal{U}$(-7, 3)	248.8	(8.031, 717.6)	-0.7177
p_2	$\mathcal{U}$(1e-7, 0.4)	0.07044	(0.0007567, 0.1557)	-0.1584
p^*_3	$\mathcal{U}$(-7, 3)	0.3163	(0.007102, 1.161)	-0.03067
p_4	$\mathcal{U}$(1e-7, 0.4)	0.2167	(0.1094, 0.2849)	-0.5402
p^*_5	$\mathcal{U}$(-7, 3)	0.01294	(0.01268, 0.01314)	-2.59
p_6	$\mathcal{U}$(1e-7, 0.4)	0.05055	(0.04957, 0.05172)	-1.879
p^*_7	$\mathcal{U}$(-7, 3)	0.000441	(0.00041, 0.0004731)	-2.23
p_8	$\mathcal{U}$(1e-7, 0.4)	0.03346	(0.03265, 0.03453)	-1.729

Table A.22: Summary of results for parameters of HL1-6 I_{CaL}. *Parameters were searched in $\log_{10}$ space and are presented in linear space. The prior for these parameters is still in the original $\log_{10}$ space.

Name	Prior	Median	89% HPDI	$\log_{10}$RSD
g_{CaT}	$\mathcal{U}$(0, 2)	0.1273	(0.1241, 0.1294)	-1.882
E_{CaT}	$\mathcal{U}$(0, 100)	78.93	(77.32, 81.12)	-1.828
p_1^*	$\mathcal{U}$(-7, 3)	173.5	(150.8, 203.4)	-1.738
p_2	$\mathcal{U}$(1e-7, 0.4)	0.03165	(0.02974, 0.03414)	-1.366
p_3^*	$\mathcal{U}$(-7, 3)	0.05556	(0.04709, 0.06503)	-1.47
p_4	$\mathcal{U}$(1e-7, 0.4)	0.1868	(0.184, 0.1886)	-2.117
p_5^*	$\mathcal{U}$(-7, 3)	7.643	(6.6, 8.867)	-1.344
p_6	$\mathcal{U}$(1e-7, 0.4)	0.1683	(0.1666, 0.1706)	-2.117
p_7^*	$\mathcal{U}$(-7, 3)	0.000136	(0.0001173, 0.0001549)	-2.008
p_8	$\mathcal{U}$(1e-7, 0.4)	0.05258	(0.05054, 0.05399)	-1.682

Table A.23: Summary of results for parameters of HL1-6 I_{CaT}. *Parameters were searched in $\log_{10}$ space and are presented in linear space. The prior for these parameters is still in the original $\log_{10}$ space.

Name	Prior	Median	89% HPDI	$\log_{10}$RSD
g_{Kr}	$\mathcal{U}$(0, 10)	0.4976	(0.4652, 0.527)	-1.403
p_1^*	$\mathcal{U}$(-7, 3)	0.0007178	(0.0006925, 0.0007432)	-2.491
p_2	$\mathcal{U}$(1e-7, 0.4)	0.0678	(0.06618, 0.06946)	-1.819
p_3^*	$\mathcal{U}$(-7, 3)	0.0006908	(0.0006688, 0.0007193)	-2.503
p_4	$\mathcal{U}$(1e-7, 0.4)	0.02852	(0.02785, 0.02899)	-1.917
p_5^*	$\mathcal{U}$(-7, 3)	0.06935	(0.06684, 0.071)	-2.126
p_6	$\mathcal{U}$(1e-7, 0.4)	0.03338	(0.03184, 0.03443)	-1.57
p_7^*	$\mathcal{U}$(-7, 3)	0.01372	(0.01347, 0.014)	-2.545
p_8	$\mathcal{U}$(1e-7, 0.4)	0.03565	(0.03523, 0.03594)	-2.21

Table A.24: Summary of results for parameters of HL1-6 I_{Kr}. *Parameters were searched in $\log_{10}$ space and are presented in linear space. The prior for these parameters is still in the original $\log_{10}$ space.

Name	Prior	Median	89% HPDI	$\log_{10}$RSD
g_{to}	$\mathcal{U}$(0, 1000)	708.1	(596.1, 871.7)	-0.8821
p_1^*	$\mathcal{U}$(-7, 3)	1.076e-6	(9.419e-7, 1.5e-6)	-1.922
p_2	$\mathcal{U}$(1e-7, 0.4)	0.1053	(0.1016, 0.1076)	-1.768
p_3^*	$\mathcal{U}$(-7, 3)	0.0001028	(1.001e-7, 0.0002588)	-0.5332
p_4	$\mathcal{U}$(1e-7, 0.4)	0.1451	(0.06731, 0.3175)	-0.2541
p_5^*	$\mathcal{U}$(-7, 3)	0.03223	(0.03213, 0.03231)	-3.236
p_6	$\mathcal{U}$(1e-7, 0.4)	0.03262	(0.03252, 0.0327)	-2.722
p_7^*	$\mathcal{U}$(-7, 3)	3.989e-5	(1.215e-5, 5.196e-5)	-1.275
p_8	$\mathcal{U}$(1e-7, 0.4)	0.237	(0.2286, 0.2711)	-1.172

Table A.25: Summary of results for parameters of HL1-6 I_{to}. *Parameters were searched in $\log_{10}$ space and are presented in linear space. The prior for these parameters is still in the original $\log_{10}$ space.

Name	Prior	Median	89% HPDI	$\log_{10}$RSD
g_{ss}	$\mathcal{U}$(0, 1)	0.07848	(0.07828, 0.0787)	-2.766
p_1^*	$\mathcal{U}$(-7, 3)	0.02376	(0.02372, 0.02381)	-3.502
p_2	$\mathcal{U}$(1e-7, 0.4)	0.02815	(0.02804, 0.02823)	-2.674
p_3^*	$\mathcal{U}$(-7, 3)	0.002228	(0.002202, 0.002251)	-2.917
p_4	$\mathcal{U}$(1e-7, 0.4)	0.06594	(0.06578, 0.06615)	-2.745

Table A.26: Summary of results for parameters of HL1-6 I_{ss}. *Parameters were searched in $\log_{10}$ space and are presented in linear space. The prior for these parameters is still in the original $\log_{10}$ space.

Name	Prior	Median	89% HPDI	$\log_{10}$RSD
g_f	$\mathcal{U}$(0, 1)	0.1074	(0.1074, 0.1074)	-4.61
κ	$\mathcal{U}$(0, 1)	0.1946	(0.1946, 0.1946)	-4.823
p_1^*	$\mathcal{U}$(-7, 3)	0.0004407	(0.0004406, 0.0004408)	-4.738
p_2	$\mathcal{U}$(1e-7, 0.4)	0.01991	(0.01991, 0.01992)	-3.816
p_3^*	$\mathcal{U}$(-7, 3)	5.662e-7	(5.661e-7, 5.663e-7)	-5.01
p_4	$\mathcal{U}$(1e-7, 0.4)	0.07792	(0.07792, 0.07792)	-4.755

Table A.27: Summary of results for parameters of HL1-6 I_f. *Parameters were searched in $\log_{10}$ space and are presented in linear space. The prior for these parameters is still in the original $\log_{10}$ space.

Name	Prior	Median	89% HPDI	$\log_{10}$RSD
g_{K1}	$\mathcal{U}$(0, 1)	0.06128	(0.06128, 0.06128)	-8.896
p_1^*	$\mathcal{U}$(-7, 3)	0.02438	(1.393e-6, 68.59)	0.2135
p_2	$\mathcal{U}$(1e-7, 0.4)	0.02152	(0.002639, 0.04179)	-0.2316
p_3^*	$\mathcal{U}$(-7, 3)	0.001753	(1.002e-7, 4.933)	-0.02473
p_4	$\mathcal{U}$(1e-7, 0.4)	0.02438	(0.004115, 0.04327)	-0.2583

Table A.28: Summary of results for parameters of HL1-6 I_{K1}. *Parameters were searched in $\log_{10}$ space and are presented in linear space. The prior for these parameters is still in the original $\log_{10}$ space.

Name	Prior	Median	89% HPDI	$\log_{10}$RSD
$K_{\mathrm{m,CaL}}$	$\mathcal{U}(0, 2)$	0.2292	(0.07568, 0.3282)	-0.4428
$a^*_{\mathrm{inact,Ca}}$	$\mathcal{U}(-3, 0)$	0.1941	(0.007558, 0.7183)	-0.2286
k_{NCX}	$\mathcal{U}(0, 20)$	2.094	(0.2, 5.151)	-0.1155
η	$\mathcal{U}(0, 1)$	0.779	(0.01487, 0.9678)	-0.3392
$I_{\mathrm{max,NaK}}$	$\mathcal{U}(0, 5)$	1.277	(0.002799, 2.678)	-0.136
V_{max}	$\mathcal{U}(0, 5)$	3.259	(1.865, 4.786)	-0.5329
k^*_{RyR}	$\mathcal{U}(-2, 1)$	1.676	(0.08006, 6.558)	0.417
k_{open}	$\mathcal{U}(0, 10)$	6.007	(1.758, 9.532)	-0.3325
k_{close}	$\mathcal{U}(0, 1)$	0.4286	(0.2153, 0.9831)	-0.2907
g_{pCa}	$\mathcal{U}(0, 5)$	1.042	(0.3335, 1.759)	-0.3424
g^*_{Nab}	$\mathcal{U}(-3, -1)$	0.004308	(0.00276, 0.005551)	-1.363
g^*_{Cab}	$\mathcal{U}(-4, -2)$	0.001034	(0.0001876, 0.001626)	-1.093
$\mathrm{Buf}_{\mathrm{tot,i}}$	$\mathcal{U}(0, 100)$	11.21	(5.536, 20.5)	-0.3522
$K_{\mathrm{m,Buf,i}}$	$\mathcal{U}(0, 2)$	1.144	(0.4205, 1.99)	-0.2808

Table A.29: Summary of results for parameters of HL1-6 whole cell model. *Parameters were searched in $\log_{10}$ space and are presented in linear space. The prior for these parameters is still in the original $\log_{10}$ space.

A.4 Derivation of the cable equation

The following derivation is adapted from [2].

We first consider a cable of cylindrical cells in a cylindrical coordinate system with radial, angular and length axes, $\mathbf{x} = (r, \theta, x)$. The cable can be viewed as a cylindrical membrane around a cytoplasmic space. We assume that the potential is constant in r and θ and only varies along the length of the cable, x, allowing it to be viewed as a one-dimensional problem.

The cable is divided into iso-potential discrete sections with length dx. In any of these sections the currents must balance. The current is composed of axial and transmembrane components. The axial component is assumed to vary linearly with the axial voltage (i.e. it is a linear ohmic current) and itself has intracellular and extracellular components:

$$\begin{aligned} V_i(x + dx) - V_i(x) &= -I_i(x) r_i dx, \\ V_e(x + dx) - V_e(x) &= -I_e(x) r_e dx, \end{aligned} \tag{A.1}$$

where V_i and V_e are intra- and extracellular voltages (mV), I_i and I_e are the intra- and extracellular components of the axial current (μA), and r_i and r_e are the resistances per unit length of the intra- and extracellular space respectively (kΩ/cm). Positive current is defined as positive charges moving in the positive axis direction.

The resistances per unit length are defined as

$$\begin{aligned} r_i &= \frac{R_i}{A_i}, \\ r_e &= \frac{R_e}{A_e}, \end{aligned} \tag{A.2}$$

where R_i and R_e are the resistivities of the intra- and extracellular media (kΩ cm), and A_i and A_e are the corresponding cross-sectional areas of each space (cm^2). Thus if the cable is considered to sit in a large bath, the extracellular resistance per unit length will be close to zero.

In the limit $dx \to 0$ and rearranging, Equation A.1 becomes

$$\begin{aligned} I_i &= -\frac{1}{r_i}\frac{\partial V_i}{\partial x}, \\ I_e &= -\frac{1}{r_e}\frac{\partial V_e}{\partial x}. \end{aligned} \tag{A.3}$$

By Kirchoff's laws, the change in axial current in the intra- or extracellular spaces must be equal to the transmembrane (radial) current, therefore

$$I_i(x) - I_i(x+dx) = I_t dx = I_e(x+dx) - I_e(x), \tag{A.4}$$

where I_t is the transmembrane current per unit length of membrane (μA/cm). Taking the limit $dx \to 0$ reduces this equation to

$$I_t = -\frac{\partial I_i}{\partial x} = \frac{\partial I_e}{\partial x}, \tag{A.5}$$

where we have defined I_t as a positive outward current. I_t is also equal to the sum of capacitive and ionic currents across the membrane,

$$I_t = p\left(C_m \frac{\partial V_m}{\partial t} + I_{\text{ion}}\right), \tag{A.6}$$

where p is the perimeter of the cable (cm), C_m is the membrane capacitance per unit area (μF/cm^2), V_m is the transmembrane potential defined $V_m = V_i - V_e$ (mV) and I_{ion} is the ionic current per unit area μA/cm^2. Generally, I_{ion} is a function of several cellular variables as outlined in Chapters 3 and 4.

Equating Equations A.4 and A.6, we arrive at the standard form of the cable equation:

$$p\left(C_m \frac{\partial V_m}{\partial t} + I_{\text{ion}}\right) = \frac{\partial}{\partial x}\left(\frac{1}{r_i + r_e}\frac{\partial V_m}{\partial x}\right). \tag{A.7}$$

A.5 Derivation of constant transmembrane potential held at one end of 1D discretely-coupled cells

Both derivations are largely adapted from Keener [2], though the second derivation from that textbook has been corrected in Appendix A.6.

Firstly, considering the steady-state solution of a fibre of N cells length L coupled at their ends by (zero-length) gap junctions. At steady-state, we expect a decaying self-similar solution subject to $\mu V_i(x+L) = V_i(x)$ and $\mu V_e(x+L) = V_e(x)$ for some decay constant $\mu < 1$. The solution can be assumed to be in the form

$$\begin{pmatrix} V_i(x) \\ V_e(x) \end{pmatrix}_n = \mu^n \Phi(\xi) = \mu^n \begin{pmatrix} \phi_i(\xi) \\ \phi_e(\xi) \end{pmatrix}, \tag{A.8}$$

where $\xi = x - nL$ is the transformed coordinate within a cell and $\Phi(\xi)$ is the self-similar solution for intra- and extracellular potentials within a cell.

We define a self-similar transmembrane potential within a cell as $\phi_m = \phi_i - \phi_e$. Within a cell, at steady state $\frac{\partial \phi_m(\xi)}{\partial t} \to 0$. We also assume a passive problem, and so any ionic current is a passive ohmic current such that $I_{\text{ion}} = \frac{\phi_m}{R_m}$ where R_m is the resistance of a unit area of membrane (kΩ cm^2). Using the cable equation (Equation 5.1) with the above assumptions and rearranging obtains

$$\frac{\partial^2 \phi_m(\xi)}{\partial \xi^2} - \frac{p(r_i + r_e)}{R_m} \phi_m(\xi) = 0, \tag{A.9}$$

which is a second order ordinary differential equation. The solution for this equation is given by

$$\phi_m(\xi) = \alpha_1 \exp(\lambda \xi) + \alpha_2 \exp(-\lambda \xi), \tag{A.10}$$

with $\lambda^2 = \frac{p(r_i + r_e)}{R_m}$.

The total current in the passive cable of cells must be zero, giving $\frac{1}{r_i}\nabla\phi_i + \frac{1}{r_e}\nabla\phi_e = 0$,

leading to the general solutions for intra- and extracellular potentials within a cell:

$$\begin{aligned}\phi_i(\xi) &= \frac{r_i}{r_i + r_e}\phi_m(\xi) + \beta, \\ \phi_e(\xi) &= \frac{-r_e}{r_i + r_e}\phi_m(\xi) + \beta.\end{aligned} \tag{A.11}$$

To find solutions for α_1, α_2, β and μ, we consider the boundary conditions at either end of the cells. Current continuity is enforced in both the intra- and extracellular spaces:

$$\begin{aligned}\nabla\phi_i(L) &= \mu\nabla\phi_i(0), \\ \nabla\phi_e(L) &= \mu\nabla\phi_e(0).\end{aligned} \tag{A.12}$$

Potential continuity is enforced in only the extracellular domain. Between the intracellular domain of cells we use the gap junction jump condition. These conditions are therefore expressed as:

$$\begin{aligned}\phi_e(L) &= \mu\phi_e(0), \\ \mu\phi_i(0) - \phi_i(L) &= \frac{R_g}{r_i}\nabla\phi_i(L).\end{aligned} \tag{A.13}$$

With these conditions, the constants α_1, α_2 and β can be evaluated as:

$$\begin{aligned}\alpha_1 &= \mu - \exp(-\lambda L), \\ \alpha_2 &= \mu - \exp(\lambda L), \\ \beta &= \frac{2r_e}{r_e + r_i}\frac{(\mu - \exp(-\lambda L))(\mu - \exp(\lambda L))}{\mu - 1},\end{aligned} \tag{A.14}$$

and $\mu < 1$ is a solution to the characteristic equation

$$\mu^2 - (2C + K_g S)\mu + 1 = 0, \tag{A.15}$$

where $C = \cosh(\lambda L)$, $S = \sinh(\lambda L)$ and $K_g = \frac{R_g\lambda}{r_i + r_e}$.

A.6 Derivation of analytical solution to injected current into a cable of 1D discretely-coupled cells

A second analytical solution may be derived which considers a current injected into the extracellular space at one end of a cable of cells. When considering gap junctions, this solution exhibits the *sawtooth* potential where either ends of connected cells is depolarised/hyperpolarised depending on the direction of current flow. This is caused by the current following the path of least resistance and flowing into the extracellular space to pass high resistance gap junctions.

The solution can be derived by considering again the steady-state form of the cable equation (Equation 5.1). Current at the ends of the cable is injected into the extracellular space and thus our conditions at the cable end are

$$\begin{aligned} \frac{1}{r_i}\frac{dV_i}{dx} &= 0, \\ \frac{1}{r_e}\frac{dV_e}{dx} &= -I, \end{aligned} \tag{A.16}$$

on $x = 0, NL$. We reform equation for transmembrane potential along the cable into trigonometric terms for convenience:

$$V(x) = A\sinh(\lambda x) + B\cosh(\lambda x), \tag{A.17}$$

where A and B are constants to be determined and λ is as in Appendix A.5 ($\lambda^2 = \frac{p(r_i+r_e)}{R_m}$).

At any point in the cable, the sum of the intra- and extracellular currents must be equal to the injected current, i.e. $-\frac{1}{r_e}\nabla\phi_e - \frac{1}{r_c}\nabla\phi_i = I$. The equations for intra- and extracellular potentials along the cable can be formulated as

$$\begin{pmatrix} \phi_i \\ \phi_e \end{pmatrix} = \frac{1}{r_e + r_i}\begin{pmatrix} r_i \\ -r_e \end{pmatrix}(A\sinh\lambda x + B\cosh\lambda x) + \begin{pmatrix} 1 \\ 1 \end{pmatrix}(-\beta I x + \gamma), \tag{A.18}$$

where γ is a constant to be determined and $\beta = \frac{r_i r_e}{r_i + r_e}$.

To solve for A, B and γ, we set $\psi = \frac{1}{r_i}\nabla\phi_i(0)$. Taking the derivative of the first row

of Equation A.18, this gives $A = a\psi + J$ where $a = \frac{r_i + r_e}{\lambda}$ and $J = \frac{r_e I}{\lambda}$.

We now consider N cells in the cable and denote ψ_n, γ_n and B_n as the values of ψ, γ and B in the nth cell where $n = 0, 1, ..., N-1$. The requirement of no intracellular current injected into the intracellular space is equivalent to $\psi_0 = \psi_N = 0$ (not $\psi_{N-1} = 0$ as ψ governs the current entering the 'left-side' of the cell, therefore we have no current entering the left-side of a ghost cell outside the domain beyond the rightmost cell to enforce no intracellular current at right boundary).

To solve for the remainder of the constants, we consider the conditions between cell domains. Enforcing either extracellular and intracellular current continuity ($\nabla\phi_{j,n}(L) = \nabla\phi_{j,n+1}(0)$ for $j = i, e$) reduces Equation A.18 to the same result:

$$a\psi_{n+1} = a\psi_n C + B_n S - J(1 - C), \tag{A.19}$$

where $C = \cosh(\lambda L)$ and $S = \sinh(\lambda L)$.

Enforcing continuity of extracellular potential ($\phi_{e,n}(L) = \phi_{e,n+1}(0)$) gives

$$\gamma_{n+1} - \gamma_n = \frac{\beta}{r_i}(B_{n+1} - B_n C - (a\psi_n + J)S) - I\beta L. \tag{A.20}$$

If we substitute the intracellular gap junction condition ($\frac{\phi_{i,n+1}(0) - \phi_{i,n}(L)}{R_g} = \frac{1}{r_i}\nabla\phi_{i,n}(L)$) into the equation for the sum of currents in the cable ($-\frac{1}{r_e}\nabla\phi_{e,n}(L) - \frac{1}{r_c}\nabla\phi_{i,n}(L) = I$) we obtain

$$\gamma_{n+1} - \gamma_n = K_g(a\psi_n C + B_n S - J(1 - C)) - \frac{\beta}{r_e}(B_{n+1} - (a\psi_n + J)S - B_n C) - I\beta L, \tag{A.21}$$

where $K_g = \frac{R_g \lambda}{r_i + r_e}$.

Solving Equations A.20 and A.21 gives separate equations for B_{n+1} and γ_{n+1} in terms of only values in cell n:

$$\begin{aligned} B_{n+1} &= (S + K_g C)a\psi_n + (C + K_g S)B_n - J(K_g(1 - C) - S), \\ \gamma_{n+1} &= \gamma_n - \lambda L\frac{\beta}{r_e}J + \frac{\beta}{r_i}K_g(a\psi_n C + B_n S + J(C - 1)). \end{aligned} \tag{A.22}$$

We can reform the equations for $a\psi_{n+1}$ (Equation A.19) and B_{n+1} (Equation A.22) into a matrix system:

$$\begin{pmatrix} a\psi \\ B \end{pmatrix}_{n+1} = \underbrace{\begin{pmatrix} C & S \\ S + K_g C & C + K_g S \end{pmatrix}}_{X} \begin{pmatrix} a\psi \\ B \end{pmatrix}_{n} - J \begin{pmatrix} 1 - C \\ K_g(1 - C) - S \end{pmatrix}. \tag{A.23}$$

To solve this system, we note that matrix X has eigenvalues $\eta_1 = \frac{1}{\mu} > 1$ and $\eta_2 = \mu$, where μ is the root of the characteristic equation A.15, and eigenvectors

$$\nu_i = \begin{pmatrix} S \\ \eta_i - C \end{pmatrix}. \tag{A.24}$$

We can replace the solution as a linear combination of the eigenvectors such that

$$\begin{pmatrix} a\psi \\ B \end{pmatrix}_{n} = \sum_{i=1}^{2} \alpha_{i,n} \nu_i, \tag{A.25}$$

and the right-hand side of the matrix problem as

$$\begin{pmatrix} 1 - C \\ K_g(1 - C) - S \end{pmatrix} = \sum_{i=1}^{2} c_i \nu_i. \tag{A.26}$$

The matrix system in Equation A.23 then becomes

$$\sum_{i=1}^{2} \alpha_{i,n+1} \nu_i = X \sum_{i=1}^{2} \alpha_{i,n} \nu_i - J \sum_{i=1}^{2} c_i \nu_i, \tag{A.27}$$

which (using the eigen property of matrix X and removing the sums) can be reduced to two recursive problems:

$$\alpha_{i,n+1} = \alpha_{i,n} \eta_i - J c_i, \qquad i = \{1, 2\}, \tag{A.28}$$

supplemented with the conditions $\alpha_{1,0} + \alpha_{2,0} = 0$ and $\alpha_{1,N} + \alpha_{2,N} = 0$. This problem has

the general solution

$$\alpha_{i,n} = (-1)^i \alpha_0 \eta_i^n - J\frac{\eta_i^n - 1}{\eta_i - 1}, \tag{A.29}$$

which automatically satisfies the first boundary condition. The constant α_0 can be discovered by enforcing the second boundary condition:

$$\alpha_0 = -J\frac{\mu}{1-\mu}\frac{\mu^N - 1}{\mu^{2N} - 1}\left(c_1 + c_2\mu^{N-1}\right), \tag{A.30}$$

where we have used the relationship between the eigenvalues and μ to reduce the equation.

Using these solutions with Equation A.25 and A.26 we arrive at a solution to the matrix system in Equation A.23:

$$\begin{aligned}
a\psi_n &= \frac{JS}{1-\mu}(c_1\mu - c_2)f_n, \\
B_n &= \frac{-J}{1-\mu}\left[(c_1\mu - c_2)\left(Cf_n + \frac{\mu^{n+1} + \mu^{N-n-1}}{1+\mu^N}\right) - (c_1 - c_2\mu)\right], \\
\gamma_{n+1} &= \gamma_n - \lambda L\frac{\beta}{r_e}J + \frac{\beta}{r_i}K_g(a\psi_n C + B_n S + J(C-1)), \\
f_n &= \frac{1 - \mu^{N-n} - \mu^n + \mu^N}{1+\mu^N}, \\
c_i &= \frac{C - 1 + \eta_i[C - 1 - K_g CS + S(K_g - 2S)]}{S(\eta_i^2 - 1)},
\end{aligned} \tag{A.31}$$

where the value of γ_0 can be chosen to fix a particular solution for the Neumann problem (e.g. to fix $\phi_e(0) = 0$ it can be shown that $\gamma_0 = \frac{r_e}{r_e + r_i}B_0$).